

UC Berkeley

UC Berkeley Electronic Theses and Dissertations

Title

Computationally-Driven Investigations Towards Better Gas Adsorption Materials

Permalink

<https://escholarship.org/uc/item/3bh08012>

Author

Mercado, Rocio

Publication Date

2018

Peer reviewed|Thesis/dissertation

**Computationally-Driven Investigations Towards Better Gas Adsorption
Materials**

by

Rocio Mercado

A dissertation submitted in partial satisfaction of the

requirements for the degree of

Doctor of Philosophy

in

Chemistry

in the

Graduate Division

of the

University of California, Berkeley

Committee in charge:

Professor Berend Smit, Chair

Professor Jeffrey A. Reimer

Professor Phillip Geissler

Professor Jeffrey R. Long

Summer 2018

**Computationally-Driven Investigations Towards Better Gas Adsorption
Materials**

Copyright 2018
by
Rocio Mercado

Abstract

Computationally-Driven Investigations Towards Better Gas Adsorption Materials

by

Rocio Mercado

Doctor of Philosophy in Chemistry

University of California, Berkeley

Professor Berend Smit, Chair

In this thesis, I investigate nanoporous materials such as metal-organic frameworks (MOFs) and covalent organic frameworks (COFs) for various gas adsorption applications using a wide array of computational methods. These types of materials are ideal for gas adsorption and separation applications due to their large internal surface areas and tunable chemistry. They are also ideally suited to study using traditional computational methods due to their well-defined structures.

In the first chapter, I introduce nanoporous materials and the various molecular mechanics methods which can be used to study them. I also introduce the topic of *in silico* materials design. Then, in the next chapter, I discuss the development of a DFT-derived force field to accurately study the gas adsorption behavior in materials which contain coordinatively unsaturated metal sites. In such materials, the most commonly used methods fail to accurately model adsorption behavior, and the introduction of the DFT-derived force field has allowed the study of flue-gas mixtures in these frameworks.

Following this work, in the third chapter we discuss the use of the DFT-derived force field to study the dynamical behavior of greenhouse gases in the same MOF series. Much of this work was done in collaboration with experimentalists who used NMR as their primary tool to probe the dynamics of these gases in the materials. Our molecular dynamics simulations complemented their NMR experiments.

In the fourth chapter, I switch gears and discuss the use of computational methods for the design of new materials, first to characterize experimentally synthesized materials, and then to construct a database of thousands of new COF structures. Finally, I conclude by sharing a summary of my findings from the various investigations discussed in this thesis and my future outlook for the field.

Contents

Contents	i
1 Introduction	1
1.1 Nanoporous Materials and Their Applications	1
1.2 Molecular Simulation Methods Used to Study Nanoporous Materials	2
2 Accurately Modeling Adsorption Behavior in MOFs	9
2.1 Existing Models Fail to Predict Gas Adsorption Behavior	9
2.2 Force Field Development from Periodic DFT Calculations	10
3 Studying Diffusion Using the DFT-Derived FF	39
3.1 Diffusive Anisotropy of Carbon Dioxide in $M_2(\text{dobdc})$	39
3.2 The Effect of the Coordinatively Unsaturated Metal Sites on CH_4 Diffusion in $M_2(\text{dobdc})$	45
4 <i>In Silico</i> Design of Nanoporous Materials	56
4.1 Enhanced Carbon Capture Using Multifunctionalized COPs	56
4.2 Design of 2D and 3D COFs for ANG Storage Applications	73
5 Summary and Future Outlook	103
A List of Abbreviations	104
B Additional Information for Chapter 2	105
C Additional Information for Chapter 3	152
C.1 Simulation Structures	152
C.2 GCMC Results	153
C.3 Self-diffusion Coefficients	160
C.4 CH_4 Binding Site Analysis	165
D Hypothetical COP-5 Structures	168

E	Additional Information for COF Database	177
E.1	<i>In Silico</i> Bond Formation using Zeo++	177
E.2	Structural Optimization in LAMMPS	178
E.3	Removing Poorly Converged Structures	179
E.4	Lists of Linkers in Library	180
E.5	Additional Investigation of Experimentally Synthesized Examples	191
E.6	Additional GCMC Results	192
E.7	GCMC Simulation Error	199
E.8	List of Topological Nets Used	201
E.9	Ranking of ANG Storage Materials	202
E.10	Estimate of Computational Time Used	217
E.11	ARPA-E MOVE Program ANG Storage Target	219
	Bibliography	220

Acknowledgments

First, thanks to my advisor, Prof. Berend Smit, for advising me during the past five years and helping me to grow into an independent researcher. I have thoroughly benefited from my experience in both the MolSim and LSMO groups, both personally and academically. Additionally, I should acknowledge some key people who taught me a lot about computational chemistry during the beginning of my PhD by directly mentoring me on my first projects: these would be Dr. Bess Vlasisavljevich, Dr. Cory Simon, and Dr. Li-Chiang Lin. Thanks to their help and patience I was able to start working on really interesting projects as soon as I joined the group.

I would also like to thank Prof. Jeff Reimer for fruitful collaborations studying methane and carbon dioxide diffusion in MOFs, as well as members of their groups, particularly Alex Forse and Velencia Witherspoon. I would also like to thank Prof. Jeff Long and everyone I've collaborated with in the Long group. In addition, I would like to thank my collaborators at BUCT – Zhonghua Xiang, Hui Wang, Zhanhu Guo, Wenchuan Wang, and Dapeng Cao. More recently, it has been great working with Ray Fu, Leopold Talirz, and Sasha Yakutovich on building a database of covalent-organic frameworks and making it accessible to other researchers online. It has also been a pleasure working with Efrem Braun, Johanna Huck, and Sudi Jawahery on a variety of recently completed projects. I would also like to thank Maciej Haranczyk for his advice and collaboration.

Finally, I would like to thank all my labmates: Amber, Andres, Bess, Cory, Daniele, Davide, Daiane, Efrem, Gloria, Greg, Henglu, Igor, Johanna, Katie, Kyuho, Leo, Lennart, Li-Chiang, Matt, Mohamad, Michelle, Pete, Olga, Ozge, Ray, Sasha, Senja, Shachi, Sondre, Sudi, Yongjin, and Zhi. Thanks also to Kristin Stangl for all of her support these past four years.

Regarding funding, this work could not have been carried out without support from a Chancellor's Graduate Research Fellowship, which supported me for the first two years of my PhD, and an NSF Graduate Research Fellowship (under grant numbers DGE 1752814 and DGE 1106400) which supported me for the final three years of my PhD. Additionally, it should be acknowledged that much of this research was funded through the Center for Gas Separations Relevant to Clean Energy Technologies, an Energy Frontier Research Center funded by the U.S. Department of Energy, Office of Science, Office of Basic Energy Sciences under Award DE-SC0001015. Parts of this research also used resources of the National Energy Research Scientific Computing Center (NERSC), a DOE Office of Science User Facility supported by the Office of Science of the U.S. Department of Energy under Contract No. DE-AC02-05CH11231.

Last but not least, I would like to thank everyone else who has supported me throughout the past five years, including my family and friends.

Chapter 1

Introduction

1.1 Nanoporous Materials and Their Applications

The field of nanoporous materials has exploded since the publication of the first porous metal-organic framework (MOF) almost exactly 20 years ago. [124, 84]

Since then, the field of *reticular chemistry*, founded on the simple idea of linking organic and inorganic building blocks through strong bonds to form extended, usually crystalline, porous networks, has exploded, leading to the discovery of tens of different classes of materials; in addition to MOFs, there are now also conjugated microporous polymers (CMPs), covalent-organic frameworks (COFs), covalent organic polymers (COPs), porous aromatic frameworks (PAFs), polymers of intrinsic microporosity (PIMs), porous polymer networks (PPNs), and zeolitic imidazolate frameworks (ZIFs). Within each class of materials, the field has grown through the synthesis and characterization of new structures, often in combination with studies seeking high-performing materials for applications such as carbon capture, methane storage, nuclear fuel reprocessing, catalysis, semiconductors, and sensing, to name a few.

For example, diamine-appended variants of the MOF $\text{Mg}_2(\text{dobpdc})$ ($\text{dobpdc}^{4-} = 4,4'$ -dioxidobiphenyl-3,3'-dicarboxylate) have demonstrated high carbon dioxide capacities and selectivities due to the cooperative insertion of carbon dioxide into the metal-amine bonds. Due to their unique adsorption mechanism, materials in this family have a low projected energy cost for carbon capture, making them competitive with with state-of-the-art amine-scrubbing methods and illustrating the potential of nanoporous materials as competitive adsorbents for carbon dioxide separations. [156, 199] Similarly, nanoporous materials have also shown promise in the field of noble gas separations; through a combination of virtual screenings and experimental measurements, the MOF SBMOF-1 was shown to have by far the highest reported xenon adsorption capacity of any published nanoporous material and a remarkable Xe/Kr selectivity under conditions pertinent to nuclear fuel reprocessing.[6]

One of the most powerful features of advanced nanoporous materials is how a small number of building blocks (e.g. metal salts, small organic molecules) can be combined

through crystal engineering techniques into various topologies to yield a seemingly infinite space of potential structures to explore. By combining different molecular building blocks, researchers can achieve incredible tunability over the chemical and geometric properties of the nanoporous materials they synthesize, enabling them to be optimized and tailored to specific applications.

However, in asking how one can design a material with great (*fill-in-the-blank*) capabilities, the reality is that the space of features one can tune in a material is so large that manually designing the best material for a given application is not practical in the age of supercomputers and big data. For this reason, computational methods have played an important role in the design and discovery of new high-performing materials. Through the development of computational models, *in silico* structure assembly, and virtual screenings, all of which will be discussed in this thesis, computational chemists contribute important leaps in information to the field of nanoporous materials. As computers have revolutionized the drug discovery landscape in the pharmaceutical industry, bringing you safer, more effective drugs from concept to market sooner, so too are computers restructuring the way in which we can now more efficiently and rationally design materials.

Before going into the specific projects to be covered in this dissertation, I will first go over the basics of some of the most common computational chemistry methods used in the study of nanoporous materials. All of these methods have played an essential role in each project discussed in the chapters that follow.

1.2 Molecular Simulation Methods Used to Study Nanoporous Materials

Force Fields

In the context of nanoporous materials, *force fields* are used in classical simulations to define the interaction energies computed between atoms in a framework, and, potentially, any adsorbate molecules present. Generally, force fields can be written as complex mathematical expressions representing the interaction energy of a system as a function of the atomic coordinates of the system.

A classical functional form for estimating the interaction energy of a system in computational chemistry was first given by Lifson in the 1960's [11]; in that work, the authors parameterized an interatomic potential to predict the molecular structures and strain energies of cycloalkanes. Following their success, more generic, all-atom force fields have since been developed to model the physics of organic molecules and proteins, of which many of these models are still being used to date.[189, 152, 136, 221] Although we now have access to significantly more powerful computers than we did 50 years ago, researchers are still using and actively developing classical force fields to estimate the thermodynamic properties in proteins, drug targets, and nanoporous materials due to their computational efficiency over higher levels of theory.

A force field is specified by defining by two things: 1) a functional form and 2) a set of corresponding parameters. The functional form and set of parameters may be chosen or derived to best reproduce experimental measurements, *ab initio* calculations, or both. The basic functional form of the potential energy in most molecular mechanics force fields relevant to nanoporous materials include *nonbonded* terms that describe the van der Waals forces and long-range electrostatics, and *bonded* terms which describe the interactions of atoms that are linked by covalent bonds (the latter are especially important when the flexibility of a material is non-negligible). Ignoring the specific functional form of each of these terms, then the general form for the total interaction energy is of the form

$$U_{\text{total}} = U_{\text{nonbonded}} + U_{\text{bonded}} \quad (1.1)$$

where $U_{\text{nonbonded}} = U_{\text{electrostatics}} + U_{\text{van der Waals}}$ and $U_{\text{bonded}} = U_{\text{bond}} + U_{\text{angle}} + U_{\text{torsional}}$. From the *bonded* terms, the bond and angle terms are usually modeled by harmonic potentials that do not allow bond breaking, such as Hooke's Law (Eq (1.2)),

$$U_{\text{bond}}(\vec{r}) = \sum_{\text{bonds}} \frac{k}{2} (r - r_0)^2, \quad (1.2)$$

where k is the force constant, r is the bond length and r_0 is the value for the bond length when all other terms in the force field are set to 0. A more accurate description of a covalent bond at higher stretching is possible through the use of the more expensive Morse potential (Eq (1.3)),

$$U_{\text{Morse}}(\vec{r}) = \sum_{\text{bonds}} D_e (1 - \exp^{-a(r-r_e)^2}), \quad (1.3)$$

where D_e is the well depth defined relative to the dissociated atoms, r is the distance between the atoms, r_e is the equilibrium bond distance, and a controls the width of the potential (the smaller a is, the larger the well). Usually a simple harmonic potential is enough to describe bonding interactions in nanoporous materials. On the other hand, the functional form for dihedral energy can be very different depending on the model; in this work, we use the following (Eq (1.4)) functional form to describe torsional interactions when optimizing structures with classical force fields,

$$U = K(1 + \cos(n\phi - d)), \quad (1.4)$$

where ϕ is the dihedral angle between a set of four atoms, n and d are integers, and K is in units of energy.

In actuality, the *nonbonded* terms are more computationally intensive than the *bonded* terms. The van der Waals term is usually calculated using either pairwise Lennard-Jones (Eq (1.5)) or Buckingham (Eq (1.6)) potentials, and the electrostatic term is usually treated using Coulomb's law (Eq (1.7)) in nanoporous materials. These potentials depend on the pairwise distances between all the atoms, r_{ij} , and on the identity of the atoms which in turn determine the remaining constants. To compute the interaction energy of the entire system, these potentials must then be summed over each pair of atoms in the system. For studying

gas separations in nanoporous materials, it is almost always sufficient to limit interactions to pairwise energies.

$$E_{ij} = 4\varepsilon_{ij} \left[\left(\frac{\sigma_{ij}}{r_{ij}} \right)^{12} - \left(\frac{\sigma_{ij}}{r_{ij}} \right)^6 \right] \quad (1.5)$$

$$E_{ij} = A_{ij} \exp^{-B_{ij}r_{ij}} - \frac{C_{ij}}{r_{ij}^6} \quad (1.6)$$

$$E_{ij} = \frac{q_i q_j}{4\pi\varepsilon_0 r_{ij}} \quad (1.7)$$

As mentioned above, in addition to the functional forms of the potentials, a force field also specifies a set of parameters for different types of atoms, chemical bonds, dihedral angles and so on. The parameter sets are usually empirical. For example, the metal centers of a material will be described using a different set of parameters than the carbon atoms. The typical parameter set includes values for the atomic masses, the van der Waals radii, the partial charges for individual atoms, and the equilibrium values of bond lengths, bond angles, and dihedral angles for each combination of bonded atoms, as well as values corresponding to the effective spring constant for each potential.

Most current force fields, including those used to study nanoporous materials, use a fixed-charge model by which each atom is assigned one value for the atomic charge that is not affected by the local electrostatic environment and remains constant throughout the simulation; active developments in next-generation force fields include better models for polarizability, in which an atom's charge can be influenced by electrostatic interactions with neighboring atoms. One example in which polarizability can be introduced into a model is via the use of Drude particles, which are massless, charge-carrying virtual particles linked by a harmonic oscillator potential to each polarizable atom. However, the widespread use of polarizability in classical force fields has been held back due to the larger computational expense associated with calculating the local electrostatic field each simulation cycle.

Different force field parameters can be derived from either *ab initio* electronic structure calculations, or from experimental data, such as enthalpy of vaporization, temperature at maximum density, dipole moments, or various spectroscopic parameters. [189, 152, 83, 140, 88, 87] In cases where a model works well generally but fails in a few select cases, it is possible to reparameterize the model to specifically model the energetics of this system more accurately without having to move to a more complicated functional form. In Chapter 2, we describe a practical method for reparameterizing a model using density functional theory (DFT) calculations.

While it is possible in molecular simulations to move away from the current molecular mechanics approaches by using quantum mechanics calculations to directly construct the interatomic potential and calculate the forces between atoms, classical force fields still have a huge advantage over such methods; because of their simple functional forms, they allow us to model systems with over tens of thousands of atoms using atomistic detail, sometimes even with incredible accuracy.

Grand Canonical Monte Carlo Simulations

Grand canonical Monte Carlo (GCMC) [63] is a Monte Carlo technique that allows researchers to model density fluctuations in a simulation box at fixed volume and temperature (i.e. the μVT ensemble). This is achieved by means of trial insertion, deletion, and exchange moves over the course of a simulation. Because of its computational efficiency and straightforward implementation, GCMC is the preferred ensemble for modeling bulk gas adsorption in rigid MOFs.

In a GCMC simulation, one first randomly chooses whether a trial insertion, deletion, or exchange move is attempted. In the case of a carbon dioxide molecule adsorbing in a MOF, this trial move would involve either placing or removing a carbon dioxide molecule in/from the pores of the framework. If insertion is chosen, a particle is placed with uniform probability density inside the system. If deletion is chosen, then one deletes one of the N particles in the system randomly. If exchange is chosen, then two particles are randomly selected from the system and their coordinates swapped. The trial move is then accepted or rejected according to the usual Metropolis acceptance rules,

$$\text{acc}(o \rightarrow n) = \min(1, q), \quad (1.8)$$

where o represents the old state of the system and n represents the new state of the system. q is given by

$$q = \frac{\alpha(n \rightarrow o)}{\alpha(o \rightarrow n)} \times \frac{p(n)}{p(o)}, \quad (1.9)$$

where $\alpha(i \rightarrow j)$ is the probability density of attempting a trial move from state i to state j and $p(i)$ is the probability density of state i . We can work out that in the case of distinguishable particles (as we have in a computer simulation) using a probability of 0.25 for both insertion and deletion moves, and 0.5 for exchange moves, $\alpha(N \rightarrow N) = 0.5$ for an exchange move, $\alpha(N \rightarrow N + 1) = 0.25V^{-1}$ for an insertion move, and $\alpha(N \rightarrow N - 1) = 0.25$ for a deletion move. The V^{-1} move comes about from placing the particle with uniform probability density anywhere in the simulation box.

To evaluate the acceptance rules of a given move then requires solving for the (classical) grand canonical probability density,

$$p(\vec{r}_1, \vec{r}_2, \dots, \vec{r}_N) = \frac{\Lambda^{-3N}}{N!} \exp^{\beta\mu N} \exp^{-\beta U_N}, \quad (1.10)$$

where N is the total number of particles, μ is the chemical potential, $\beta = 1/k_B T$, and Λ is the de Broglie thermal wavelength.

Therefore, for a trial *insertion* of a new particle, one obtains the following value for q ,

$$\begin{aligned}
q &= \frac{\alpha(N+1 \rightarrow N)}{\alpha(N \rightarrow N+1)} \times \frac{p(N+1)}{p(N)} \\
&= \frac{0.25}{0.25V^{-1}} \times \Lambda^{-3} \exp^{\beta\mu} \exp^{-\beta(U_{N+1}-U_N)},
\end{aligned}$$

leading to the following acceptance rule:

$$\text{acc}(N \rightarrow N+1) = \min \left(1, \frac{V e^{\beta\mu}}{(N+1)\Lambda^3} \exp^{-\beta(U_{N+1}-U_N)} \right).$$

For a trial *deletion*, one obtains the following value for q ,

$$\begin{aligned}
q &= \frac{\alpha(N-1 \rightarrow N)}{\alpha(N \rightarrow N-1)} \times \frac{p(N-1)}{p(N)} \\
&= \frac{0.25V^{-1}}{0.25} \times \Lambda^3 \exp^{-\beta\mu} \exp^{-\beta(U_{N-1}-U_N)},
\end{aligned}$$

and thus the following acceptance rule:

$$\text{acc}(N \rightarrow N-1) = \min \left(1, \frac{N\Lambda^3 \exp^{-\beta\mu}}{V} \exp^{-\beta(U_{N-1}-U_N)} \right).$$

Finally, for an *exchange* move, one obtains the following value for q ,

$$\begin{aligned}
q &= \frac{\alpha(N' \rightarrow N)}{\alpha(N \rightarrow N')} \times \frac{p(N')}{p(N)} \\
&= \frac{0.5}{0.5} \times \exp^{-\beta(U_{N'}-U_N)},
\end{aligned}$$

and thus the following acceptance rule:

$$\text{acc}(N \rightarrow N') = \min \left(1, \exp^{-\beta(U_{N'}-U_N)} \right).$$

In all GCMC simulations in this dissertation, U_N is computed using classical *force fields* (discussed above).

Molecular Dynamics Simulations

Because many molecular systems of practical importance typically consist of thousands of particles, it is impossible to determine the dynamics of such complex systems analytically. As a result, molecular dynamics (MD) [63] is an important computational method for studying the physics and time-evolution of large molecular systems. In MD, atoms and molecules

interact over a pre-defined time period, allowing us to study the dynamics of a system. In the field of nanoporous materials, MD is commonly used to study the diffusion of gases through a framework, as is done in Chapter 3. The trajectories of a system of interacting atoms are determined by numerically integrating Newton's equations of motion, where the forces between the particles are calculated using force fields.

Let \vec{r}^N denote the set of vectors that define the center of mass of each of the atoms in a system, such as a group of gas molecules adsorbed in the pores of a MOF. We can write out \vec{r}^N as $\{\vec{r}_1, \vec{r}_2, \dots, \vec{r}_N\}$. The particles in the system each have d degrees of freedom, where usually $d = 3$ for MD simulations of nanoporous materials. The N particles interact as defined by the force field chosen, which would specify a continuous interaction potential, $V(\vec{r}^N)$, for each pair of atoms. Defining the mass of each particle i as m_i and the total force acting on particle i at time t as F_i , Newton's equation of motion for each particle $i \in \{1, \dots, N\}$ can then be written as

$$F_i = m_i \frac{d^2 \vec{r}_i}{dt^2} = m_i \ddot{\vec{r}}_i. \quad (1.11)$$

Using only pairwise additive potentials, the force that a particle j exerts on particle i is

$$f_{ij} = -\nabla_i V(r_{ij}), \quad (1.12)$$

where $r_{ij} = \|\vec{r}_i - \vec{r}_j\|$ is the distance between a pair of atoms.

In the canonical (NVT) ensemble, the number of molecules (N), volume (V), and temperature (T) are conserved. The only quantity which is allowed to vary is the energy of the system, which is exchanged with a *thermostat*. One popular thermostating method, and the one used for all MD simulations in this work, is the use of a Nosé-Hoover thermostat or Nosé-Hoover chains; simulations using such thermostats are commonly used because of their accuracy and efficiency in constant-temperature MD simulations. In an equilibrium NVE MD simulation, the new molecular positions and velocities are obtained by integrating Newton's equation of motion numerically for each atom (Eq (1.11)). This results in a set of $d \times N$ coupled second-order ordinary differential equations and $d \times N$ degrees of freedom. The equations are discretized and new positions and velocities for each atom are found numerically by integrating forward in time according to the following general algorithm:

1. Begin by specifying the initial conditions (number of particles N , initial temperature T , time-step, boundary conditions, force field, molecular connectivity, density, etc).
2. Then, specify all the atomic positions, \vec{r}_i , and assign them initial velocities, \vec{v}_i .
3. Then, for the specified number of time-steps:
 - a) Compute all forces, energies, and the temperature (in the NVT ensemble).
 - b) Integrate the equations of motion and update the positions and velocities of all atoms in the system. How this is done in practice will depend on the MD integrator used.

- c) Sample system properties at regular intervals, rescaling velocities if necessary.

After the trajectories are complete, they can be further analyzed to compute other thermodynamic properties, such as diffusion coefficients from the mean-squared displacements of the adsorbed gas molecules. This additional analysis, including the visualisation of the trajectories can be just as computationally expensive as producing the trajectories themselves. Furthermore, it is not trivial to obtain a canonical ensemble distribution of conformations and velocities using these algorithms. This heavily depends on the system size, the time-step used, the thermostat choice and parameters, and the integrator used.

***In Silico* Structure Assembly**

In order to be able to use any of the above methods, one must first have a molecular structure of the framework to be studied. Often these can be attained through X-ray diffraction experiments; however, sometimes, it is not possible to isolate ordered or pure enough crystals of a material, in which case a crystal structure cannot be solved for that material. Additionally, sometimes we would like to study structures which have never been synthesized before. For both of these reasons, *in silico* structure assembly is a powerful tool that can be used to characterize and create new nanoporous materials.

Although there exist various methods for *in silico* structure assembly [201], the method we describe herein (Chapter 4) takes place in seven steps:

1. The linker chemistry to be mimicked in the *in silico* assembly process is selected.
2. The linkers to be used in assembling the structures are constructed.
3. Topological nets are obtained from the Reticular Chemistry Structure Resource. [172]
4. The linkers and nets are assembled into frameworks using Zeo++. [142, 230]
5. The energies of the assembled structures are optimized using either classical force fields, semiempirical methods, or *ab initio* methods.
6. Structures which do not converge or contain extraneous bonds are removed.
7. Interpenetrated structures are assembled from the frameworks.

The successfully assembled structures can then be used in classical molecular simulations, such as the type of GCMC or MD simulations discussed above, to compute relevant thermodynamic properties. For gas separations in nanoporous materials, these are typically the equilibrium gas uptake or the heat of adsorption of a molecule (at a given pressure).

Chapter 2

Accurately Modeling Adsorption Behavior in MOFs with Coordinatively Unsaturated Metal Sites

2.1 Existing Models Fail to Predict Gas Adsorption Behavior

By 2014, it had been extensively demonstrated that while generic, classical force fields such as UFF and Dreiding worked very well for modeling adsorption in most nanoporous materials, they failed in the cases of adsorption in materials with open-metal sites, such as HKUST-1 and the $M_2(\text{dobdc})$ series, also known as MOF-74 and M-CPO-27 in the literature.[68, 16, 51, 129, 201]

Previous work by other researchers had aimed to resolve this issue by reparameterizing these force fields to reproduce the desired properties in MOFs, as with the development of BTW-FF,[18] or by reparameterizing only the potentials involved with the problematic materials. Recently, many researchers have reparameterized existing models using *ab initio* electronic structure calculations.[28, 54, 75, 16] Notably, force fields generalizable to coordinatively unsaturated metal site structures from only a small number of single-point electronic structure calculations have been developed to study CO_2 adsorption in MOFs using Møller-Plesset second-order perturbation theory (MP2).[51, 129] In [51], quantum calculations based on a non-empirical model potential (NEMO) decomposition of the total energy of the $\text{Mg}_2(\text{dobdc})\text{-CO}_2$ and $\text{Mg}_2(\text{dobdc})\text{-N}_2$ systems were decomposed into electrostatic, repulsive and attractive contributions (include dispersion, exchange interactions, and polarization) before reparameterization. While better reproducing the adsorption behavior of these gases in $\text{Mg}_2(\text{dobdc})$, the use of cluster calculations constrains the methodology and prevents it from being easily transferable to other systems. In [129], these constraints

were eliminated via the use of density functional theory (DFT) calculations with periodic boundary conditions; this reparameterization scheme led to force fields that not only correctly predicted the adsorption isotherms of CO₂ and H₂O in Mg- and Zn₂(dobdc), but also the binding geometries and transport properties. As such, we chose to extend upon this methodology by applying it not only to the combination of CO₂ and H₂O in the Mg- and Zn₂(dobdc) frameworks, but also to CH₄, an important flue gas component, in these and the remaining first-row transition metal M₂(dobdc) analogues.

2.2 Force Field Development from Periodic DFT Calculations

Overview

In this work [163], we develop accurate force fields from DFT calculations with periodic boundary conditions for use in molecular simulations involving M₂(dobdc) (M₂(dobdc); dobdc⁴⁻ = 2,5-dioxidobenzenedicarboxylate; M = Mg, Mn, Fe, Co, Ni, Zn) and frameworks of similar topology. In these systems, conventional force fields fail to accurately model gas adsorption due to the strongly binding coordinatively unsaturated metal sites. The DFT-derived force fields predict the adsorption of CO₂, H₂O, and CH₄ inside these frameworks much more accurately than other common force fields. We show that these force fields can also be used for M₂(dobpdc) (dobpdc⁴⁻ = 4,4'-dioxidobiphenyl-3,3'-dicarboxylate), an extended version of M₂(dobdc), and thus are a promising alternative to common force fields for studying materials similar to M₂(dobdc) for carbon capture applications. Furthermore, it is anticipated that the approach can be applied to other metal-organic framework topologies to obtain force fields for different systems. We have used this force field to study the effect of contaminants such as H₂O and N₂ upon these materials' performance for the separation of CO₂ from the emissions of natural gas reservoirs and coal-fired power plants. Specifically, mixture adsorption isotherms calculated with these DFT-derived force fields showed a significant reduction in the uptake of many gas components in the presence of even trace amounts of H₂O vapor. The extent to which the various gases are affected by the concentration of H₂O in the reservoir is quantitatively different for the different frameworks and is related to their heats of adsorption. Additionally, significant increases in CO₂ selectivities over CH₄ and N₂ are observed as the temperature of the system is lowered.

This section is based on the following publication:

Mercado, R., Vlasisavljevich, B., Lin, L.-C., Lee, K., Lee, Y., Mason, J.A., Xiao, D.J., Gonzalez, M.I., Kapelewski, M.T., Neaton, J.B., and Smit, B., 2016. Force Field Development from Periodic Density Functional Theory Calculations for Gas Separation Applications Using Metal-Organic Frameworks. *Journal of Physical Chemistry C*, 120, pp.12590-12604.

Introduction

Efficient separation of gas mixtures plays an important role in various industrial processes, such as the separation of carbon dioxide from coal-gas flues and of methane from natural gas feeds, both of which have significant environmental implications. Because of their large internal surface areas, preferential adsorption of certain gas components over others, and excellent tunability, metal-organic frameworks (MOFs) have been regarded as a promising class of materials for these and other gas separation applications (e.g. carbon capture, separations of hydrocarbon mixtures, noble gas separations). MOFs are nanoporous crystalline materials consisting of organic linkers and inorganic metal sites. These materials are also considered for gas storage applications such as hydrogen and methane storage.[19, 66, 35, 210, 104, 200]

$M_2(\text{dobdc})$ is a well-known metal-organic framework composed of either magnesium or first-row transition metal nodes ($M = \text{Mg, Mn, Fe, Co, Ni, Cu, or Zn}$) linked by 2,5-dioxido-1,4-benzenedicarboxylate (dobdc^{4-}) linkers to form one-dimensional hexagonal channels lined with coordinatively unsaturated metal sites (Figure 2.1).[192] This MOF has a large adsorption capacity and selectivity for CO_2 over many gases.[19, 210, 147, 242, 25, 164] During the crystallization of such frameworks from solution, solvent molecules directly coordinate to the metal sites. Once the MOF crystals are formed, the material is activated by removing these solvent molecules, leaving behind unsaturated metal sites (i.e. so-called open-metal sites). These coordinatively unsaturated metal sites provide strong binding for guest molecules and bestow the frameworks with remarkable capacities and selectivities for CO_2 over more weakly binding gases like N_2 or CH_4 . [187, 107, 128, 184, 119]

Because these coordinatively unsaturated metal site MOFs are high-performing materials for CO_2/N_2 separations, it is of fundamental interest to accurately describe the interactions of the gases with these coordinatively unsaturated metal sites. Knowledge of these interactions is of practical importance in molecular simulations. For example, screening huge libraries of both existing and hypothetical materials for CO_2 adsorption using Monte Carlo simulations can accelerate the discovery of materials that are both impervious to contaminants and have large capacities for CO_2 without spending valuable time synthesizing and testing materials that do not possess these qualities. Molecular simulations can be especially valuable when the synthesis of these materials is tricky or time-consuming.[126, 105, 114, 113] One of the challenges with using molecular simulations to accelerate the discovery of new materials is that common force fields, such as the Universal Force Field (UFF)[189] and the Dreiding force field[152], do not adequately describe the interaction strength between guest adsorbates and the coordinatively unsaturated metal sites present in many of these high-performing structures, yielding only a poor estimation of their gas adsorption and separation performances in molecular simulations. [114, 201] Motivated by the lack of adequate force fields for studying CO_2 separations in these systems, many groups have focused on developing better models and improving the accuracy of existing models for these systems using *ab initio* calculations.[28, 54, 75, 16] Similarly, in previous work, we have presented methodologies for developing force fields generalizable to coordinatively unsaturated metal

site structures from only a small number of single-point *ab initio* calculations using various levels of theory.[51, 129] We found that using DFT calculations with periodic boundary conditions removed any constraints imposed by the use of cluster calculations, and led to force fields that not only correctly predict adsorption isotherms but also binding geometries and transport properties.[129] Additionally, most of the first-row $M_2(\text{dobdc})$ frameworks are well studied experimentally, allowing for easy comparison between any new calculations and the assortment of existing data in the literature.

In previous work [129], the authors were limited to studying H_2O and CO_2 adsorption in Mg- and $Zn_2(\text{dobdc})$. Here, we extend that work to study H_2O , CO_2 , and CH_4 adsorption in six $M_2(\text{dobdc})$ ($M = \text{Mg, Mn, Fe, Co, Ni, and Zn}$) frameworks by developing force fields for the series of isostructural MOFs from DFT calculations with periodic boundary conditions. This allows us to obtain systematic insights on how changing the metal center affects the gas adsorption properties in $M_2(\text{dobdc})$.

Although these materials have been widely studied, the performance of $M_2(\text{dobdc})$ in the aforementioned gas separations remains largely unknown; moreover, equilibrium adsorption isotherms for mixtures of gases in MOFs were entirely absent from the literature until recently.[148] Given the challenges of measuring adsorption equilibria of gas mixtures, our force fields allow us to carefully study the interaction of gas mixtures with MOFs through the use of molecular simulations. We use our force fields to address the separation of CO_2 from other gases at conditions relevant to natural gas and post-combustion flue gas feeds. Additionally, we show that our force fields can be used to model adsorption in other frameworks with similar coordinatively unsaturated metal sites, such as $M_2(\text{dobpdc})$.

Methods

Overview. Our force fields were developed to model interactions between CH_4 , H_2O , and CO_2 with six $M_2(\text{dobdc})$ frameworks ($M = \text{Mg, Mn, Fe, Co, Ni, and Zn}$). Because of the challenge posed by the significant elongation observed in the apical oxygen-metal bond lengths in $Cu_2(\text{dobdc})$ (which leads to an elongation of the c -axis lattice constants when compared to the other $M_2(\text{dobdc})$ structures),[119] we chose not to develop force field parameters for $Cu_2(\text{dobdc})$ as that would require significant alterations to our fitting procedure.

First, we describe the types of force fields that were used. In cases where the pairwise nonbonding interactions between framework atoms and guest molecules were fit, we describe the potentials using Buckingham + Coulomb interactions (Eq (2.1)), where for each pair of atoms in the system five parameters are specified: A_{ij} , B_{ij} , C_{ij} , q_i , and q_j (the pre-exponential term, exponential term, attractive term, and point charges, respectively). This leads to the following expression for the interaction energy:

$$E_{ij} = \begin{cases} \infty, & \text{if } r_{ij} < R_{\min} \\ A_{ij} \exp^{-B_{ij}r_{ij}} - S_g \frac{C_{ij}}{r_{ij}^6} + \frac{q_i q_j}{4\pi\epsilon_0 r_{ij}}, & \text{if } r_{ij} \geq R_{\min}. \end{cases} \quad (2.1)$$

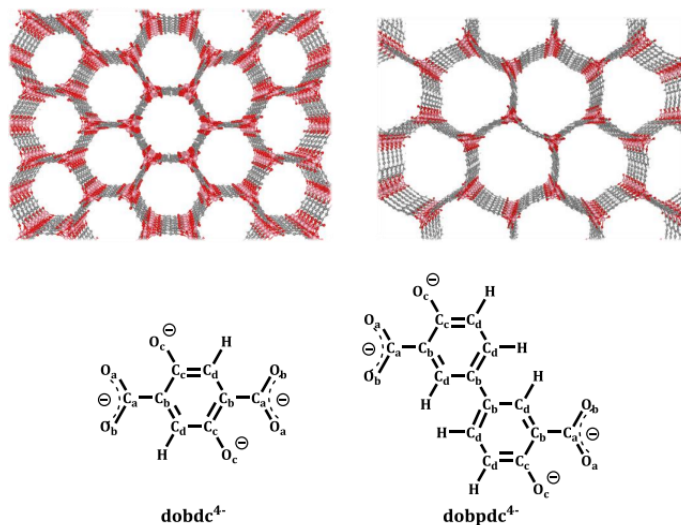


Figure 2.1: Definition of atom-types in the frameworks. $M_2(\text{dobdc})$ and ligand (left). $M_2(\text{dobpdc})$ and ligand (right). All metal atom-types and hydrogen atom-types are considered equivalent in the force fields for both sets of frameworks. Color key – M = pink, O = red, C = gray, H = white.

Here, r_{ij} is the distance between atoms i and j , ϵ_0 is the permittivity of free space, R_{\min} is used to prevent the conventional Buckingham potential from going to negative infinity at short distances, and S_g is a scaling factor.

This scaling factor was introduced in [129]. In the proposed approach, only the repulsive parameters are fit (A_{ij} and B_{ij}). Because the C_{ij} parameters are taken from the literature and the charges are chosen prior to fitting, the “repulsive” portion of the energy may turn out to be negative after the energy decomposition step. Because this would suggest that the attractive portion of the energy is not large enough, the smallest scaling factor required for the repulsive portion of the energy to be positive at all points is applied to the attractive term in the potential. This choice was tested and found to be reasonable in [129].

Interaction parameters were determined for the oxygen atoms in CO_2 interacting with all of the framework atoms except hydrogen. As the oxygen atoms dominate the interaction, we did not further refine the interaction parameters for the carbon in CO_2 with any framework atoms, and instead Lorentz-Berthelot mixing rules were used to determine Lennard-Jones parameters from UFF [189] and EPM2 [83] parameters. Interaction parameters were determined for both the hydrogen and the oxygen atoms in H_2O interacting with all framework atoms except hydrogen and O_a (for more details, please see the *Force Field Parameterization* section; for atom-type labels, see Figure 2.1).[129] O_a interaction parameters were left out of the parametrization loop to allow for convergence of the remaining interaction parameters. A united atom model was used for CH_4 , and interaction parameters were determined for CH_4 interactions with all framework atoms except hydrogen.

For guest-guest nonbonding interactions, as well as the specific nonbonding interactions

between the framework and guest atoms mentioned above as exceptions to the fitting procedure, Lennard-Jones + Coulomb potentials were used (Eq (2.2)).

$$E_{ij} = 4\varepsilon_{ij} \left[\left(\frac{\sigma_{ij}}{r_{ij}} \right)^{12} - \left(\frac{\sigma_{ij}}{r_{ij}} \right)^6 \right] + \frac{q_i q_j}{4\pi\varepsilon_0 r_{ij}} \quad (2.2)$$

Four parameters were specified for each pair of atoms in the system: ε_{ij} , σ_{ij} , q_i , and q_j (the energy parameter, distance parameter, and point charges, respectively). Lorentz-Berthelot mixing rules were employed to determine interactions between different atom-types from the UFF force field and the respective guest models (TraPPE for CH₄ [140], EPM2 for CO₂ [83], and TIP4P-Ew for H₂O [88, 87]). The point charges for the guest atoms were also adopted from the guest models.

In all simulations, frameworks and guest molecules were treated as rigid. More details regarding the fitting will be presented in the *Energy Decomposition* and *Force Field Parameterization* sections.

Structure Optimization. Geometry optimizations were performed for each framework using density functional theory with periodic boundary conditions as implemented in the Vienna *Ab initio* Simulation Package (VASP).[111] All DFT calculations were performed with PBE [182] and vdW-DF2 [118] functionals, a plane wave basis set, projector augmented wave (PAW) pseudopotentials, and periodic boundary conditions. [182, 112, 14] Spin polarized calculations were performed for Fe, Co, and Ni. The starting magnetic moments were chosen on the basis of the high spin state of the +2 oxidation state of each metal (4, 3, and 2 for Fe, Co, and Ni, respectively). The spins were ferromagnetically coupled down the *c*-axis and antiferromagnetically coupled across the *ab*-plane. For transition metals sites with unpaired electrons (Mn, Fe, Co, and Ni), on-site Hubbard-U corrections were employed with values of 3.8, 4.0, 3.3, and 6.4, respectively. These values have been previously determined to reproduce the oxidation energies of metal oxides.[227] The cutoff in the plane wave basis was taken to be 1000 eV, and Γ -point sampling was used.

Atom-Types Identification and Approaching Paths Determination. Force fields were fit for three different guests: CH₄, H₂O, and CO₂. In our force fields, each unique atom-type in the guest interacts differently with each unique atom-type in the framework, meaning that each pairwise interaction requires new A_{ij} , B_{ij} , and C_{ij} parameters as well as new point charges q_i and q_j . M₂(dobdc) is composed of four different elements: the metal atom-type, carbon, oxygen, and hydrogen. Considering the local environment of each element in the framework, there are three unique oxygen atom-types (O_a, O_b, O_c), and four unique carbon atom-types (C_a, C_b, C_c, C_d; Figure 2.1). All of the metal atoms and hydrogen atoms are in the same local environment in M₂(dobdc).

The first step in our methodology for fitting a given set of pairwise interaction parameters is to determine the approaching path of a given guest molecule toward the target atom-type. This orientation is determined by minimizing the repulsive energy between the guest molecule and other the framework atom-types (i.e. those that are not the target atom). This procedure ensures that the pairwise repulsive interaction between the guest molecule and the

target atom dominates the total repulsive energy. The UFF force field and guest force field (along with Lorentz-Berthelot mixing rules) are used to determine these paths. For each path, we use 31 configurations at 0.1 Å intervals apart (from 2.0 to 5.0 Å) to compute the interaction energy with DFT.

Interaction Energy Calculation. Once the approaching path has been determined between each pair of atoms, the interaction energies for each configuration along the path are computed using van der Waals corrected DFT and periodic boundary conditions. The interaction energy is defined as the difference in the energy between the MOF and bound guest molecule and their individual energies at infinite separation. Our DFT calculations were performed at the same level of theory as was used for the structure relaxation; however, we found that a dispersion-corrected functional is required to properly describe framework-guest interactions. For this reason, following ref [119], single-point calculations to determine total energies were performed for the framework alone with vdW-DF2.[118]

Energy Decomposition. The interaction energies for these configurations are then decomposed into long-range Coulomb interactions ($\sum_{ij} \frac{q_i q_j}{4\pi\epsilon_0 r_{ij}}$), short-range exchange repulsion ($\sum_{ij} -A_{ij} \exp^{-B_{ij} r_{ij}}$), and dispersion ($-\sum_{ij} S_g \frac{C_{ij}}{r_{ij}^6}$). The long-range Coulomb contribution is computed by employing the Ewald summation technique. Partial atomic charges for the framework atoms are computed using the REPEAT scheme [22] with the electrostatic potentials obtained from DFT-PBE for the structure relaxation of the framework atoms. Charges for the guest molecules are taken from the guest molecule models (i.e. TIP4P-Ew, EPM2, TraPPE). [83, 140, 88, 87] The attraction contribution is computed using C_6 dispersion coefficients ($C_{ij} = 4\epsilon_{ij}\sigma_{ij}^6$) that are derived from UFF using Lorentz-Berthelot mixing rules for H₂O and CH₄ and from the Grimme method[72] for CO₂. A global scaling factor, $S_g \geq 1$, is used to ensure an entirely positive-definite repulsive energy after the energy decomposition is done for each path, as the C_6 terms are assumed to give reasonable relative energies but may be off in their absolute values.

Force Field Parameterization. In decomposing the energy along each path, the point charges of all atoms in the system as well as the attractive C_{ij} terms are fixed, leaving only two parameters, A_{ij} and B_{ij} , to be fit for each pairwise interaction. Before fitting A_{ij} and B_{ij} , we create an initial guess for each pairwise interaction by mapping the UFF Lennard-Jones parameters to the Buckingham parameters. The corresponding pairwise repulsive parameters A_{ij} and B_{ij} are then optimized by a grid search method so as to minimize the difference between the DFT interaction energy and the force field energy along the approaching path for this pair. Although each path was designed to probe a specific pairwise interaction, it is impossible to eliminate interactions with the other framework atoms, and the A_{ij} and B_{ij} parameters for a given pair are thus dependent on every other pairwise interaction in the system. As a result, the fitting is done in a self-consistent manner: once the first set of two parameters is optimized for the first pairwise interaction (while holding all other pairs of parameters fixed), the second set of two parameters is optimized for the next pairwise interaction, and so on, until parameters have been fit for each pairwise interaction; we then go back and reoptimize each set of two parameters following the same order as above for N

cycles until they reach convergence.

To determine the order in which these parameters are fit for each approaching pair, the ratio of the computed repulsive energy between the approached pair to the total repulsive energy along a path is computed for each pairwise interaction; the A_{ij} and B_{ij} parameters are then fit sequentially for each approaching pair from the highest to lowest ratio, and repeated iteratively until all of the parameters have converged. For more details, see [129].

In the case of CH_4 and CO_2 , this fitting procedure was performed for *framework*-C(CH_4) and *framework*-O(CO_2) interactions in $\text{M}_2(\text{dobdc})$, with the exception of *framework*-C(CO_2), H(*framework*)-O(CO_2), and H(*framework*)-C(CH_4) interactions. The interactions left out of the fitting procedure are instead described with a Lennard-Jones potential and the C_6 dispersion coefficients, obtained from Grimme’s DFT-D2 method in the case of CO_2 . [72] The σ parameters used in the Lennard-Jones potentials were fixed to have a value equal to the sum of the atomic van der Waal radii for each pairwise interaction. As mentioned above, except for the H-*approaching* path, all other paths (M, O_a , O_b , O_c , C_a , C_b , C_c , C_d) were included in the iterative fitting procedures for C(CH_4) and O(CO_2). Upon convergence of the parameters for $\text{Mg}_2(\text{dobdc})$, the interaction parameters involving all but the metal atoms are then held fixed while reoptimizing metal-C(CH_4) and metal-O(CO_2) interactions for all of the other frameworks (Mn, Fe, Co, Ni, Zn).

In the case of H_2O , this procedure is repeated for fitting all *framework*-O(H_2O) interactions and some *framework*-H (H_2O) interactions. For each metal (M = Mg, Mn, Fe, Co, Ni, Zn), the paths included in the iterative fitting procedure were M-, O_b -, O_c -, C_a -, C_b -, C_c -, C_d -O(H_2O) and O_b -, C_b -H(H_2O). It is worth noting that the O_a -O(H_2O) path was left out of the fitting procedure for all metals as including it led to no convergence in the interaction parameters. This is because the energies along the O_a path were similar in magnitude to the metal path, and it was not possible to probe the O_a interaction without having large contributions from the metal atom interactions. Because the metal and O_a parameters were highly dependent on each other, the O_a parameters were fixed so as to get a better fit for the interaction energies along metal path. H-O(H_2O), M-H(H_2O), and H-H(H_2O) paths were also not included in the fitting procedure. As they are very similar, interaction parameters for the same pair of atom-types in the different metal frameworks are then averaged together and fixed to the resulting values. The pairwise interaction terms involving the metal atoms are then reoptimized for each framework so as to minimize the difference between the energies computed by the force field and the energies computed from DFT along each approaching path. For the force field parameters, see Tables S4-S9.

Classical Molecular Simulations. Monte Carlo (MC) simulations are used to calculate the adsorption properties of the three gases of interest in each framework. Total interaction energies in these simulations include electrostatics, short-range repulsion, and dispersion interactions, computed using the force field parameters obtained as described above. The nonelectrostatic potentials are truncated and shifted to zero at a cutoff radius of 12.8 Å. Ewald summations are used to compute long-range Coulomb contributions. The simulation box is composed of multiple unit cells such that the distances between two successive planes of (1,0,0), (0,1,0), and (0,0,1) are at least twice the cutoff radius. For any

interactions not parametrized by our force fields, Lennard-Jones + Coulomb potentials were used with Lorentz-Berthelot mixing rules. These parameters were from the UFF force field, the respective guest models for CH₄ and H₂O, and from Grimme’s method[72] for CO₂. Details regarding the force field parameters used herein are given in Tables S4-S9.

Metal-Organic Framework Synthesis. All reagents were obtained from commercial vendors and used without further purification. Mn₂(dobdc), Cu₂(dobdc), Fe₂(dobdc), and Zn₂(dobdc) were synthesized according to literature procedures.[25, 187, 67, 196] Mg₂(dobpdc) was also synthesized and activated according to the literature procedure. [156] The successful synthesis and activation of the compounds was confirmed by comparing the X-ray powder diffraction patterns and Langmuir surface areas to those previously reported.

Low-Pressure CO₂ Adsorption Measurements. Low pressure (0-1.2 bar) isotherm measurements were completed; approximately 100 mg of activated sample in an ASAP tube equipped with a Transeal was placed on the analysis port of a Micromeritics ASAP 2020 equipped with an HD transducer. The surface area was measured on the sample in the ASAP tube with an isothermal jacket in liquid N₂ (77 K) and calculated with the Micromeritics software. CO₂ and CH₄ isotherms were measured on the ASAP 2020 HD instrument as well, with temperature control via a Julabo circulating water bath.

High-Pressure CH₄ and CO₂ Adsorption Measurements. High-pressure CH₄ and CO₂ adsorption isotherms in the range of 0–90 and 0–50 bar, respectively, were measured on an HPVA-II-100 from Particulate Systems, a Micromeritics company. In a typical measurement, 0.5–1.0 g of activated sample was loaded into a tared stainless steel sample holder inside a glovebox under a N₂ atmosphere. Prior to connecting the sample holder to the VCR fittings of the complete high pressure assembly inside the glovebox, the sample holder was weighed to determine the sample mass. The sample holder was then transferred to the HPVA-II-100, connected to the instrument’s analysis port via an OCR fitting, and evacuated at room temperature for at least 2 h. The sample holder was placed inside an aluminum recirculating dewar connected to a Julabo FP89-HL isothermal bath filled with either Julabo Thermal C2 fluid or Syltherm from Dow Chemical. The temperature stability of the isothermal bath is ± 0.02 °C. Methods for accurately measuring the relevant sample freespace, which involve the expansion of He from a calibrated volume at 0.7 bar and 25 °C to the evacuated sample holder, were described in detail previously.[146] Nonideality corrections were performed using the CH₄ and CO₂ compressibility factors tabulated in the NIST Refprop database at each measured temperature and pressure.[122]

CH₄ and CO₂ Isotherm Fitting and Isothermic Heats of Adsorption Prior to fitting the CH₄ and CO₂ adsorption isotherms, experimentally measured excess adsorption (n_{ex}) was converted to total adsorption (n_{tot}) using total pore volumes (V_p), as determined from N₂ isotherms at 77 K ($P/P_0 = 0.9$), and the bulk gas density at each temperature and pressure from the NIST Refprop database (Eq (2.3)).[122]

$$n_{tot} = n_{ex} + V_p \times \rho_{bulk}(P, T) \quad (2.3)$$

Total CH₄ adsorption isotherms for each M₂(dobdc) framework were then fit with either

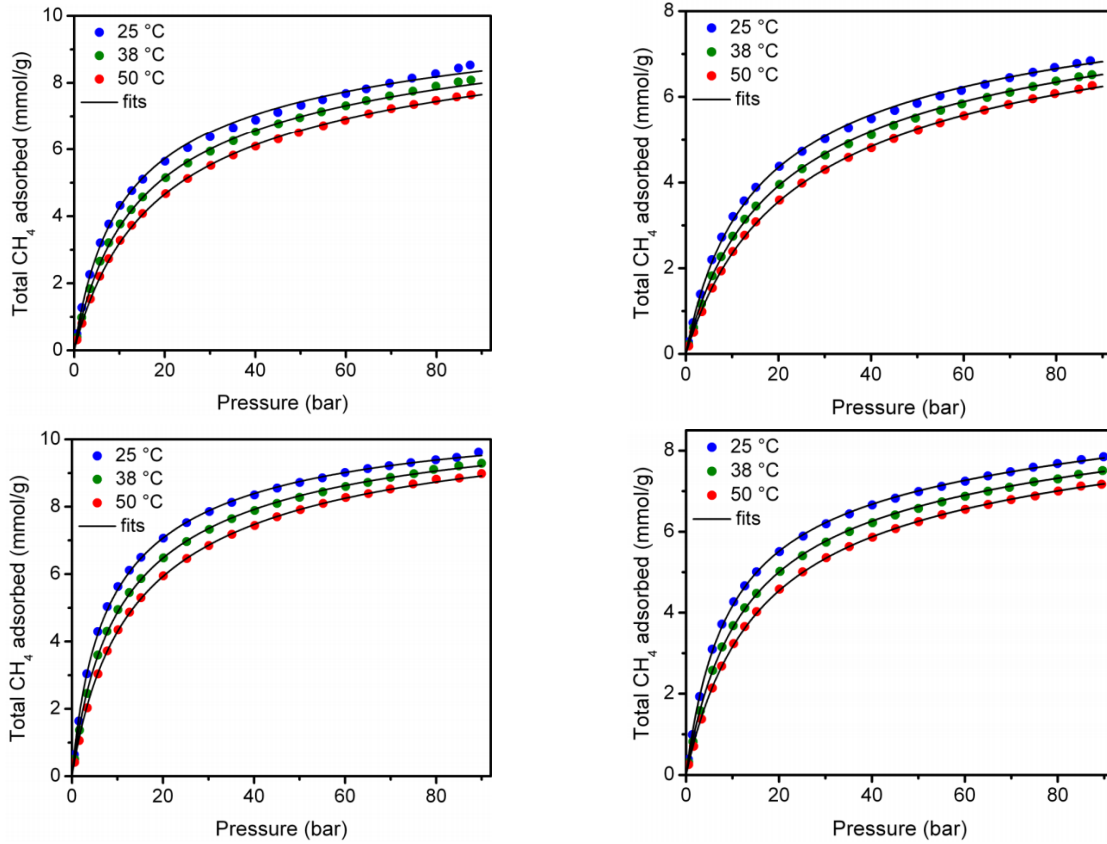


Figure 2.2: Total CH₄ adsorption isotherms measured in Mn₂(dobdc) (top left), Cu₂(dobdc) (top right), Fe₂(dobdc) (bottom left), and Zn₂(dobdc) (bottom right) at 25, 38, 50, °C and the corresponding dual-site Langmuir fits (black lines).

a single- or dual-site Langmuir equation (Eq (2.4)), where n is the total amount adsorbed in mmol g⁻¹, P is the pressure in bar, $n_{sat,i}$ is the saturation capacity in mmol g⁻¹, and b_i is the Langmuir parameter in bar⁻¹ for up to two sites 1 and 2. The Langmuir parameter can be expressed using Eq (2.5), where S_i is the site-specific molar entropy of adsorption in J mol⁻¹K⁻¹, E_i is the site-specific binding energy in kJ mol⁻¹, R is the gas constant in J mol⁻¹K⁻¹, and T is the temperature in K. Plots of the total adsorption isotherms with the corresponding single- or dual-site Langmuir fits can be found in Figure 2.2. Note that isotherm data at all measured temperatures were fit simultaneously with one set of parameters.

$$n = \frac{n_{sat,1}b_1P}{1 + b_1P} + \frac{n_{sat,2}b_2P}{1 + b_2P} \quad (2.4)$$

$$b_i = \exp^{-S_i/R} \exp^{1000E_i/RT} \quad (2.5)$$

Using the single- and dual-site Langmuir fits, the isosteric heat of adsorption can be calculated for each material as a function of the total amount of CH_4 adsorbed using the Clausius-Clapeyron relation (Eq (2.6)). The isosteric heat of adsorption for a single-site Langmuir model is constant by definition. For a dual-site Langmuir model, however, it is necessary to derive an expression for the loading dependence of the isosteric heat of adsorption (Eq (2.7)). Note that, as written, Eqn (2.7) gives the isosteric heat of adsorption as a function of pressure, rather than the amount adsorbed. Heats of adsorption as a function of the amount adsorbed can be calculated using Eq (2.4).

$$-Q_{st} = RT^2 \left(\frac{\partial \ln P}{\partial T} \right)_n \quad (2.6)$$

$$-Q_{st} = \frac{E_1 n_{sat,1} b_1 (1 + b_2 P)^2 + E_2 n_{sat,2} b_2 (1 + b_1 P)^2}{n_{sat,1} b_1 (1 + b_2 P)^2 + n_{sat,2} b_2 (1 + b_1 P)^2} \quad (2.7)$$

The CH_4 and CO_2 isotherms for $\text{Mg}_2(\text{dobpdc})$ were fit using a modified version of the Langmuir equation, the Langmuir-Freundlich equation (Eqn. (2.8)) to obtain better fits to the data. It is worth noting that while multiple sites are most likely occupied in the pores, any sites beyond the coordinatively unsaturated metal sites are similar enough in binding enthalpy that the dual-site approximation is adequate. Combined low- and high-pressure isotherms were fit for CO_2 and the high-pressure isotherms were fit for CH_4 at all temperatures simultaneously in Microsoft Excel using the Solver add-on. In Eq (2.8), q_{sat} is the saturation loading for site A or B (mmol g^{-1}), b is the Langmuir parameter associated with site A or B (bar^{-1}), and p is the pressure. The value for b is calculated using Eq (2.5).

$$n = \frac{q_{sat,A} b_A p^{v_A}}{1 + b_A p^{v_A}} + \frac{q_{sat,B} b_B p^{v_B}}{1 + b_B p^{v_B}} \quad (2.8)$$

Parameters for all the fits are given in Tables B.22 – B.24. The isosteric heats of adsorption were calculated as described above using the Clausius-Clapeyron relation.

QEq Reparameterization In the Rappe-Goddard charge equilibration method (QEq)[188], atomic charges are obtained by solving the QEq equations relating the atomic parameters (electronegativity and hardness for each atomic species) and atomic charges. These equations can be written in the matrix form as

$$\begin{pmatrix} J & 1 \\ 1^\dagger & 0 \end{pmatrix} \begin{pmatrix} Q \\ \lambda \end{pmatrix} = \begin{pmatrix} -\chi \\ 0 \end{pmatrix} \quad (2.9)$$

where Q is a $N \times 1$ column vector $Q = (q_1, q_2, \dots)^\dagger$, λ is the Lagrange multiplier by the charge conservation condition, $\chi = (\chi_1, \chi_2, \dots)^\dagger$ is the electronegativity column vector and J is the interaction matrix. J between two atoms A and B is obtained as

$$J_{AB} = \sum_{\vec{T}} (1 - \delta_{A,B} \delta_{\vec{T},0}) \int \int \frac{\rho_A(\vec{r}_1; \vec{R}_A) \rho_B(\vec{r}_2; \vec{R}_B + \vec{T})}{|\vec{r}_1 - \vec{r}_2|} d\vec{r}_1 d\vec{r}_2 + \delta_{A,B} J_{AA}^0 \quad (2.10)$$

Element	χ (eV)	J (eV)
C	5.384	8.004
O	13.567	19.391
Mg	3.091	7.486
Mn	2.273	7.764
Co	4.361	6.873
Ni	5.920	5.677
Fe	5.417	6.004
Zn	7.673	4.236

Table 2.1: Optimized QEq electronegativity (χ) and hardness (J) parameters.

where ρ_A and ρ_B are the unit charges which are given by a single normalized s-type Slater orbital (STO). The STO is $\rho_A(\vec{r}_1; \vec{R}_A) = N_n |\vec{r} - \vec{R}_A|^{n-1} \exp^{-\xi_i |\vec{r} - \vec{R}_A|}$ for an atom A with an outer valence orbital belonging to n th shell. ξ_A is the decay parameter which is inversely proportional to the atom's covalent radius. \vec{T} is a lattice vector for each unit cell, and vectors \vec{R}_A and \vec{R}_B indicate the atom's positions within a unit cell. The optimized QEq parameters are given in Table 2.1

Single Crystal X-ray Diffraction A methanol solvated crystal of Co₂(dobdc) was mounted on a Kapton loop using epoxy. A minimal amount of epoxy was applied to ensure that the crystal pores remained accessible. The sample was then placed in a custom-made gas cell goniometer head equipped with a gas loading valve and a borosilicate glass cap with an O-ring seal. The cell was evacuated under reduced pressure with a turbomolecular pump at 473 K for 4 hours to remove solvent molecules filling the pores and bound onto the Co sites within the crystal. Data was collected at Beamline 11.3.1 at the Advanced Light Source, Lawrence Berkeley National Laboratory using synchrotron radiation ($\lambda = 0.77490$ Å) with a Bruker AXS APEX II CCD detector on a D8 diffractometer. The structure of the desolvated crystal was obtained from a preliminary data set to confirm the absence of solvent bound onto the Co sites. The cell was then warmed to room temperature and exposed to air to allow ambient moisture to fill the pores. The crystal was then cooled immediately to a final temperature of 100 K followed by data collection. The crystal was found to be an obverse/reverse twin based on the diffraction pattern. CELL_NOW was used to determine the orientation matrices and the domains were related by a 180° rotation around the reciprocal axis 0 1 -0.5. Raw data for both matrices were integrated corrected for Lorentz and polarization effects using Bruker AXS SAINT software and corrected for adsorption using TWINABS. TWINABS was used to produce a merged HKLF4 file, for structure solution and initial refinement, and an HKLF5 file for final structure refinement. The HKLF5 file contained the merged reflections of the second component and those that overlapped with the first component were split into two reflections. TWINABS indicated the twin fraction to be 46:54. The structure was solved using direct methods with SHELXT and refined using SHELXL operated in the OLEX2 interface.

Thermal parameters were refined anisotropically for all non-hydrogen atoms. Non-H₂O hydrogen atoms were placed in ideal positions. H₂O molecules were located inside the pores of the metal-organic framework and their site occupancy factors were allowed to refine freely, then were fixed in the final refinement. Disorder of some of the unbound H₂O molecules (O7A, O7B, and O8) required the use of the similar ADP restraint on their oxygen atoms. Hydrogen atoms on two of the H₂O molecules, O4 and O5, were located in the electron difference map. The O–H distances of these H₂O molecules were fixed at 0.84 Å. Hydrogen atoms on the rest of the H₂O molecules, O6A to O10, could not be located in the electron difference map and were omitted in the refinement but not the formula. All hydrogen atoms were refined using the riding model.

Results and Discussion

I. Fitting the Guest-Framework Interactions. We first derived a force field for CO₂ adsorption in M₂(dobdc) (M = Mg, Fe, Co, Ni, and Zn). We use the EPM2[83] model for CO₂ molecules and UFF [189] force field parameters for the framework atoms as a starting point. The derived force field for CO₂ in M₂(dobdc) nicely reproduces our DFT energies. As an example, the resulting force field nicely reproduces DFT energies along all of the paths for Co₂(dobdc) as shown in Figure 2.3. Single-point energies along the various approaching paths for Fe- and Ni₂(dobdc) are available in Figures S2 and S3, and illustrate the agreement between the DFT-derived force field and the DFT energies along all of the paths for these frameworks as well. For a comparison of single-point energies in Mg- and Zn₂(dobdc), see [129].

Although UFF was intended to be a very generalizable force field, it was not parametrized with metal sites in the training set that were similar enough to the metal sites present in M₂(dobdc), and as a result the model does not necessarily predict the energetics of these systems accurately. The way this inaccuracy is manifested in M₂(dobdc) is that UFF tends to overestimate the repulsion from guests at short distances in the entire series of frameworks. Indeed, this is one of the reasons why UFF fails to accurately model the gas adsorption properties of M₂(dobdc), as it leads to an underprediction of the various gases’ binding energies in the frameworks such that the adsorption capacities of M₂(dobdc) for various flue gas components are considerably underestimated. Parameters for Mn were also fit originally, but the fitted potential led to unrealistic uptake at low pressures (< 10 Pa). The force field energies for CO₂ in Mn₂(dobdc) did indeed match the DFT energies after fitting, and as such we believe that it is not a poor fit that led to a prediction of unrealistic CO₂ uptakes. The reasons behind this phenomenon could actually be quite complicated, perhaps due to the use of the Buckingham potential or Grimme’s C₆ correction. Therefore, we chose to leave Mn₂(dobdc) out of the CO₂ reparameterization such that a working Mn potential for CO₂ obtained using the method outlined herein is not available at this moment.

We then derived a force field for H₂O adsorption in M₂(dobdc) (M = Mg, Mn, Fe, Co, Ni, Zn). We use the TIP4P-Ew[88, 87] model for H₂O molecules and UFF force field parameters for the framework atoms to start off. [88] The resulting force field nicely reproduces DFT

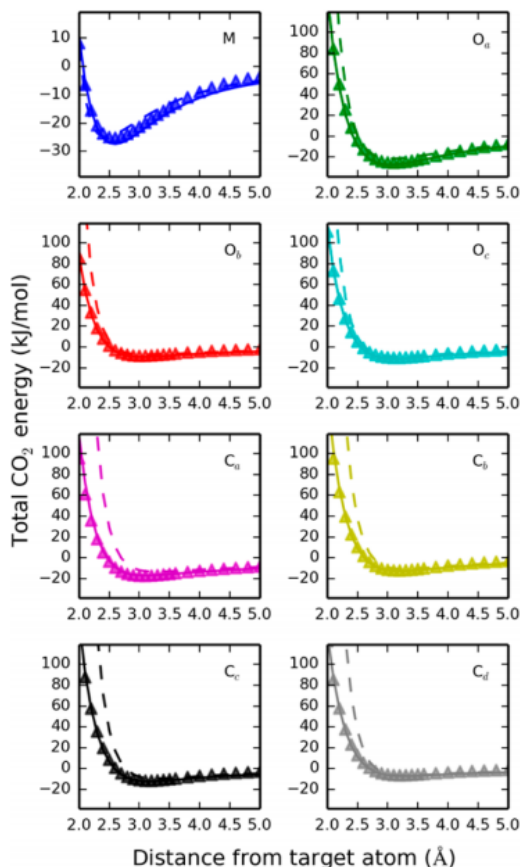


Figure 2.3: Comparison of CO_2 -framework interaction energies in $\text{Co}_2(\text{dobdc})$ obtained from the DFT calculations (triangular markers), the DFT-derived force field (solid line), and the UFF force field (dashed line) along the various approaching paths.

energies along all of the $\text{O}(\text{H}_2\text{O})$ and $\text{H}(\text{H}_2\text{O})$ approaching paths considered for $\text{Co}_2(\text{dobdc})$ (shown as an example in Figure 2.4). Additionally, a comparison of single-point energies for Mn-, Fe-, and $\text{Ni}_2(\text{dobdc})$ along the various approaching paths for H_2O is available in Figures S12-S14. For a comparison of single-point energies in Mg- and $\text{Zn}_2(\text{dobdc})$, see [129].

We then derived a force field for CH_4 adsorbed in $\text{M}_2(\text{dobdc})$ ($\text{M} = \text{Mg}, \text{Mn}, \text{Fe}, \text{Co}, \text{Ni}, \text{Zn}$). We use the TraPPE[140] model for CH_4 molecules and UFF force field parameters for the framework atoms to begin.[140] The resulting force field nicely reproduces DFT energies along all of the paths for $\text{Co}_2(\text{dobdc})$, shown as an example in Figure 2.5. Moreover, a comparison of single-point energies along all approaching paths for Mg-, Mn-, Fe-, Ni-, and $\text{Zn}_2(\text{dobdc})$ is available in Figures S21-S25. Comparison with the energies computed using the UFF force field once again shows using the UFF force field leads to an overprediction of the short-range repulsion and, as a result, noticeably smaller values for the interaction energies along each path.

We obtained very reasonable agreement for the guest-framework interaction energies for

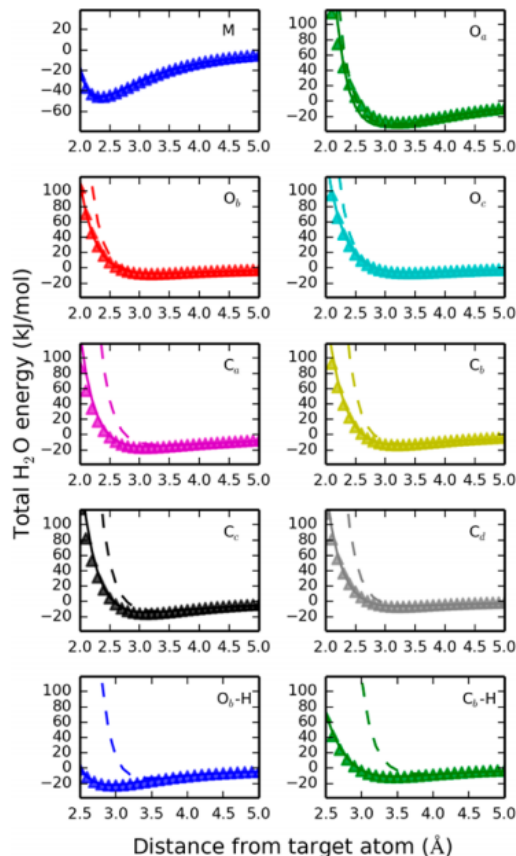


Figure 2.4: Comparison of H₂O-framework interaction energies in Co₂(dobdc) obtained from the DFT calculations (triangular markers), the DFT-derived force field (solid line), and the UFF force field (dashed line) along the various approaching paths.

all gases and MOFs. Most notably, we obtain a poorer overall fit for the CH₄ DFT energies than for the other two guests. We see that for CH₄, the energies computed using the derived force field do not reproduce the very minimum DFT energy along the metal paths, although away from this minimum the energies are reproduced quite well. In the worst cases, the minima along a given metal path deviate from the DFT minima by roughly 6 kJ mol⁻¹, or about 25% of the total binding energy. The energies along the other (non-metal) CH₄ paths, however, are well reproduced using the DFT force field in all frameworks, with the exception of Co₂(dobdc) path energies, which exhibit relatively poor agreement below 3.0 Å. Moreover, the fits for CO₂ are generally better than for H₂O, as the derived force field does not always reproduce the minimum DFT energy along each of the H₂O paths. Nonetheless, the DFT-derived force field energies are generally in good agreement with the calculated DFT energies, and in all cases a significant improvement from energies computed using UFF.

II. Gas Adsorption in M₂(dobdc). *II.a. CO₂.* The total adsorption isotherms are computed using the DFT-derived force field and compared to the experimental isotherms for

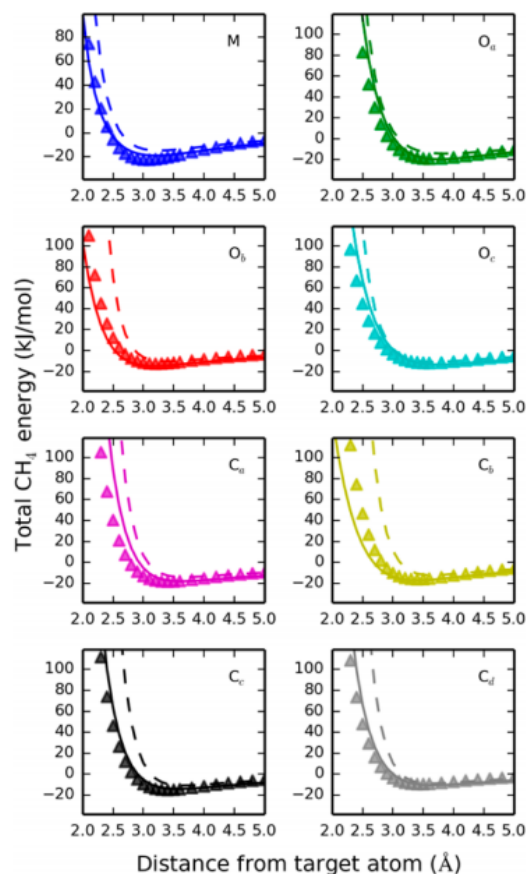


Figure 2.5: Comparison of CH_4 -framework interaction energies in $\text{Co}_2(\text{dobdc})$ obtained from the DFT calculations (triangular markers), the DFT-derived force field (solid line), and the UFF force field (dashed line) along the various approaching paths.

CO_2 in $\text{M}_2(\text{dobdc})$ (Figure 2.6).[187] For this family of MOFs, it has been established via the isosteric heats of adsorption and X-ray diffraction data that 20-30% of the metal sites are inaccessible in some $\text{M}_2(\text{dobdc})$ structures.[187] There are many methods by which isotherms are commonly scaled as a way to account for structural defects in synthesized materials and thus allow for a clearer comparison between the computed and measured isotherms.[51, 129, 211, 48, 39] For simplicity, we scaled all of the computed isotherms by 85% regardless of the framework as approximately this percentage of metal sites is accessible in each synthesized framework. A comparison between isotherms computed using the UFF force field and the experimental isotherms for CO_2 in these same frameworks can also be found in Figure 2.6. The unmodified computed isotherm data at 287, 298, and 313 K are available in Figures S4-S6. As expected, lowering the temperature leads to a higher loading over the entire pressure range considered. With our new DFT-derived force field, the predicted CO_2 isotherms are in good agreement with the experimental isotherms, especially at lower pressures. Below 0.6 bar, the trend in the isotherms (ordered by decreasing CO_2 uptake: Mg, Ni, Co, Fe, Zn) is

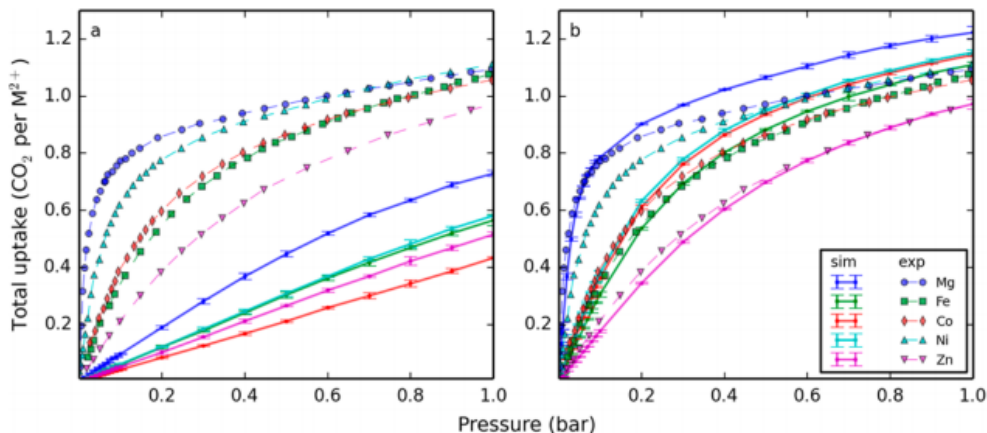


Figure 2.6: Comparison between the experimental and simulated isotherms using the UFF and EPM2 force fields (a) and the DFT-derived force field (b) for CO_2 inside $\text{M}_2(\text{dobdc})$ at 298 K. The experimental data of Queen et al [187] are indicated by the large geometric markers and dashed lines, whereas the corresponding scaled isotherms from simulation are indicated by solid lines. Error bars are plotted for simulation data but smaller than the markers in most cases.

accurately reproduced with the DFT-derived force field but not with the UFF force field. Of the computed isotherms, predictions for CO_2 in $\text{Ni}_2(\text{dobdc})$ deviate the most from the experimental measurements, but it should be noted that the isotherm computed using the DFT-derived force field is in significantly better agreement with the experimental results than the isotherm computed using the UFF force field. While this difference could arise from a number of factors (including unavoidable defects in the crystalline structure), it is certainly possible that the electronic structure at the Ni center is described less accurately than the other metals simply due to the level of theory employed. For example, recall that the Hubbard-U correction is used for these systems and the U value for Ni is quite high (6.4). In view of that, we wish to stress that the performance of any *ab initio* force field is dependent on the level of theory used.

A comparison of probability densities computed for 216 CO_2 molecules inside each $\text{M}_2(\text{dobdc})$ framework (corresponding to 1.5 guest molecules per metal site) using the DFT-derived force field (Figure 2.7) and neutron powder diffraction (NPD) experiments[187] shows that our force field can reproduce experimental observations. All probability density plots were created using PEGrid and VisIt[29] by binning positions of guest molecules from three (for CO_2 and CH_4) and ten (for H_2O) 100,000 cycle *NVT* simulations into $0.2 \times 0.2 \times 0.2 \text{ \AA}^3$ voxels. The appearance of two major CO_2 binding sites under these conditions, with the first being the stronger and more occupied binding site at the metal and the second weaker site lying nearly parallel to the channel walls between two of the primary sites, is clearly captured by our simulations.

Some of the key differences between CO_2 adsorption in the different metal frameworks

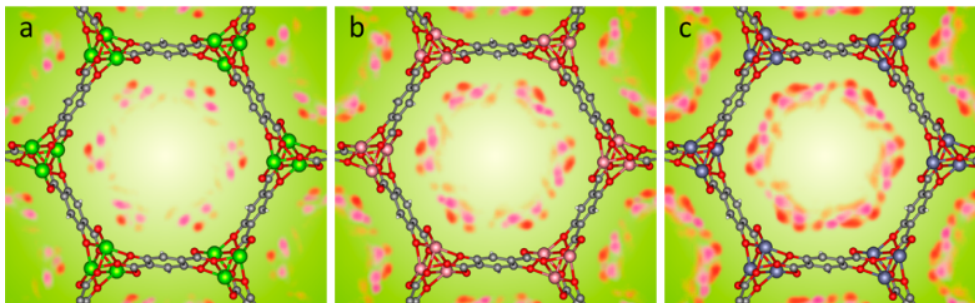


Figure 2.7: Probability density plots computed using the DFT-derived force field for CO_2 in (a) Mg_2 -, (b) Co -, and (c) $\text{Zn}_2(\text{dobdc})$, respectively, at 100 K. Orange clouds represent the density corresponding to the oxygen atoms in CO_2 , whereas magenta clouds correspond to the density from the carbon atoms. Darker colors correspond to a higher probability of finding a guest at those positions. Framework color key – C = gray, O = red, H = white, Mg = lime green, Co = pink, Zn = slate.

are highlighted in Figure 2.7. In $\text{Mg}_2(\text{dobdc})$, the framework with the largest affinity for CO_2 , the probability density illustrates how any adsorbed CO_2 is significantly less mobile than in both Co - and $\text{Zn}_2(\text{dobdc})$. Similarly, the secondary binding sites are less apparent in $\text{Mg}_2(\text{dobdc})$ than in the other frameworks. This suggests that due to the larger difference in energy between the primary and secondary sites, all of the primary binding sites must be occupied, while only one-half of the secondary ones are filled in $\text{Mg}_2(\text{dobdc})$; on the other hand, in Co - and $\text{Zn}_2(\text{dobdc})$ the secondary and primary binding sites are significantly more occupied due to the secondary and primary binding sites being closer in energy. In $\text{Zn}_2(\text{dobdc})$, the framework with the lowest binding energy for CO_2 of all of the frameworks studied, a more extensive distribution in the binding site occupancy is apparent along the surface of the framework in addition to a higher mobility indicated by the broadness of the observed density clouds. Additional probability density maps for all of the metal frameworks studied can be found in Figures S7-S11.

II.b. H_2O . The total adsorption isotherms computed using the DFT-derived force field for H_2O in $\text{M}_2(\text{dobdc})$ are shown in Figure 2.8 along with experimentally measured isotherms from the literature. Using our model, we observe a trend in step of the computed isotherms related to heat of adsorption, which is not observed experimentally. The greater is the binding energy for H_2O at the metal site, the sooner the step in the isotherm occurs. We also observe a slightly different mechanism for H_2O adsorption in $\text{Mg}_2(\text{dobdc})$, in which H_2O has the largest binding energy, than in the other five frameworks. The gradual increase in uptake at low pressures followed by the sharp increase in uptake after the uptake reaches c.a. 1 H_2O per M^{2+} suggests that due to the large binding energy, all of the metal sites become occupied first such that the metal- H_2O interaction is stronger than H_2O - H_2O interactions, but that once all of the metal sites are occupied H_2O - H_2O interactions take over and H_2O condenses into the pores giving rise to the inflection. On the other hand, for the five other frameworks, H_2O adsorption is much less than 1 H_2O per M^{2+} right before the inflections in

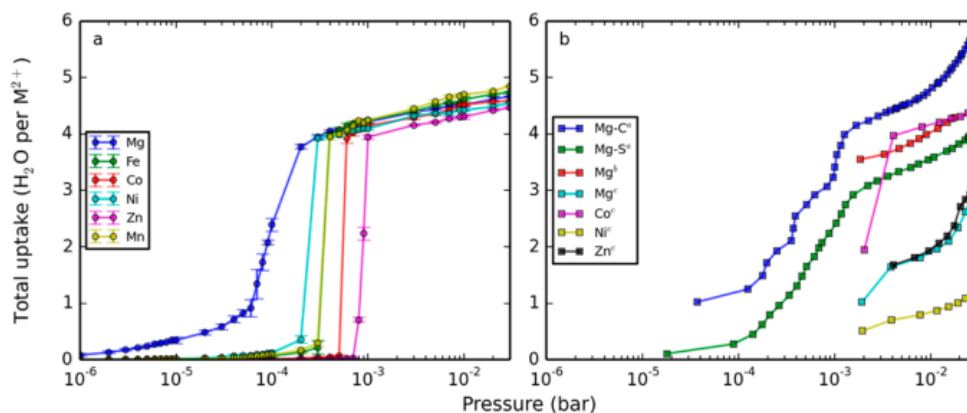


Figure 2.8: Comparison between adsorption isotherms computed using the DFT-derived force field (a) and experimentally measured (b) for H_2O inside $\text{M}_2(\text{dobdc})$ at 298 K. The experimental data of ^aYang et al [242], ^bSchoenecker *et al* [198], and ^cGlover et al [69] are shown for the various metal frameworks studied. Error bars are plotted for simulation data but smaller than the markers in most cases.

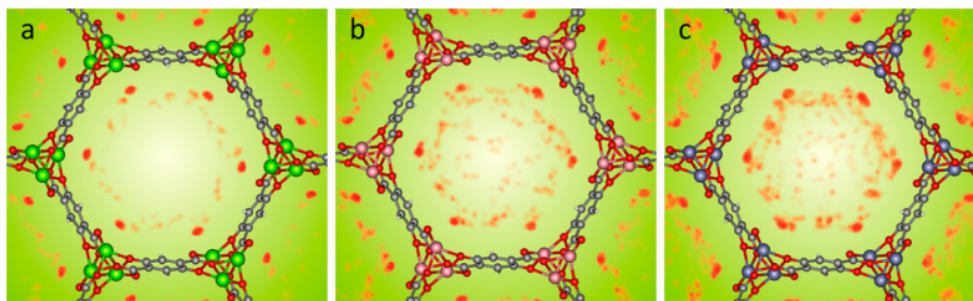


Figure 2.9: Probability density plots computed using the DFT-derived force field for H_2O in (a) Mg -, (b) Co -, and (c) $\text{Zn}_2(\text{dobdc})$, respectively, at 100 K. Orange clouds represent the density corresponding to the oxygen atoms in H_2O . Darker colors correspond to a higher probability of finding a guest at those positions. Framework color key – C = gray, O = red, H = white, Mg = lime green, Co = pink, Zn = slate.

the isotherms occur, suggesting that once a single H_2O molecule binds in each framework it becomes more favorable to add another H_2O molecule right next to it, thus leading to H_2O condensation in the pores.

One of the challenges with studying H_2O adsorption in these frameworks, perhaps due to the large H_2O binding energies and/or H_2O behavior in a confined environment, is that experimentally it is difficult to accurately and reliably measure adsorption isotherms, and isotherms collected for the same metal framework are often in stark disagreement between different groups or even different samples. Although the lack of conclusive adsorption isotherms for H_2O in the various $\text{M}_2(\text{dobdc})$ frameworks studied here prevents us from evaluating the

predictive power of our obtained H₂O force field, it is worth noting the differences between the multistep character observed in the measured isotherms and the single-step character predicted by our model. Nonetheless, the purpose of deriving this force field for H₂O was not to study single-component H₂O adsorption in MOFs, but to be better equipped to study the separations of other gases from wet mixtures where H₂O is present in negligible amounts. As such, we expect our force field to be suitable for this type of analysis, as our force field was parametrized to DFT binding energies for one H₂O molecule in the framework at a time and thus should be more accurate at lower concentrations of H₂O where H₂O–H₂O interactions do not play a dominant role. With regards to the choice of the initial H₂O model (TIP4P-Ew[88]), we initially considered other nonpolarizable H₂O models (i.e. SPC, SPC/E, TIPnP, TIPnP-Ew) due to their simple potential forms.[88, 87, 138, 97, 222, 26, 137, 135, 191, 168] Many groups have analyzed the performance of different H₂O models in Mg₂(dobdc),[193] and it has been shown that models with more than three sites provide better quantitative agreement with predicted binding geometries from DFT calculations, and that five-site models give the best agreement.[180] However, in grand canonical Monte Carlo simulations, the TIP5P-Ew model shows a very different adsorption mechanism as compared to TIP4P-Ew, which is not observed in experimental data. For these reasons, the TIP4P-Ew model was chosen over the other models considered. In addition, adsorption isotherms computed using the TIP4P-Ew model and UFF to study H₂O adsorption in Mg₂(dobdc) show a saturation of the framework at lower pressures than TIP3P and TIP5P-Ew, as well as the higher uptake after the step in the isotherm occurs.[193, 180] This last observation makes it attractive to use for the purposes of studying separations of wet gas mixtures in M₂(dobdc) as using this H₂O model would provide a loose upper-bound from simulation for each framework’s sensitivity to H₂O.

Another challenge when modeling H₂O adsorption in these frameworks stems from any substantial rearrangements in the framework structure, which come about as a result of H₂O adsorption. Our force field will be more accurate in the limit that the framework does not distort much upon H₂O binding, and in the limit that the chosen H₂O model is adequate at describing the H₂O in the pores at higher pressures.

A comparison of probability densities computed for 216 H₂O molecules inside the M₂(dobdc) frameworks using the DFT-derived force field (Figure 2.9) and binding geometries obtained from single-crystal X-ray diffraction (XRD) experiments (Figure 2.10) shows that with our DFT-derived H₂O force field, we are able to reproduce the experimentally observed oxygen positions for guest H₂O molecules in Co₂(dobdc). We observe the appearance of the multiple binding sites seen experimentally, the most occupied being that over the metal center, followed by many others both along the walls of the channels and near the centers of the pores. From the computed probability densities, it is evident that there is significant disorder in the secondary binding sites. This disorder in the secondary binding sites manifests itself as many little clouds of high density as opposed to the broad clouds observed for CO₂, indicating that there are many local minimums in the way H₂O can arrange itself in the pores at these conditions, and once a configuration finds such a minimum the H₂O molecules rarely move. Configurations would have to be sampled for significantly longer at 100 K to see an

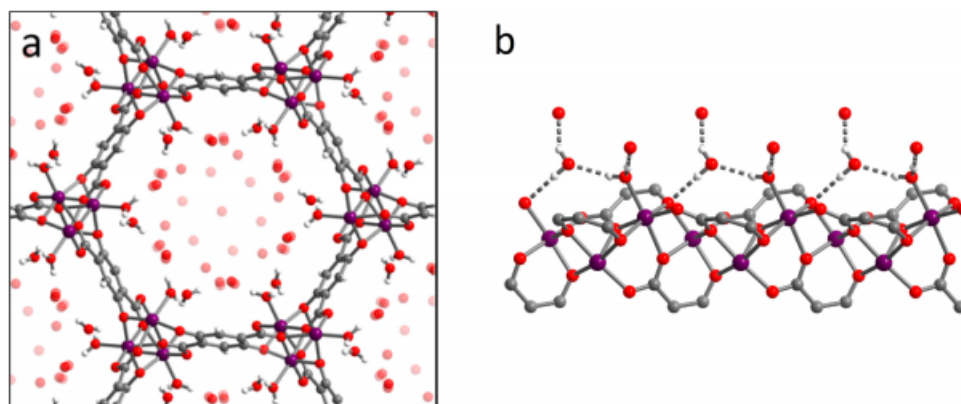


Figure 2.10: XRD crystal structure with disorder for $\text{Co}_2(\text{dobdc})$ framework saturated with H_2O at 100 K. (a) View down the pores of the channel. (b) View along the c -axis of one metal chain. Color key – C = gray, O = red, H = white, Co = purple.

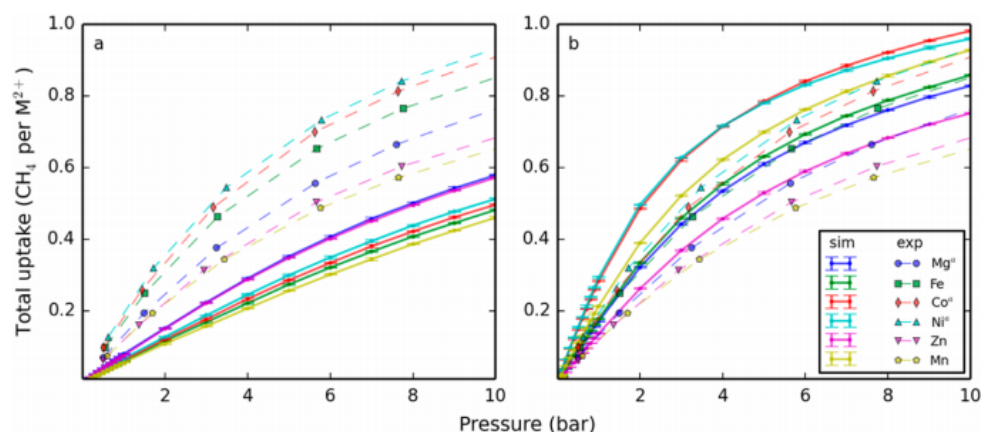


Figure 2.11: Comparison between the experimental and simulated isotherms computed using the UFF and TraPPE force fields (a) and the DFT-derived force field (b) for CH_4 in $\text{M}_2(\text{dobdc})$ at 298 K. The experimental data of Mason et al [146] are indicated by the geometric markers and dashed lines for the Mg, Co, and Ni frameworks. Isotherms were measured in this work for the Fe, Zn, and Mn frameworks for comparison with simulation. The corresponding scaled isotherms from simulation are indicated by the solid lines. Error bars are plotted for simulation data but in most cases smaller than the markers.

adequate distribution of the secondary binding sites. Nonetheless, disorder in the secondary sites is also observed experimentally, where in the solvated structure certain H_2O molecules are disordered over multiple positions as shown in Figure 2.10a. The appearance of these secondary binding sites is not observed when using the UFF force field.

Some of the differences between H_2O adsorption in the different metal frameworks, with similar trends to those observed in CO_2 adsorption, are also highlighted in Figure 2.9. In

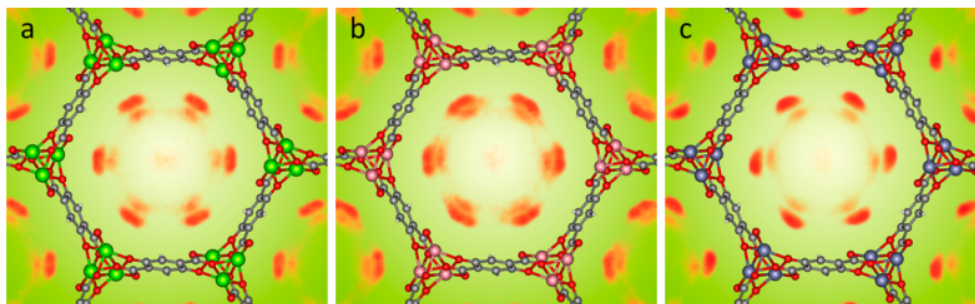


Figure 2.12: Probability density plots computed using the DFT-derived force field for CH_4 in (a) Mg_2 -, (b) Co_2 -, and (c) $\text{Zn}_2(\text{dobdc})$, respectively, at 100 K. Orange clouds represent the density corresponding to the carbon atoms in CH_4 . Darker colors correspond to a higher probability of finding a guest at those positions. Framework color key – C = gray, O = red, H = white, Mg = lime green, Co = pink, Zn = slate.

$\text{Mg}_2(\text{dobdc})$, which has the largest affinity for H_2O of all six frameworks studied, the secondary, tertiary, and weaker binding sites are significantly less apparent than in the other frameworks, suggesting once again that all of the primary binding sites are fully occupied while the other sites are only partially occupied at these conditions. However, in $\text{Co}_2(\text{dobdc})$, the weaker binding sites are significantly more occupied. In $\text{Zn}_2(\text{dobdc})$, the framework with the weakest binding affinity for H_2O at the metal site of the three frameworks shown in Figure 2.9, the weaker binding sites have a higher occupancy still. This is in sharp contrast to what is observed when using the UFF force field, where H_2O spends the majority of its time at or near the metal site for all frameworks studied in this work. Additional probability density maps for all of the metal frameworks studied can be found in Figures S15-S20.

II.c. CH_4 . We now compare the total adsorption isotherms computed using the DFT-derived force field with the experimental isotherms for CH_4 in $\text{M}_2(\text{dobdc})$ (Figure 2.11). Because not all of the metal sites are accessible, the computed isotherms were again scaled down to 85%. A comparison between the isotherms computed using the UFF force field and the experimental isotherms for CH_4 in these same frameworks can also be found in Figure 2.11. Unscaled CH_4 isotherms computed at 287, 298, and 313 K are available in Figures S26-S28.

With our new DFT-derived force field, the calculated isotherms are in good agreement with the experimental isotherms, especially at lower pressures. The experimentally observed trends are also reproduced using our simulations at lower pressures (ordered by decreasing CH_4 uptake at 1 bar: $\text{Ni} > \text{Co} > \text{Fe} > \text{Mg} > \text{Zn}$), except in the case of $\text{Mn}_2(\text{dobdc})$, which we predict to have a CH_4 uptake between Fe and Co at 1 bar but is experimentally observed to have one of the lowest uptakes. At this level of theory, this suggests an incomplete activation and higher fraction of inaccessible metal sites in the as-synthesized $\text{Mn}_2(\text{dobdc})$ crystals.

A comparison of probability densities computed for 216 CH_4 molecules inside three different $\text{M}_2(\text{dobdc})$ frameworks using the DFT-derived force field is shown in Figure 2.12. In the

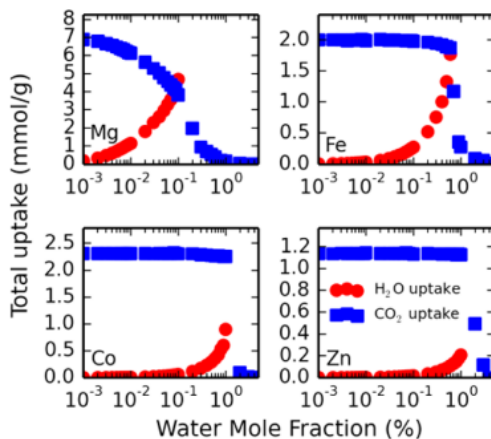


Figure 2.13: Computed $\text{CO}_2/\text{H}_2\text{O}$ mixture isotherms in $\text{Mg}_2(\text{dobdc})$ (top left), $\text{Fe}_2(\text{dobdc})$ (top right), $\text{Co}_2(\text{dobdc})$ (bottom left), and $\text{Zn}_2(\text{dobdc})$ (bottom right) at 313 K and 0.15 bar, illustrating the drop in CO_2 uptake with increasing H_2O mole fraction in the reservoir. The red circular markers symbolize H_2O adsorption, whereas the blue square markers symbolize CO_2 adsorption.

case of CH_4 , we see exactly three binding sites in all six frameworks at 100 K. Furthermore, the CH_4 molecule appears less localized than both CO_2 and H_2O at this primary binding site, an observation that is supported by the significantly weaker binding energy of CH_4 in all $\text{M}_2(\text{dobdc})$ frameworks as compared to the two other guests.

Differences in CH_4 adsorption in the six different metal-organic frameworks studied are also more subtle when compared to the adsorption behavior of the other guests; this is not surprising because the differences in the binding energies and in the adsorption isotherms are also smaller. As mentioned above, three distinct binding sites are apparent in each framework, with the primary binding site centered around the metal, a secondary binding site adjacent to the primary site (further inside the pore and slightly offset in the z -direction), and a tertiary site right in the center of the pore. In frameworks where there is a stronger interaction between CH_4 and the ligand atom-types, the densities of the primary and secondary binding sites are wider and more spread out along the channel walls, as expected. Additional probability density maps for all of the metal frameworks studied can be found in Figures S33-S38.

II.d. N_2 . N_2 isotherms computed at 287, 298, and 313 K using the UFF force field for the framework and the TraPPE[140] force field for the guest atoms are given in Figures S39-S41. While this gas is of interest for studying gas separations in certain gas compositions, the UFF and TraPPE force fields are adequate for modeling adsorption in these frameworks. Because the binding energy is not underestimated to as great of an extent when using the UFF force field to study N_2 adsorption in simulations as it is for CO_2 and H_2O , we did not reparameterize N_2 .

III. Mixture Adsorption in $\text{M}_2(\text{dobdc})$. Below we show two different examples of

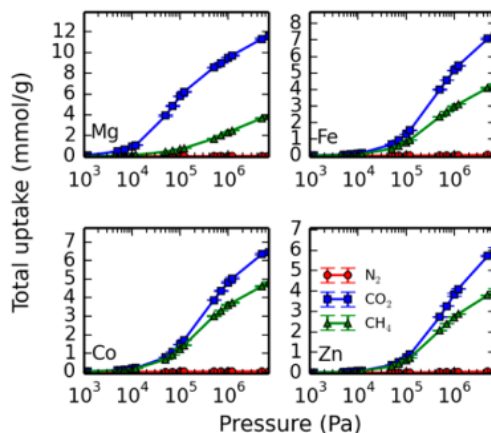


Figure 2.14: Computed N₂/CO₂/CH₄ mixture isotherms in Mg-MOF-74 (top left), Fe₂(dobdc) (top right), Co₂(dobdc) (bottom left), and Zn₂(dobdc) (bottom right) at 313 K. The red circular markers symbolize N₂ adsorption, the green triangular markers symbolize CH₄ adsorption, and the blue square markers symbolize CO₂ adsorption. The mole fraction of gases in the reservoir is fixed at all pressures to 0.05 N₂, 0.1 CO₂, and 0.85 CH₄.

gas mixtures, which we can study using our force fields. In theory there exists a large number of combinations of gases and conditions, which could be relevant for a specific application, especially considering that different power plants would operate under a range of optimal conditions. To be the most relevant and minimize the number of calculations, we have carefully chosen to study the separations below. We have studied CO₂/H₂O adsorption at a fixed temperature and pressure with varying compositions of CO₂ and H₂O so as to consider the H₂O sensitivity of these frameworks, something that would be relevant for carbon capture from wet flues. We also studied the adsorption of dry N₂/CO₂/CH₄ gas mixtures at a composition of 5% N₂, 10% CO₂, and 85% CH₄ at two temperatures and a range of pressures as these would be relevant to carbon capture applications from both natural gas and coal-fired power plant flue gases.

III.a. CO₂/H₂O. By computing binary mixture isotherms of CO₂ and H₂O in the various frameworks, we can study the frameworks' sensitivity to H₂O under conditions relevant for CO₂ capture from post-combustion flue gas. For all five frameworks, we looked at CO₂ uptake versus an increasing H₂O mole fraction in a binary mixture of CO₂ and H₂O (Figure 2.13). We observed that the positions of the inflection points in these mixture isotherms are correlated to the binding energy for H₂O in the framework. In other words, the larger is the binding energy for H₂O, the lower is the H₂O mole fraction at which CO₂ uptake decreases. For example, in Mg₂(dobdc), the framework with the largest DFT binding energy (-66.9 kJ mol⁻¹), H₂O uptake is greater than CO₂ uptake in the framework at a mere 0.1% mole fraction of H₂O in the gas reservoir under conditions of 313 K and 0.15 bar. Conversely, in Zn₂(dobdc), the framework with the weakest H₂O binding energy from DFT (-46.3 kJ mol⁻¹), H₂O uptake becomes greater than CO₂ uptake in the framework when the mole

fraction of H_2O increases to 2% under the same conditions. All of the other frameworks ($M = \text{Fe}, \text{Co}, \text{and Ni}$) perform somewhere in between. While $\text{Zn}_2(\text{dobdc})$ can tolerate an order of magnitude more of H_2O than $\text{Mg}_2(\text{dobdc})$ before becoming completely useless for carbon capture purposes, most flue gases are composed of significantly more than 2% H_2O (at 40 °C, assuming nearly complete H_2O saturation, the partial pressure of H_2O would be approximately 74 mbar, meaning most flue gases would have an H_2O mole fraction of about 7%). Thus, none of the $\text{M}_2(\text{dobdc})$ frameworks mentioned above are likely suitable for carbon capture applications from any wet sources. This is in agreement with recently reported $\text{CO}_2/\text{N}_2/\text{H}_2\text{O}$ equilibrium adsorption isotherms.[148] However, our simulations are able to show exactly how quickly CO_2 uptake is expected to decrease in the presence of H_2O , which is something that cannot be explicitly determined from the multicomponent isotherm measurements without difficulty. For $\text{CO}_2/\text{H}_2\text{O}$ mixture isotherms in $\text{Ni}_2(\text{dobdc})$, see Figure S45.

We did not analyze the separation performance of $\text{M}_2(\text{dobdc})$ for wet binary mixtures containing N_2 nor CH_4 , as they are weaker binding gases than CO_2 and we expect H_2O to saturate the framework at even lower mole fractions than in the case of the $\text{CO}_2/\text{H}_2\text{O}$ binary mixtures.

III.b. $\text{N}_2/\text{CO}_2/\text{CH}_4$. Three-component mixture isotherms were also computed at 313 K and with a typical natural gas reservoir composition of 5% N_2 , 10% CO_2 , and 85% CH_4 , conditions that would be relevant for the purification of natural gas streams using pressure-swing adsorption technology.[71] We find that all of the metal frameworks adsorb significantly more CO_2 than the two other gases, with $\text{Mg}_2(\text{dobdc})$ unsurprisingly being the most selective for CO_2 (Figure 2.14). We also find that lowering the temperature dramatically improves the ratio of CO_2 adsorbed (see Figures B.30 – B.30). These materials are promising for natural gas purification as they adsorb significantly more CO_2 than CH_4 despite the CO_2 being present at a much lower concentration in the gas mixture. Notably, $\text{Mg}_2(\text{dobdc})$ has a higher ratio of CO_2 to CH_4 adsorbed at all pressures than all of the other frameworks studied. Using our force field, mixtures of even greater complexity could be analyzed in these and similar frameworks.

IV. Transferability: Gas Adsorption in $\text{M}_2(\text{dobpdc})$. While these parameters are fit specifically for $\text{M}_2(\text{dobdc})$ structures, we expect that they should remain valid for $\text{M}_2(\text{dobdc})$ analogues. Therefore, we compute the adsorption of the different guests in the family of extended $\text{M}_2(\text{dobdc})$ structures, $\text{M}_2(\text{dobpdc})$ ($M = \text{Mg}, \text{Mn}, \text{Fe}, \text{Co}, \text{Ni}, \text{Zn}$; $\text{dobpdc}^{4-} = 4,4'$ -dioxido-3,3'-biphenyldicarboxylate). This family of framework is very similar to $\text{M}_2(\text{dobdc})$, the main difference being the larger pores due to the slightly longer linker, which possesses two phenyl rings instead of one. We show here the results of gas adsorption in these frameworks from simulations using our force fields.

It should be noted that while we expect our force fields to remain accurate for frameworks possessing similar character characteristics to $\text{M}_2(\text{dobdc})$ (i.e. coordinatively unsaturated metal sites, 1D hexagonal channels), we do not expect them to be valid models for frameworks which do not possess these characteristics and which differ significantly in their chemical environments. That is, the more different a structure is from $\text{M}_2(\text{dobdc})$, the less accurate

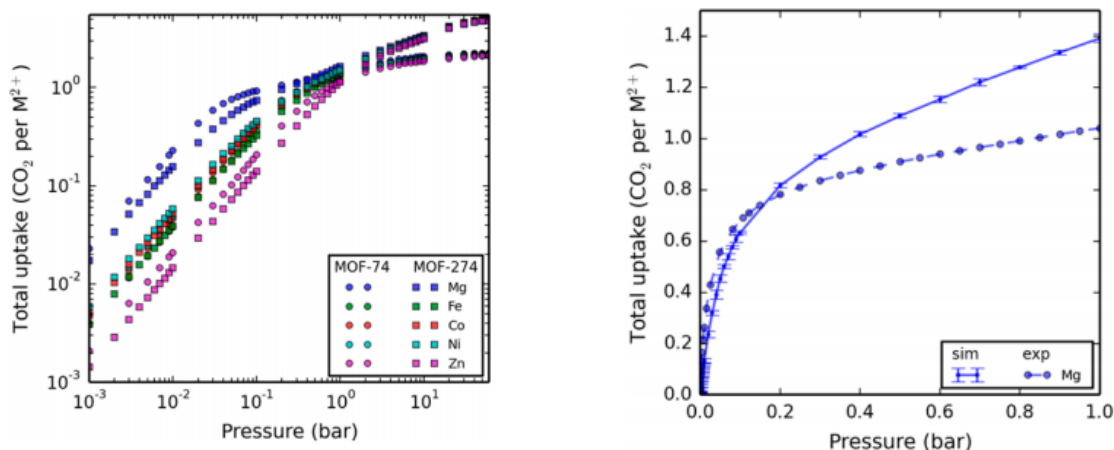


Figure 2.15: (left) Comparison of CO₂ adsorption isotherms computed at 298 K using the DFT-derived force field in M₂(dobdc) (circular markers) and M₂(dobpdc) (square markers) frameworks on a logarithmic plot. (right) Comparison between the experimental and simulated isotherms computed using the DFT-derived force field for CO₂ in Mg₂(dobpdc) at 298 K. Isotherms were measured in this work for the Mg framework for comparison with simulation. The corresponding scaled isotherm from simulation is shown by the solid lines. Error bars are plotted for simulation data but in most cases smaller than the markers.

our force field will be at capturing the appropriate energies of the system. Furthermore, if the structure of the framework varies significantly during adsorption, or if it is known to be considerably flexible, then our rigid model will also not be suitable for modeling such a system. These aspects should be considered before deciding whether or not our models are appropriate for use in simulations of gas adsorption in a given framework, but deciding when a system is “different enough” will be left to the discretion of the user.

At the moment it is not known whether the framework distorts upon the adsorption of gases, something that could have a significant impact on the adsorption behavior of M₂(dobpdc), especially at higher pressures. We believe our predictions to be correct in the limit that the M₂(dobpdc) frameworks do not distort significantly during gas adsorption as we are using a rigid approximation. In addition, as in the case of the M₂(dobdc) frameworks, we expect our predictions to be most accurate below loadings of one molecule per metal site.

To maintain neutral frameworks, atomic charges in the various M₂(dobpdc) structures are obtained using the Rappé-Goddard charge equilibration method (QEq[188]) with reoptimized parameters. Among parameters for QEq method, the atomic electronegativity (Ξ) and hardness (J) for each atom type are reoptimized by minimizing the error between QEq and REPEAT-derived charges, while employing the decay parameters for a single normalized s-type Slater orbital from the OpenBabel software.[170] The QEq parameters for all elements were optimized with the exception of hydrogen parameters, which were fixed to the original values.[188] Our QEq parametrization was trained to reproduce REPEAT charges in six different M₂(dobdc) (M = Mg, Mn, Fe, Co, Ni, Zn) frameworks. The QEq parametrization

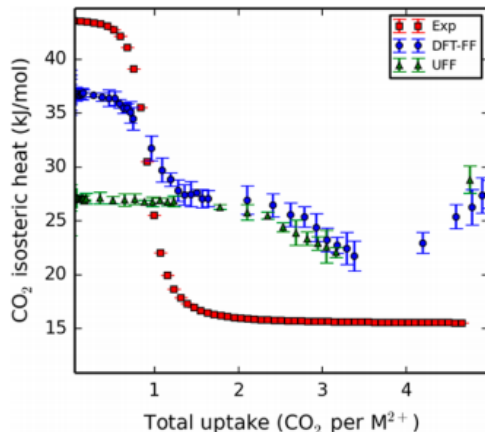


Figure 2.16: Comparison between the experimental (red squares) and simulated heats of adsorption as a function of the uptake computed using the DFT-derived force field (blue circles) and the UFF force field (green triangles) for CO_2 in $\text{Mg}_2(\text{dobpdc})$. Error bars are plotted for simulation data.

was performed with our in-house optimization code by minimizing the summation of the differences between the REPEAT charges and the new charges from the QEq formalism for the whole training set. Reoptimized parameters are summarized in Table 2.1.

IV.a. CO_2 . Computed total CO_2 adsorption isotherms in $\text{M}_2(\text{dobpdc})$ frameworks using the DFT-derived force field are available in Figure 2.15. When comparing with $\text{M}_2(\text{dobdc})$ results (Figure 2.15), we observe very similar uptakes in $\text{M}_2(\text{dobpdc})$ at very low pressures. That is, below 0.1 bar, the isotherms for the same metal in the regular and extended frameworks are almost overlapping, with only a slightly higher uptake observed in each respective $\text{M}_2(\text{dobdc})$ framework. However, above 1 bar, the isotherms for the two sets of frameworks diverge significantly, with $\text{M}_2(\text{dobpdc})$ frameworks exhibiting a much larger uptake than the $\text{M}_2(\text{dobdc})$ frameworks. Furthermore, CO_2 isotherms in all $\text{M}_2(\text{dobpdc})$ frameworks exhibit triple-site Langmuir behavior, as opposed to the dual-site Langmuir behavior observed in $\text{M}_2(\text{dobdc})$ frameworks.

Simulation results for CO_2 adsorption in $\text{Mg}_2(\text{dobpdc})$ using the DFT-derived force field are compared to experimental measurements in Figure 2.15. Furthermore, the heats of adsorption for CO_2 in $\text{Mg}_2(\text{dobpdc})$ computed using the DFT-derived FF and the UFF force field are compared to experimental measurements in Figure 2.16. We find that while the computed and measured isotherms are in good agreement at low pressures, the experimentally obtained heats of adsorption for CO_2 neither capture the triple-site behavior that is observed in simulations using the DFT-derived force field nor the increase in the heat of adsorption observed at higher uptakes (due to favorable guest-guest interactions) when using both the DFT-derived force field and the UFF force field. This is not surprising as experimentally the isosteric heats end up giving averaged out information on the many binding sites if they are not different enough in energy. Nonetheless, using the DFT-derived force

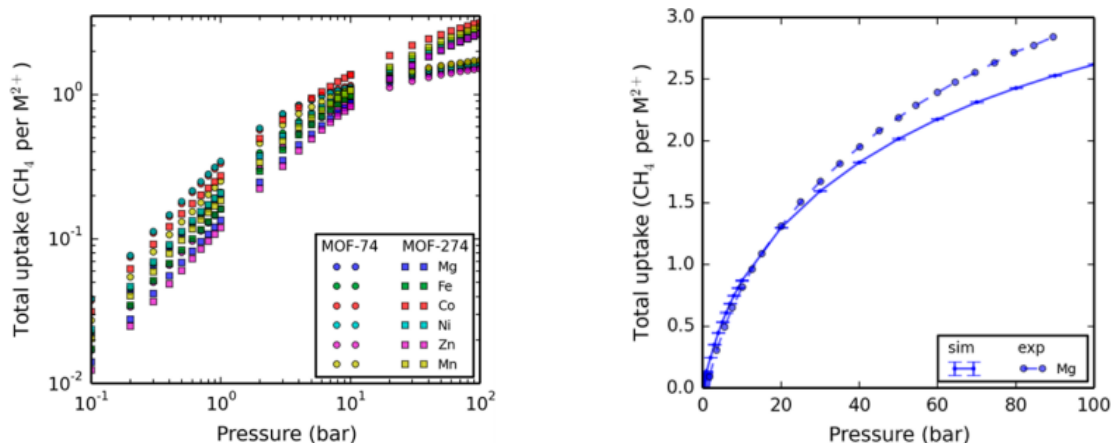


Figure 2.17: (left) Comparison of CH₄ adsorption isotherms computed at 298 K using the DFT-derived force field in M₂(dobdc) (circular markers) and M₂(dobpdc) (square markers) frameworks on a logarithmic plot. (right) Comparison between the experimental and simulated isotherms computed using the DFT-derived force field for CH₄ in Mg₂(dobpdc) at 298 K. Isotherms were measured in this work for the Mg framework for comparison with simulation. The corresponding unscaled isotherm from simulation is shown by the solid lines. Error bars are plotted for simulation data but in most cases smaller than the markers.

field, we are able to capture the inflection point observed in the isosteric heat at an uptake of c.a. 1 CO₂/M²⁺, which is not seen when using the UFF force field. A second inflection point in the heat of adsorption is observed at an uptake of c.a. 2.8 CO₂/M²⁺ with both models used in simulation, followed by a gradual increase in the heat of adsorption with the increasing uptake.

IV.b. CH₄. Computed total CH₄ adsorption isotherms for M₂(dobpdc) frameworks using the DFT-derived force field are available in Figure 2.17. As in the case of CO₂, we observe adsorption behavior in the extended frameworks similar to that found in M₂(dobdc) frameworks below 1 bar (Figure 2.17), but we find a higher uptake in the extended structures above this pressure due to the larger pore volume. Furthermore, similar to the case of CO₂, at low (<1 bar) pressures we actually observe slightly lower uptake in each M₂(dobpdc) framework than what was observed in the corresponding M₂(dobdc) framework.

Simulation results for CH₄ adsorption in Mg₂(dobpdc) using the DFT-derived force field are compared to experimental measurements in Figure 2.17. In addition, the heats of adsorption for CH₄ in Mg₂(dobpdc) computed using the DFT-derived FF and the UFF force field are compared to experimental measurements in Figure 2.18. We find that not only are the computed and experimentally obtained isotherms in good agreement, but that the heats of adsorption are also in very good agreement. Although below uptakes of 0.5 CH₄ per M²⁺ the UFF force field leads to better agreement with the experimentally measured isosteric heat of adsorption, the DFT-derived force field does a better job than the UFF force field of reproducing the trend in the heat of adsorption throughout the range of CH₄

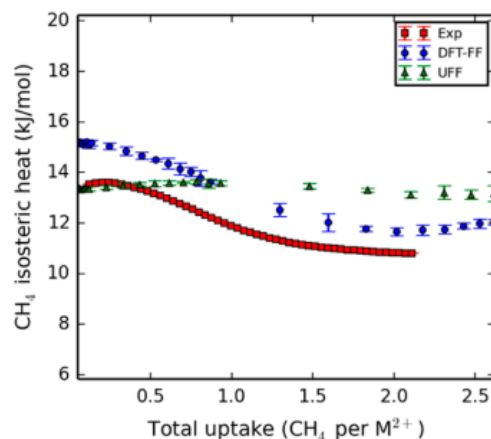


Figure 2.18: Comparison between the experimental (red squares) and simulated heats of adsorption as a function of the uptake computed using the DFT-derived force field (blue circles) and the UFF force field (green triangles) for CH₄ in Mg₂(dobpdc). Error bars are plotted for simulation data.

uptakes observed, and heats of adsorption computed with the DFT-derived force field are always within 1.6 kJ mol⁻¹ of the experimental values. As a result, we can see that the DFT-derived force field is transferable to this system for studying CH₄ adsorption across the entire range of pressures considered here.

Conclusion

We developed accurate, nonpolarizable force fields for H₂O, CO₂, and CH₄ in MOFs possessing strong-binding coordinatively unsaturated metal sites from DFT calculations. Using these force fields, we can make more accurate predictions of the adsorption properties of complex gas mixtures in M₂(dobdc), including the different adsorption mechanisms and selectivities observed between the six metal frameworks studied here.

From our simulations, we concluded that Mg₂(dobdc) would be the best of the M₂(dobdc) frameworks for separating CO₂ from dry natural gas feeds of interest, as has also been shown by other groups. In the case of tertiary mixtures, we found that all of the metal frameworks adsorb significantly more CO₂ than CH₄ and N₂, with almost no N₂ adsorbed under natural gas purification conditions. We also demonstrated that lowering the temperature of the adsorption process from 313 to 287 K significantly improves the ratio of CO₂ adsorbed over the two other guests. As it has the largest CO₂ binding energy of the six frameworks studied, Mg₂(dobdc) adsorbed the greatest amount of CO₂ when no H₂O was present. However, all of the M₂(dobdc) frameworks studied herein become saturated with H₂O in the presence of CO₂/H₂O binary mixtures composed of greater than 1% mole fraction of H₂O. As a result, none of these frameworks would be suitable for gas separations from any wet mixtures, especially if the mixture is composed of more weakly binding gases than CO₂.

Finally, we showed that in spite of the limitations of the above materials, our force field can be used to predict adsorption behavior in other frameworks, such as the extended $M_2(\text{dobdc})$ framework, $M_2(\text{dobpdc})$. Because our force field is a promising means for studying adsorption in these and similar frameworks, our model (and models developed using similar methods) can be used to discover new materials of similar topologies for targeted carbon capture applications and to explore the properties of existing materials. In fact, we used this force field extensively to study the diffusion of CO_2 and CH_4 in $M_2(\text{dobdc})$, which will be discussed in the following chapter (Chapter 3). We anticipate that the method presented here can be used to develop nonpolarizable force fields for other frameworks where existing models are not accurate enough for modeling adsorption processes of interest.

Additional Information in Appendix

Force field parameters. Guest-framework interaction energies along approaching paths. Probability density plots for all guests in the various frameworks. Additional mixture isotherms.

Chapter 3

Using the DFT-Derived Force Field to Study Diffusion in $M_2(\text{dobdc})$

In the previous chapter, we developed a force field for modeling CO_2 , H_2O , and CH_4 adsorption in the $M_2(\text{dobdc})$ series and saw that it performed better than the previous generations of force fields.

This chapter now focuses on work using this force field to study the dynamics of CO_2 and CH_4 in these same systems. In the first section, *Diffusive Anisotropy of Carbon Dioxide in $M_2(\text{dobdc})$* , we use the DFT-derived force field to investigate the diffusion behavior of CO_2 in $\text{Zn}_2(\text{dobpdc})$ using MD simulations, and demonstrate that under the assumptions of having a perfect crystal, the diffusive anisotropy that is observed experimentally is unable to be reproduced in simulations using both a rigid and a flexible $\text{Zn}_2(\text{dobdc})$ framework. This led us to conclude that the unexpected diffusion along the *ab*-plane of CO_2 observed experimentally is likely enabled through the presence of defects in the material, which have yet to be characterized. In the second section, *The Effect of the Coordinatively Unsaturated Metal Sites on CH_4 Diffusion in $M_2(\text{dobdc})$* , we investigate the diffusive behavior of CH_4 in $\text{Zn}_2(\text{dobdc})$ via a similar combination of computational and experimental investigations, and find that while the simulations generally corroborate the experimental diffusion coefficients and exchange rates observed at high loadings, at low loadings they are not in agreement, prompting further questions.

3.1 Diffusive Anisotropy of Carbon Dioxide in $M_2(\text{dobdc})$

Overview

In this work, we investigate the diffusion of CO_2 in $\text{Zn}_2(\text{dobpdc})$ ($\text{dobpdc}^{4-} = 4,4'$ -dioxidobiphenyl-3,3'-dicarboxylate), which features 1D porosity at the nanoscale. An understanding of the interplay between the framework structure and gas diffusion is crucial

for the practical application of these materials as adsorbents, since the rate of gas diffusion within the adsorbent pores determines the required size (and therefore cost) of the adsorbent column or membrane.

We study the diffusion of CO₂ within the pores of Zn₂(dobpdc) using a combination of pulsed field gradient (PFG) nuclear magnetic resonance (NMR) spectroscopy and MD simulations. The residual chemical shift anisotropy for pore-confined CO₂ allows PFG NMR measurements of self-diffusion coefficients in different crystallographic directions, and our analysis of the entire NMR line shape as a function of the applied field gradient provides a precise determination of the self-diffusion coefficients. In addition to observing CO₂ diffusion through the channels parallel to the crystallographic *c*-axis (self-diffusion coefficient $D_{\parallel} = (5.8 \pm 0.1) \times 10^{-9} \text{ m}^2 \text{ s}^{-1}$ at a pressure of 625 mbar CO₂), we unexpectedly find that CO₂ is also able to diffuse between the hexagonal channels in the crystallographic *ab*-plane ($D_{\perp} = (1.9 \pm 0.2) \times 10^{-10} \text{ m}^2 \text{ s}^{-1}$), despite the walls of these channels appearing impermeable by single-crystal X-ray crystallography and flexible lattice MD simulations. Observation of such unexpected diffusion in the *ab*-plane suggests the presence of defects that enable effective multidimensional CO₂ transport in a metal-organic framework with nominally 1D porosity, which is corroborated by simulation.

This section is based on the following publication:

Forse, A.C., Gonzalez, M.I., Siegelman, R.L., Witherspoon, V.J., Jawahery, S., Mercado, R., Milner, P.J., Martell, J.D., Smit, B., Blümich, B. and Long, J.R., 2018. Unexpected Diffusion Anisotropy of Carbon Dioxide in the Metal-Organic Framework Zn₂(dobpdc). *Journal of the American Chemical Society*, 140(5), pp.1663-1673.

Introduction

Frameworks in the MOF-74 family such as M₂(dobdc) (dobdc⁴⁻ = 2,5-dioxido-1,4-benzenedicarboxylate; M = Mg, Mn, Fe, Co, Ni, Cu, Zn, Cd) [192, 45, 46, 44, 246, 13, 196, 42] and the expanded variants M₂(dobpdc) (dobpdc⁴⁻ = 4,4'-dioxidobiphenyl-3,3'-dicarboxylate; M = Mg, Mn, Fe, Co, Ni, Zn) [155, 156, 74] demonstrate promise for the separation of CO₂ from coal flue gas mixtures[25, 147, 187] as well as for CO₂/CH₄ separations, due to the presence of the coordinatively unsaturated metal sites along 1D hexagonal pores.[192, 19] Notably, their CO₂ capture performance has been found to improve dramatically upon appending diamines to the metal sites. The diamine-appended frameworks cooperatively adsorb CO₂ via the formation of ammonium carbamate chains, resulting in low regeneration energies and dramatically improved performance even in the presence of water.[155, 156, 148, 199, 165, 121, 95]

Despite the promising nature of this series of materials for a variety of gas separations, an understanding of gas diffusion in this class of materials is incomplete. The importance of strong CO₂-metal interactions in dictating local energy barriers for diffusive motion between different binding sites in Mg₂(dobdc) has previously been illustrated.[23] NMR spectroscopy has also been used to probe the hopping dynamics and resulting average orientations of

CO₂ molecules in the pores of Mg₂(dobdc) via the measurement of residual chemical shift anisotropies.[127, 139] Despite this, little is known about the long-range diffusive motion of molecules within MOFs. In particular, the magnitude and directionality of gas diffusion within the 1D nanosized pores of these adsorbents are not well studied, even though such parameters have a substantial impact on their practical utility, such as the breakthrough time of different gases in a separation. By understanding the diffusion of gases such as CO₂ in this class of MOFs, we hope to guide the design of new materials with improved gas transport properties.

Pulsed-field gradient (PFG) NMR spectroscopy allows the measurement of self-diffusion coefficients of pore-confined molecules [102, 205, 220, 125, 61, 60] and uses pulses of magnetic field gradients to encode and decode the positions of the molecules. To do a PFG NMR measurement, a series of NMR experiments are first carried out with magnetic field gradient pulses of increasing strength, and self-diffusion coefficients are subsequently obtained by fitting the decay of the NMR signal intensity as a function of the field gradient. PFG NMR spectroscopy is a powerful characterization technique, as it can also be used to measure diffusion anisotropy.[64, 216] For example, aligning single crystals of a material at different orientations relative to the magnetic field gradient direction (the direction in which diffusion is measured) allows one to probe the diffusion of adsorbed molecules in different crystallographic directions.[12, 21, 50] An alternative approach that does not require oriented single crystals is to make use of residual anisotropic NMR interactions in static polycrystalline samples, wherein the resonance frequency is dependent on the crystallite orientation. Using the latter approach, residual quadrupole interactions (²H NMR) combined with PFG experiments have been used to measure the diffusion anisotropy of ²H₂O in a polycrystalline liquid crystal sample.[21] Later studies employed similar approaches based on residual chemical shift anisotropies.[50, 99, 178] In particular, the qualitative analysis of powder line shapes for CO₂ adsorbed in a MOF can be used to determine the preferred crystallographic direction for self-diffusion.[178, 179]

Here, we utilize the residual chemical shift anisotropy of CO₂ confined in the nanopores of Zn₂(dobpdc) to extract the diffusion anisotropy as a function of gas pressure. The large single crystals of this material (up to c.a. 750 μm in length) facilitate the measurement of diffusion of the pore-confined gas molecules, because exchange with the gas outside of the pores is negligible under the experimental conditions. The quantitative analysis of the evolution of the entire spectral line shape with increasing pulsed field gradient strength leads to the precise determination of self-diffusion coefficients parallel (D_{\parallel}) and perpendicular (D_{\perp}) to the hexagonal channels. Because of the shorter timescales involved and atomistic level detail attainable, MD simulations and *in situ* single-crystal X-ray diffraction measurements were used to support the proposed hypothesis explaining the anomalous diffusive behavior.

Methods

Synthesis and NMR Experiments. For details on the synthesis of these materials, as well as details on the NMR experiments, please consult the published work [62].

Molecular Dynamics Simulations. MD simulations were performed in the *NVT* ensemble using LAMMPS [183] with a time step of 1.0 fs and the Nosé-Hoover chain thermostat.[169, 86] The dynamics of CO₂ were treated using a rigid-body time integrator.[101] The CO₂ molecules were modeled using the TraPPE force field [229], and framework-CO₂ interactions were modeled using the previously parameterized DFT-derived force field discussed in Chapter 2.[163] The flexible lattice simulations required a molecular model for the framework atoms. Bond, angle, dihedral, and torsion parameters for linker molecules were taken from the consistent valence force field [36], while Zn²⁺ ions were modeled using a cationic dummy model.[47] Lorentz-Berthelot mixing rules were used to calculate cross-interactions between Zn²⁺ and linker atoms. For simulations at different pressures, the framework was loaded with a number of CO₂ molecules corresponding to previously published isotherms.[163] All MD simulations were equilibrated for 1 ns, and production runs lasted at least 10 ns to ensure that the mean-squared displacement (MSD) became linear as a function of time. The order-*n* algorithm [49] was used to calculate the MSD as a function of time, and the 1D self-diffusion coefficients were obtained by fitting the slope of the linear regime as per Eq (3.1) below.

$$D = \frac{1}{2} \lim_{t \rightarrow \infty} \frac{d}{dt} \langle [r(t) - r(0)]^2 \rangle \quad (3.1)$$

Results

NMR measurements are briefly summarized for comparison to the MD simulations below. In PFG NMR measurements of a Zn₂(dobpdc) sample dosed *ex situ* with 625 mbar of ¹³CO₂, magnetic field gradient pulses were applied along the laboratory *z*-direction (i.e. parallel to *B*₀). Upon application of pulsed magnetic field gradients of increasing magnitude, the right-hand edge of the spectrum decays more rapidly than the left-hand edge. Face-indexing of a single crystal confirmed that the *c*-axis, which is aligned with the 1D pores, runs along the long axis of the needle-like Zn₂(dobpdc) crystals. Using this observation and our prior assignments of the spectra, we obtained CO₂ self-diffusion coefficients both parallel (*D*_∥) and perpendicular (*D*_⊥) to the hexagonal channels of Zn₂(dobpdc), resulting in the following values of *D*_∥ = (5.8 ± 0.1) × 10⁻⁹ m² s⁻¹ and *D*_⊥ = (1.9 ± 0.2) × 10⁻¹⁰ m² s⁻¹. These values suggest that the self-diffusion of CO₂ is c.a. 30 times faster along the hexagonal channels compared to diffusion between the channels at this pressure. However, it was surprising that gas diffusion perpendicular to the channels is possible at all, given the apparent lack of pore windows between neighboring channels in the *ab*-plane. We note that the measured values are of similar order to self-diffusion values of bulk liquids, though they are more than 3 orders of magnitude smaller than the self-diffusion coefficient of gaseous CO₂ (1.1 × 10⁻⁵ m² s⁻¹ at 25 °C, 1 bar). [231] The measured values are of similar order to the diffusion of CO₂ in other large-pore MOFs, such as HKUST-1 (*D* = 1.7 × 10⁻⁹ m² s⁻¹) [217], Zn₂(bdc)₂(dabco) (*D*_∥ = 1.1 × 10⁻⁸ m² s⁻¹ and *D*_⊥ = 3.7 × 10⁻⁹ m² s⁻¹) [178], and MIL-47(V) (*D* = 10⁻⁸-10⁻⁹ m² s⁻¹, depending on loading level).[194]

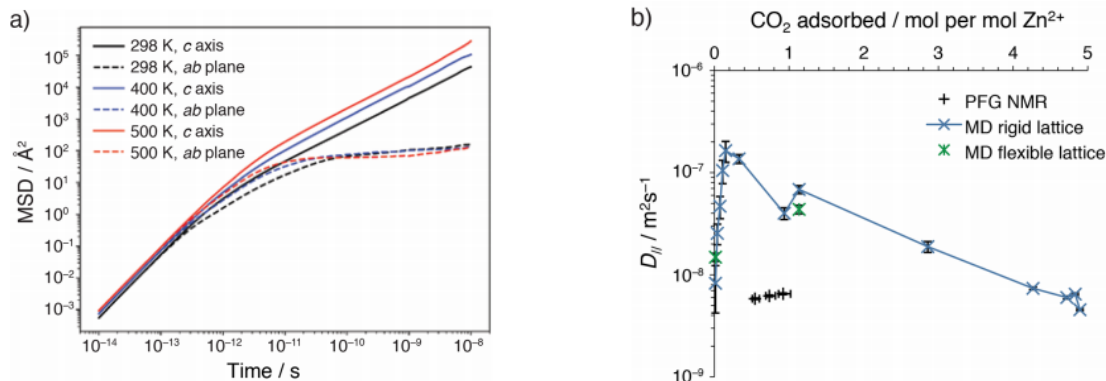


Figure 3.1: (a) MSDs in different crystallographic directions from flexible MOF MD simulations at 298, 400, and 500 K and a CO₂ pressure of 1 bar. Individual 1D MSDs were calculated for the a and b directions, and the average is shown in the plot. (b) Self-diffusion coefficients (298 K) along the *c*-axis ($D_{||}$) at a range of pressures. Values are shown for rigid and flexible lattice MD simulations as well as those obtained using PFG NMR.

Molecular Dynamics Simulations. To further probe CO₂ diffusion in Zn₂(dobpdc), and determine whether or not the CO₂ molecules can in fact diffuse along the *ab*-plane in a perfect crystal structure, we ran MD simulations using (i) a fully flexible MOF lattice model and (ii) a rigid MOF lattice.

Figure 3.1 shows the time-evolution of the mean square displacement (MSD) of CO₂ molecules in the different crystallographic directions for the flexible lattice model with a CO₂ pressure of 1 bar. Since $\log(\text{MSD})$ is given by $\log(nD) + \log(t)$ in the diffusive regime, a slope of 1 and a *y*-intercept of $\log(nD)$ are anticipated on a log-log plot, provided that sufficiently long times are probed to reach this regime. Inspection of the plot in Figure 3.1 thus informs an assessment of the diffusion behavior of CO₂ in Zn₂(dobpdc). Long-range self-diffusion of CO₂ occurs along the *c*-axis, as anticipated, with the diffusive regime (slope = 1) being reached at times longer than c.a. 10 ps (Figure 3.1). In contrast, diffusion of CO₂ in the *ab*-plane is limited to displacements within a single pore, with no diffusive jumps occurring between different channels. This observation is reflected by the apparent plateauing of the MSD in the *ab*-plane at long times, with the diffusive regime never being reached. At 298 K, the MSD climbs to c.a. 160 Å² at a time of 10 ns, corresponding to a RMSD of c.a. 13 Å, which, as expected, is less than the pore diameter of c.a. 22 Å. Similar behavior is apparent at all three studied temperatures of 298, 400, and 500 K, as well as at a lower pressure of 0.01 bar, indicating the absence of a thermally activated diffusion mechanism that could allow CO₂ to move between pores.

MD simulations with a rigid lattice also revealed the absence of long-range diffusion in the *ab*-plane at all CO₂ loadings considered. These observations from MD simulations, which are based upon the assumption of perfect crystals, are in contrast to the results from PFG NMR experiments, where crystal defects may affect CO₂ diffusion.

The self-diffusion coefficients along the c -axis (D_{\parallel}) determined from MD simulations in a rigid framework are shown in Figure 3.1. These simulations allowed access to pressures from 10 mbar to 100 bar (a much wider range of pressures, and therefore CO₂ loadings, than was accessible with the NMR apparatus at the time) and reveal loading-dependent diffusion behavior. A clear increase in D_{\parallel} is observed at very low loadings, followed by decreases at higher loadings. We postulate that at the lowest loadings, the small D_{\parallel} values result from the high density of coordinatively unsaturated metal sites. Indeed, DFT calculations of CO₂ diffusion pathways in a similar MOF, Mg₂(dobdc), have shown that the energy barrier for CO₂ to move from a metal site to a neighboring unoccupied metal site is c.a. 300 meV (c.a. 30 kJ mol⁻¹).^[23] After some of the metal sites become occupied by CO₂, additional lower energy pathways may give rise to the observed increase in D_{\parallel} , particularly diffusive motion of CO₂ through the pore center, which bypasses interaction with metal sites that are already occupied by other CO₂ molecules (for Mg₂(dobdc), a barrier <40 meV or >4 kJ mol⁻¹).^[23] The availability of these additional pathways is exemplified by the upturn in D_{\parallel} between 750 and 1000 mbar, which also corresponds to the point at which a loading of 1 CO₂ per Zn²⁺ site is surpassed in the simulations. At higher CO₂ loadings, the observed decreases in D_{\parallel} are due to increased CO₂-CO₂ collisions.

Finally, we note that PFG NMR gives smaller self-diffusion values than MD by a factor of c.a. 10, with such discrepancies not uncommon in the literature.^[96, 58] In the present case, differences in the experimental and simulated values likely arise from both the presence of crystal defects in the experiment and small errors in the parametrization of the force fields used for simulations.

Conclusion

Through this project, we demonstrated how the residual chemical shift anisotropy for CO₂ confined in the pores of Zn₂(dobpdc) allows measurement of the diffusion anisotropy using PFG NMR spectroscopy, and how MD simulations can be used to understand the reasons behind this diffusion anisotropy due to the higher resolution possible in computer experiments as opposed to NMR experiments. Surprisingly, we find that the pore-confined gas is able to diffuse between adjacent framework channels in the ab -plane, with self-diffusion coefficients of $D_{\parallel} = (5.8 \pm 0.1) \times 10^{-9} \text{ m}^2 \text{ s}^{-1}$ and $D_{\perp} = (1.9 \pm 0.2) \times 10^{-10} \text{ m}^2 \text{ s}^{-1}$ at 298 K and a pressure of 625 mbar of CO₂. Measurements at gas pressures between 625 and 2026 mbar gave very similar diffusion values, while MD simulations showed significant variations in the self-diffusion coefficients at more extreme pressures. Because *in situ* single-crystal X-ray diffraction experiments revealed no obvious structural distortions upon the adsorption of CO₂ and flexible lattice MD simulations revealed no diffusion between different channels in the ab -plane, we concluded that defects in the synthesized material are likely responsible for the observed nonzero diffusion in the ab -plane. We believe that an understanding of the diffusion anisotropy opens considerable opportunities for crystal engineering for CO₂ capture as well as other gas storage and separation applications, both for adsorbents and mixed-matrix membranes.

3.2 The Effect of the Coordinatively Unsaturated Metal Sites on CH₄ Diffusion in M₂(dobdc)

Overview

In this work, we investigated how methane diffusion depends on methane loading in three analogues of the M₂(dobdc) series (M = Mg, Ni, Zn) through a combination of NMR experiments and molecular simulations. Our investigations of methane diffusion via NMR relaxometry complemented with MD simulations suggest that the coordinatively unsaturated metal sites serve to interrupt both the translational and rotational motion of methane via primary adsorption events at low density. At higher gas loadings inside the pores, CH₄-CH₄ interactions become more significant, and as CH₄-CH₄ collisions become more frequent and the self-diffusion coefficients begin to exponentially decrease again.

We find that the Ni₂(dobdc) analogue has the strongest influence on the observed R_1 rates of methane in M₂(dobdc), possibly attributed to increased rotational correlation times. Two D_s coefficients were observed for all loadings from the NMR experiments, with the slow D_s measured being in good agreement with those from simulations. From molecular dynamics simulations, we find that the self-diffusion coefficient is maximized at loadings corresponding to a single molecule along a given *ab*-plane in the pore, suggesting that favorable CH₄-CH₄ interactions at higher pressures lead to a decrease in the D_s at higher loadings. Finally, we observe that the self-diffusion coefficient of methane is inversely related to the binding energy at the coordinatively unsaturated metal sites, such that it is fastest in the Zn₂(dobdc) framework and slowest in the Ni₂(dobdc) framework.

This section is based on the following work (to be soon submitted):

Witherspoon, V. J., Mercado, R., Braun, E., Bachman, J., Long, J. R., Blümich, B., Smit, B., Reimer, J. A. The Influence of the Coordinatively Unsaturated Metal Sites on Methane Dynamics in M₂(dobdc). *In Preparation*.

Introduction

Isorecticular MOFs are a subclass of MOFs that retain a single topology while allowing for systematic variation in important pore attributes, such as the composition of the framework or the pore diameters. M₂(dobdc) (also known as M-MOF-74, where M = Mg, Mn, Fe, Co, Ni, Cu, Zn and dobdc⁴⁻ = 2,5-dioxido-1,4-benzenedicarboxylate) is part of an isorecticular family of structures that has shown great potential for applications in gas storage and separation technologies due to the presence of strongly-adsorbing coordinatively unsaturated metal sites. [117, 210, 187] Improvements to this class of materials for selective methane interactions is important for chemical processes such as natural gas enrichment and the separation of methane from power plant flues. [146, 201, 197] Motivated by the number of important environmental applications involving methane adsorption in MOFs, researchers have frequently investigated the potential of M₂(dobdc) for natural gas storage and sepa-

rations, demonstrating that the choice of transition metal in the framework significantly influences the MOF’s adsorptive capacity for methane. [146, 163]

Neutron scattering characterization of CH₄ in the dhtp analogue (dhtp = 2,5-dihydroxyterephthalate) of M₂(dobdc) has shown the presence of primary adsorption sites located directly above the coordinatively unsaturated metal sites as well as the presence of secondary adsorption sites that can be found along the *c*-axis between the primary binding sites; tertiary binding sites have also been observed in the center of the pores for certain adsorbents in M₂(dobdc), including methane and carbon dioxide. [232, 187] Other studies have investigated CH₄ adsorption in M₂(dobdc) and shown how the nickel analogue of M₂(dobdc) displays the highest volumetric uptake for CH₄ at 35 bar (230 v STP/v). [146, 163] The other M₂(dobdc) analogues display significantly lower uptakes – Mg₂(dobdc) has a 35-bar CH₄ uptake of 200 v STP/v, and Zn₂(dobdc) has a 35-bar CH₄ uptake of 188 v STP/v.

Differences in CH₄ uptake between the various M₂(dobdc) analogues at low pressures are primarily due to the binding energies associated with the adsorption of CH₄ to the coordinatively unsaturated metal sites. The experimentally reported sub-ambient pressure CH₄ isotherms exhibit metal-dependent differences. Computational investigations [163, 120] have ranked the relative binding energies of CH₄ adsorbed in M₂(dobdc) from highest to lowest as Ni > Mg > Zn, in line with results for the CH₄ adsorption isotherms. These studies have also reported differences among binding energies associated with the secondary adsorption sites. Analysis of spatial probability distributions produced from grand canonical Monte Carlo (GCMC) simulation data demonstrated that CH₄ molecules spend a larger fraction of their time inside the pores near the coordinatively unsaturated metal sites in frameworks with stronger heats of adsorption.[163]

While many studies have evaluated indirectly the effect of energetics on a system’s suitability for gas separations (e.g. fitting transient breakthrough data), few studies have systematically studied the effect of host-guest energetics on mass transport in MOFs. [212] The transport of CH₄ in Ni₂(dobdc) was investigated previously via permeation experiments for mixed-membrane applications, where it was found that these macroscopic methods yielded averaged mass-transfer coefficients with contributions from both the intercrystalline and intracrystalline regimes. [27] However, these contributions were not separable due to the nature of the experiment. Understanding the transport contributions of small molecules in MOFs has proven challenging, with few experimental techniques available to assess mass-transfer coefficients associated with the intracrystalline regime. [100] In this regime, systematic variations in the pore attributes are influential.

Nuclear magnetic resonance (NMR) [186] is a robust and proven technique that has been implemented to understand the motion of adsorbed gases via observation of their self-diffusion (D_s) coefficients and relaxation rate constants. [205, 108, 128, 206, 62] Furthermore, MD simulations [30, 62] performed as a function of loading in other systems have indicated that the observed intracrystalline D_s coefficient is a strong function of the interaction strength of the adsorbate with the framework. [115] In this work, we thus set out to gain a better understanding of the gas adsorption dynamics in M₂(dobdc) through the combination of NMR measurements and MD simulations, with MD simulations complementing the experiments

at conditions that are not experimentally accessible.

Methods

NMR Sample Preparation The $M_2(\text{dobdc})$ analogues were prepared via the synthetic routes reported previously. [3] For each analogue, the synthesized material was activated and placed in a glovebox under argon before transferring it to a valved NMR glass tube. The samples were then activated again for 12 hours at 180 °C and 0.01 mbar. Samples were cooled to 40 °C and held at the desired equilibrium pressure for thirty minutes to an hour before closing the valve on the NMR tube. The sample was allowed to cool to room temperature and transferred to the NMR probe where it was re-heated to 40 °C for thirty minutes before performing experiments.

NMR Measurements A 13 Interval Bi-Polar Pulse Field Gradient Stimulated Echo experiment with z-spoiler as described in [34] was performed with a Bruker Avance III 700 MHz spectrometer using a Diff30 insert in the Mic5 Bruker imaging probe. Diffusion times ranged from 1 – 2.5 ms while the gradient strength ranged from 0 – 17 T/m in 48 steps. The observed attenuation was processed using a 1D inverse Laplace transformation as implemented in the Kea Prospa Software. The reported values are the logarithm mean diffusivity distributions at variable pressure and constant temperature cycled 3 – 5 times in random order. The R_1 (longitudinal relaxation rate) constant was obtained using an Inversion Recovery Pulse Sequence (180-90-Acquire) and the R_2 (transverse relaxation rate) constant was measured by implementing the Carr-Purcell-Meiboom-Gill pulse sequence with spectroscopic acquisitions. [24] For all sample loadings, R_1 was lower than R_2 and the stimulated echo diffusion rate was significantly greater than both the R_1 and R_2 . The diffusion time was limited to 2.5 ms due to potential evidence of diffusive diffraction [20] at longer times.

MD Simulations The D_s coefficients were computed for CH_4 in $M_2(\text{dobdc})$ ($M = \text{Mg}, \text{Ni}, \text{Zn}$) from MD simulations performed using LAMMPS. [183, 195] The systems were simulated in the canonical ensemble at loadings corresponding to the equilibrium uptake values as determined from GCMC simulations at pressures ranging from 0.1 bar and 100 bar and 313 K. After equilibration for one nanosecond, each system was simulated for ten nanoseconds with a timestep of one femtosecond using a Nosé-Hoover thermostat. For framework- CH_4 interactions, the previously discussed DFT-derived force field [163] was used. CH_4 - CH_4 interactions were taken from TraPPE[140]. Non-bonding interactions were cut-off and shifted at 12.5 Å, and all unit cells were sufficiently replicated so as to avoid interaction between periodic replica.

The D_s coefficients of adsorbed CH_4 were computed from these equilibrium simulations using the Einstein equation, which relates the self-diffusivity of a molecule to its mean-squared displacement (MSD). The D_s coefficients were calculated from the CH_4 MSDs in each framework in the diffusive regime (2 – 100 ps) as generated using the order- n algorithm described previously.[49]

For the low-density simulations, the error bars for the D_s coefficients were estimated by splitting up each 10 ns trajectory into ten 1 ns trajectories and calculating the standard

deviation of the ten D_s coefficients computed for each 1 ns trajectory. For the higher density trajectories, the error bars for the D_s coefficients were estimated by running three different simulations at the same set of conditions but with a different random seed, and calculating the standard deviation of the three D_s coefficients computed for each 10 ns trajectory.

CH₄ Hopping Rates In order to estimate the hopping rate of CH₄ between the two different binding sites in each M₂(dobdc) framework, the average exchange rate was calculated by counting the number of times a CH₄ molecule transitioned from a primary binding site (2.8 - 3.0 Å from the metal) to a secondary binding site (3.5 - 3.7 Å from the metal), or vice versa, per nanosecond of time. The distances for the binding sites were determined from the spatial distribution of the CH₄ around the metals; peaks in the CH₄ density corresponding to the two densest binding sites occur near 2.9 Å and 3.6 Å for all three frameworks (see Appendix). The widths of 0.2 Å around the peak density of each binding site were chosen such that it would be unambiguous which binding site the CH₄ is located at. If, for example, a CH₄ molecule crossed into the intermediate region, and then back to the same site, this was not counted as an exchange event.

Results and Discussion

To understand spin-lattice relaxation phenomena in MOFs, one must first consider the many mechanisms that contribute to the spin-lattice relaxation of free and adsorbed species: intramolecular contributions, intermolecular contributions, and spin-rotation contributions.

In the experiments, contributions from intramolecular interactions are predominately dipole-dipole interactions from ¹H-¹H and ¹H-¹³C pairs in a single molecule. These may be neglected for most pure gases near or above room temperature. [92] Contributions from chemical shift anisotropy are important for the observation of nuclei with large chemical shift ranges, but this does not apply to CH₄ because protons have a very narrow chemical shift span. Other types of contributions to the spin-lattice relaxation can be generally classified as intermolecular interactions. These may be represented by ¹H-¹H, ¹H-metal, and ¹H-¹³C pairwise interactions between different CH₄ molecules or between CH₄ and the framework atoms. The contribution often considered to be dominant for gaseous species is spin-rotation relaxation, stemming from the coupling between molecular rotational angular momentum and the nuclear spin. [110, 154]

Spin-rotation dominated relaxation gives relaxation rates that are sensitive to the density. For the case of pure gases, researchers have found that in the low density regime, relaxation correlates to the number of binary collisions. [92] As the frequency of collision increases, molecular impacts perturb the angular momentum, effectively shortening the correlation time, and the R_1 approaches a maximum; this maximum occurs when the nuclear Larmor frequency and the collision frequency are equal to each other. Then, the observed R_1 may enter the reciprocal regime, where its value decreases linearly with the gas density.

This expected behavior for intermediate to high densities of CH₄ gas adsorbed in ZIF-8 has been reported previously.[206] In addition to the traditional density dependent contributions from inter- and intramolecular dipole-dipole interactions, it was proposed that the

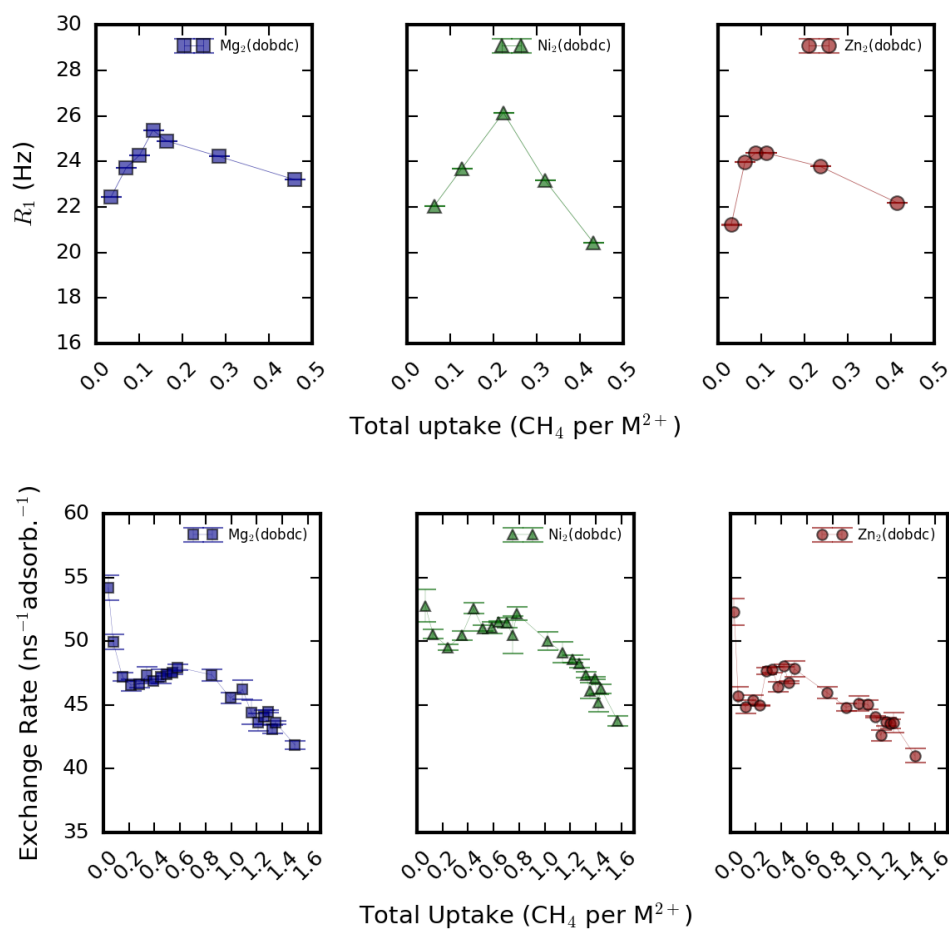


Figure 3.2: (top) The R_1 constant of CH_4 adsorbed in the Mg, Ni, and Zn analogues of $\text{M}_2(\text{dobdc})$ as a function of adsorbed number of molecules per coordinatively unsaturated metal site. Interpolated lines are shown as guides. (bottom) Plot of the exchange rates between two different binding sites calculated from MD simulations in the three $\text{M}_2(\text{dobdc})$ frameworks. All experiments and simulations were at 313 K. Note the different axes.

spin-rotation mechanism is influenced by interactions with the framework. A surface relaxivity term, ρ_s , was introduced to describe the slope of the observed spin-lattice relaxation rates with decreasing density in the different frameworks; it is proportional to the strength of interaction between the frameworks and the gases. Similar behavior has been noted for pure gases.[93]

In contrast to previous observations [206] of CH₄ in porous media, we observe the R_1 of CH₄ gas in M₂(dobdc) initially increase with increasing density at low pressures (Figure 3.2, top). We posit that this is due to the strong attraction of CH₄ to the coordinatively unsaturated metal sites as well as to larger rates of exchange between the primary and secondary sites. Whereas in pure gases the only interaction strong enough to interrupt the rotational trajectory of a molecule is a collision, the angular momentum of an adsorbed CH₄ molecule at low density is more likely to be interrupted by adsorption to the metal site. For pure CH₄ the transition from the low density to the high density regime occurs at a pressure close to 15 bar. This deviation from normal gaseous behavior may be attributed to the initial localization of the gas molecules to the primary adsorption sites located directly above the coordinatively unsaturated metal sites. [232, 163] At sub-ambient pressures, the primary sites remain undersaturated, and as such the probability of finding a molecule at a coordinatively unsaturated metal site is still higher than the probability of finding it elsewhere in the pore. According to GCMC simulations, the coordinatively unsaturated metal sites remain unsaturated until approximately 10 – 20 bar in all three frameworks. In this low pressure regime, rotational diffusion is mainly influenced by the CH₄ hopping frequency between the coordinatively unsaturated metal sites, or the low loading free energy barrier for translational motion. This phenomenon has been observed for adsorbed liquid species and is often referred to as *reorientations mediated by translational displacements*. [207]

The trend in the R_1 for each M₂(dobdc) framework is that as the CH₄ loading is increased, the R_1 passes through a maximum correlated with the binding energy of that metal analogue; this is qualitatively representative of the frequency of an adsorption event, analogous to the frequency of collisions for free gases. The collision rates at the the maximum R_1 measurements for CH₄ from NMR relaxation experiments are approximately 26.1 Hz in Ni₂(dobdc), 25.4 Hz in Mg₂(dobdc), and 24.4 Hz in Zn₂(dobdc) at 40 °C. Notably, the R_1 for CH₄ adsorbed in the Zn analog is maximized near an uptake of 0.09 CH₄ molecules per metal site (CH₄/M²⁺), whereas in Mg it is maximized closer to 0.12 CH₄/M²⁺, and in the Ni analogue it is maximized at an even larger uptake of roughly 0.22 CH₄/M²⁺ (Figure 3.2); this observation suggests that metal–CH₄ interactions in the Zn and Mg analogues allow for more CH₄–CH₄ collisions or interactions inside their pores. The trend in the R_1 constants in the linear regime is Ni > Mg > Zn. This corresponds to a relative adsorption enthalpy in each framework. The adsorption enthalpies at a loading of 0.2 CH₄/M²⁺ are 21.0 kJ/mol, 18.6 kJ/mol, and 16 kJ/mol for Ni₂(dobdc), Mg₂(dobdc), and Zn₂(dobdc), respectively. [233, 146]

Similarly, the exchange rates were calculated from the MD trajectories at all conditions studied in each framework (Figure 3.2, bottom). These are the rates at which a CH₄ molecule

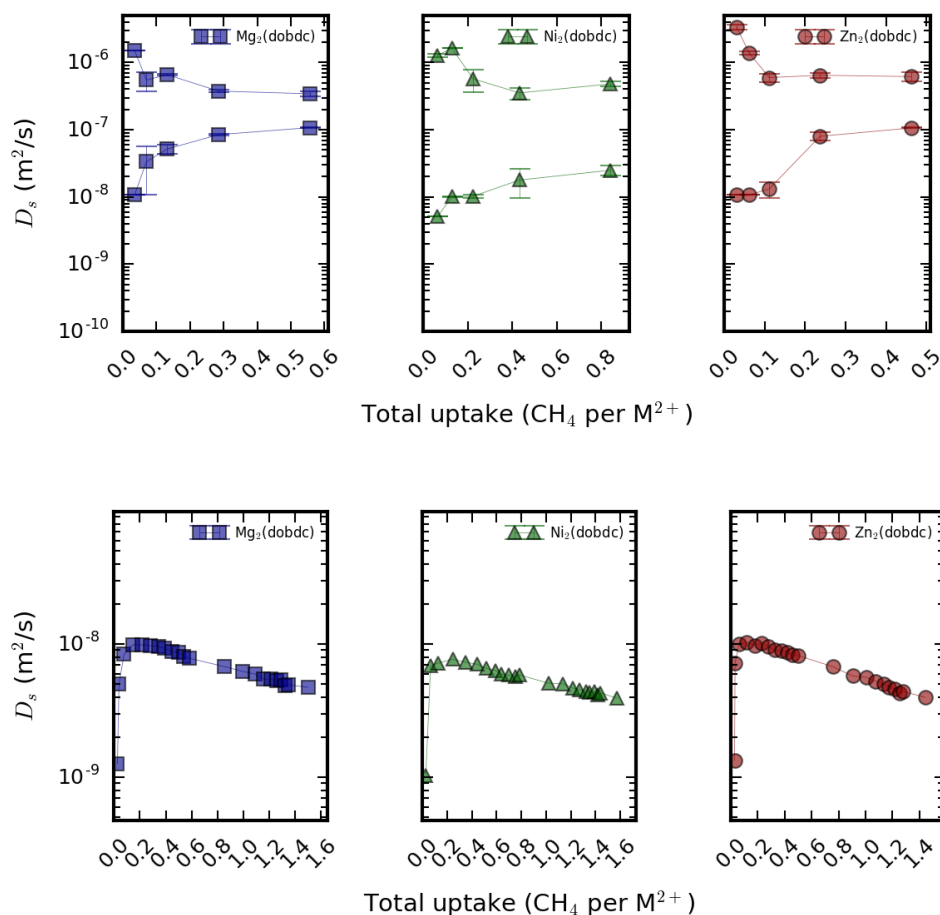


Figure 3.3: The D_s coefficients of CH₄ in Ni, Mg, and Zn analogues of M₂(dobdc) measured by NMR for 2 ms of diffusion time (top) and computed from 1 ns MD trajectories (bottom). In the experimental diffusion coefficients, the faster D_s coefficient is attributed to intercrystalline diffusion, whereas the slower D_s coefficient is attributed to diffusion inside the frameworks, or intracrystalline diffusion. Note the different axes.

moves from a primary binding site to a secondary binding site; for practical purposes, the primary binding site was defined as 2.8 – 3.0 Å from the metal and the secondary binding site was defined as 3.5 – 3.7 Å away from the metal (Figures C.9 – C.14). The trend in the calculated exchange rates is in agreement with experimental measurements – exchange between the two sites is greatest in the Ni₂(dobdc) framework and lowest in the Zn₂(dobdc) framework – at almost all conditions. However, at CH₄ loadings below between 0.01 and 0.16 CH₄/M²⁺, the exchange rates decrease significantly for all three frameworks, which is not experimentally observed. Then, the exchange rates increase in all three frameworks up to a loading of 0.8 CH₄/M²⁺ before decreasing again.

The analysis of the pulsed field gradient experiments led to the observation of binary D_s coefficients, meaning there exist two populations each associated with its own D_s coefficient, a fast one on the order of 10^{-7} m²/s, and a slower one on the order of 10^{-7} m²/s – and a smaller D_s coefficient on the order of 10^{-9} m²/s. We surmise that the faster D_s coefficient is due to rapid exchange between the free gas in the intercrystalline space and the adsorbed gas in the MOF, while the slower D_s coefficient is due to intracrystalline CH₄ diffusion. All analogues of M₂(dobdc) possess small crystal sizes, approximately 10 μm in length and a few microns in width for the as-synthesized powders, such that the diffusive path of a molecule can still be hundreds of microns in length in a 2.5 ms experimental diffusion time.

At all loadings, the magnitudes of the intracrystalline D_s coefficients in each metal analogue, ranked from largest to smallest, are: Zn > Mg > Ni. This is strictly true in simulation; however, at low pressures, experimental measurements of the slow D_s coefficient show that Mg > Zn > Ni. Nonetheless, the general trend is not surprising, as it suggests a weaker interaction between adsorbate and framework atoms (such as in the Zn framework) allows for faster translational motion. On the other hand, a stronger interaction (such as that in the Ni framework) hinders this motion by keeping the adsorbate at the metal site longer. This is in agreement with the relaxation behavior, which indicates that rotational diffusion is mediated by frequent translational displacements.

MD simulations containing more CH₄ molecules per unit cell than coordinatively unsaturated metal sites were carried out so as to see if the D_s coefficient increased after all the coordinatively unsaturated metal sites were occupied, as the CH₄ spends the majority of its time during simulation at these sites. From these simulations, we observe that the D_s coefficient increases with the pressure from 0.1 to 1 bar (0.01 to 0.2 CH₄/M²⁺), peaking at about 10^{-8} m²/s and decreasing slowly with increasing pressures of CH₄ in the pores, as shown in Figure 3.3.

We observed through both experiment and simulation that the D_s coefficients are inversely related to the binding energy at the coordinatively unsaturated metal sites (U_{binding} : Ni > Mg > Zn). As such, they are generally fastest in the Zn₂(dobdc) framework and slowest in the Ni₂(dobdc) framework. As mentioned earlier, we hypothesize that the fast NMR D_s coefficient may be attributed to the faster exchange between adsorbed CH₄ and intercrystalline CH₄, whereas the slow NMR D_s coefficient may be attributed to intracrystalline diffusion.

Although the D_s coefficients calculated from simulations differed by one order of magnitude to their counterparts calculated from experiments, they displayed similar trends at loadings greater than $0.1\bar{6}$ CH₄/M²⁺. The trends in these D_s coefficients can be explained. The maximum in D_s for each framework occurs at a loading of roughly one CH₄ molecule per six coordinatively unsaturated metal sites ($0.1\bar{6}$ CH₄/M²⁺), which corresponds to a single CH₄ molecule at a given *ab*-plane along the *c*-axis; above this loading, there would likely be two CH₄ molecules near each other (on the same *ab*-plane) which would cause the binding strength to be greater due to favorable CH₄–CH₄ interactions, slowing down the molecule and thus leading to a smaller D_s . Before this maximum in the D_s coefficient, the increase in D_s can be explained by the growing presence of additional CH₄ molecules in the dilute

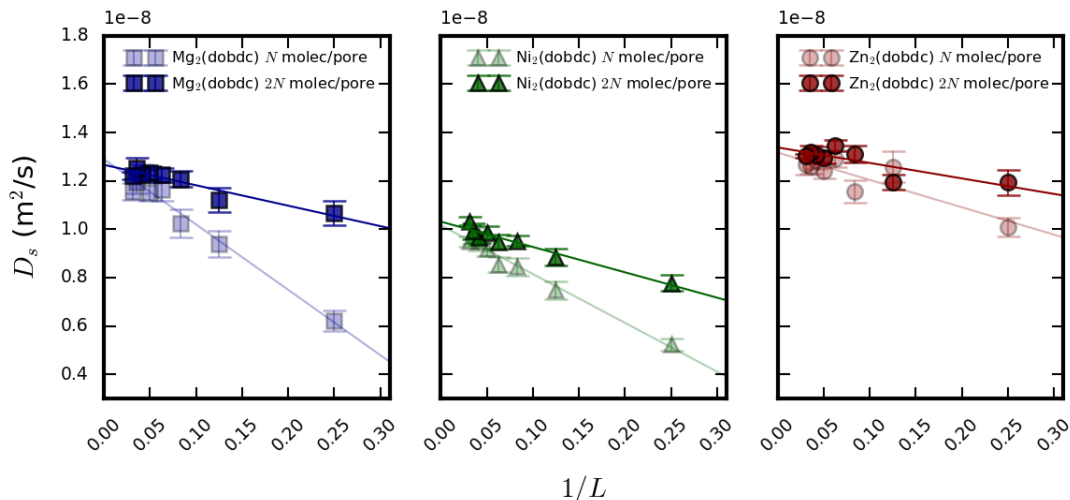


Figure 3.4: The D_s coefficients of CH_4 in Ni, Mg, and Zn analogues of $\text{M}_2(\text{dobdc})$ calculated at low, constant densities as a function of $1/L$, where L is the number of periodic replicas along the c -axis. The densities of CH_4 in each framework correspond to a value of $0.027 \text{ CH}_4/\text{M}^{2+}$ for the N molec/ \AA^3 dataset, and to a value of $0.055 \text{ CH}_4/\text{M}^{2+}$ for the $2N$ molec/ \AA^3 dataset (details in Table 3.1). The colored lines indicate linear fits to the data.

pores, which leads to a greater number of collisions and thus a larger distance traveled by each molecule.

At the lowest CH_4 uptakes considered in this work (c.a. $0.027 \text{ CH}_4/\text{M}^{2+}$), simulations of CH_4 in $\text{M}_2(\text{dobdc})$ would imply simulation boxes with only one or two CH_4 molecules inside if carried out in the same way as at all other uptakes. This is problematic for two reasons: 1) the temperature is not well defined for a single/few particle(s) and 2) determining how these molecules are distributed in the pores (six pores per simulation supercell) is also not well defined. To address these concerns, as well as assess that the D_s coefficients computed at these pressures were better defined, we carried out simulations at the same low CH_4 densities corresponding to the lowest pressure simulations in each framework ($0.027 \text{ CH}_4/\text{M}^{2+}$), but with both increasing c -axis lengths, l , of the simulation supercell (where $l \in \{4, 8, 12, 16, 20, 24, 28, 32\}$), and increasing numbers of CH_4 atoms, N , in the pores (N or $2N$ per pore, uniformly distributed, where $N \in \{1, 2, 3, 4, 5, 6, 7, 8\}$).

Indeed, we found that as we increased the number of molecules in the simulation box while keeping the densities fixed, the self-diffusion coefficients slowly increased up to a point and then converged (Figure 3.4). The D_s coefficients converged faster in the cases of $2N$ CH_4 atoms in the pores (double the density as the N CH_4 atoms per pore simulations). This is not surprising as not only is the temperature better defined the more molecules there are in the system, but the sampling statistics are also better. As shown by the y-intercepts of the linear fits in Figure 3.4, which extrapolate the diffusion coefficient to an infinitely-long

	Mg	Ni	Zn
N molec per \AA^3	2.988×10^{-4}	3.048×10^{-4}	3.039×10^{-4}
$2N$ molec per \AA^3	5.976×10^{-4}	6.096×10^{-4}	6.078×10^{-4}

Table 3.1: Densities of CH₄ in molecules per cubic angstrom (molec/ \AA^3) used in the low density simulations. In these simulations, the number of CH₄ molecules and number of unit cell replicas varied, but the densities kept the same. All of the N molec per \AA^3 densities correspond to a value of $0.027 \text{ CH}_4/\text{M}^{2+}$, and all of the $2N$ molec per \AA^3 densities correspond to a value of $0.055 \text{ CH}_4/\text{M}^{2+}$.

simulation box, the D_s is greatest in the Zn framework and smallest in the Ni framework at low CH₄ densities (low density D_s coefficients – Mg = $1.266\text{e-}08 \text{ m}^2/\text{s}$, Ni = $1.032\text{e-}08 \text{ m}^2/\text{s}$, Zn = $1.338\text{e-}08 \text{ m}^2/\text{s}$). This is also in agreement with the trend seen in the D_s from simulations at larger densities (Figure 3.3), as the D_s was found to be inversely related to the binding energy of CH₄ at the coordinatively unsaturated metal site in each framework.

Conclusion

The combination of computational and NMR studies presented in this work has elucidated a relationship between the strength of the coordinatively unsaturated metal sites in the isorecticular M₂(dobdc) series and the dynamics of CH₄ adsorbed in these frameworks. In this work, the MD simulations were key to fully understanding the diffusion of CH₄ in the various frameworks since it was not experimentally possible to reach low CH₄ densities.

From NMR experiments, we found that the Ni₂(dobdc) analogue has the strongest influence on the observed R_1 rates of CH₄ in M₂(dobdc), which we attribute to increased rotational correlation times. Furthermore, two D_s coefficients were observed for all frameworks and loadings from the experiments, with the slow D_s coefficient that arises from intracrystalline diffusion being in good agreement with the self-diffusion coefficients calculated from simulations.

From simulation, we found that the D_s coefficients are maximized at loadings corresponding to a single CH₄ molecule being present along a given ab -plane in each pore, suggesting that favorable CH₄-CH₄ interactions at higher pressures and a greater number of collisions lead to decreases in the D_s at higher loadings. On the other hand, before a loading of one CH₄/M²⁺ in each structure, we find that the diffusion coefficient slowly increases until it reaches a maximum; we attribute this increase to an enhancement in the distance an adsorbate can travel due to a greater number of collisions in otherwise very dilute pores. At very low CH₄ loadings (c.a. $0.027 \text{ CH}_4/\text{M}^{2+}$), simulations of CH₄ in M₂(dobdc) were carried out in increasingly larger and larger simulation boxes (keeping the CH₄ density in the pores fixed) to show a similar trend in the calculated D_s coefficients; as we increase the number of molecules in the simulation box while keeping the densities fixed, the self-diffusion coefficients slowly increase until converging at a constant value. We attributed this behavior to an

increase in the number of intermolecular collisions at these very dilute densities when there are simply more adsorbents in the simulation box, similar to the reason the D_s coefficient increases in each framework at loadings below one $\text{CH}_4/\text{M}^{2+}$.

Additionally, we found that the magnitudes of the intracrystalline CH_4 D_s coefficients are overall smallest in the Ni framework and largest in the Zn framework. This corresponds to the coordinatively unsaturated metal sites interacting most strongly with adsorbed CH_4 in the $\text{Ni}_2(\text{dobdc})$ framework and most weakly in the $\text{Zn}_2(\text{dobdc})$ framework, as the more strongly a CH_4 molecule interacts with the framework, the less distance it can travel over a fixed amount of time.

In agreement with experiments, we found that the exchange rate between the primary and secondary binding sites in simulations is greatest in the $\text{Ni}_2(\text{dobdc})$ framework and smallest in the $\text{Zn}_2(\text{dobdc})$ framework. This is interesting because the CH_4 heat of adsorption is largest in the Ni framework and lowest in the Zn framework, so although the Ni has a stronger interaction with adsorbed CH_4 , the energy barrier between the primary and secondary adsorption sites appears to be lower in $\text{Ni}_2(\text{dobdc})$ than in $\text{Zn}_2(\text{dobdc})$. The greater exchange in the Ni framework also helps explain the overall lower D_s coefficients at all CH_4 loadings; having greater exchange events occurring in a framework is analogous to having a greater number of collisions, which enhance the diffusion up to a point, until the framework becomes too crowded with adsorbates and greater number of collisions begin to decrease the distance a given adsorbate can travel. We thus conclude that CH_4 displays an overall lower D_s coefficient in the Ni framework at loadings greater than $0.1\bar{6}$ $\text{CH}_4/\text{M}^{2+}$ not only because favorable CH_4 - CH_4 interactions contribute to a deeper energy well at the primary binding site, thus slowing down the adsorbates, but also because exchange between the primary and secondary binding sites is more frequent at higher CH_4 loadings than in the Mg and Zn frameworks.

None of these studies on CH_4 and CO_2 diffusion presented in this chapter would have been possible without the parameterization of the DFT-derived force field, illustrating the value of having inexpensive yet accurate models of adsorption in promising nanoporous materials for studying the thermodynamics of adsorbates. Having a better understanding of an adsorbate's behavior at the atomic scale can help us understand the mechanism of adsorption and diffusion in nanoporous materials, and thus lead to the better design of materials for gas separation applications.

Additional Information

Uptakes at pressures of interest. Heats of adsorption at pressures of interest. Mean-squared displacements. Log-log MSD plots. MSD fits. DFT-derived FF vs UFF. Probability densities.

Chapter 4

In Silico Design of Nanoporous Materials

While the previous two chapters have focused on studying real systems for gas adsorption and separation applications, in this chapter the focus shifts instead to the computational generation of new structures. In the first section, *Enhanced Carbon Capture Using Multifunctionalized COPs*, the focus is on creating structures for a covalent organic polymer (COP) whose structure is unable to be solved via experiment alone. In the second section, *Design of 2D and 3D COFs for ANG Storage Applications* the focus is on assembling a database of novel covalent organic frameworks (COFs) for virtual screening applications.

4.1 Enhanced Carbon Capture Using Multifunctionalized COPs

Overview

In this work [240], we investigate the use of COPs for carbon capture applications via the use of computational methods and experiments.

Porous covalent polymers are attracting increasing interest in the fields of gas adsorption, gas separation, and catalysis due to their versatile polymer chemistry, large internal surface areas, and ultrahigh hydrothermal stabilities. While precisely manipulating the porosities of porous organic materials for targeted applications remains challenging, we show how a large degree of diversity can be achieved in COPs by incorporating multiple functionalities into a single framework, as is done for crystalline porous materials. Here, we synthesized 17 novel, porous COPs with finely tuned porosities, a wide range of Brunauer–Emmett–Teller (BET) specific surface areas ($430 - 3624 \text{ m}^2 \text{ g}^{-1}$), and a broad range of pore volumes ($0.24 - 3.50 \text{ cm}^3 \text{ g}^{-1}$), all achieved by tailoring the length and geometry of building blocks. Furthermore, we are the first to successfully incorporate more than three distinct functional groups into one phase for porous organic materials, which has been previously demonstrated in crystalline

metal-organic frameworks (MOFs). COPs decorated with multiple functional groups in one phase can lead to enhanced properties that are not simply linear combinations of the pure component properties. For instance, in the dibromobenzene-lined frameworks, the bi- and multifunctionalized COPs exhibit selectivities for carbon dioxide over nitrogen twice as large as any of the singly functionalized COPs. These multifunctionalized frameworks also exhibit a lower parasitic energy cost for carbon capture at typical flue gas conditions than any of the singly functionalized frameworks. Despite the significant improvement, these frameworks do not yet outperform the current state of the art technology for carbon capture. Nonetheless, the tuning strategy presented here opens up avenues for the design of novel catalysts, the synthesis of functional sensors from these materials, and the improvement in the performance of existing COPs by multifunctionalization.

This section is based on the following publication:

Xiang, Z., Mercado, R., Huck, J.M., Wang, H., Guo, Z., Wang, W., Cao, D., Haranczyk, M. and Smit, B., 2015. Systematic tuning and multifunctionalization of covalent organic polymers for enhanced carbon capture. *Journal of the American Chemical Society*, 137 (41), pp.13301-13307.

Introduction

Reducing anthropogenic carbon dioxide emission has become one of the most important social and environmental challenges facing our planet today. Due to a continued increase in the total use of fossil fuels in the foreseeable future, an essential contribution to the reduction of carbon dioxide in the atmosphere is the development of efficient carbon-capture technologies. [203] Carbon capture by nanoporous materials has attracted attention due to its potential to significantly reduce the energy requirements for this process.[59, 35, 90] Among these materials, porous covalent polymers [9, 244, 37, 234, 241, 175, 239, 238, 177] are a promising class because of their ultrahigh hydrothermal stabilities and high-yielding syntheses. Unlike MOFs, these materials only contain light elements (C, N, O, H, etc.). Although much progress has been made in manipulating the sequential arrangement of monomer units in a polymer chain, conventional polymer synthetic approaches tend to produce materials with an unsatisfying porous nature (e.g. low specific surface area (SSA) and small pore volume).[4, 8, 70, 132] Determining how to best control the porous properties of these statistically polymerized materials in a similar fashion to crystalline MOFs [56, 66] and covalent organic frameworks (COFs) [57] remains a great challenge.

Recently, Cooper and co-workers employed Sonogashira-Hagihara coupling chemistry to prepare a series of conjugated microporous polymers (CMPs) with controllable surface areas and pore dimensions by varying the monomer length. [94] Nonetheless, the BET SSAs of these CMPs remain relatively low (512–1018 m² g⁻¹). Although it has been shown that having alkynyl functional groups in covalent polymer networks can lead to cross-linked structures, it has also been shown that three-dimensional alkynyl polymers generally have higher surface areas than two-dimensional polymers. [237, 131, 209] In this work, we show how using the efficient Ullmann cross-coupling reaction with a combination of three-dimensional

and two-dimensional linkers can lead to polymers with increased surface areas. Using the novel tuning strategy presented here, we synthesized 17 novel multiblock COPs with finely tuned porosities by tailoring the length and geometry of the building blocks (Table 4.2). These synthesized multiblock COPs exhibit a wide BET SSA range of 430 – 3624 m² g⁻¹ and a large pore volume range of 0.24 – 3.50 cm³ g⁻¹.

As the number of different materials that can be synthesized and fully tested is small compared to the total number of possible materials, in the spirit of the Material Genomic Initiative (MGI), we used a computational approach to enumerate a large number of possible materials and predict their performance using molecular simulations.[85] We use this approach to elucidate a relationship between the various linkers, the attainable topologies, and a material’s capacity for CO₂.

Methods

COP Synthesis. Materials: 1,5-cyclooctadiene (cod), tris(4-bromophenyl)amine (TBA), 1,3,5-tris(4-bromophenyl)benzene (TBB) and CaH₂ were obtained from Sigma Aldrich. 1,3,5-tris((4-bromophenyl)ethynyl)benzene (TBEB), 2,4,6-tris-(4-bromo-phenyl)-[1,3,5]triazine (TBT) and 5,10,15,20-terakis-(4’-bromo-biphenyl-4-yl)-porphyrin (TBBPP) were obtained from Asta Tech (Chengdu). 1,4-dibromobenzene (DB), 4,4’-dibromobiphenyl (2DB), 9,10-dibromoanthracene (DA), 2,6-dibromo-naphthalene (2,6-DN), 1,4-dibromonaphthalene (DN), 5,8-dibromoquinoxaline (DBQ), 1,3,5-tribromobenzene (XTBB), 1,4-dibromo-2-nitrobenzene (DB-NO₂), 2,5-dibromoaniline (DB-NH₂), 2,5-di-bromotoluene (DB-CH₃), 2,5-dibromobenzene sulfonyl chloride (DB-SO₂Cl), 2,5-dibromohydroquinone (DB-OH) and dry DMF were obtained from Alfa Aesar. Tetrakis(4-bromo phenyl)methane (TBM) was purchased from Huangminglong Chem. Ltd. Cod was dried over CaH₂ prior to use.

The percent yields were calculated based on the efficiency of conversion of moles of carbon in the reagent to moles of carbon in the polymer produced. The percentage carbon in the product was measured using elemental analysis and compared to hypothetical percentages of carbon and hydrogen in these compounds. The hypothetical percentages were computed assuming a 1:2 ratio of tetrahedral monomer to linear monomer (e.g. 1:2 TBM:DB in COP-5), a 3:4 ratio of tetrahedral monomer to trigonal monomer (e.g. 3:4 TBM:XTBB in COP-10), and a 1:1 ratio of tetrahedral monomer to square planar linker (e.g. 1:1 TBM:TBBPP in COP-15) in the synthesized polymers. The above ratios were determined assuming that each monomer connects to the other type of monomer in the structure, an assumption which is largely supported by the data. The more the elemental analyses deviate from the hypothetical percentages, the less accurate this assumption is. This is particularly the case for COP-17 and COP-21, which deviate by 8% carbon and 6.6% carbon, respectively, and also contain the highest fraction of amine-functionalized monomers. On the other hand, all other COPs deviate from the hypothetical percentages by no more than 5% carbon. Nonetheless, using other methods of characterization we were unable to determine the reason for these deviations. We performed measurements of the halide content in the COPs using the Ion Chromatograph (DX-600, DIONEX). However, we found the bromine content to

be too low to be detected in the samples. These results further confirmed the efficiency of Yamamoto-type Ullmann cross-coupling reaction, [9] such that the products contain very low amounts of the halide as has been previously discussed in the literature.[244] In the synthesis of COP-5, we optimized the reagent ratios so as to maximize the BET surface area of the polymer; we found that COP-5 displays the largest BET surface area when we use a 1:2 ratio of TBM:DB.

Synthesis of COPs 5–20. COP-5: cod (0.50 mL, 3.96 mmol) was added to a solution of [Ni(cod)₂] (1.125 g, 4.09 mmol) and 2,2'-bipyridyl (0.640 g, 4.09 mmol) in dry DMF (65 mL), and the mixture was stirred until all solids completely dissolved. TBM (0.167 g, 0.262 mmol) and DB (0.123 g, 0.523 mmol) were subsequently added to the resulting purple solution. The reaction vessel was heated at 85 °C overnight under a nitrogen atmosphere. After cooling to room temperature, 10 mL concentrated HCl were added to the deep purple suspension, which changed into an aqua transparent solution. After filtration, the residue was washed using CHCl₃ (5×15 mL), THF (5×15 mL) and H₂O (5×15 mL), in this order, and dried under vacuum to give COP-5 powder (108 mg, 84% yield). The product was then immersed in absolute ethanol for 24 hours. The ethanol-contained sample was evacuated using supercritical CO₂ in a SFT-100XW critical point dryer (SepTech Co., Ltd.). The ethanol-containing samples were soaked in liquid CO₂ over a period of one day. Then, liquid CO₂ was vented at a rate lower than the rate of filling (the flow rate of CO₂ was in the range of 50-100 mL min⁻¹) to maintain the pressure at 1300 psi. The filling rate of CO₂ was controlled by the flow rates of the pump and the venting rate was controlled by the export-valve. Meanwhile, the temperature was raised to 40 °C above the critical point of CO₂. The cell was held above the critical point for 4 hours. After supercritical activation, the pressure of the chamber is reduced to 1 atm, during which CO₂ molecules escape from the pores in gas form. The dried sample was placed in containers and stored in a desiccator. Elemental analysis calculated (%) for C₃₇H₂₄: C 94.83, H 5.17; found (%): C 90.82, H 5.236. **COP-6:** The synthesis is similar to that of the above COP-5 except for the raw materials and corresponding amounts. To obtain COP-6, we used TBM (0.167 g, 0.262 mmol) and 2DB (0.123 g, 0.523 mmol) as the monomers and heated the reaction vessel at 85 °C to produce COP-6 powder (136 mg, 91% yield). The other experimental procedures are the same to those of COP-5. Elemental analysis calculated (%) for C₄₉H₃₂: C 94.80, H 5.20; found (%): C 90.97, H 5.26. **COP-7:** The synthesis is similar to that of the above COP-5 except for the raw materials and corresponding amounts. To obtain COP-7, we used TBM (0.167 g, 0.262 mmol) and DA (0.176 g, 0.523 mmol) as the monomers and heated the reaction vessel at 85 °C to produce COP-7 powder (123 mg, 66% yield). The other experimental procedures are the same to those of COP-5. Elemental analysis calculated (%) for C₅₃H₃₂: C 95.17, H 4.83; found (%): C 90.17, H 4.90. **COP-8:** The synthesis is similar to that of the above COP-5 except for the raw materials and corresponding amounts. To obtain COP-8, we used TBM (0.167 g, 0.262 mmol) and 2,6-DN (0.150 g, 0.523 mmol) as the monomers and heated the reaction vessel at 85 °C to produce COP-8 powder (133 mg, 86% yield). The other experimental procedures are the same to those of COP-5. Elemental analysis calculated (%) for C₄₅H₂₈: C 95.03, H 4.97; found (%): C 91.85, H 5.03. **COP-9:** The synthesis is similar to

that of the above COP-5 except for the raw materials and corresponding amounts. To obtain COP-9, we used TBM (0.167 g, 0.262 mmol) and DN (0.150 g, 0.523 mmol) as the monomers and heated the reaction vessel at 85 °C to produce COP-9 powder (120 mg, 78% yield). The other experimental procedures are the same to those of COP-5. Elemental analysis calculated (%) for $C_{45}H_{28}$: C 95.03, H 4.97; found (%): C 91.82, H 5.22. **COP-10**: The synthesis is similar to that of the above COP-5 except for the raw materials and corresponding amounts. To obtain COP-10, we employed TBM (0.213 g, 0.336 mmol) and XTBB (0.141 g, 0.449 mmol) as the monomers and heated the reaction vessel at 85 °C to produce COP-10 powder (102 mg, 73% yield). The other experimental procedures are the same to those of COP-5, except for an updated washing procedure which includes an additional wash with methanol, followed by a Soxhlet extraction with toluene, and finally a wash with water to remove any residual nickel present in these samples. Elemental analysis calculated (%) for $C_{99}H_{60}$: C 95.16, H 4.84; found (%): C 94.86, H 4.56. **COP-11**: The synthesis is similar to that of the above COP-5 except for the raw materials and corresponding amounts. To obtain COP-11, we used TBM (0.213 g, 0.336 mmol) and TBEB (0.276 g, 0.449 mmol) as the monomers and heated the reaction vessel at 85 °C to produce COP-11 powder (245 mg, 88% yield). The other experimental procedures are the same to those of COP-5, except for an updated washing procedure which includes an additional wash with methanol, followed by a Soxhlet extraction with toluene, and finally a wash with water to remove any residual nickel present in these samples. Elemental analysis calculated (%) for $C_{195}H_{108}$: C 95.56, H 4.44; found (%): C 93.76, H 4.32. **COP-12**: The synthesis is similar to that of the above COP-5 except for the raw materials and corresponding amounts. To obtain COP-12, we used TBM (0.213 g, 0.336 mmol) and TBA (0.215 g, 0.449 mmol) as the monomers and heated the reaction vessel at 85 °C to produce COP-12 powder (201 mg, 92% yield). The other experimental procedures are the same to those of COP-5. Elemental analysis calculated (%) for $C_{147}H_{96}N_4$: C 92.03, H 5.05, N 2.92; found (%): C 90.13, H 4.66, N 3.50. **COP-13**: The synthesis is similar to that of the above COP-5 except for the raw materials and corresponding amounts. To obtain COP-13, we used TBM (0.213 g, 0.336 mmol) and TBB (0.242 g, 0.449 mmol) as the monomers and heated the reaction vessel at 85 °C to produce COP-13 powder (211 mg, 87% yield). The other experimental procedures are the same to those of COP-5, except for an updated washing procedure which includes an additional wash with methanol, followed by a Soxhlet extraction with toluene, and finally a wash with water to remove any residual nickel present in these samples. Elemental analysis calculated (%) for $C_{171}H_{108}$: C 94.96, H 5.04; found (%): C 94.18, H 4.97. **COP-15**: The synthesis is similar to that of the above COP-5 except for the raw materials and corresponding amounts. To obtain COP-15, we used TBM (0.248 g, 0.393 mmol) and TBBPP (0.483 g, 0.393 mmol) as the monomers and heated the reaction vessel at 85 °C to produce COP-15 powder (358 mg, 70% yield). The other experimental procedures are the same to those of COP-5. Elemental analysis calculated (%) for $C_{93}H_{58}N_4$: C 90.70, H 4.75, N 4.55; found (%): C 85.62, H 4.22, N 4.64. **COP-16**: The synthesis is similar to that of the above COP-5 except for the raw materials and corresponding amounts. To obtain COP-16, we used TBM (0.167 g, 0.262 mmol) and DB-NO₂ (0.147 g, 0.523 mmol) as the monomers and heated the reaction vessel at 85 °C to produce COP-16 powder (90 mg,

54% yield). The other experimental procedures are the same to those of COP-5. Elemental analysis calculated (%) for $C_{27}H_{22}N_2O_4$: C 73.95, H 5.06, N 6.39; found (%): C 70.15, H 5.39, N 4.92. **COP-17**: The synthesis is similar to that of the above COP-5 except for the raw materials and corresponding amounts. To obtain COP-17, we used TBM (0.167 g, 0.262 mmol) and DB-NH₂ (0.131 g, 0.523 mmol) as the monomers and heated the reaction vessel at 85 °C to produce COP-17 powder (92 mg, 60% yield). The other experimental procedures are the same to those of COP-5. Elemental analysis calculated (%) for $C_{27}H_{16}N_2$: C 88.01, H 4.38, N 7.61; found (%): C 76.01, H 5.43, N 4.92. **COP-18**: The synthesis is similar to that of the above COP-5 except for the raw materials and corresponding amounts. To obtain COP-18, we used TBM (0.167 g, 0.262 mmol) and DB-CH₃ (0.131 g, 0.523 mmol) as the monomers and heated the reaction vessel at 85 °C to produce COP-18 powder (108 mg, 79% yield). The other experimental procedures are the same to those of COP-5. Elemental analysis calculated (%) for $C_{29}H_{18}$: C 95.05, H 4.95; found (%): C 90.36, H 5.64. **COP-19**: The synthesis is similar to that of the above COP-5 except for the raw materials and corresponding amounts. To obtain COP-19, we used TBM (0.167 g, 0.262 mmol) and DB-SO₂Cl (0.175 g, 0.523 mmol) as the monomers and heated the reaction vessel at 85 °C to produce COP-19 powder (163 mg, 82% yield). The other experimental procedures are the same to those of COP-5. Elemental analysis calculated (%) for $C_{27}H_{12}O_4S_2Cl_2$: C 60.68, H 2.26, S 11.98; found (%): C 58.76, H 2.36, S 9.29. **COP-20**: The synthesis is similar to that of the above COP-5 except for the raw materials and corresponding amounts. To obtain COP-20, we used TBM (0.167 g, 0.262 mmol) and DB-OH (0.140 g, 0.523 mmol) as the monomers and heated the reaction vessel at 85 °C to produce COP-20 powder (75 mg, 54% yield). The other experimental procedures are the same to those of COP-5. Elemental analysis calculated (%) for $C_{27}H_{24}O_2$: C 85.22, H 6.36; found (%): C 84.44, H 5.968.

Synthesis of Multifunctional COPs. **COP-21**: cod (0.50 mL, 3.96 mmol) was added to a solution of [Ni(cod)₂] (1.125 g, 4.09 mmol) and 2,2'-bipyridyl (0.640 g, 4.09 mmol) in dry DMF (65 mL), and the mixture was stirred until all solids completely dissolved. TBM (0.165 g, 0.262 mmol), DB-NH₂ (0.066 g, 0.262 mmol) and DB-OH (0.070 g, 0.262 mmol) were the comonomers, heated the reaction vessel at 85 °C to produce COP-21 powder (65 mg, 51% yield). Supercritical CO₂ drying process was used for activation. Elemental analysis calculated (%) for $C_{27}H_{25}ON$: C 85.44, H 6.64, N 3.69. Found (%): C 78.84, H 5.08, N 2.83. **COP-22**: All the experimental procedures are similar to those of the above COP-21 except for the comonomers (TBM (0.167 g, 0.262 mmol), DB-NH₂ (0.044 g, 0.174 mmol), DB-OH (0.047 g, 0.174 mmol) and DB-SO₂Cl (0.058 g, 0.174 mmol)). The reaction vessel was heated at 85 °C and activated with supercritical CO₂ to produce COP-22 powder (83 mg, 56% yield). Elemental analysis calculated (%) for $C_{111}H_{72}O_6N_2S_2Cl_2$: C 80.12, H 4.36, N 1.68, S 3.85. Found (%): C 78.52, H 5.357, N 1.923, S 3.745.

Experimental Characterizations. **Powder X-ray diffraction (PXRD)** measurements were performed on a D/MAX 2000 X-ray diffractometer, with a copper K α line ($\lambda = 1.54178$ Å) as the incident beam. **FT - IR spectroscopy** was performed on a AC-80MHZ (Bruker) instrument with a wave range of 4000 – 400 cm⁻¹. **Scanning electron microscopy (SEM)** images were obtained on a Cambridge S250MK3 SEM instrument.

SEM element mapping images were recorded on a Zeiss SUPRA 55 SEM instrument with an accelerating voltage of 20 kV, combined with energy-dispersive X-ray spectroscopy (EDX) for determination of material compositions. **Transmission electron microscopy (TEM)** images were obtained on an H-800 TEM instrument and JEM-3010 high-resolution TEM instrument. **Elemental analyses** (C, H, N and S) were performed on a Thermo Fisher Scientific Elemental Analyzer (Ea1112, Beijing Research Institute of Chemical Industry, SINOPEC). **Inductively coupled plasma (ICP) spectroscopy** measurements were carried out on a vario EL cube (Elementar Analysensysteme GmbH). **Solid-State NMR** spectra were measured on a Bruker AV300 spectrometer operating at 75.5 MHz for ^{13}C and 300.1 MHz for ^1H . The ^{13}C CP/MAS (Cross-Polarization with Magic Angle Spinning) experiments were carried out at MAS rates of 11.0 kHz using densely packed powders of the evacuated COPs in 4 mm ZrO_2 rotors. The ^1H $\pi/2$ pulse was 2.4 μs , and two-pulse phase modulation (TPPM) decoupling was used during the acquisition. The spectra were measured using a contact time of 3.5 ms and a relaxation delay of 5.0 s. **N_2 adsorption/desorption isotherms** were measured at 77 K with a Micromeritics ASAP 2020. The samples of 150 mg were degassed at 200 $^\circ\text{C}$ for 24 h. Pore size distribution data were calculated from the N_2 adsorption isotherms based on the DFT model in the Micromeritics ASAP 2020 software package (assuming slit pore geometry). Ultra-high-purity grade He (99.999%) and N_2 (99.9992%) were used for all adsorption measurements. **IGA-003 gravimetric CO_2 and N_2 adsorption measurements.** The CO_2 and N_2 isotherms at 298 K were measured by using a Hiden Isochema Intelligent Gravimetric Analyzer (IGA-003). Prior to the measurement, approximately 30 mg of sample were loaded into the IGA-003 and degassed at 10^{-3} Pa at 200 $^\circ\text{C}$ for 24 h. The measurements were then carried out in a water bath. The buoyancy corrections were carried out as in our previous publications.[236]

Prediction of Adsorption Selectivities of Binary Mixture by IAST. The single- and dual-site Langmuir adsorption model-based IAST has been applied to explore the adsorption selectivity of porous materials according to our previous method.[90] The selectivity for component x over component y can be evaluated from the predicted adsorption amount of each component of the mixture by the IAST theory using the following equation,

$$S_{i/j} = \frac{x_i/x_j}{y_i/y_j},$$

where x_i , x_j and y_i , y_j denote the molar fractions of species i and j in the adsorbed and bulk phases, respectively.

Parasitic Energy Calculation of a Binary Coal Flue Gas Mixture. Parasitic energy is defined as the sum of a heating requirement, Q , necessary to capture CO_2 , and a compression work term, W_{comp} , necessary to compress (up to 150 bar) and transport the captured CO_2 gas to its final storage location. The most important value for a power plant is the reduction of electricity output. As such, the heating requirement must be converted into electrical energy using the Carnot efficiency η_{carnot} . Additionally, the heating energy for the process is provided from the power plant's own production (turbine efficiency of 75%). Consequently, we obtain the equation

$$E_{\text{parasitic}} = 0.75\eta_{\text{carnot}}Q + W_{\text{comp}}.$$

As previously described,[90] the heating term consists of a sensible heat and desorption heat requirement to allow for the CO₂ to separate from N₂. The relation used for this procedure is given by

$$Q_{\text{thermal}} = \frac{C_p m_{\text{sorbent}} \Delta T}{m_{\text{CO}_2}} + \frac{\Delta h_i \Delta \sigma_i + \Delta h_{\text{N}_2} \Delta \sigma_{\text{N}_2}}{m_{\text{CO}_2}}$$

The involved parameters are the specific heat capacity C_p , the mass of the adsorbent m_{sorbent} , the temperature difference between the adsorption and desorption stages ΔT , the mass of captured CO₂ m_{CO_2} , the heats of adsorption for both gases Δh_i , and their corresponding working capacities $\Delta \sigma_i$. To estimate the compression work requirement, we used a model of a multi-stage compressor defined previously. [90] For the minimization procedure, we covered a desorption temperature and pressure range of 333 – 473 K and 0.01 – 3 atm.

Generation of COP-5 database structures with different topologies. COP-5 database was generated *in silico*, where the building blocks (TBM and DB) were positioned together according to a given net topology. To achieve the hypothetical COP structures, we mimicked the Ullmann cross-coupling synthetic route described in the experimental procedure. The first monomer positioned along the net is the tetrahedral linker, TBM, and the second monomer is the linear dibromide linker, DB. The linkers are connected such that a new carbon-carbon bond is formed between the two carbons bonded to bromide substituents; the bromide substituents are subsequently removed from the structure. In this route, only carbon-carbon bonds are formed between different types of linkers, giving rise to polymeric chains of the form –TBM-DB-TBM-DB– in the resulting structure. As such, each TBM molecule ends up bound to four DB linkers in a tetrahedral arrangement, whereas the DB linker connects two tetrahedral TBM units in a linear fashion. This resulted in an initial prediction for a material structure of this topology.

All nets were downloaded from the RSCR.[172] Nets were chosen based on agreeing symmetry between the linkers, edges, and vertices of comprising the net. In total, 50 nets were found to result in potential frameworks, including the common diamond (**dia**) net.

Using this *in silico* design procedure and structure assembly algorithms previously reported, [143, 145, 141] we achieved 50 hypothetical COP-5 structures (Tables D.1 – D.9). The resulting framework structures were then relaxed using the semi-empirical PM6 electronic structure method implemented in MOPAC2012. [208, 109] Periodic boundary conditions were used in these calculations, and the period unit cell parameters were also permitted to relax. To describe dispersion and hydrogen bonds, we used the DH2 correction to PM6.[190] The suitability of the PM6-DH2 method to porous polymers has been verified previously.[82]

Grand Canonical Monte Carlo Simulations Grand canonical Monte Carlo (GCMC) simulations were used to study the adsorption of CO₂ in the materials. All the GCMC simulations were performed by using the MUSIC code.[73] BET surface areas were determined from the calculated isotherms.[226] CO₂ and N₂ were modeled as 3-site rigid linear

Molecules	Atom	ϵ/k_B (K)	σ (Å)	q (e)
N ₂ (3-site)	N	36.0	3.31	-0.482
	COM	0	0	0.964
CO ₂	C	27.0	2.80	+0.70
	O	79.0	3.05	-0.35
adsorbents	C	47.9	3.47	
	H	7.66	2.85	

Table 4.1: Force field parameters for adsorbates and adsorbents.

molecules in which the Lennard-Jones (LJ) potential parameters were taken from TraPPE force field.[185] A combination of the site-site LJ and Coulombic potentials was used to calculate the CO₂-CO₂ intermolecular interactions. N₂ was represented by a 1-site model with the corresponding parameters taken from [171]. The Dreiding force field [153] was used to describe the interactions of framework atoms. All LJ cross interaction parameters were obtained using Lorentz–Berthelot mixing rules,

$$\epsilon_{ij} = (\epsilon_{ii}\epsilon_{jj})^{1/2}\sigma_{ij} = \frac{\sigma_{ii} + \sigma_{jj}}{2}.$$

All LJ parameters used are given in Table 4.1. In order to compare with the experimental data, the absolute uptake N_{abs} obtained in the GCMC simulation was converted into the excess uptake N_{ex} using

$$N_{\text{ex}} = N_{\text{abs}} - \rho_g V_g,$$

where ρ_g is the density of bulk gas calculated from the Peng-Robinson equation of state (EOS), and V_g is the free volume of adsorbent accessible to the gas molecules.

Results

The nickel-catalyzed Yamamoto-type Ullmann cross-coupling reaction is an efficient method for obtaining highly condensed networks of quasi-ordered porous organic polymers.[218, 38, 214] Recently, research groups used a tetrahedral monomer, TBM, to synthesize two similar quasi-ordered porous covalent polymers: a porous aromatic framework (PAF), PAF-1, with a high surface area of 5640 m² g⁻¹, and a porous polymer network (PPN), PPN-4, with an even higher surface area of 6461 m² g⁻¹. [9, 244, 176] These findings motivated us to use TBM as a core monomer in synthesizing new structures by connecting it with other rigid monomers to form tunable covalent polymers. Unfortunately, the synthesized COP-5 prepared with TBM and DB exhibits a much lower surface area, 1744 m² g⁻¹, than the theoretically predicted value, 5302 m² g⁻¹, for COP-5 in the **dia** topology (Figure 4.1a). However, the long linkers between two neighboring core monomers allow other topologies to form.

To investigate how to avoid the formation of these competing structures, we screened the porosities of COP-5 with more than 46 different crystalline topologies (Figure 4.1b and

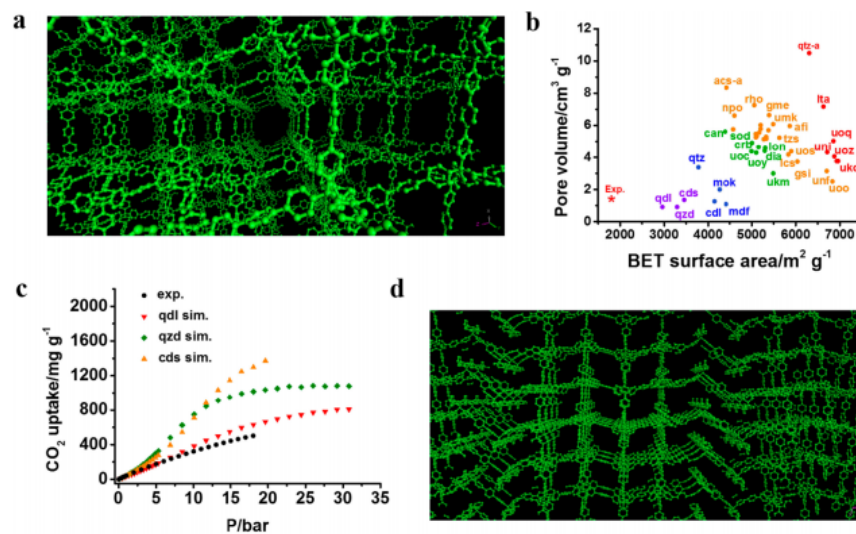


Figure 4.1: Screening hypothetical COP-5 structures using atomistic simulations. (a) Structure of COP-5 with **dia** topology generated *in silico*. (b) Scatterplot illustrating BET surface area versus pore volume for the COP-5 structures with different topologies generated *in silico*, along with the experimental result. (c) Comparison of computed CO₂ isotherms in COP-5 with the **qdl**, **qzd**, and **cds** topologies, with the experimental results at 298 K. (d) Structure of COP-5 with **qdl** topology generated *in silico*.

Tables D.1 – D.9) and verified the predicted CO₂ adsorption isotherms with experimental results (Figure 4.1c). Although the synthesized materials are not necessarily crystalline, from a computational point of view, crystalline models are more easily constructed than amorphous models and thus we used such models to allow for a quicker, simpler screening of the materials. Furthermore, previous work on PPNs [143, 145] has shown how experimental measurements of gas adsorption in these and similar classes of materials can be reproduced in simulations using crystalline models. These examples illustrate that these models give a sensible representation of these materials, and for these reasons, we assume a crystalline order in our model structures. Our initial models suggested that this was only a viable assumption for COP-5, as simple (i.e. non-interpenetrated, crystalline) models for other COPs we looked at (COP-10, -11, -12, -13, -14) possessed significantly larger surface areas and pore volumes compared to the synthesized materials regardless of the topologies we considered. It is possible that due to their length and flexibility, the longer linkers lead to other properties which we did not consider in our models. Nonetheless, in agreement with previous results, we found that the shorter linkers in COP-5 led to more favorable properties for CO₂ capture and separation, as they avoid the creation of too much empty space in the structures. For COP-5 our molecular simulation results indicate a comparable agreement with the experimental data. For example, the CO₂ isotherms of COP-5 in the **qdl** topology (Figure 4.1d) could well reproduce the experimental results, confirming the success of copolymerization in the multiblock COPs using Yamamoto-type Ullmann cross-coupling.

COP	Monomer 1	Monomer 2	Monomer 3	Monomer 4
COP-5		DB		
COP-6		2DB		
COP-7		DA		
COP-8		2,6-DN		
COP-9		DN		
COP-10		XTBB		
COP-11		TBEB		
COP-12		TBA		
COP-13	TBM	TBB		
COP-15		TBBPP		
COP-16		DB-NO ₂		
COP-17		DB-NH ₂		
COP-18		DB-CH ₃		
COP-19		DB-SO ₂ Cl		
COP-20		DB-OH		
COP-21		DB-OH	DB-NH ₂	
COP-22		DB-OH	DB-NH ₂	DB-SO ₂ Cl

Table 4.2: Summary of the monomers used to build each COP synthesized in this work.

Encouraged by these results, we further used TBM as a core monomer to copolymerize with other extended building blocks of different lengths and geometries (C_2 , C_3 , and C_4) to synthesize a series of multiblock COPs (Figure 4.2a; Table 4.2). The geometries and lengths of the comonomers (Figure 4.2b) enabled us to tailor the porosities of these as-synthesized multiblock COPs, similar to the way that the porosity is tuned in crystalline MOFs. [52, 41, 130]

Fourier transform infrared (FT-IR) spectroscopy and solid state ¹³C CP/MAS NMR measurements confirmed the successful phenyl-phenyl coupling in this series of multiblock COPs, and the preservation of the comonomer backbones in each multiblock COP. The PXRD spectra and TEM images suggested these multiblock COPs exhibit long-range amorphous features and tend to form spherical morphologies. Our synthesized multiblock COPs exhibit high thermal stability and show negligible deterioration at up to 500 °C. In particular, only 20% weigh loss occurs at up to 800 °C for all of the as-synthesized multiblock COPs.

We further measured the N₂ adsorption isotherms at 77 K to evaluate the porosities of these multiblock COPs. The results are summarized in Table 4.3.

These results show that the porosities can be systematically tuned by tailoring the geometry and length of the comonomers. For example, the pore-size distributions of the as-synthesized multiblock COPs constructed with T₄ and C₂ monomers show a well-defined dependence on the length and geometry of the C₂ monomers. It is worth mentioning that

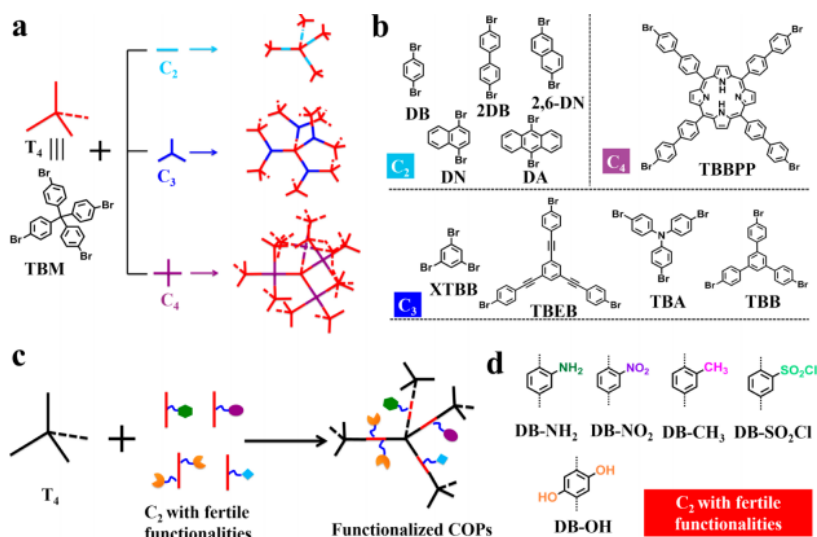


Figure 4.2: The scheme for porosity manipulation and functionalization in multiblock COPs. (a) The porosity of the polymers was tuned by connecting TBM with linkers of three distinct geometries. (b) The C_2 , C_3 , and C_4 comonomers. (c) Strategy for functionalization of the COPs. (d) The C_2 comonomers with multiple functionalities used in this work.

the multiblock COPs constructed with the T_4 and C_3 building blocks exhibit a highly porous nature, except in the case of structures formed from TBEB since the alkynyl functional group tends to form cross-linked structures which reduce its porous capacity.[209, 131, 237] Most notably, COP-10, which is copolymerized from TBM and TBB, possesses an extremely high BET SSA of $3337 \text{ m}^2 \text{ g}^{-1}$ and a pore volume of $2.25 \text{ cm}^3 \text{ g}^{-1}$, which are among the largest in the field of covalent organic materials,[234] and even larger than those of similar analogues, such as multiblock polymers of intrinsic microporosity (PIMs)[157] and CMPs.[94]

To introduce functional groups into COPs, we functionalized the C_2 monomers with various functional groups, including $-OH$, $-NH_2$, $-NO_2$, $-CH_3$, $-SO_2Cl$, and copolymerized these monomers with TBM (Figure 4.2c,d). The backbones of these functionalized COPs were characterized using similar techniques. Whereas most reported synthetic techniques focus on a single functional group, the methodology introduced in this work allows us to incorporate more than two different functional groups into a framework at once.[40] We simultaneously incorporated two and three comonomers, $DB-NH_2$, $DB-OH$, and $DB-SO_2Cl$, along with TBM into one phase using a one-pot method to prepare a bifunctionalized COP-21 ($-OH + -NH_2$) and multifunctionalized COP-22 ($-OH + -NH_2 + -SO_2Cl$). These functionalized COPs also exhibit high porosities. In particular, COP-20 possesses an extremely high BET SSA of $3624 \text{ m}^2 \text{ g}^{-1}$ and a pronounced pore volume of $3.50 \text{ cm}^3 \text{ g}^{-1}$. The pore volume of $3.5 \text{ cm}^3 \text{ g}^{-1}$ is the largest ever reported in the field of covalent organic materials to the best of our knowledge,[234] close to the benchmark of $4.4 \text{ cm}^3 \text{ g}^{-1}$ for MOF NU-100E reported as of 2015 (when this work was published).[56]

Generally, a high SSA and a large pore volume in a porous material often correlate with a

COP	BET SSA ^a	Lang. SSA	PV ^b	MV ^c	σ_{CO_2} ^d	σ_{N_2} ^e	$E_{\text{parasitic}}$ ^f	Select. ^g
COP-5	1744	2569	1.40	0.70	503	41		
COP-6	1279	1882	1.09	0.51	453	37		
COP-7	1305	1916	1.18	0.41	345	31		
COP-8	1634	2396	1.33	0.55	525	52		
COP-9	1305	1907	0.92	0.56	352	35		
COP-10	3337	4984	2.25	1.32	896	79		
COP-11	1112	1654	1.09	0.33	332	34		
COP-12	2609	3852	1.86	0.98	770	66		
COP-13	2787	4123	1.91	1.11	680	57		
COP-15	1112	1638	0.93	0.44	421	40		
COP-16	3233	4794	2.34	1.38	797	66		
COP-17	1505	2193	1.02	0.66	446	42	1831	8.4
COP-18	2828	4157	1.83	0.58	694	56	2766	4.8
COP-19	1330	1943	0.95	0.58	445	37	2009	7.8
COP-20	3624	5431	3.50	1.24	767	66	2615	4.5
COP-21	568	844	0.47	0.26	219	24	1608	13.7
COP-22	430	617	0.21	0.21	203	20	1632	13.3

Table 4.3: Summary of the porosities and CO₂ capture performance of COPs studied in this work. ^aThe BET SSAs were calculated in the region of P/P₀ = 0.05 – 0.3. SSAs = specific surface areas; units in m² g⁻¹. ^b Pore volume determined at P/P₀ = 0.9997. The pore volume in this work refers to the total pore volume including the surface condensation. Units in cm³ g⁻¹. ^c The micropore volume derived using the t-plot method based on the Halsey thickness equation. Units in cm³ g⁻¹. ^d The CO₂ uptake at 298 K and 18 bar. Units in mg g⁻¹. ^e The N₂ uptake at 298 K and 18 bar. Units in mg g⁻¹. ^f Parasitic energy for the cost of carbon capture from a 14:86 CO₂:N₂ gas mixture at 40 °C and 1 atm. Units in kJ/kg. ^g The IAST-predicted adsorption selectivity at 313 K and 1 atm.

high gas uptake.[76] By tailoring both the lengths and geometries of the building blocks, we can synthesize COPs with wide range of BET SSAs (from 430 to 3624 m² g⁻¹, Figure 4.3a) and a large range of pore volumes (from 0.24 to 3.50 cm³ g⁻¹, Figure 4.3b). Interestingly, the BET SSAs of these COPs depend linearly on the pore volumes (Figure 4.3c).

The CO₂ and N₂ adsorption isotherms in these multiblock COPs are presented in Figure 4.3d,f. Of these COPs, COP-10 exhibits the highest CO₂ uptake of 896 mg g⁻¹ at 298 K and 18 bar, which placed it among the top ten materials with the highest CO₂ storage capacity in the field of MOFs and COFs under similar conditions as of 2015. [210, 235] This uptake is much larger than in its analogues under similar conditions: COF-8 (502 mg g⁻¹), COF-5 (441 mg g⁻¹), and COF-10 (412 mg g⁻¹) reported in [65]; PPN-2 (486 mg g⁻¹) and PPN-1 (393 mg g⁻¹) reported in [131]; BCMBP (100) (585 mg g⁻¹) reported in [37]; and PAF-1 (876 mg g⁻¹) reported in [9]. This uptake is also very close to the threshold of COF-103

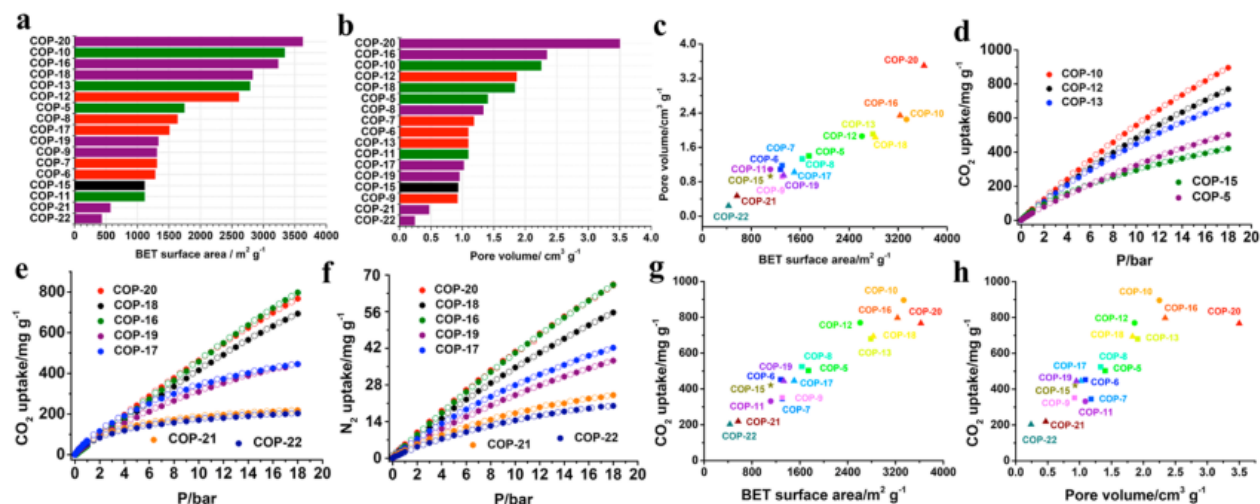


Figure 4.3: The porosities of the as-synthesized multiblock COPs in this study and their gas adsorption performance at 298 K. (a) BET SSA results for the series of COPs. (b) Pore volume results for the series of COPs. (c) BET SSA versus pore volume for the series of COPs. (d) CO_2 adsorption isotherms for nonfunctionalized COPs. (e) CO_2 adsorption isotherms for functionalized COPs. (f) N_2 adsorption isotherms for functionalized COPs. Solid and open symbols represent adsorption and desorption, respectively. (g) BET SSA versus CO_2 storage capacity at 18 bar. (h) Pore volume versus CO_2 storage capacity at 18 bar.

(1038 mg g^{-1}) measured under similar conditions. [65]

An instructive first check to gain insights on the suitability of these functionalized multiblock COPs for their application in carbon capture is to estimate their CO_2/N_2 selectivities. For this reason, we measured N_2 adsorption isotherms at 298 K in these materials (Figure 4.3f). Likewise, N_2 adsorption capacity largely correlates with surface area and pore volume. COP-20 possesses the largest surface area and pore volume among the functionalized multiblock COPs, and it shows the highest N_2 uptake of 66 mg g^{-1} at 18 bar and 298 K.

We used Ideal Adsorbed Solution Theory (IAST) to predict CO_2/N_2 gas mixture adsorption in each COP at a gas composition of 14:86, 40 °C and 1 atm, which corresponds to typical flue gas from a coal fired power plant at adsorption conditions relevant for a post-combustion process. [167] Adsorption isotherms of the pure components were fit by single- and dual-site Langmuir equations with satisfactory agreement. The final floating parameters are given in Table 4.4.

The resulting selectivities of the six COPs under investigation are listed in Table 4.3. At first glance, none of the analyzed structures stand out in their calculated selectivities, which range from 4.5 to 13.7. However, both materials tethered with multiple functional groups perform better than the singly functionalized polymers. With decreasing selectivities follow the $-\text{NH}_2$ and $-\text{SO}_2\text{Cl}$ functionalized materials, with polymers functionalized with $-\text{CH}_3$ and

Adsorbent	Adsorbate	$\sigma_{sat,i,1}$	$k_{H,i,1}$	$\sigma_{sat,i,2}$	$k_{H,i,2}$
COP-17	CO ₂	2.3615	1.2325	18.131	0.8091
	N ₂	0.9328	14.131		
COP-18	CO ₂	1.3652	0.1212	110.88	0.9511
	N ₂	0.1599	5.7937		
COP-19	CO ₂	1.2539	0.7476	26.299	0.7516
	N ₂	3.2825	0.1187		
COP-20	CO ₂	24.374	0.5478	76.348	0.6604
	N ₂	9.0080	0.1751		
COP-21	CO ₂	2.5340	2.1505	5.0426	0.3098
	N ₂	1.5711	0.1019		
COP-22	CO ₂	2.6496	1.8774	5.6904	0.2044
	N ₂	1.2725	0.0087		

Table 4.4: Parameters of single- and dual-site Langmuir equation fits to pure CO₂ and N₂ isotherms at 298 K. The units of σ are mmol g⁻¹; the units of k_H are mmol g⁻¹ bar⁻¹.

–OH groups performing the worst.

Evaluating materials for their application in carbon capture solely on the basis of their selectivity results does not provide a true picture of their performance. As shown in previous work[90] and other literature,[5] individual material properties, such as uptake, selectivity, and working capacity are not sufficient in the ranking procedure for a post-combustion process. Instead, a combination of these criteria is more appropriate. A potential means to evaluate materials for carbon capture is using the parasitic energy. This model, based on the minimization of the energy penalty additionally imposed on a power plant by applying carbon capture and sequestration, was first introduced in [247]. The advantages of this metric, compared to the previously mentioned criteria, are that it is not only the combination of several thermodynamic properties, but also that the optimization of the process conditions depend on a material-by-material basis. Parasitic energy is defined as

$$E_{\text{parasitic}} = 0.75\eta_{\text{carnot}}Q + W_{\text{comp}}$$

where Q and W_{comp} represent the heating and compression energy requirements, 0.75 corresponds to the typical turbine efficiency, and η_{carnot} is the Carnot efficiency for transforming heat into electrical energy.

Figure 4.4 shows the rankings of the six analyzed COPs in comparison to other known materials. COPs 17–22 are illustrated as orange circles and are among the average performers. Similar to the selectivity results, COP-18 and COP-20 (–CH₃ and –OH functionalized) performed the worst, exhibiting the largest parasitic energies of 2766 and 2615 kJ/kg_{CO₂}. The –SO₂Cl and –NH₂ functionalized materials, COP-19 and COP-17, performed 24–34% better than COP-18. A further improvement in performance is observed in the multifunctionalized COP-22 and COP-21 ($E_{\text{parasitic}}$'s: 1631 and 1608 kJ/kg_{CO₂}). Interestingly, these

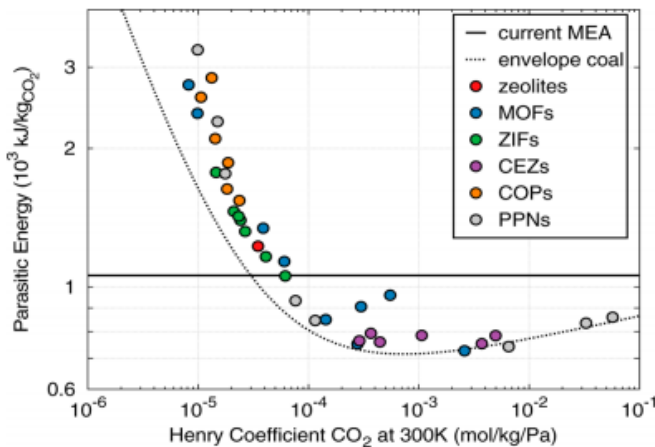


Figure 4.4: Parasitic energy as a function of the Henry coefficient at 300 K. The black solid line illustrates the performance of the current state of the art technology, amine-scrubbing ($1060 \text{ kJ/kg}_{\text{CO}_2}$). The black dashed line depicts the performance envelope line for coal flue gas of the all-silica zeolites investigated in [126]. The COPs under investigation in this work are marked as orange circles. The other materials are based on the results of [90].

multifunctionalized COPs containing functional groups ($-\text{SO}_2\text{Cl}$ and $-\text{NH}_2$) demonstrated better parasitic energies than the singly functionalized COPs. It must be pointed out, however, that the most promising material analyzed in this work exhibits a parasitic energy twice as high as the best performing material discovered thus far. Thus, despite improvements upon singly functionalized COPs, COP-21 displays a greater parasitic energy cost than the current state of the art technology, amine-scrubbing (solid line in Figure 4.4). The numerical values of the parasitic energies for the COPs can be found in Table 4.3.

An important observation can be made by examining the PPN-6 series in Figure 4.4. PPNs possess very similar framework structures to COPs. Thus, studying the improvements in performance within this series achieved by gradually functionalizing the framework can provide interesting insights for the related class of COPs. The performance of PPN-6 can be improved significantly from bare PPN-6 (c.a. $2290 \text{ kJ/kg}_{\text{CO}_2}$) by converting it into either the lithium salt analogue (c.a. $934 \text{ kJ/kg}_{\text{CO}_2}$) or the sulfonic acid grafted one (c.a. $846 \text{ kJ/kg}_{\text{CO}_2}$), as well as by functionalizing it with various different amine groups, i.e. PPN-6- CH_2DETA , PPN-6- CH_2TAEA , and PPN-6- CH_2TETA (860 , 835 , and $742 \text{ kJ/kg}_{\text{CO}_2}$). [90] Similar parasitic energy improvements may also be expected by integrating elongated amine chains into the various COP frameworks. Therefore, these results illustrate how incorporating multiple functional groups within a single COP can lead to a significant improvement in the carbon capture properties of nanoporous materials.

Conclusion

As a result of this work, we developed a systematic strategy for preparing multifunctionalized covalent organic polymers (COPs), and used computational methods to generate various potential topologies for one particular material, COP-5. Using our synthetic strategy, we synthesized 17 novel multiblock COPs with finely tuned porosities. The COPs studied in this work have remarkably high porosities and hydrothermal stabilities, which are critical for the adoption of these materials for industrial applications. By tailoring the length and geometry of building blocks, we can tune the BET SSAs and pore volumes of these COPs. As a result, we synthesized a material, COP-20, with the largest measured pore volume in the field of porous organic materials, $3.5 \text{ cm}^3 \text{ g}^{-1}$. Our synthetic approach also allows us to incorporate different functional groups into COPs; we successfully incorporated 5 distinct functional groups, i.e. $-\text{NO}_2$, $-\text{NH}_2$, $-\text{CH}_3$, $-\text{SO}_2\text{Cl}$ and $-\text{OH}$, in groups of two and three into individual COPs. Notably, functionalizing COPs with multiple groups in one phase can lead to improved properties that are not simply linear combinations of those of the pure components. When two and three distinct functional groups are incorporated, i.e. $-\text{NH}_2$, $-\text{SO}_2\text{Cl}$ and $-\text{OH}$, into one phase, the multifunctionalized COP-21 and COP-22 exhibit enhanced selectivities, roughly twice as large as that of any of the singly functionalized COPs. Therefore, incorporating multiple functional groups within a single COP may very well be useful for improving the carbon capture properties of a given material. Furthermore, at typical flue gas conditions both of these materials performed the best and displayed the lowest parasitic energies (1608 and 1632 $\text{kJ}/\text{kg}_{\text{CO}_2}$) among all the frameworks studied, and of the singly functionalized frameworks, the amine functionalized COP-17 performed best. In a similar PPN study, it was observed that functionalizing the frameworks with longer amine chains improved their carbon capture performance. For these reasons, we anticipate that functionalizing the polymers presented here with longer amine chains that extend into the pore space will lead to further reduction in the parasitic energies of these frameworks. The controlled synthesis approach presented in this work has opened up new possibilities for tuning the porous properties of porous organic polymers for a variety of applications, including the design of catalysts and functional sensors.

Additionally, the work presented here motivated the research to be presented in the following section of this chapter, *Design of 2D and 3D COFs for ANG Storage Applications*; although here the focus was on investigating the application of these materials for carbon capture, preliminary results from simulations suggested that these materials would also make very promising methane storage materials. As such, this led us to the construction of a database made up of similar types of organic, aromatic linkers and to screening this new database for high-performing methane storage materials; this will be discussed next.

Additional Information in Appendix

Hypothetical COP-5 structures.

4.2 Design of 2D and 3D COFs for ANG Storage Applications

Overview

Here we present a database of 69,840 largely novel COFs assembled *in silico* from 666 distinct organic linkers and four established synthetic routes. Due to their light weights and high internal surface areas, the frameworks are promising materials for methane storage applications. To assess their methane storage performance, we used grand-canonical Monte Carlo simulations to calculate their deliverable capacities. We demonstrate that the best structure, composed of carbon-carbon bonded triazine linkers in the **tbd** topology, has a predicted 65-bar deliverable capacity of 216 v STP/v, better than the best methane storage materials published to date. Using our approach we also discovered other high-performing materials, with 300 structures having calculated deliverable capacities greater than 190 v STP/v, and 10% of these outperforming 200 v STP/v. To encourage screening studies of these materials for other applications, all structures and their properties have been made available on the Materials Cloud, and online platform created for the facile sharing of materials science resources.

This section is based on the following publication:

Mercado, R., Fu, R.-S., Yakutovich, A. V., Talirz, L. Haranczyk, M. and Smit, B., 2018. <i>In Silico</i> Design of 2D and 3D Covalent Organic Frameworks for Methane Storage Applications. <i>Chemistry of Materials</i> , <i>Just Accepted</i> .

Introduction

Covalent organic frameworks (COFs) are nanoporous, crystalline materials formed from covalent linkages between organic molecules. [32, 78, 219, 160, 159, 224, 43] Characterized by their large internal surface areas, regular pore structures, and low densities, these frameworks are attractive candidates for gas adsorption applications, such as carbon capture and methane storage. [160, 159, 224] Their reticular chemistry allows them to be tuned for particular applications with high specificity by manipulating their composition and topology. Compared to similar materials like zeolites and metal-organic frameworks (MOFs), COFs have high hydrothermal stabilities and low molecular weights, being composed entirely of light elements such as carbon, nitrogen, oxygen, and hydrogen. Unlike these materials, relatively few COFs have been designed computationally; [98, 159, 161, 145, 144, 174] this novelty makes them attractive materials to study as their gas storage landscape may not have been fully explored.

In this study, we follow a similar structure generation approach to Martin *et al.* [145], who built a database of hypothetical porous polymer networks (PPNs). Their database comprises of 17,846 predicted materials assembled in the **dia** topology from commercially available monomers based on established synthetic routes to imine and boronate ester linkages. In later work, Martin *et al.* [144] assembled 4147 COF structures using the prevalent **ctn** and

bor nets, and boroxine and imine linkages. More recently, Tong *et al.* [215] published a curated CoRE COF database of 187 experimentally synthesized COF structures made by removing solvent and disorder from published structures.

Most studies on COF applications have focused on gas separations and hydrogen storage.[65, 77, 161, 240]. In this work, however, we investigate the possible application of COFs for natural gas (NG) storage. We are interested in NG as a possible alternative to petroleum due to its growing availability and potentially lower, but nonzero, greenhouse gas emissions per unit of energy generated. [166, 228, 158, 89, 1, 134, 116] Largely composed of methane, NG has a lower carbon content than conventional transportation fuels because it has roughly 55% carbon per unit energy compared to coal and 73% compared to petroleum; it also burns at lower temperatures than most liquid hydrocarbons, leading to decreased NO_x emissions. [158] The use of NG is thus key to lowering our dependence on petroleum as we transition to more sustainable fuels in coming decades.[116]

The main drawback to NG is that under ambient conditions, the energy density of NG is 0.038 MJ/L, 0.11% that of gasoline; we cannot therefore store enough NG in a reasonably sized vehicular fuel tank to achieve an acceptable driving range without a densification strategy. [201] Current methods for the densification and storage of NG include compressed natural gas (CNG), liquefied natural gas (LNG), and, recently, adsorbed natural gas (ANG).

For use in vehicles, NG is typically compressed to and stored at 200 – 300 bar in high-strength tanks via a costly, multi-stage compression process. [158, 31, 201] CNG has an energy density of roughly 8.8 MJ/L at 200 bar and ambient temperatures, 25% that of gasoline. [7] LNG consists of purified NG condensed by cooling to nearly 111 K and stored in double-walled vacuum-insulated pressurized tanks; it has an energy density of 22.5 MJ/L, 65% that of gasoline. [31, 53] The high energy cost and special infrastructure required for the storage and handling of LNG pose a challenge for use in powering small, everyday vehicles. [243]

ANG is NG adsorbed into tanks packed with nano- or microporous material. Adsorption leads to an increased storage density of NG at lower storage pressures.[162, 201] The use of solid adsorbents could lead to a NG density competitive with that of CNG at lower storage pressures by exploiting the favorable van der Waals interactions between methane and a material's pore walls. The expensive infrastructure required of LNG or CNG would not be necessary with a reduced storage pressure such that fuel tanks could be made lighter and more conformable. The challenge of ANG is packing as much methane as possible in a given volume at the gentlest conditions possible; we therefore focus in this work on finding materials with optimal volumetric methane uptakes at the operating pressures. Volumetric quantities are more directly related to the driving range of a vehicle than gravimetric quantities. [146]

ANG storage is a particularly attractive application for COFs due to their light weights and high internal surface areas. [146, 201] To date, only limited screening has been performed on COFs, and we demonstrate that there exist COFs which perform better for ANG storage than the record-holding materials. In this work, we also investigate which features lead to enhanced ANG storage in COFs .

Methods

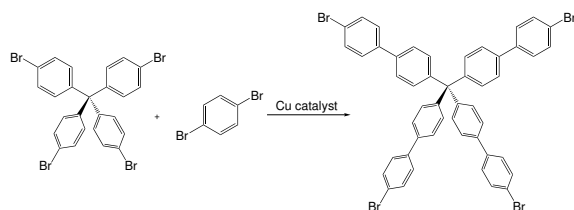
In Silico Structure Assembly

Framework generation for the database takes place in seven steps:

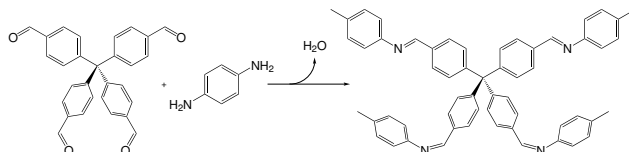
1. **Linker Chemistry Selection** The linker chemistry that we want to mimic with the *in silico* structure assembly process is selected.
2. **Construction of Linkers** The linkers to be used in assembling the structures are built and relaxed via a steepest-descent algorithm using the Universal Force Field (UFF). [189]
3. **Topological Net Selection** Topological nets are obtained from the Reticular Chemistry Structure Resource. [172]
4. **Structure Assembly** The linkers and nets are assembled into frameworks using Zeo++. [142, 230]
5. **Structure Relaxation** The energies of the assembled structures are optimized using the Dreiding force field in LAMMPS. [183, 195]
6. **Database Cleaning** Structures which do not converge or contain extraneous bonds are removed.
7. **Interpenetrated Structure Assembly** Interpenetrated structures are assembled from the frameworks with large enough void volumes.

1. Linker Chemistry Selection In the synthesis of any crystalline framework, reversible bond formation is key on a time scale that allows for the correction of defects during the self-assembly process.[224, 204] This is why, before assembling any structures, we selected four types of covalent linkages for the bond-formation chemistry in the database: *carbon-carbon*, *imine*, *amine*, and *amide* bonds. We chose the first two linkages because there are known synthetic routes to carbon-carbon bonds via cross-coupling reactions [240] in porous organic materials (Figure 4.5a) and because imine bond formation via imine condensation reactions[224] is well studied in COFs (Figure 4.5b). Furthermore, Waller *et al.* [225] recently demonstrated how amine and amide bonds (Figures 4.5c – 4.5d) are attainable in COFs from the reduction and oxidation of imine bonded COFs.

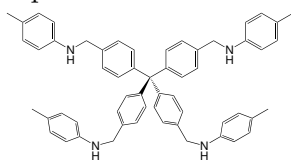
The overarching challenge in synthesizing frameworks from cross-coupling reactions is that linking organic building blocks by strong covalent bonds often results in amorphous structures because reversible bond formation is not happening on a time scale that allows for the correction of defects. [245, 224] This can be affected by the solvent choice or the reaction conditions, such as the temperature and pressure of the reaction vessel, but can also be very dependent on the type of bond to be formed. As such, it is easier to synthesize crystalline covalently-linked frameworks from condensation reactions than from cross-coupling reactions.



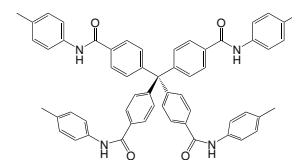
(a) Example carbon-carbon bond formation via Ullmann cross-coupling [55] reaction.



(b) Example imine bond formation via imine condensation reaction.



(c) amine linkages



(d) amide linkages

Figure 4.5: Examples of bond-forming chemistry mimicked in the database.

Since amide and amine frameworks can be attained from the oxidation and reduction of the imine frameworks, we anticipate that structures formed from linking building blocks with amine and amide bonds will be of similar difficulty to synthesize.

In the assembly process, we also considered a fifth set of structures, which is those containing *mixed* bond types. These structures arose from attempts at creating amide, amine, and imine bonded structures from nets with two non-linear linkers and multiple edges. These types of structures contain $-N=N-$ and $-(H)C-C(H)-$ bonds in addition to amide, amine, and imine bonds. In this case, the aforementioned synthetic routes cannot exclusively be utilized to synthesize these structures, but we chose to include them in the database as many of them are promising candidates for ANG storage.

2. Construction of Linkers One important criterion for a set of linkers to be able to form extended crystalline COFs, rather than cages, is that the linkers be rigid. [202] So as to satisfy this requirement, we constrain the linker library to consist exclusively of organic molecules with rigid backbones.

In order to find linkers for carbon-carbon bond formation, we start from a single benzene ring, which is successively functionalized with alkoxy, amine, amide, halogen, thiol, and nitro groups. Acceptable linkers are aromatic heterocycles containing two or more bromine atoms, which can then participate in cross-coupling reactions. We assume that all bromine atoms lead to successful carbon-carbon bond formation. In addition, we demand that the linkers be (a) commercially available and (b) of linear, trigonal, or tetragonal symmetry.

Based on the above constraints, we devised a library of 111 aromatic linkers containing

Bond	Linker A	Linker B
amide	C=O-terminated	N-H-terminated ^a
amine	CH ₂ -terminated	N-H terminated ^a
C-C	C-terminated ^b	C-terminated ^b
imine	CH-terminated	N-terminated

Table 4.5: Bond terminations used in the formation of the four types of bonds discussed in this work. Superscripts indicate bond terminations which are identical.

90 linear linkers with C₁ or C₂ symmetry, six trigonal linkers with C₃ or D₃ symmetry, and 15 tetragonal linkers with C₄, D₄, or T_d symmetry. By design, the majority of the linkers have not been previously used for the *in silico* generation of COF structures. For a complete list of these linkers, including IUPAC names for the precursors and their structures, please consult Tables E.1 – E.9 in the Appendix.

For the five other sets of precursors to the amide, amine, and imine bonded structures, we replaced the bromine atoms from the carbon-carbon bonded structure precursors with the linker terminations described in Table 4.5. Details on how these linker terminations were determined are given in *Structure Assembly*.

We relax each linker using the Universal Force Field (UFF) [189] with the steepest-descent optimizer in Avogadro [80, 79] before adding dummy atoms at the connection points. An additional configuration was considered for each tetragonal precursor (*linker97* – *linker111*) to the amide, amine, and imine bonds; in these configurations, the scaffold of the linkers remain the same but the terminations are flipped before adding the dummy atoms. This was done so as to increase the number of structures which successfully assemble because the majority of structures in the database are composed of at least one tetragonal linker.

3. Topological Net Selection As mentioned above, each framework is characterized by two linkers, one net, and the type of bond formed. The net determines the connectivity and arrangement in space of the linkers, and are identified by unique three-letter acronyms that can be followed by dashes with letters and/or symbols to specify additional details (nets are identified throughout this manuscript in **bold**). [172] The quintessential example is the **dia** net, which consists of tetrahedral vertices arranged in the same way as the network of carbon atoms in diamond.[15] Structures are assembled by placing linear linkers along the net edges and non-linear linkers at the nodes. We used every possible net on the Reticular Chemistry Structure Resource (RCSR) [172] containing either (a) a single vertex matching the crystallographic symmetry of a non-linear linker in the library or (b) two unique vertices matching the crystallographic symmetries of two non-linear linkers in the library. A complete list of the 839 nets used in this work is available in the Appendix. This combination of nets and linkers yielded 470,072 COF candidates, roughly a third of what is expected from combinatorics (see Appendix).

4. Structure Assembly Each set of linkers results from taking the precursors to each bond type, removing atoms which will be lost after formation of the new bond, and placing

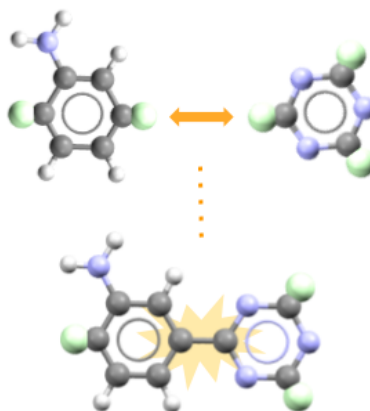


Figure 4.6: Schematic illustrating *in silico* bond formation in the database. In this particular example, *linker1* is coming together with *linker91* to form a carbon-carbon bond. Dummy atoms are shown in green.

dummy atoms at the connection points. Bonds are then formed *in silico* using the *Zeo++ Framework Builder* [142, 230, 141] tool by taking the two linkers and bringing them closer together until the dummy atoms overlap (Figure 4.6).

We can control which bond forms by changing the identity of the atoms around the dummy atoms. We refer to the collection of these atoms and the dummy atoms as the *termination* of that linker. To form the bond types mentioned in the previous section, we came up with the terminations given in Table 4.5. Generally, these terminations were chosen to minimize clashing atoms at the connection points.

From this step, 470,072 COF candidates were successfully generated using *Zeo++*. This number does not include structures which were discarded because of either a) clashing atoms or b) large root mean squared displacement errors at the connection points. For further details on how the linker terminations and dummy atoms are added to the linkers, please see the Appendix. For further details on the *in silico* bond formation step, see the Appendix.

5. Structure Relaxation The preliminary COFs generated using the *Zeo++ Framework Builder* minimize the root mean square displacement between linkage sites on each linker. The large size of the database meant that only classical models could feasibly be used to relax the 470,072 initial structures. Despite the obvious limitations of using classical force fields to optimize the internal energies of nanoporous structures, especially those limited to pairwise interactions (e.g. the lack of π -stacking interactions), they have been previously used to relax COFs and COF-like structures successfully. [145, 144] The structural optimizations were performed in LAMMPS [183, 195] using the Dreiding [153] force field for bond, angle, dihedral, and torsional terms, no charges, and a cutoff of 12.5 Å for non-bonding interactions. The Dreiding force field [153] was chosen for computational efficiency

yet adequate agreement with *ab initio* methods. [145, 144] Input files were prepared in a high-throughput manner using *lammps_interface*. [17] Non-bonding interactions were cut-off and shifted at 12.5 Å, and all unit cells were sufficiently replicated so as to avoid interaction between periodic replica. Approximately 70% of structures successfully converged. For full details, please see the Appendix.

6. Database Cleaning As the next step, any chemically unstable or poorly-assembled structures are removed from the database in a high-throughput manner. Some of the structures contained extraneous or missing bonds due to the error threshold that was used when assembling the structures in the Zeo++ *Framework Builder*; in other cases, structures contained extraneous bonds due to the way bonds are identified from nearest neighbors when preparing the LAMMPS topology files. Full details on this procedure are presented in the Appendix.

7. Interpenetrated Structure Assembly Interpenetrated COF structures have been widely reported in the literature in cases where the pores are large enough to fit entire copies of a framework in the void space. Two examples of experimentally reported interpenetrated frameworks are COF-300 and COF-320. [219, 245]

In turn, we found that many of the COFs in the database could also form interpenetrated structures. To find out if a framework can interpenetrate, we progressively displace a copy of the framework by fixed intervals of 0.5 Å along one or more of the lattice vectors. If there are no overlapping atoms in a trial interpenetrated structure, the structure is saved. If possible, the process is repeated with additional copies of the framework in the pores to form structures with higher levels of interpenetration. Approximately a third of the frameworks were able to form interpenetrated structures.

Calculating Geometric Properties

Upon completion of the database, we computed the geometric surface area of each framework using Zeo++. [230, 81] The geometric surface area is computed by first determining the accessibility of the pores. Then, for each framework, 5000 MC insertions of a 1.82 Å radius spherical probe (the kinetic radius of a methane molecule) are used to integrate the accessible and inaccessible surface areas. Using Zeo++ we also computed the largest included sphere diameter, the largest free sphere diameter, and the largest included sphere along a free sphere path diameter.

Screening Database for ANG Storage Applications

In this subsection, we outline the procedure used to screen our COFs using grand-canonical Monte Carlo (GCMC) simulations; performing these calculations, we are able to rank the materials from the *deliverable capacity* (DC). The DC is defined as the difference between the methane stored per volume of material at the *storage pressure* in a fully loaded tank and the methane that remains at the *depletion pressure*. We have chosen to calculate DCs using a storage pressure of 65 bar and a depletion pressure of 5.8 bar (65-bar DCs).

This depletion pressure set by the Advanced Research Projects Agency-Energy (ARPA-E) is required to produce a pressure gradient steep enough to drive ANG from the adsorbent to the engine, and is based on the MOVE program ANG storage target designed to be competitive with 250-bar CNG. [2, 201] Using the 65-bar DC to determine a material’s performance for ANG storage takes into account that a material must not only store a large amount of methane at the fueling station, but also have released as much as possible when the time comes to refuel the engine. Throughout this paper, we use the term *high-performing* to refer to a large 65-bar DC.

To determine the methane uptake for the database structures, we performed GCMC simulations for all frameworks in contact with methane reservoirs at both the storage and depletion pressures. Before running any GCMC simulations, Zeo++ was used to determine which structures contain blocked pockets, pores which would be inaccessible to a spherical probe approximately the size of a methane molecule. For structures containing inaccessible pores, blocked pocket files were generated using 100 MC insertions of a 1.82 Å radius sphere per cubic angstrom. Accurately identifying blocked pockets is important for calculating the true DC of a framework since methane must be excluded from binding in closed-off pores.

Each GCMC simulation consisted of 5000 initialization cycles followed by 5000 production cycles. Thermodynamic averages for the heat of desorption (HoD) and the total methane uptake were collected every production cycle (for details on the convergence of these calculations, see the Appendix). For each framework, the helium void fraction was determined by probing the framework with a helium molecule using the Widom particle insertion method of Talu and Meyers. [213, 173] Fugacities were calculated using the Peng-Robinson equation of state.

All GCMC simulations were done at 298 K. The Dreiding force field was used for non-bonding interactions involving framework atoms, and the TraPPE[140] united-atom model for non-bonding interactions involving methane; Lorentz-Berthelot mixing rules were used to obtain cross-terms. All potentials were truncated at 12.8 Å, with tail corrections. Unit cells were replicated until the distance along any direction in the simulation box was longer than twice the cut-off.

For each COF, the 65-bar DC is calculated as follows,

$$\text{DC}_{65 \text{ bar}}^{\text{v STP/v}} = (\sigma_{65 \text{ bar}} - \sigma_{5.8 \text{ bar}}) * M(\text{CH}_4) * \frac{\rho_{\text{COF}}}{\rho_{\text{CH}_4}},$$

where σ is the total methane uptake in units of mol/kg, $M(\text{CH}_4)$ is the molar mass of methane, ρ_{COF} is the framework density, and ρ_{CH_4} is 0.717 kg/m³, the density of methane at STP.

Bond type	2D-layered	3D, non-interp.	3D, interp.
amide	691	3901	2024
amine	950	3294	1481
C–C	4078	13,432	3638
imine	2816	19,662	10,052
mixed	106	2097	1618

Table 4.6: Breakdown of database structures.

Results and Discussion

Characterization of the COF Database

Throughout the paper, we make a distinction between 2D-layered and 3D structures. The 2D structures refer to the set of frameworks composed of stacked 2D layers held on to the next by dispersion interactions. The 3D structures are the set of frameworks containing three dimensional networks of covalently bound atoms. Structures are identified using the following naming scheme: *linkerA_linkerB_net* if non-interpenetrated and *linkerA_linkerB_net_interp_#* if interpenetrated, where *linkerA* and *linkerB* indicate the linkers and their respective linker terminations, *net* indicates the topology, and *#* indicates the degree of interpenetration.

The database in this work contains 18,813 interpenetrated 3D structures, 42,386 non-interpenetrated 3D structures, and 8641 2D-layered structures, for a total of 69,840 structures. A breakdown by bond type is given in Table 4.6.

The reason for the larger number of carbon-carbon and imine bonded structures in the database is due to the procedure used to assemble them; the fewer atoms there are around the active site of the linker, the less likely there are to be overlapping atoms when the linkers are connected, so the structure is less likely to be discarded. There are also many more carbon-carbon bonded structures because these structures are not restricted to nets containing a single edge.

The results of the geometric surface area calculations are shown in Figure 4.7. As a whole, the carbon-carbon bonded structures had smaller surface areas than all other sets of structures, likely a result of the shorter carbon-carbon bonds formed; carbon-nitrogen bonds are all slightly longer. For reference, an average C–C bond is 154 pm in length, while an average C–N single bond is 174 pm long and an average C=N double bond is 129 pm long. [91]

The average framework densities for the five sets of 2D and 3D structures are listed in Table 4.7. For the entire set of 2D structures, the average density is 286.2 kg/m³; on the other hand, the average density of the entire set of 3D structures is 231.0 kg/m³. As expected, the 2D-layered structures are generally more dense than the 3D structures. For both sets of structures, the carbon-carbon bonded structures are the most dense, and the imine bonded structures the least dense.

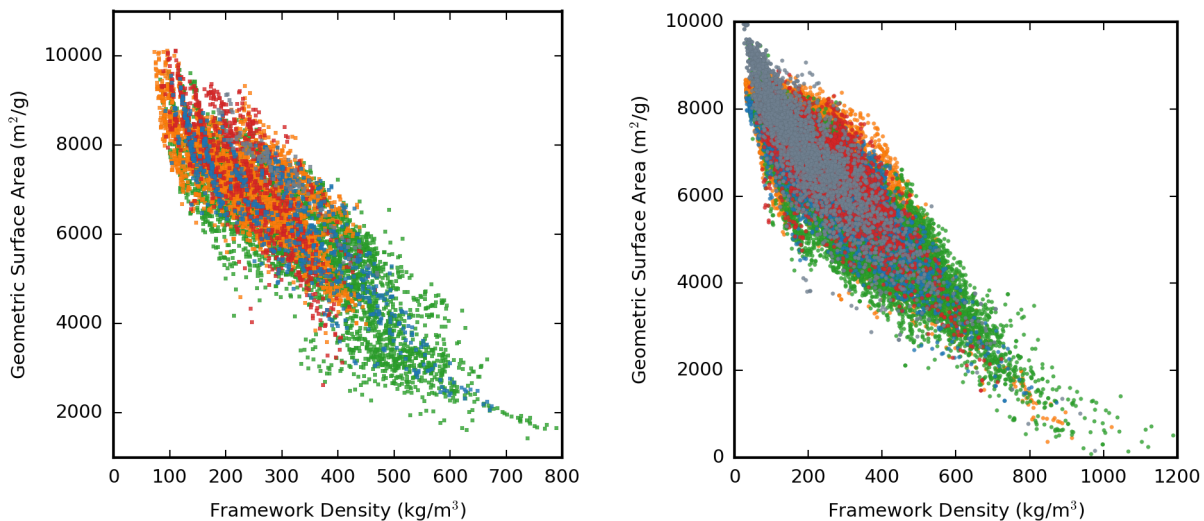


Figure 4.7: Scatter plots of geometric surface area versus framework density for the 2D structures (left) and 3D structures (right) assembled in this work. Color key: blue=amide, red=amine, orange=imine, green=C-C, grey=mixed.

Bond Type	ρ_{avg} , 2D	σ , 2D	ρ_{avg} , 3D	σ , 3D
imine	238.9	86.6	193.6	99.9
mixed	296.4	70.9	195.8	118.7
amine	235.6	81.0	229.4	104.8
amide	314.6	130.6	249.7	117.1
C-C	325.6	132.3	297.7	152.9

Table 4.7: Average framework density, ρ_{avg} , and standard deviation, σ , for each set of structures. Units are in kg/m^3

Comparison to Experimentally Synthesized Examples

Here we provide a comparison of our structures to experimental structures to demonstrate the reliability of our approach. As the majority of the structures in our database are new, there are only a few synthesized examples for structures in our database; two such rare examples are COF-300 and TAPB-PDA COF. [219, 204, 151, 223]

COF-300 is the first material we compare to. Experimental data suggests it assembles in a five-fold interpenetrated configuration, and it is also the highest level of interpenetration that we were able to obtain. COF-300 corresponds to *linker109_N-linker87_CH-dia_interp-5* in the database. Using our assembly process, we were able to obtain not only non- and five-fold interpenetrated structures of this framework, but also two-, three-, and four-fold interpenetrated structures. The five-fold interpenetrated structure is illustrated in Figure 4.8.

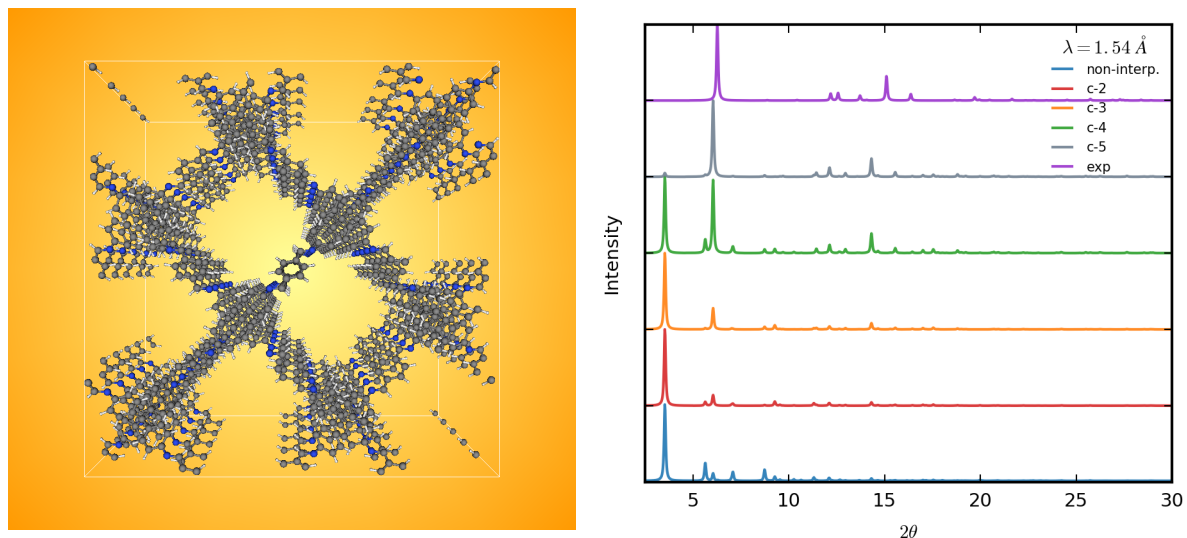


Figure 4.8: (left) Five-fold interpenetrated structure of the *linker109_N-linker87_CH_dia* (COF-300) framework assembled in the database. (right) PXRD patterns computed for COF-300 analogues in the database using a 1.54 Å wavelength. Results plotted using a 0.1 FWHM. *c-n* in the legend refers to the *n*-fold interpenetrated structure. The top pattern was calculated from the experimental structure reported in Uribe *et al.* [219]

Comparing the powder X-ray diffraction (PXRD) pattern of the COF-300 analogues in the database, we see that the PXRD pattern of the five-fold interpenetrated structure best agrees with the pattern for the reported COF-300 structure (Figure 4.8). This demonstrates that our computationally assembled structures are in fact realistic, as computed PXRD patterns are notoriously difficult to match to experimental results unless there is very good agreement between the structures. All PXRD patterns were computed using Mercury. [133]

Another example of a synthesized COF from the database is TAPB-PDA COF. [204] This 2D-layered structure corresponds to the *linker96_N-linker87_CH_hcb* framework in the database (Figure 4.9).

To verify that the TAPB-PDA COF analogue in the **hcb** topology is indeed a close match to the experimental structure, we calculated the PXRD spectra for all three analogues assembled herein (Figure 4.9), including **hnb** and **hca** analogues. Indeed, the diffraction pattern for *linker96_N-linker87_CH_hcb* matches very closely with those reported by Dichtel’s group for their synthesized material and for their eclipsed TAPB-PDA COF model, confirming again that our method leads to realistic structures. [204, 151, 223]

To the best of our knowledge, methane adsorption isotherms have not been measured in either framework, so validation of the DCs is not possible for these structures. Nonetheless, the force fields used for the GCMC simulations have been previously shown to predict methane isotherms in good agreement with experiment for frameworks devoid of open-metal sites, including COFs and PPNs,[145, 144, 201] and are therefore not revalidated here.

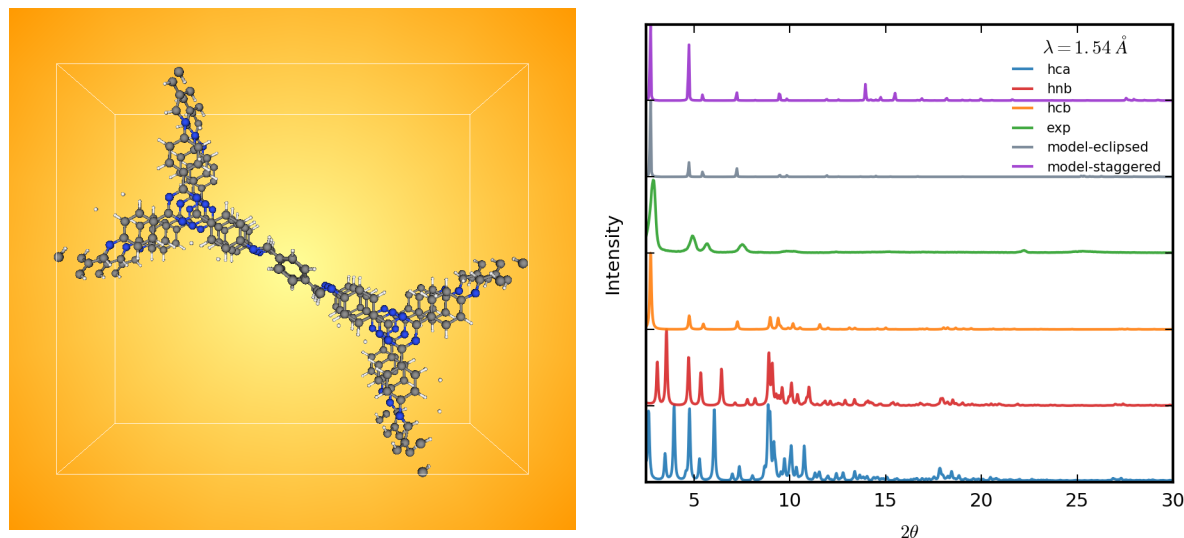


Figure 4.9: (left) Structure of the 2D-layered *linker96_N-linker87_CH_hcb* framework (TAPB-PDA COF) in the database. (right) PXRD patterns computed for TAPB-PDA COF analogues in the database using a 1.54 Å wavelength. Results plotted using a 0.1 FWHM. *c-n* in the legend refers to the *n*-fold interpenetrated structure. The bottom three patterns correspond to structures in the database, whereas the top three patterns were reported by Matsumoto *et al.* [151]

Showing that our structure assembly and relaxation approach leads to realistic structures is sufficient validation of the approach. Further comparisons of the COF-300 and TAPB-PDA analogues can be found in the Appendix.

Analysis of the GCMC Simulations

The results of the GCMC simulations for all structures are shown in Figures 4.10 and 4.11.

In Figure 4.10a, the distributions in the HoDs at the depletion pressure are shown, where differences between the five sets of structures are emphasized using different colors for each bond type. Figure 4.10c plots histograms of the differences in the HoDs at the adsorption and depletion pressures (ΔHoD) for the five sets of structures, illustrating why some sets contain more high-performing ANG storage materials than others. Being negatively skewed, Figure 4.10c also shows that the HoDs are generally larger at the storage pressures than at the depletion pressures due to favorable methane-methane interactions which lead to non-Langmuir adsorption behavior in a material. We illustrate in Figure 4.10d how a larger ΔHoD correlates with a larger DC. For materials with more positive ΔHoD s, attractive methane-methane interactions beat out the opposing effects caused by the decreasing number of available adsorption sites; this behavior is exemplified in materials with long and

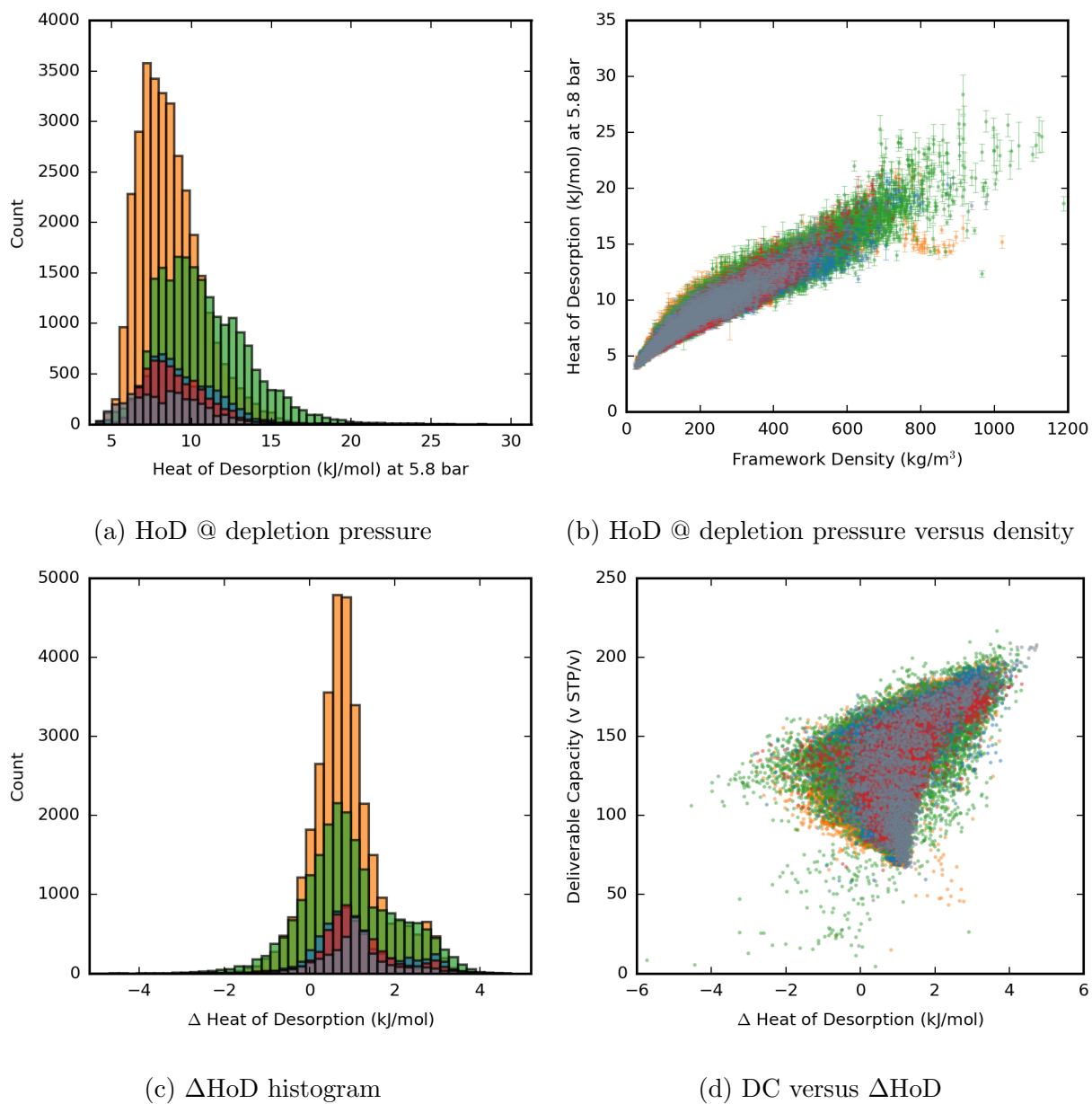


Figure 4.10: Plots of the methane HoDs at the depletion pressure (a and b) and Δ HoDs (c and d) for all structures. All results calculated at 298 K. Color key: blue=amide, red=amine, orange=imine, green=C-C, grey=mixed.

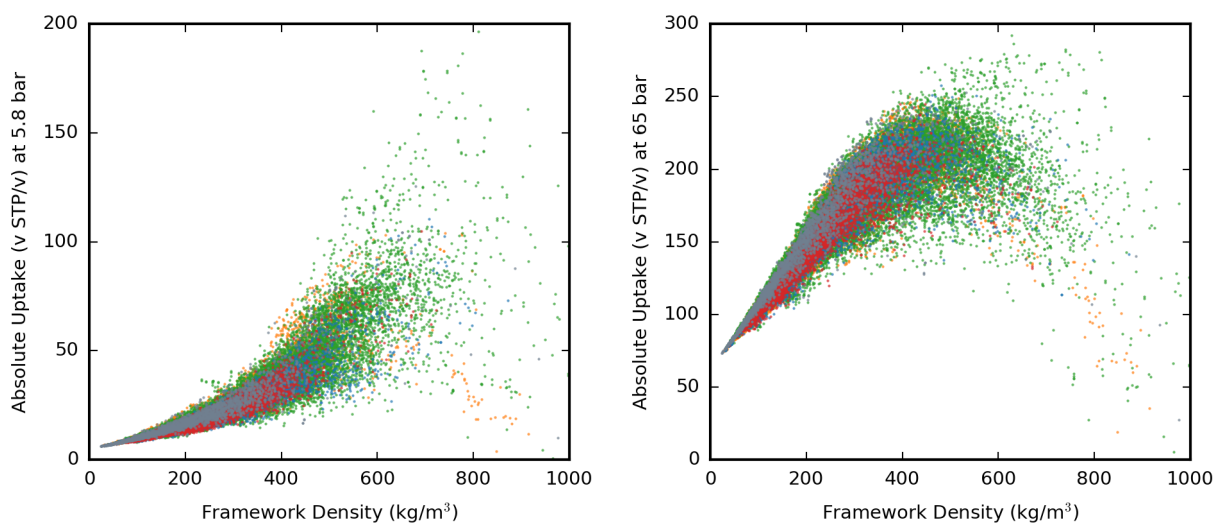


Figure 4.11: Plots of the methane uptakes at the depletion (left) and storage (right) pressure versus the framework densities for all structures. All results calculated at 298 K. Color key: blue=amide, red=amine, orange=imine, green=C-C, grey=mixed.

narrow pores. On the other hand, in materials with negative ΔH_{oD} s, competition of the gas molecules for adsorption sites outweighs the attractive methane-methane interactions; the latter case leads to classic Langmuir-type adsorption. While these types of frameworks do not necessarily have the worst DCs, they will not have the optimal adsorption behavior at the specified conditions for ANG storage. On the other hand, materials where the ΔH_{oD} is near zero tend to span a large range of DCs, including many materials that are better than those with negative ΔH_{oD} , but also including some of the worst performing materials.

In Figure 4.11 we plot the results for the uptakes at the depletion and storage pressures as a function of framework density. Overall, the trends in the GCMC results are similar for both the 2D and 3D structures.

Deliverable Capacities

As can be seen in the following section, there is a handful of 2D-layered structures with DCs approaching that of the record-holding materials, and an even greater number of 3D structures that surpass them. For reference, some of the top performing ANG storage MOFs in the literature at the same set of conditions are: HKUST-1 and MOF-5, which both exhibit 65-bar DCs of about 185 v STP/v; UTSA-76a, which exhibits a DC of 189 v STP/v; and Co(bdp), which has a DC of 197 v STP/v. [201, 123, 149] To the best of our knowledge, the current best performing COF for ANG storage reported in the literature is COF-102, which has a demonstrated 80-bar volumetric capacity of 203 v STP/v. [65] As such, throughout this discussion we focus on high-performing ANG storage materials with calculated 65-bar DCs

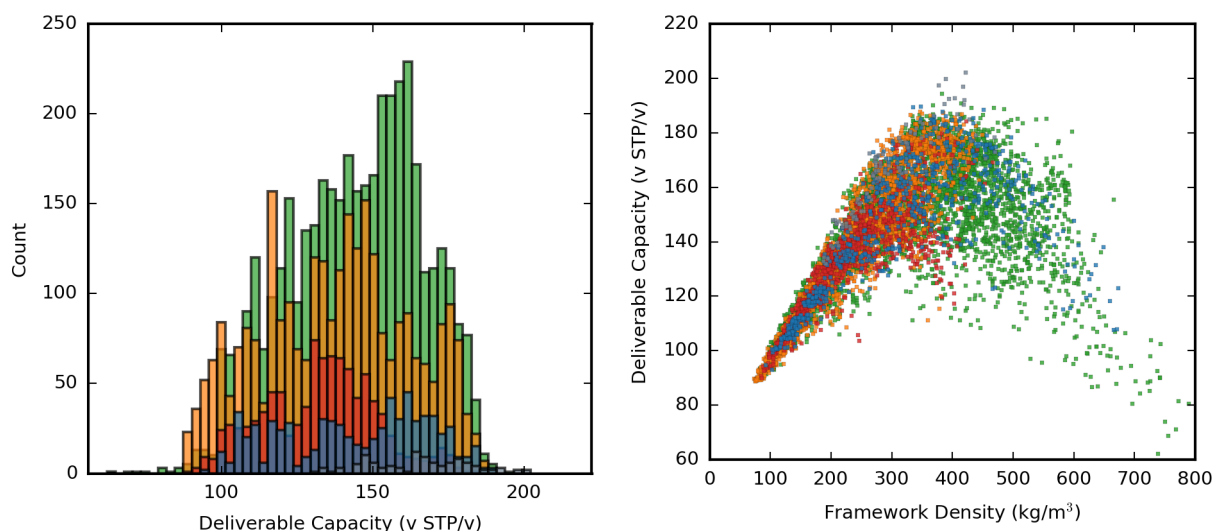


Figure 4.12: Calculated 65-bar DCs at 298 K for the 2D structures, plotted as a histogram (left) and versus the framework densities (right). Color key: blue=amide, red=amine, orange=imine, green=C-C, grey=mixed.

greater than 190 v STP/v, as those are the materials that are likely to be competitive with the current best known materials. The results are broken down for each set of 2D-layered and 3D structures below.

Distributions in the 65-bar DCs calculated for the 2D structures are shown in Figure 4.12. From the five sets of structures considered, it is noticeable that the mixed bond structures generally have the best DCs when compared to the four other sets; one mixed bond structure has a 65-bar DC > 200 v STP/v and nine have DCs > 190 v STP/v. No other sets of 2D structures have DCs > 200 v STP/v. In addition, none of the 2D amide, amine, and imine bonded structures have DCs > 190 v STP/v, although nine amide bonded structures were predicted to have DCs > 185 v STP/v. The carbon-carbon bonded structures have the second largest density of structures near the high-performance limit, with three structures having DCs > 190 v STP/v. Additionally, 44% of the top fifty 2D structures are carbon-carbon bonded structures. Although it appears that among the 2D structures the amine bonded frameworks might in general be worse performing for ANG applications, this may simply be due to there being fewer amine bonded structures in the database such that we may not be fully sampling the space of promising amine bonded structures. Instead, this set of structures has a larger average density than optimal.

Distributions in the 65-bar DCs calculated for the 3D structures are plotted in Figure 4.13. Because 3D structures can contain stronger adsorption sites than the 2D-layered structures (e.g. binding pockets vs layers), it is not surprising that a lot more 3D structures in the database were predicted to have 65-bar DCs > 200 v STP/v. While no amide, amine, and imine bonded structures in the database have DCs > 200 v STP/v, 24 carbon-carbon

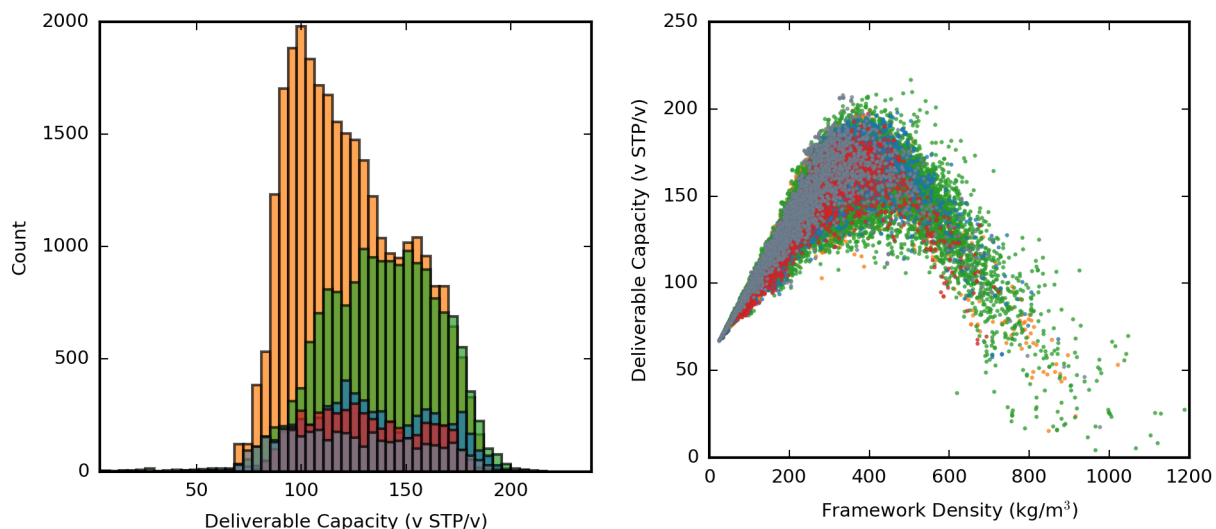


Figure 4.13: Calculated 65-bar DCs at 298 K for the 3D structures, plotted as a histogram (left) and versus the framework densities (right). Color key: blue=amide, red=amine, orange=imine, green=C-C, grey=mixed.

bonded structures and nine mixed bond structures were predicted to have DCs > 200 v STP/v. Furthermore, 50 amide, five amine, 164 carbon-carbon, 43 imine, and 30 mixed bond structures have predicted DCs > 190 v STP/v, for a total of 292 3D structures predicted to have DCs > 190 v STP/v. Structure snapshots for the top four 3D materials are shown in Figure 4.21. Furthermore, of the top fifty 3D structures, 72% of them were carbon-carbon bonded structures, suggesting that structures containing this bond in the database better sample the space of high-performing ANG storage materials.

For both the 2D and 3D frameworks, the DCs tend to be maximized in structures with densities close to 400 kg/m^3 . There are also plenty of structures at this density which are not good for ANG storage. However, this maximum in the DC can be explained by looking at the uptakes at the storage and depletion pressures as a function of the framework densities (Figure 4.11). At the depletion pressure, the methane uptakes are generally increasing with increasing framework density; however, at the storage pressure, the largest methane uptakes are found in the range of $300 - 600 \text{ kg/m}^3$. Thus, we expect the DCs, which are the differences of these values, to be maximized in the low end of this range, where the uptake at the storage pressure is maximized and the uptake at the depletion pressure is minimized. This relationship between the framework density and the DC of a material has been observed before in other classes of materials. [201] In PPNs, a similar class of materials to COFs, it was found that the density also peaks with respect to the framework density around 400 kg/m^3 . However, in MOFs, zeolitic imidazolate frameworks (ZIFs), and zeolites, it was found that the optimum materials for ANG storage occur at the slightly larger densities of 600 kg/m^3 , 800 kg/m^3 , and 1400 kg/m^3 , respectively. These densities are inversely correlated

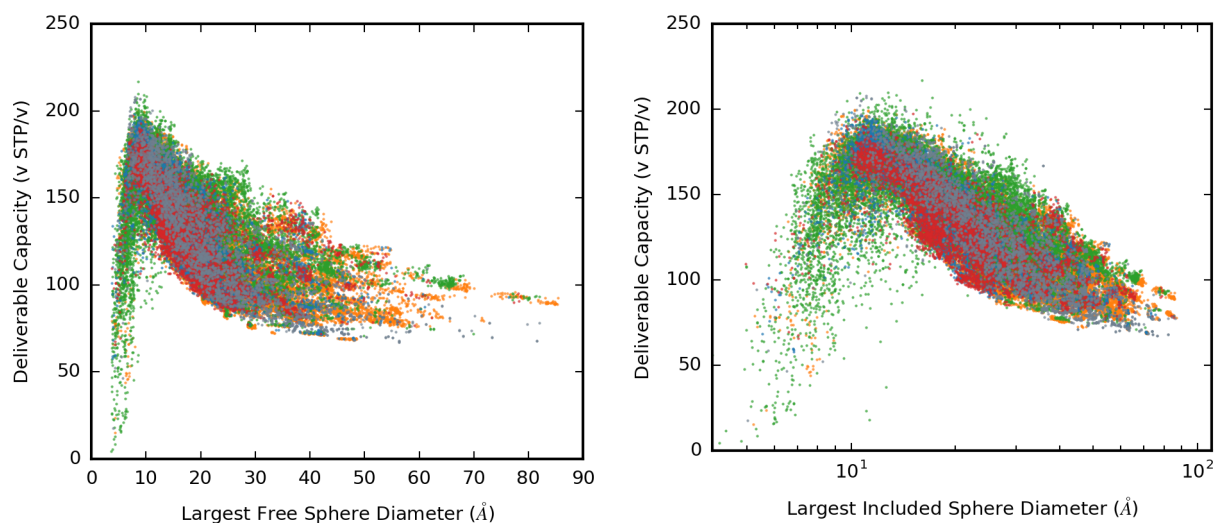


Figure 4.14: DC versus the largest free sphere diameter (left) and versus the largest included sphere diameter (right) of all structures in the database. Note the two different axes (linear and log); these are used to highlight the subtle differences in the small and large pore diameter regimes. Color key: blue=amide, red=amine, orange=imine, green=C-C, grey=mixed.

with the size of the largest included sphere in the materials, where in the PPNs the DCs are maximized in materials with largest included sphere diameters of 12 Å, and in zeolites the DCs are maximized in materials with largest included sphere diameters closer to 7 Å. This is because zeolites, which are denser than PPNs, tend to have smaller pore diameters. For comparison, the best performing COFs in our database also have largest included sphere diameters of 12 Å (Figure 10; right). There is also a correlation between the DC and the largest free sphere diameters of the frameworks, with the DC tending to a maximum at values of 8 Å for the largest free sphere diameter (Figure 4.14; left).

Compared to the pore diameter and framework density, the geometric surface area is not as correlated with the deliverable capacity (Figure 4.15); the best performing structures have geometric surface areas spanning 4000 – 6000 m²/g.

Performance by Topology

In order to understand if frameworks of the same topology display similar performances for ANG storage, we have visualized the DCs for each set of structures using different colors to represent a few select topologies (Figures 4.16 and 4.17).

Of the 2D structures, the topology which appears in the most high-performing structures was the **sql** net, appearing in 44% of the top fifty structures when ranked by 65-bar DC (Figure 4.16). The **hcb** and **bex** nets are also common, accounting for the remaining 28% and 20% of the best fifty frameworks. If we take a look at the best structures from each bond

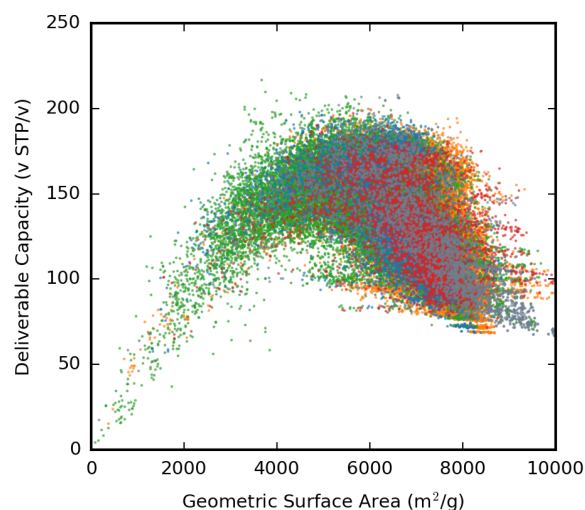


Figure 4.15: DC versus the geometric surface area of all structures in the database. Color key: blue=amide, red=amine, orange=imine, green=C-C, grey=mixed.

type, we see that the **sql** topology accounts for >94% of the top fifty of each set of amide, amine, and imine structures – but only 14% of the top fifty carbon-carbon bonded structures. Instead, the **hcb** net accounts for the majority (48%) of the top fifty carbon-carbon bonded structures. From the mixed bond structures, the best topologies are the **bex** and **pnd** nets, found in 80% and 16%, respectively, of the best performing materials. However, although the **hcb** net accounts for the majority of the best performing carbon-carbon bonded frameworks (Figure 4.16d), it also accounts for the majority of the worst performing amide and amine bonded frameworks (92% and 58%) (Figures 4.16a – 4.16b). This is interesting because in the carbon-carbon bonded frameworks, the framework densities spanned by the **hcb** structures range from roughly 100 – 600 kg/m³ (Figure 4.16d), whereas in the amide, amine, and imine bonded frameworks, the range of densities only spans from about 100 – 400 kg/m³ (Figures 4.16a – 4.16c). As previously discussed, the best ANG storage structures tend to have framework densities of around 400 kg/m³, so it is not surprising that the carbon-nitrogen bonded **hcb** structures will not perform as well; they are not spanning this space. Unsurprisingly, the amide, amine, and imine bonded structures have lower densities in general, since the average carbon-nitrogen bond is slightly longer than the average carbon-carbon bond and therefore leads to wider pores (Figure 10).

Notably, the **sql** topology, which accounts for the majority of the high-performing 2D amide, amine, and imine bonded structures, also accounts for the majority (54%) of the worst fifty 2D carbon-carbon bonded structures. In this case, we see that the **sql** structures span a range of framework densities from 300 – 800 kg/m³ in the carbon-carbon bonded structures (Figure 4.16d), whereas the carbon-nitrogen bonded structures span a lower range of densities (200 – 500 kg/m³; Figures 4.16a – 4.16c). Again, the longer length of the carbon-nitrogen

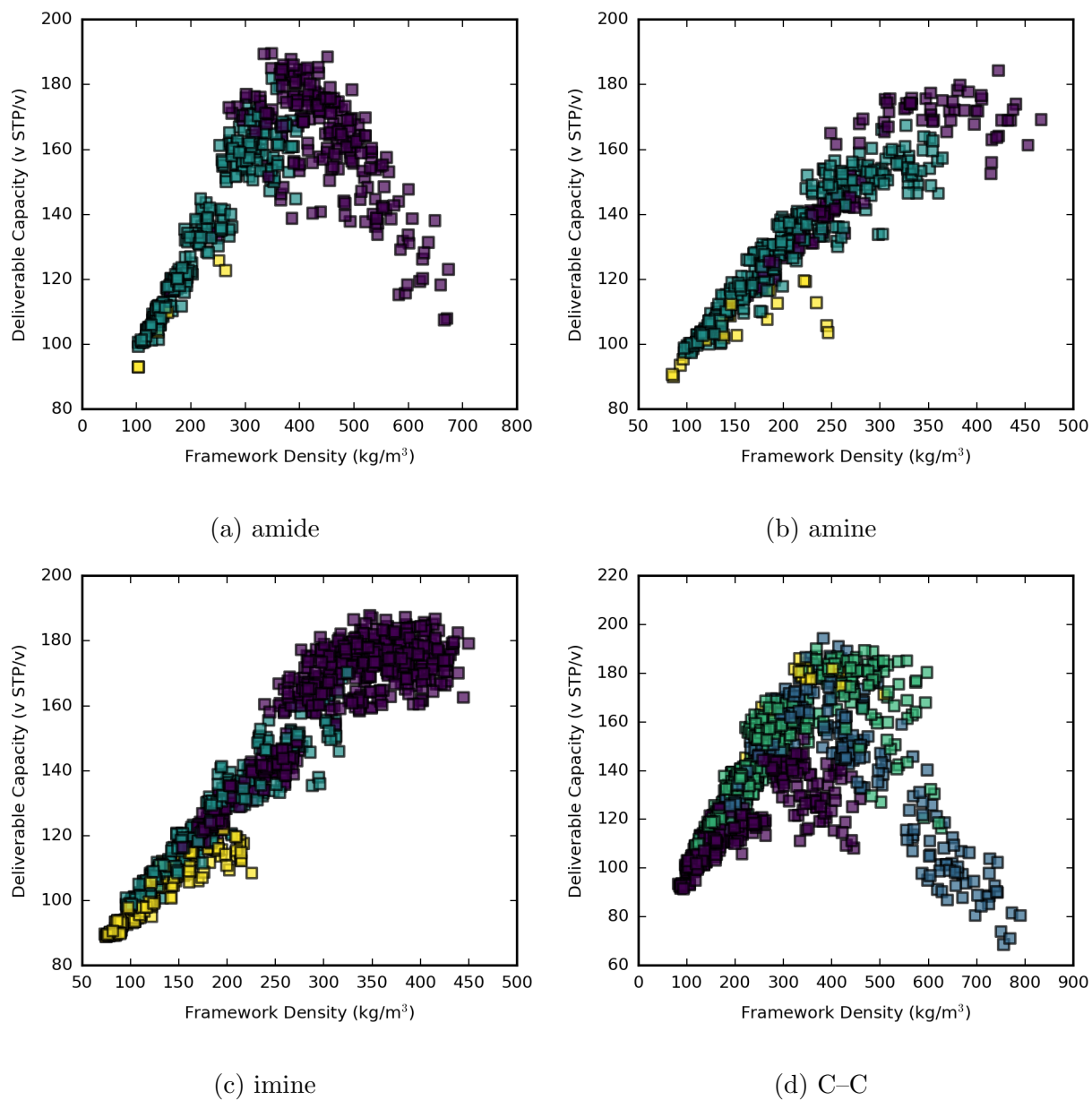


Figure 4.16: ANG storage performance plotted by topology for four sets of 2D structures. The different colors of the data points correspond to different topologies – key: (a) yellow - **hca**, blue - **hcb**, purple - **sql**; (b) yellow - **hca**, blue - **hcb**, purple - **sql**; (c) yellow - **hca**, blue - **hcb**, purple - **sql**; (d) purple - **hca**, green - **hcb**, yellow - **bex**, blue - **sql**.

bond appears to have shifted what would be an unfavorable (too dense) framework density for ANG storage in a carbon-carbon bonded framework to a better (less dense) one. This is also evident when looking at the distribution of the largest free sphere and largest included sphere diameters (Figure 4.14), where the carbon-carbon bonded structures extend much farther into the small pore diameter regime than the other bond types, and the amine and imine bonded frameworks extend much further into the large pore diameter regime. Overall, the **sql** net accounts for 32% of the worst fifty structures for ANG storage. However, the most common net in the worst 2D structures was the **hca** net, which appears in 62% of the bottom fifty overall structures, and is also the most common topology in the worst fifty imine bonded structures (74%).

For the 2D mixed bond structures, both the best and worst net is the **bex** net, which accounts for 80% of the top fifty mixed bond structures and 72% of the worst fifty mixed bond structures. Nonetheless, the worst mixed bond structures are not nearly as bad as the worst structures from the four other groups, with the worst 2D mixed bond structure having a density of 192.1 kg/m³ and a methane DC of 131.9 v STP/v. For comparison, all the other sets of structures have DCs spanning well below 100 v STP/v (Figure 4.12).

Within the 3D structures, the best overall topology is less well defined, as 25 different nets can be found in the top fifty ANG storage materials. From the amide bonded structures, the most frequently observed nets in the top fifty materials are the **qzd** and **pth** nets (34% and 20%). In the top fifty amine bonded structures, the most common nets are the **pts** and **qzd** nets (24% and 18%). In the top fifty carbon-carbon bonded structures, the most common nets are **ukk** and **uon** (16% and 14%); notably, the commonly-observed **dia** net appears in 8% of these structures. In the top fifty imine bonded structures, the **pth** and **pts** nets are the most common (46% and 26%). In the top fifty mixed bond structures, the most common nets are the **jph**, **clh**, and **bto-e** nets (14%, 12%, and 12%).

Unlike in the best 3D structures, there are clearly nets in the 3D materials which are ubiquitous in poor performing materials (Figure 4.17). These are the **tcb**, **nbo**, **lvt**, and **bod** nets. Of the worst fifty overall 3D structures for ANG storage, 28% of them have the **lvt** topology and 18% of them have the **tcb** topology. Furthermore, in the worst fifty amide bonded structures, 88% of the frameworks are in the **nbo** topology. From the worst fifty amine bonded structures, 32% are in the **lcv** topology (Figure 4.17b). Now, 28% of carbon-carbon bonded structures contain the **lvt** net. From the set of the worst fifty imine bonded structures, 62% of structures are in the **nbo** net (Figure 4.17c). Finally, from the set of the worst fifty mixed bond structures, 38% of the structures are in the **bod** topology.

We expect these conclusions about good and bad topologies to hold for any set of materials spanning a similar chemical space (i.e. similar densities, compositions); however, the less similar a set of structures is to the database herein, the more likely the observed trends are to be different. For example, for a set of metalated structures it would not be reasonable to believe that the worst and best topologies will be the same as for our purely organic materials.

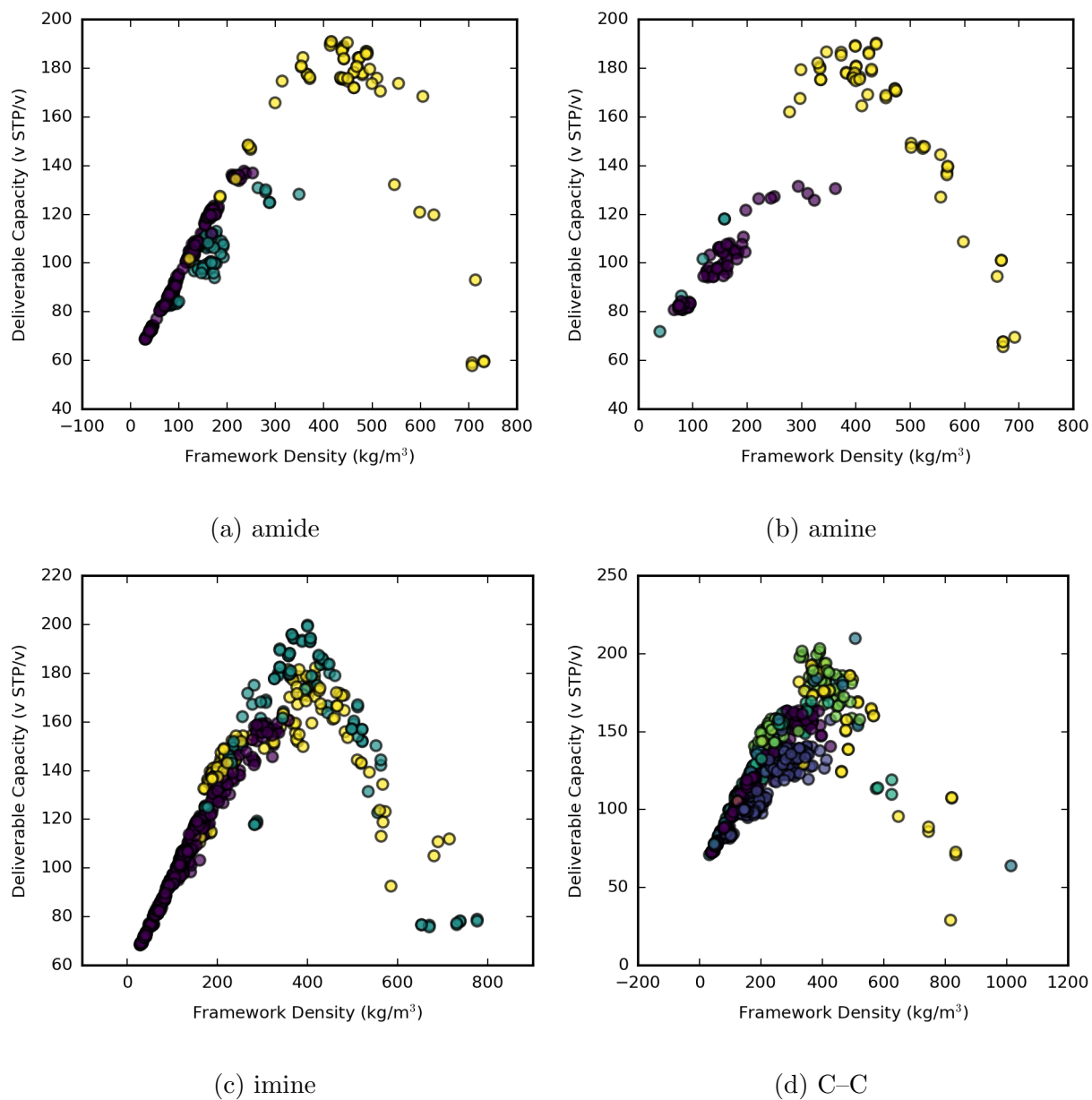


Figure 4.17: ANG storage performance plotted by topology for four sets of 3D structures. The different colors of the data points correspond to different topologies – key: (a) purple - **nbo**, blue - **lcv**, yellow - **pts**; (b) blue - **nbo**, purple - **lcv**, yellow - **pts**; (c) purple - **nbo**, yellow - **ukk**, blue - **pts**; (d) purple - **nbo**, indigo - **lcv**, light blue - **jph**, green - **ukk**, blue - **bod**, yellow - **pts**.

Best 2D Materials				
amide	amine	carbon-carbon	imine	mixed
linker87 (2%)	linker91 (1%)	linker103 (7%)	linker105 (7%)	linker107 (10%)
linker42 (3%)	linker42 (2%)	linker58 (7%)	linker42 (7%)	linker98 (10%)
linker81 (3%)	linker57 (2%)	linker81 (8%)	linker103 (9%)	linker92 (13%)
linker108 (15%)	linker92 (2%)	linker92 (16%)	linker102 (12%)	linker93 (13%)
linker99 (32%)	linker99 (47%)	linker91 (25%)	linker107 (12%)	linker91 (14%)

Worst 2D Materials				
amide	amine	carbon-carbon	imine	mixed
linker96 (1%)	linker46 (2%)	linker8 (2%)	linker9 (2%)	linker97 (8%)
linker7 (2%)	linker62 (2%)	linker53 (3%)	linker30 (3%)	linker94 (11%)
linker89 (2%)	linker65 (2%)	linker111 (12%)	linker32 (3%)	linker96 (13%)
linker8 (4%)	linker89 (3%)	linker109 (16%)	linker96 (5%)	linker95 (16%)
linker95 (49%)	linker95 (48%)	linker95 (18%)	linker95 (45%)	linker98 (32%)

Table 4.8: Top five most common linkers in the best and worst fifty 2D materials by bond type (percentage of top fifty 2D materials containing linker in parentheses).

Best 3D Materials				
amide	amine	carbon-carbon	imine	mixed
linker42 (6%)	linker92 (5%)	linker111 (6%)	linker101 (9%)	linker108 (6%)
linker47 (7%)	linker101 (7%)	linker92 (9%)	linker104 (9%)	linker109 (6%)
linker105 (8%)	linker99 (7%)	linker99 (9%)	linker108 (11%)	linker102 (8%)
linker99 (17%)	linker102 (9%)	linker108 (21%)	linker103 (13%)	linker91 (25%)
linker108 (21%)	linker108 (29%)	linker91 (30%)	linker99 (13%)	linker92 (25%)

Worst 3D Materials				
amide	amine	carbon-carbon	imine	mixed
linker83 (2%)	linker22 (4%)	linker100 (8%)	linker62 (2%)	linker91 (3%)
linker88 (2%)	linker98 (4%)	linker92 (8%)	linker64 (2%)	linker93 (5%)
linker102 (4%)	linker102 (6%)	linker91 (9%)	linker89 (2%)	linker96 (9%)
linker103 (4%)	linker103 (16%)	linker105 (10%)	linker108 (19%)	linker94 (14%)
linker97 (45%)	linker110 (16%)	linker110 (13%)	linker97 (31%)	linker95 (62%)

Table 4.9: Top five most common linkers in the best and worst fifty 3D materials by bond type (percentage of top fifty 3D materials containing linker in parentheses).

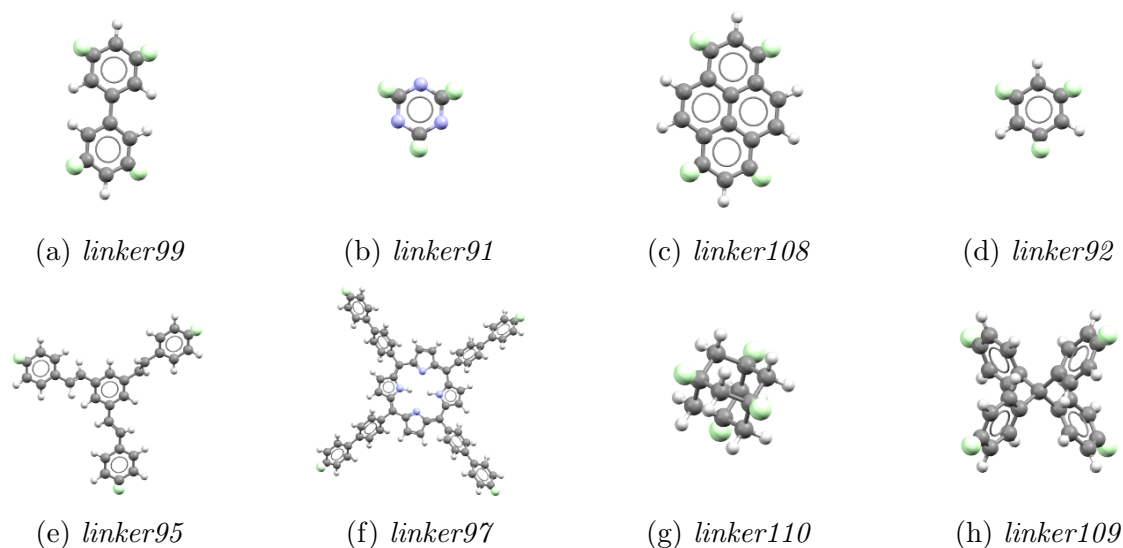


Figure 4.18: Examples of linkers frequently observed in the best performing (top row) and worst performing (bottom row) materials. Key: gray - carbon, light blue - nitrogen, white - hydrogen, light green - linkage sites.

Performance by Linker

If we analyze the performance of the 2D structures for ANG storage based on the linkers which make up the structures, we find that *linker91* and *linker99* (Figure 4.18) are the two most predominant linkers, appearing in 17% and 16% of the top fifty 2D structures. In fact, *linker99* appears in 32% of the top fifty 2D amide bonded structures and 47% of the top fifty 2D amine bonded structures, whereas *linker91* appears in 25% of the top fifty 2D carbon-carbon bonded structures and 14% of the top fifty 2D mixed bond structures. For a complete breakdown of the most common linkers in each set of 2D structures, please see Table 4.8. We would like to draw attention to *linker91*, a triazine linker, because triazine frameworks have been previously reported in the literature and demonstrated large carbon dioxide uptakes. [103]

On the other hand, the linkers appearing in the worst fifty 2D structures for ANG storage are *linker95* and *linker109* (31% and 11%; Figure 4.18). *linker95* stands out from the others in that it is a very large and extended molecule, and structures containing this linker tend to have very low densities. It frequently appears in the worst performing structures from each set (Table 4.8), as do porphyrin-based linkers such as *linker97* and *linker98*.

Analyzing the 3D structures, we see that *linker91* also has a strong presence in the best fifty overall 3D materials (35%). Moreover, we find that *linker108* (Figure 4.18), a pyrene linker, is present in 21% of the top fifty 3D materials. For a complete breakdown of the most frequently appearing linkers in each set of 3D structures, please see Table 4.9.

In the worst performing 3D materials we find *linker95* again, which is especially present in the worst fifty 3D mixed bond structures. Another notable linker which frequently appears

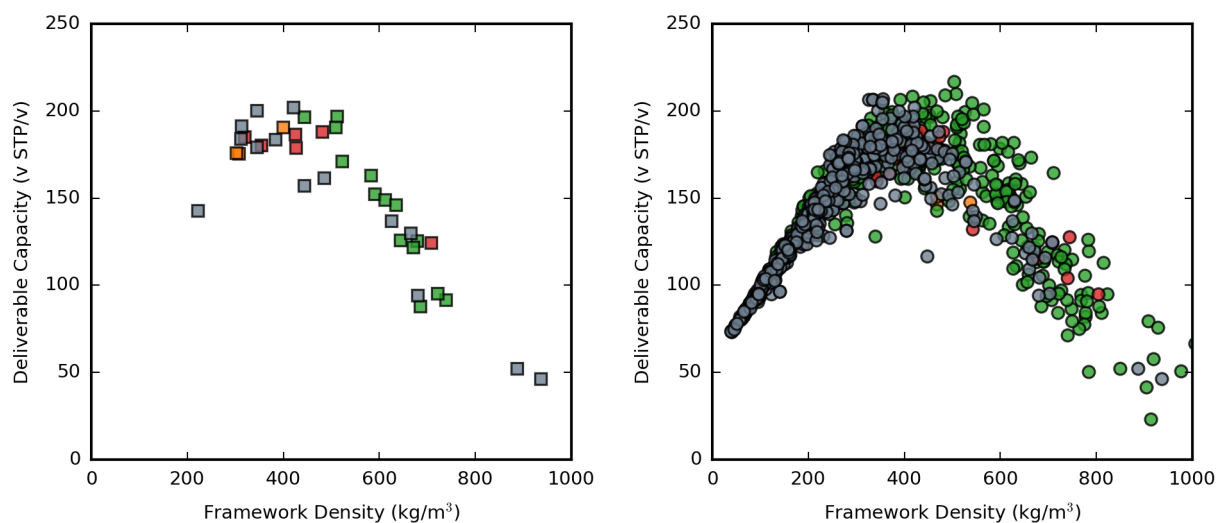


Figure 4.19: DCs of all the structures containing the same linkers as those found in the best performing 2D framework (left; *linker108* and *linker91*) and 3D framework (right; *linker91* only) in this work. Color key: red=amine, orange=imine, green=C-C, grey=mixed.

is *linker110* (Figure 4.18), an adamantane-based linker. It is particularly interesting that this linker appears in many of the worst performing 3D structures because Martin *et al.* [145] found it was a key component in two of the best 65-bar DC materials from their database. In a similar contradiction, *linker108* is also frequently observed in both the worst and best performing 3D structures (Table 4.9). Figure 4.19 illustrates how some of the linkers found in the best performing structures can be simultaneously found in bad methane storage materials; in other words, having a certain linker in a material is not a sufficient condition for good methane storage performance.

Best Performing Structures

The best 2D structure for ANG storage from the database is the mixed bond structure *linker108_CH_linker91_N_bex* (Figure 4.20). This structure has a density of 421.3 kg/m³ and a calculated DC of 202.2 v STP/v, which is remarkable for a 2D-layered material.

The first thing to note is that of the top ten 2D materials for ANG storage, none of the structures are amide, amine, or imine bonded frameworks, leading one to naively conclude that the carbon-carbon bonded structures are objectively better for ANG storage. However, there are two to four times as many carbon-carbon bonded structures in the database as any other type of bond, so what is more likely is that the chemical space is simply being sampled better by this set of structures.

Consequently, the 3D structure with the largest predicted DC is the carbon-carbon bonded structure *linker91_C_linker91_C_tbd*. This structure has a density of 503.1 kg/m³

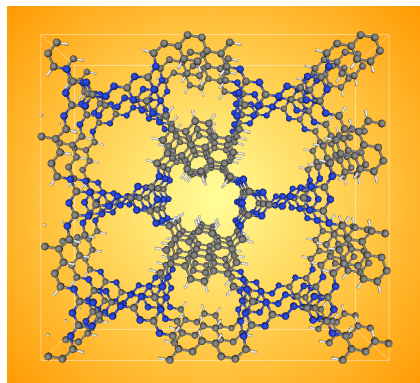


Figure 4.20: Snapshot of the best 2D ANG storage framework from the database, *linker108_CH_linker91_N_bex*, taken looking down the crystallographic *c*-axis.

and a DC of 216.8 v STP/v. Unsurprisingly, all of the top ten 3D structures have DCs greater than the best 2D-layered structure. The top four 3D structures are illustrated in Figure 4.21.

Although there are no amide, amine, and imine bonded structures present in the top ten ANG storage materials, there were many frameworks from these sets of structures with large DCs rivaling the top performing materials in the literature reported to this date. We would like to encourage experimental chemists to synthesize these materials, and as such have included extended lists of the top ANG storage materials from the database in the Appendix.

Worst Performing Structures

While it is valuable to understand what makes materials good for ANG storage applications, it can also be instrumental to understand what properties unite the worst performing structures; this way, experimentalists can avoid these if their aim is to synthesize only top ANG storage materials.

Among the worst performing 2D structures, the most commonly observed net is **hca**, as previously mentioned. The worst performing 3D structures were generally all very low or high density structures, such that they either had too much methane adsorbed at the depletion pressure, or they could not attain a sufficiently high methane uptake at the storage pressure. Among the worst overall ten materials, we find that all the frameworks are carbon-carbon bonded, and the majority are in the **sql** topology. The carbon-carbon bonded structures in the database span the widest range of performances, evidenced by most of the worst *and* best structures being carbon-carbon bonded. Lists of the worst ten frameworks from each set of 2D and 3D structures can be found in the Appendix.

As an illustration, snapshots of the worst two 2D-layered frameworks for ANG storage are shown in Figure 4.22, and snapshots of the worst four 3D structures are shown in Figure

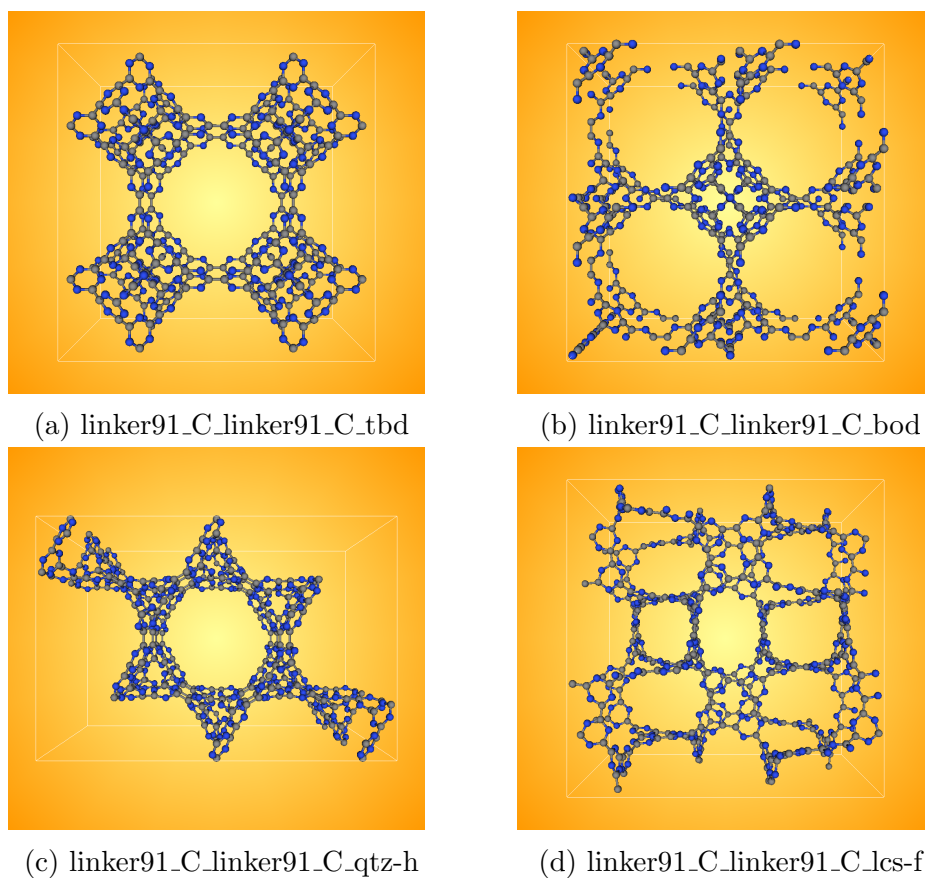


Figure 4.21: Snapshots of the top four 3D structures for ANG storage applications from the database. All snapshots are taken looking down the crystallographic c -axis of each structure.

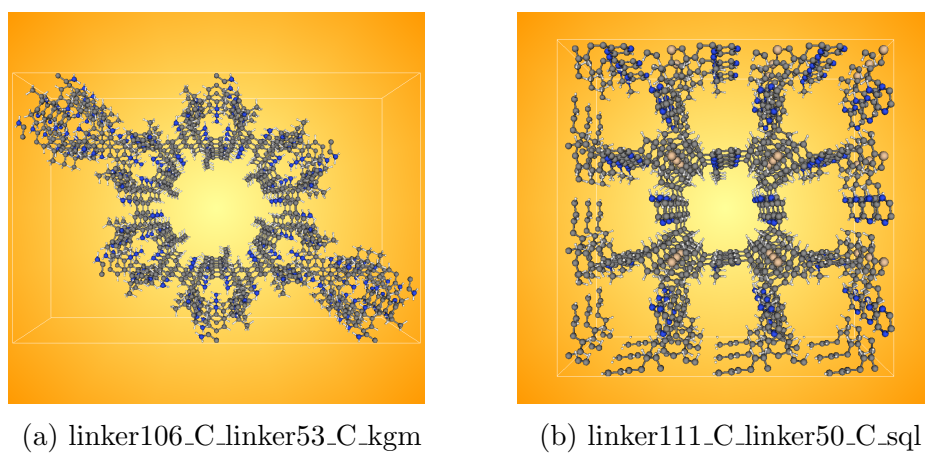


Figure 4.22: Snapshots of the worst two 2D-layered structures for ANG storage applications from the database. All snapshots are taken looking down the crystallographic c -axis of each structure.

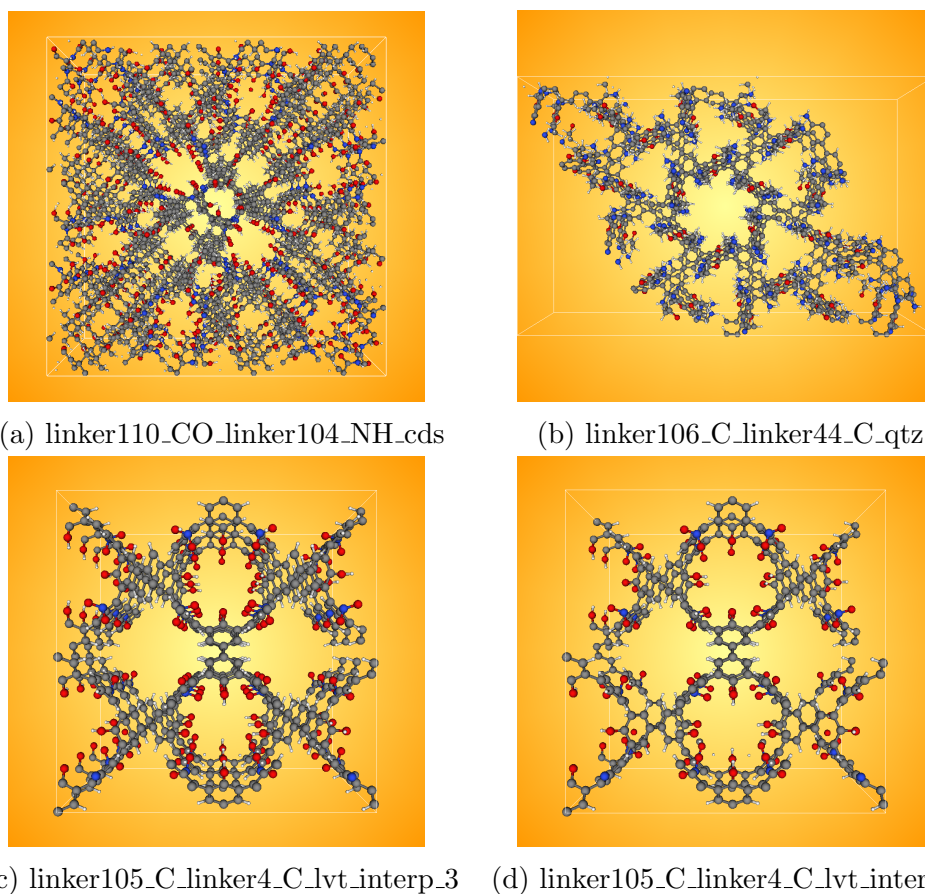


Figure 4.23: Snapshots of the worst four 3D structures for ANG storage applications from the database. All snapshots are taken looking down the crystallographic c -axis of each structure.

4.23. One thing that stands out is how relatively rough are the surfaces of these materials when compared to the surfaces of the best structures.

Structures Formed from Most Commonly Observed Nets

According to the symmetry hypothesis, there are a small number of structures which are expected to be formed during syntheses, these being the most symmetric structures.[224] Because these structures are more likely to be easily synthesized, we consider the performance of the top performing structures assembled from the most common topologies in COFs.

In the case of triangular and tetrahedral building blocks, which are *linker91* through *linker96* and *linker109* through *linker111*, respectively, the most commonly observed nets in the literature are the **ctn** and **bor** topologies. The top performing materials for ANG storage in the database assembled from the **ctn** topology are *linker111_C_linker91_C_ctn*, *linker111_C_linker92_C_ctn*, and *linker110_C_linker94_C_ctn*; all three structures have 65-bar DCs greater than 190 v STP/v. From the **bor** topology they are *linker111_C_linker92_C_bor*,

linker109_C_linker92_C_bor, and *linker103_N_linker92_CH_bor*, and all three of these structures have 65-bar DCs greater than 188 v STP/v.

On the other hand, the **dia** and **pts** nets are frequently observed for structures assembled from tetrahedral and linear building blocks. The top performing ANG storage materials in the database assembled from the **dia** net are *linker108_C_linker81_C_dia*, *linker108_C_linker87_C_dia*, and *linker108_C_linker58_C_dia*; all three structures have 65-bar DCs greater than 198 v STP/v. The top performing materials assembled from the **pts** net are

linker100_N_linker103_CH_pts, *linker103_CH_linker100_N_pts*, and *linker101_N_linker107_CH_pts*; all three of these structures have 65-bar DCs greater than 195 v STP/v.

In 2D structures assembled from trigonal and linear building blocks, the **hcb** net is frequently observed experimentally. [65] The best materials built from this net are *linker91_C_linker81_C_hcb*, *linker91_C_linker41_C_hcb*, and *linker91_C_linker85_C_hcb*, which all have 65-bar DCs greater than 188 v STP/v.

Conclusion

We created a database of over 69,000 novel COF structures and studied their suitability for ANG storage in a high-throughput manner. In doing so, we have provided examples of likely top performing materials with four different types of chemistries; of these structures, 304 structures have a calculated 65-bar DC of over 190 v STP/v, and 34 of these have a calculated 65-bar DC of over 200 v STP/v. We found that the set of carbon-carbon bonded 3D structures has the largest percentage of promising structures, so if crystalline materials can be synthesized with carbon-carbon bonds linking organic building units, this will open the way to many high-performing ANG storage materials. This is likely due to the shorter carbon-carbon bond, which endows a given carbon-carbon bonded structure with a slightly higher density than in its amide, amine, and imine bonded counterparts; thus, a larger percentage of carbon-carbon bonded structures have optimal ANG storage densities. This bodes well for researchers actively working on synthesizing fully crystalline carbon-carbon bonded COFs. The best structure in the database is predicted to be *linker91_C_linker91_C_tbd*, a structure composed of carbon-carbon bonded triazine linkers in the **tbd** topology. This structure has a framework density of 503.1 kg/m³ and a predicted DC of 216.8 v STP/v, higher than the current best ANG storage MOF. In addition, we have identified many high-performing imine, amide, and amine bonded frameworks; these are more readily synthesized using existing methods.

COF-300 and TAPB-PDA COF are the only two known structures in the database which have been experimentally reported. COF-300 is assembled from *linker109_N* and *linker87_CH*, and there exist 24 non-interpenetrated structures in the database assembled from these two linkers in various topologies (46 including interpenetrated structures). TAPB-PDA COF is assembled from *linker96_N* and *linker87_CH*, and there are three total structures in the database made from this combination of linkers. Regarding the stability of the

structures, in the case of COF-300 it is suspected that the **dia-c5** topology is attainable, and in the case of TAPB-PDA COF the **hcb** topology is the one that has been experimentally reported. However, this does not mean that other topologies are not attainable for the combination of linkers used to make the above structures, as different synthetic conditions could in theory yield to different topologies using crystal engineering techniques. As discussed in the section *Database Cleaning*, we have removed *a priori* a number of structures which were chemically unreasonable, meaning that from the computational point of view there is no reason to assume that any of the 69,840 structures in the database should not be synthesizable. Of course, synthesizability is not limited to thermodynamic considerations, but also to kinetics, and it is now the topic of ongoing work to determine the relative free energies of formation of the structures in the database using higher levels of theory.

In addition to building many promising new structures, we have analyzed the performance of the different frameworks by topology and linker in the hopes of providing guidance to synthetic chemists attempting to synthesize these or other high-performing COFs for ANG storage applications. We found that the 3D set of carbon-carbon bonded structures had the largest percentage of promising ANG storage materials, but also that extended aromatic linkers such as triazine- and pyrene-based linkers tended to be present in many of the best ANG storage structures. In the amide, amine, and imine bonded structures, the **qzd**, **pth**, and **pts** nets tended to be the most frequently occurring in top performing ANG materials, whereas in the best carbon-carbon bonded structures, the most common nets were **ukk**, **uon**, and **dia**. The **sql** net was interesting in that it was observed in the majority of the best performing carbon-nitrogen bonded structures, but also in the majority of the worst carbon-carbon bonded structures. This phenomenon is attributed to the longer length of the C–N bond as compared to the C–C bond, which means the optimal ANG storage densities of the C–N bonded structures are shifted to sub-optimal values when the C–N bonds are replaced with carbon-carbon bonds.

Here we provide a recipe of properties that would endow a material with superior ANG storage performance: a framework density near 400 kg/m³, a largest free sphere diameter of approximately 9 Å, a largest included sphere diameter of approximately 12 Å, and a geometric surface area between 4000 – 6000 m²/g. However, knowing what combination of linkers, bonds, and topology would result in a material with these properties *a priori* is a challenging task. Computational studies like this one are thus paramount for narrowing down the chemical space of potential structures to focus investigations on through high-throughput virtual screenings.

Despite our analysis, it is impossible to anticipate what every research group would find most relevant, so we have made the structures and all their properties (including surface areas, densities, pore volumes, chemical formulas, linkers, topological nets, and much more) available on the Materials Cloud platform so that individual researchers can filter for the properties they find most important. [150] For example, if the set of properties discussed above is not ideal for a researcher hoping to synthesize and test a new structure, then they can use the Materials Cloud to filter for specific framework properties, view the structures online, or even download the entire dataset. With this in mind, the diverse nature of the database

structures leads us to anticipate that there also exist high-performing materials for other gas separation and storage applications in the database (e.g. carbon capture, hydrogen storage, or noble gas separations). For instance, we hypothesize that the amine bonded COFs designed herein will have promising applications in carbon capture applications due to the potential for chemisorption of carbon dioxide at amine sites inside the frameworks. In addition, as the materials are entirely aromatic, there may also be structures with promising semiconductor properties lurking in the database, as has been previously shown in iron-intercalated COFs. [174] We leave the study of structures in the database for these promising applications for future work.

Additional Information in Appendix

Details on the *in silico* bond forming procedure. Details on the structural relaxations. Details on removing poorly converged structures from database. Details on linkers in library. Additional comparison to experimentally synthesized examples. Additional GCMC results. GCMC simulation error. List of topological nets used in framework assembly. Lists of top ten frameworks for each bond type. Complete list of frameworks with DCs greater than 190 v STP/v. Lists of the worst 2D and 3D structures. Sample adsorption isotherms. Estimate of computational time used at each step of structure assembly process. ARPA-E MOVE Program ANG Storage Target.

Database Available on the Materials Cloud

All of the COF structures and their properties reported in this work are available on the Materials Cloud platform at <https://doi.org/10.24435/materialscloud:2018.0003/v2>.

Chapter 5

Summary and Future Outlook

For my dissertation, I have applied various advanced computational chemistry methods to the investigation of nanoporous materials for gas adsorption applications. First, in Chapter 2, I dove into the development of a classical DFT-derived force field for more accurate simulations in MOFs with coordinatively unsaturated metal sites. In Chapter 3, I showed how this force field could be used to study the diffusion of carbon dioxide and methane in $M_2(\text{dobdc})$; therein, my coworkers and I investigated the diffusion of these gases at low-pressures (pressures which were not accessible experimentally for the experiments performed) through MD simulations, and then used simulations at experimentally-accessible conditions to explain the observed phenomena. Finally, in Chapter 4, I dove into the construction of hypothetical materials *in silico* – first to help characterize the unsolvable structure of a new synthesized material, COP-5, and then to assemble a database of tens of thousands of new COFs.

As an outlook, I believe that these methods will continue to be successfully used to study adsorption in nanoporous materials for decades to come. Although higher levels of theory can be used to study a given material in greater detail and with potentially greater accuracy, the sheer low computational cost of these classical molecular simulation methods allows us to run computer simulations in nanoporous materials on timescales that are far above and beyond what is currently accessible through *ab initio* methods. Nonetheless, it is important to balance the lower computational cost with the potentially disastrous accuracy in some cases, such as with the use of generic force fields for modeling gas adsorption in materials with coordinatively unsaturated metal sites. In such cases, the parameterization of a new model may be necessary, but it is worth it if the thermodynamic properties that one wishes to study are essential to understanding whether a material can be effectively implemented in a given application, as we have done here.

Appendix A

List of Abbreviations

CMP = conjugated microporous polymer
COF = covalent organic framework
COP = covalent organic polymer
MOF = metal-organic framework
PAF = porous aromatic framework
PIM = polymer of intrinsic microporosity
PPN = porous polymer network
ZIF = zeolitic imidazolate framework
cod = 1,5-cyclooctadiene
TBA = tris(4-bromophenyl)amine
TBB = 1,3,5-tris(4-bromophenyl)benzene
TBEB = 1,3,5-tris((4-bromophenyl)ethynyl)benzene
TBT = 2,4,6-tris-(4-bromo-phenyl)-[1,3,5]triazine
TBBPP = and 5,10,15,20-terakis-(4'-bromo-biphenyl-4-yl)-porphyrin
DB = 1,4-dibromobenzene
2DB = 4,4'-dibromobiphenyl
DA = 9,10-dibromo-anthracene
2,6-DN = 2,6-dibromo-naphthalene
DN = 1,4-dibromonaphthalene
DBQ = 5,8-dibromoquinoxaline
XTBB = 1,3,5-tribromobenzene
DB-NO₂ = 1,4-dibromo-2-nitrobenzene
DB-NH₂ = 2,5-dibromoaniline
DB-CH₃ = 2,5-di-bromotoluene
DB-SO₂Cl = 2,5-dibromobenzene sulfonyl chloride
DB-OH = 2,5-dibromohydroquinone

Appendix B

Additional Information for Force Field Development from Periodic DFT Calculations

Atom Type	Mg	Mn	Fe	Co	Ni	Zn
M	1.560	1.343	1.288	1.189	1.298	1.209
O _a	-0.899	-0.754	-0.753	-0.720	-0.789	-0.719
O _b	-0.752	-0.717	-0.707	-0.673	-0.696	-0.671
O _c	-0.903	-0.806	-0.794	-0.725	-0.785	-0.740
C _a	0.900	0.850	0.870	0.846	0.895	0.841
C _b	-0.314	-0.296	-0.337	-0.308	-0.349	-0.298
C _c	0.456	0.396	0.432	0.391	0.418	0.376
C _d	-0.234	-0.203	-0.195	-0.177	-0.173	-0.170
H	0.186	0.187	0.196	0.177	0.181	0.172

Table B.1: Atomic charges (e) of the framework atoms in $M_2(\text{dobdc})$.

Atom Type	Mg	Mn	Fe	Co	Ni	Zn
M	1.3202	1.3813	1.3037	1.2715	1.2863	0.9189
O _a	-0.7209	-0.7232	-0.7343	-0.7290	-0.7314	-0.6882
O _b	-0.7222	-0.7291	-0.7259	-0.7231	-0.7201	-0.7069
O _c	-0.7171	-0.7260	-0.7285	-0.7222	-0.7196	-0.6836
C _a	0.8393	0.8231	0.8216	0.8391	0.8335	1.0511
C _b	-0.1249	-0.1217	-0.1106	-0.1164	-0.1163	-0.1698
C _c	0.4713	0.4568	0.4679	0.4827	0.4496	0.6160
C _d	-0.2002	-0.2064	-0.1913	-0.1917	-0.1854	-0.1909
H	0.1267	0.1266	0.1303	0.1297	0.1302	0.1350

Table B.2: Atomic charges (e) of the framework atoms in M₂(dobpdc).

Atom Type	Charge
O(CO ₂) ^a	-0.3256
C(CO ₂) ^a	0.6512
O(H ₂ O) ^b	0.0
H(H ₂ O) ^b	0.52422
M(H ₂ O) ^b	-1.04844
C(CH ₄) ^c	0.0
H(CH ₄) ^c	-
N(N ₂) ^c	-0.482
NCOM(N ₂) ^c	0.964

Table B.3: Atomic charges (e) of the guest molecules. ^aEPM2; ^bTIP4P-Ew; ^cTraPPE.

Atom Type	ϵ (K)	σ (Å)
Mg ^a	55.919	2.691
Mn ^a	6.54912	2.63795
Fe ^a	6.54912	2.59430
Co ^a	7.05290	2.55866
Ni ^a	7.55668	2.52481
Zn ^a	62.46851	2.46155
O _a , O _b , O _c ^a	30.2267	3.118145
C _a , C _b , C _c , C _d ^a	52.8734	3.430851
H ^a	22.1662	2.571134
O(CO ₂) ^b	80.507	3.033
C(CO ₂) ^b	28.129	2.757
O(H ₂ O) ^c	81.9	3.1643
H(H ₂ O) ^c	22.1662	2.571134
M(H ₂ O) ^c	-	-
C(CH ₄) ^d	148.0	3.73
H(CH ₄) ^d	-	-
N(N ₂) ^d	36.0	3.31
N _{COM} (N ₂) ^d	-	-

Table B.4: Lennard-Jones parameters for guest molecules and framework atoms. ^aUFF; ^bEPM2; ^cTIP4P-Ew; ^dTraPPE.

Atom 1	Atom 2	A_{ij} (K)	B_{ij} (\AA^{-1})	C_{ij} ($\text{K}\text{\AA}^6$)
Mg	O(CO ₂)	2.47320E7	3.965	4.08795E5
O _a	O(CO ₂)	3.3788254669E7	3.805	1.4313206634E5
O _b	O(CO ₂)	2.6778651722E7	3.78	1.4313206634E5
O _c	O(CO ₂)	2.634324168E7	3.705	1.4313206634E5
C _a	O(CO ₂)	2.765001156E7	3.840	2.2631166802E5
C _b	O(CO ₂)	2.1483617388E7	3.515	2.2631166802E5
C _c	O(CO ₂)	2.992168789E7	3.84	2.2631166802E5
C _d	O(CO ₂)	1.314693952E7	3.315	2.2631166802E5
Atom 1	Atom 2	ε (K)	σ (\AA)	
H	O(CO ₂)	56.900	2.343	
Mg	C(CO ₂)	190.6212	2.816	
O _a	C(CO ₂)	69.958	2.794	
O _b	C(CO ₂)	69.958	2.794	
O _c	C(CO ₂)	69.958	2.794	
C _a	C(CO ₂)	87.738	2.904	
C _b	C(CO ₂)	87.738	2.904	
C _c	C(CO ₂)	87.738	2.904	
C _d	C(CO ₂)	87.738	2.904	
H	C(CO ₂)	68.317	2.453	

Table B.5: Derived force-field parameters of CO₂ inside Mg₂(dobdc). Three parameters (A_{ij} , B_{ij} , C_{ij}) with the units (K, \AA^{-1} , $\text{K}\text{\AA}^6$) are shown where the Buckingham potential is adopted. When the 12-6 Lennard-Jones potential is used, two parameters (ε , σ) are shown with the units (K, \AA).

Atom 1	Atom 2	A_{ij} (K)	B_{ij} (\AA^{-1})	C_{ij} ($\text{K}\text{\AA}^6$)
Fe	O(CO ₂)	0.9351191861E7	3.265	5.6221159595E5
O _a	O(CO ₂)	3.3788254669E7	3.805	1.4313206634E5
O _b	O(CO ₂)	2.6778651722E7	3.78	1.4313206634E5
O _c	O(CO ₂)	2.634324168E7	3.705	1.4313206634E5
C _a	O(CO ₂)	2.765001156E7	3.840	2.2631166802E5
C _b	O(CO ₂)	2.1483617388E7	3.515	2.2631166802E5
C _c	O(CO ₂)	2.992168789E7	3.84	2.2631166802E5
C _d	O(CO ₂)	1.314693952E7	3.315	2.2631166802E5
Atom 1	Atom 2	ϵ (K)	σ (\AA)	
H	O(CO ₂)	56.900	2.343	
Fe	C(CO ₂)	174.381	3.014	
O _a	C(CO ₂)	69.958	2.794	
O _b	C(CO ₂)	69.958	2.794	
O _c	C(CO ₂)	69.958	2.794	
C _a	C(CO ₂)	87.738	2.904	
C _b	C(CO ₂)	87.738	2.904	
C _c	C(CO ₂)	87.738	2.904	
C _d	C(CO ₂)	87.738	2.904	
H	C(CO ₂)	68.317	2.453	

Table B.6: Derived force-field parameters of CO₂ inside Fe₂(dobdc). Three parameters (A_{ij} , B_{ij} , C_{ij}) with the units (K, \AA^{-1} , $\text{K}\text{\AA}^6$) are shown where the Buckingham potential is adopted. When the 12-6 Lennard-Jones potential is used, two parameters (ϵ , σ) are shown with the units (K, \AA).

Atom 1	Atom 2	A_{ij} (K)	B_{ij} (\AA^{-1})	C_{ij} ($\text{K}\text{\AA}^6$)
C _o	O(CO ₂)	1.5659103747E7	3.515	5.6221159595E5
O _a	O(CO ₂)	3.3788254669E7	3.805	1.4313206634E5
O _b	O(CO ₂)	2.6778651722E7	3.78	1.4313206634E5
O _c	O(CO ₂)	2.634324168E7	3.705	1.4313206634E5
C _a	O(CO ₂)	2.765001156E7	3.84	2.2631166802E5
C _b	O(CO ₂)	2.1483617388E7	3.515	2.2631166802E5
C _c	O(CO ₂)	2.992168789E7	3.84	2.2631166802E5
C _d	O(CO ₂)	1.314693952E7	3.315	2.2631166802E5
Atom 1	Atom 2	ε (K)	σ (\AA)	
H	O(CO ₂)	56.900	2.343	
C _o	C(CO ₂)	174.381	3.014	
O _a	C(CO ₂)	69.958	2.794	
O _b	C(CO ₂)	69.958	2.794	
O _c	C(CO ₂)	69.958	2.794	
C _a	C(CO ₂)	87.738	2.904	
C _b	C(CO ₂)	87.738	2.904	
C _c	C(CO ₂)	87.738	2.904	
C _d	C(CO ₂)	87.738	2.904	
H	C(CO ₂)	68.317	2.453	

Table B.7: Derived force-field parameters of CO₂ inside Co₂(dobdc). Three parameters (A_{ij} , B_{ij} , C_{ij}) with the units (K, \AA^{-1} , $\text{K}\text{\AA}^6$) are shown where the Buckingham potential is adopted. When the 12-6 Lennard-Jones potential is used, two parameters (ε , σ) are shown with the units (K, \AA).

Atom 1	Atom 2	A_{ij} (K)	B_{ij} (\AA^{-1})	C_{ij} ($\text{K}\text{\AA}^6$)
Ni	O(CO ₂)	1.09926908E7	3.340	5.6221159595E5
O _a	O(CO ₂)	3.3788254669E7	3.805	1.4313206634E5
O _b	O(CO ₂)	2.6778651722E7	3.78	1.4313206634E5
O _c	O(CO ₂)	2.634324168E7	3.705	1.4313206634E5
C _a	O(CO ₂)	2.765001156E7	3.840	2.2631166802E5
C _b	O(CO ₂)	2.1483617388E7	3.515	2.2631166802E5
C _c	O(CO ₂)	2.992168789E7	3.84	2.2631166802E5
C _d	O(CO ₂)	1.314693952E7	3.315	2.2631166802E5
Atom 1	Atom 2	ϵ (K)	σ (\AA)	
H	O(CO ₂)	56.900	2.343	
Ni	C(CO ₂)	174.381	3.014	
O _a	C(CO ₂)	69.958	2.794	
O _b	C(CO ₂)	69.958	2.794	
O _c	C(CO ₂)	69.958	2.794	
C _a	C(CO ₂)	87.738	2.904	
C _b	C(CO ₂)	87.738	2.904	
C _c	C(CO ₂)	87.738	2.904	
C _d	C(CO ₂)	87.738	2.904	
H	C(CO ₂)	68.317	2.453	

Table B.8: Derived force-field parameters of CO₂ inside Ni₂(dobdc). Three parameters (A_{ij} , B_{ij} , C_{ij}) with the units (K, \AA^{-1} , $\text{K}\text{\AA}^6$) are shown where the Buckingham potential is adopted. When the 12-6 Lennard-Jones potential is used, two parameters (ϵ , σ) are shown with the units (K, \AA).

Atom 1	Atom 2	A_{ij} (K)	B_{ij} (\AA^{-1})	C_{ij} ($\text{K}\text{\AA}^6$)
Zn	O(CO ₂)	6.87804E6	3.065	5.62211E5
O _a	O(CO ₂)	3.3788254669E7	3.805	1.4313206634E5
O _b	O(CO ₂)	2.6778651722E7	3.78	1.4313206634E5
O _c	O(CO ₂)	2.634324168E7	3.705	1.4313206634E5
C _a	O(CO ₂)	2.765001156E7	3.840	2.2631166802E5
C _b	O(CO ₂)	2.1483617388E7	3.515	2.2631166802E5
C _c	O(CO ₂)	2.992168789E7	3.84	2.2631166802E5
C _d	O(CO ₂)	1.314693952E7	3.315	2.2631166802E5
Atom 1	Atom 2	ϵ (K)	σ (\AA)	
H	O(CO ₂)	56.900	2.343	
Zn	C(CO ₂)	174.381	3.014	
O _a	C(CO ₂)	69.958	2.794	
O _b	C(CO ₂)	69.958	2.794	
O _c	C(CO ₂)	69.958	2.794	
C _a	C(CO ₂)	87.738	2.904	
C _b	C(CO ₂)	87.738	2.904	
C _c	C(CO ₂)	87.738	2.904	
C _d	C(CO ₂)	87.738	2.904	
H	C(CO ₂)	68.317	2.453	

Table B.9: Derived force-field parameters of CO₂ inside Zn₂(dobdc). Three parameters (A_{ij} , B_{ij} , C_{ij}) with the units (K, \AA^{-1} , $\text{K}\text{\AA}^6$) are shown where the Buckingham potential is adopted. When the 12-6 Lennard-Jones potential is used, two parameters (ϵ , σ) are shown with the units (K, \AA).

Atom 1	Atom 2	A_{ij} (K)	B_{ij} (\AA^{-1})	C_{ij} ($\text{K}\text{\AA}^6$)
Mg	O(H ₂ O)	2.1931100E7	3.945	1.70117E5
O _a	O(H ₂ O)	*	*	*
O _b	O(H ₂ O)	3.49219254E7	3.873333333	1.912564E5
O _c	O(H ₂ O)	1.596628636E7	3.39	1.912564E5
C _a	O(H ₂ O)	2.508447536E7	3.735	3.382927333E5
C _b	O(H ₂ O)	1.815318598E7	3.351666667	3.382927333E7
C _c	O(H ₂ O)	1.196513109E8	4.385	3.382927333E5
C _d	O(H ₂ O)	5.841036937E6	3.035	3.382927333E5
H	O(H ₂ O)	*	*	*
Mg	H(H ₂ O)	*	*	*
O _a	H(H ₂ O)	4.034918849E6	3.976666667	5.487547333E4
O _b	H(H ₂ O)	4.034918849E6	3.976666667	5.487547333E4
O _c	H(H ₂ O)	4.034918849E6	3.976666667	5.487547333E4
C _a	H(H ₂ O)	3.03027689E6	3.519166667	9.996881667E4
C _b	H(H ₂ O)	3.03027689E6	3.519166667	9.996881667E4
C _c	H(H ₂ O)	3.03027689E6	3.519166667	9.996881667E4
C _d	H(H ₂ O)	3.03027689E6	3.519166667	9.996881667E4
H	H(H ₂ O)	*	*	*

Table B.10: Derived force-field parameters of H₂O inside Mg₂(dobdc). Three parameters (A_{ij} , B_{ij} , C_{ij}) with the units (K, \AA^{-1} , $\text{K}\text{\AA}^6$) are shown where the Buckingham potential is adopted. Otherwise, the 12-6 Lennard-Jones potential is used. *Obtained directly from the Lorentz-Berthelot mixing rule with parameters given in Table B.4.

Atom 1	Atom 2	A_{ij} (K)	B_{ij} (\AA^{-1})	C_{ij} ($\text{K}\text{\AA}^6$)
Mn	O(H ₂ O)	5.144483425E7	4.255	5.523216479E4
O _a	O(H ₂ O)	*	*	*
O _b	O(H ₂ O)	3.49219254E7	3.873333333	1.912564E5
O _c	O(H ₂ O)	1.596628636E7	3.39	1.912564E5
C _a	O(H ₂ O)	2.508447536E7	3.735	3.382927333E5
C _b	O(H ₂ O)	1.815318598E7	3.351666667	3.382927333E5
C _c	O(H ₂ O)	1.196513109E8	4.385	3.382927333E5
C _d	O(H ₂ O)	5.841036937E6	3.035	3.382927333E5
H	O(H ₂ O)	*	*	*
Mn	H(H ₂ O)	*	*	*
O _a	H(H ₂ O)	4.034918849E6	3.976666667	5.487547333E4
O _b	H(H ₂ O)	4.034918849E6	3.976666667	5.487547333E4
O _c	H(H ₂ O)	4.034918849E6	3.976666667	5.487547333E4
C _a	H(H ₂ O)	3.03027689E6	3.519166667	9.996881667E4
C _b	H(H ₂ O)	3.03027689E6	3.519166667	9.996881667E4
C _c	H(H ₂ O)	3.03027689E6	3.519166667	9.996881667E4
C _d	H(H ₂ O)	3.03027689E6	3.519166667	9.996881667E4
H	H(H ₂ O)	*	*	*

Table B.11: Derived force-field parameters of H₂O inside Mn₂(dobdc). Three parameters (A_{ij} , B_{ij} , C_{ij}) with the units (K, \AA^{-1} , $\text{K}\text{\AA}^6$) are shown where the Buckingham potential is adopted. Otherwise, the 12-6 Lennard-Jones potential is used. *Obtained directly from the Lorentz-Berthelot mixing rule with parameters given in Table B.4.

Atom 1	Atom 2	A_{ij} (K)	B_{ij} (\AA^{-1})	C_{ij} ($\text{K}\text{\AA}^6$)
Fe	O(H ₂ O)	7.981137955E7	4.605	5.278553E4
O _a	O(H ₂ O)	*	*	*
O _b	O(H ₂ O)	3.49219254E7	3.873333333	1.912564E5
O _c	O(H ₂ O)	1.596628636E7	3.39	1.912564E5
C _a	O(H ₂ O)	2.508447536E7	3.735	3.382927333E5
C _b	O(H ₂ O)	1.815318598E7	3.351666667	3.382927333E5
C _c	O(H ₂ O)	1.196513109E8	4.385	3.382927333E5
C _d	O(H ₂ O)	5.841036937E6	3.035	3.382927333E5
H	O(H ₂ O)	*	*	*
Fe	H(H ₂ O)	*	*	*
O _a	H(H ₂ O)	4.034918849E6	3.976666667	5.487547333E4
O _b	H(H ₂ O)	4.034918849E6	3.976666667	5.487547333E4
O _c	H(H ₂ O)	4.034918849E6	3.976666667	5.487547333E4
C _a	H(H ₂ O)	3.03027689E6	3.519166667	9.996881667E4
C _b	H(H ₂ O)	3.03027689E6	3.519166667	9.996881667E4
C _c	H(H ₂ O)	3.03027689E6	3.519166667	9.996881667E4
C _d	H(H ₂ O)	3.03027689E6	3.519166667	9.996881667E4
H	H(H ₂ O)	*	*	*

Table B.12: Derived force-field parameters of H₂O inside Fe₂(dobdc). Three parameters (A_{ij} , B_{ij} , C_{ij}) with the units (K, \AA^{-1} , $\text{K}\text{\AA}^6$) are shown where the Buckingham potential is adopted. Otherwise, the 12-6 Lennard-Jones potential is used. *Obtained directly from the Lorentz-Berthelot mixing rule with parameters given in Table B.4.

Atom 1	Atom 2	A_{ij} (K)	B_{ij} (\AA^{-1})	C_{ij} ($\text{K}\text{\AA}^6$)
Co	O(H ₂ O)	6.87328111204921E7	4.605	5.277523E4
O _a	O(H ₂ O)	*	*	*
O _b	O(H ₂ O)	3.49219254E7	3.873333333	1.912564E5
O _c	O(H ₂ O)	1.596628636E7	3.39	1.912564E5
C _a	O(H ₂ O)	2.508447536E7	3.735	3.382927333E5
C _b	O(H ₂ O)	1.815318598E7	3.351666667	3.382927333E5
C _c	O(H ₂ O)	1.196513109E8	4.385	3.382927333E5
C _d	O(H ₂ O)	5.841036937E6	3.035	3.382927333E5
H	O(H ₂ O)	*	*	*
Co	H(H ₂ O)	*	*	*
O _a	H(H ₂ O)	4.034918849E6	3.976666667	5.487547333E4
O _b	H(H ₂ O)	4.034918849E6	3.976666667	5.487547333E4
O _c	H(H ₂ O)	4.034918849E6	3.976666667	5.487547333E4
C _a	H(H ₂ O)	3.03027689E6	3.519166667	9.996881667E4
C _b	H(H ₂ O)	3.03027689E6	3.519166667	9.996881667E4
C _c	H(H ₂ O)	3.03027689E6	3.519166667	9.996881667E4
C _d	H(H ₂ O)	3.03027689E6	3.519166667	9.996881667E4
H	H(H ₂ O)	*	*	*

Table B.13: Derived force-field parameters of H₂O inside Co₂(dobdc). Three parameters (A_{ij} , B_{ij} , C_{ij}) with the units (K, \AA^{-1} , $\text{K}\text{\AA}^6$) are shown where the Buckingham potential is adopted. Otherwise, the 12-6 Lennard-Jones potential is used. *Obtained directly from the Lorentz-Berthelot mixing rule with parameters given in Table B.4.

Atom 1	Atom 2	A_{ij} (K)	B_{ij} (\AA^{-1})	C_{ij} ($\text{K}\text{\AA}^6$)
Ni	O(H ₂ O)	9.77309858E7	4.85	5.271733776E4
O _a	O(H ₂ O)	*	*	*
O _b	O(H ₂ O)	3.49219254E7	3.873333333	1.912564E5
O _c	O(H ₂ O)	1.596628636E7	3.39	1.912564E5
C _a	O(H ₂ O)	2.508447536E7	3.735	3.382927333E5
C _b	O(H ₂ O)	1.815318598E7	3.351666667	3.382927333E5
C _c	O(H ₂ O)	1.196513109E8	4.385	3.382927333E5
C _d	O(H ₂ O)	5.841036937E6	3.035	3.382927333E5
H	O(H ₂ O)	*	*	*
Ni	H(H ₂ O)	*	*	*
O _a	H(H ₂ O)	4.034918849E6	3.976666667	5.487547333E4
O _b	H(H ₂ O)	4.034918849E6	3.976666667	5.487547333E4
O _c	H(H ₂ O)	4.034918849E6	3.976666667	5.487547333E4
C _a	H(H ₂ O)	3.03027689E6	3.519166667	9.996881667E4
C _b	H(H ₂ O)	3.03027689E6	3.519166667	9.996881667E4
C _c	H(H ₂ O)	3.03027689E6	3.519166667	9.996881667E4
C _d	H(H ₂ O)	3.03027689E6	3.519166667	9.996881667E4
H	H(H ₂ O)	*	*	*

Table B.14: Derived force-field parameters of H₂O inside Ni₂(dobdc). Three parameters (A_{ij} , B_{ij} , C_{ij}) with the units (K, \AA^{-1} , $\text{K}\text{\AA}^6$) are shown where the Buckingham potential is adopted. Otherwise, the 12-6 Lennard-Jones potential is used. *Obtained directly from the Lorentz-Berthelot mixing rule with parameters given in Table B.4.

Atom 1	Atom 2	A_{ij} (K)	B_{ij} (\AA^{-1})	C_{ij} ($\text{K}\text{\AA}^6$)
Zn	O(H ₂ O)	1.2592600E7	3.56	1.41379E5
O _a	O(H ₂ O)	*	*	*
O _b	O(H ₂ O)	3.49219254E7	3.873333333	1.912564E5
O _c	O(H ₂ O)	1.596628636E7	3.39	1.912564E5
C _a	O(H ₂ O)	2.508447536E7	3.735	3.382927333E5
C _b	O(H ₂ O)	1.815318598E7	3.351666667	3.382927333E5
C _c	O(H ₂ O)	1.196513109E8	4.385	3.382927333E5
C _d	O(H ₂ O)	5.841036937E6	3.035	3.382927333E5
H	O(H ₂ O)	*	*	*
Zn	H(H ₂ O)	*	*	*
O _a	H(H ₂ O)	4.034918849E6	3.976666667	5.487547333E4
O _b	H(H ₂ O)	4.034918849E6	3.976666667	5.487547333E4
O _c	H(H ₂ O)	4.034918849E6	3.976666667	5.487547333E4
C _a	H(H ₂ O)	3.03027689E6	3.519166667	9.996881667E4
C _b	H(H ₂ O)	3.03027689E6	3.519166667	9.996881667E4
C _c	H(H ₂ O)	3.03027689E6	3.519166667	9.996881667E4
C _d	H(H ₂ O)	3.03027689E6	3.519166667	9.996881667E4
H	H(H ₂ O)	*	*	*

Table B.15: Derived force-field parameters of H₂O inside Zn₂(dobdc). Three parameters (A_{ij} , B_{ij} , C_{ij}) with the units (K, \AA^{-1} , $\text{K}\text{\AA}^6$) are shown where the Buckingham potential is adopted. Otherwise, the 12-6 Lennard-Jones potential is used. *Obtained directly from the Lorentz-Berthelot mixing rule with parameters given in Table B.4.

Atom 1	Atom 2	A_{ij} (K)	B_{ij} (\AA^{-1})	C_{ij} ($\text{K}\text{\AA}^6$)
Mg	C(CH ₄)	2.53493890949595E8	4.915	4.37687550998677E5
O _a	C(CH ₄)	1.84274181646751E7	2.965	4.74764836775231E5
O _b	C(CH ₄)	2.02985676591117E7	3.265	4.74764836775231E5
O _c	C(CH ₄)	1.00698098255734E7	2.790	4.74764836775231E5
C _a	C(CH ₄)	7.6229282723786E7	3.995	8.19149364225640E5
C _b	C(CH ₄)	3.55134324787367E7	3.280	8.19149364225640E5
C _c	C(CH ₄)	2.31595395497581E8	4.370	8.19149364225640E5
C _d	C(CH ₄)	2.5593502565099E6	2.315	8.19149364225640E5
H	C(CH ₄)	*	*	*

Table B.16: Derived force-field parameters of CH₄ inside Mg₂(dobdc). Three parameters (A_{ij} , B_{ij} , C_{ij}) with the units (K, \AA^{-1} , $\text{K}\text{\AA}^6$) are shown where the Buckingham potential is adopted. Otherwise, the 12-6 Lennard-Jones potential is used. *Obtained directly from the Lorentz-Berthelot mixing rule with parameters given in Table B.4.

Atom 1	Atom 2	A_{ij} (K)	B_{ij} (\AA^{-1})	C_{ij} ($\text{K}\text{\AA}^6$)
Mn	C(CH ₄)	3.41630376603476E8	5.095	1.55889760298808E5
O _a	C(CH ₄)	5.04763091085359E7	3.260	5.17925276482070E5
O _b	C(CH ₄)	2.67404792326220E7	3.370	5.17925276482070E5
O _c	C(CH ₄)	1.18819828009600E7	2.900	5.17925276482070E5
C _a	C(CH ₄)	4.44960734333736E7	3.775	8.93617488246153E5
C _b	C(CH ₄)	2.04288832099980E7	3.070	8.93617488246153E5
C _c	C(CH ₄)	1.62070733259247E8	4.155	8.93617488246153E5
C _d	C(CH ₄)	2.75770705006260E6	2.340	8.93617488246153E5
H	C(CH ₄)	*	*	*

Table B.17: Derived force-field parameters of CH₄ inside Mn₂(dobdc). Three parameters (A_{ij} , B_{ij} , C_{ij}) with the units (K, \AA^{-1} , $\text{K}\text{\AA}^6$) are shown where the Buckingham potential is adopted. Otherwise, the 12-6 Lennard-Jones potential is used. *Obtained directly from the Lorentz-Berthelot mixing rule with parameters given in Table B.4.

Atom 1	Atom 2	A_{ij} (K)	B_{ij} (\AA^{-1})	C_{ij} ($\text{K}\text{\AA}^6$)
Fe	C(CH ₄)	4.05574587622367E8	5.220	1.36299701291943E5
O _a	C(CH ₄)	5.70958861989127E7	3.375	4.74764836775231E5
O _b	C(CH ₄)	2.98578963852476E7	3.445	4.74764836775231E5
O _c	C(CH ₄)	1.23644073529895E7	2.925	4.74764836775231E5
C _a	C(CH ₄)	3.82488656704762E7	3.635	8.19149364225640E5
C _b	C(CH ₄)	2.86296629441642E7	3.220	8.19149364225640E5
C _c	C(CH ₄)	1.61013997865697E8	4.160	8.19149364225640E5
C _d	C(CH ₄)	2.98037840853350E6	2.390	8.19149364225640E5
H	C(CH ₄)	*	*	*

Table B.18: Derived force-field parameters of CH₄ inside Fe₂(dobdc). Three parameters (A_{ij} , B_{ij} , C_{ij}) with the units (K, \AA^{-1} , $\text{K}\text{\AA}^6$) are shown where the Buckingham potential is adopted. Otherwise, the 12-6 Lennard-Jones potential is used. *Obtained directly from the Lorentz-Berthelot mixing rule with parameters given in Table B.4.

Atom 1	Atom 2	A_{ij} (K)	B_{ij} (\AA^{-1})	C_{ij} ($\text{K}\text{\AA}^6$)
Co	C(CH ₄)	1.78357917927342E9	6.185	1.75040015006866E5
O _a	C(CH ₄)	4.6031867655764E7	3.270	6.04246155895748E5
O _b	C(CH ₄)	1.252026689438E7	3.165	6.04246155895748E5
O _c	C(CH ₄)	1.0928739573964E7	2.750	6.04246155895748E5
C _a	C(CH ₄)	8.7508391893836E7	3.550	1.04255373628718E6
C _b	C(CH ₄)	4.93117782455E5	1.920	1.04255373628718E6
C _c	C(CH ₄)	2.5342449515063E8	4.215	1.04255373628718E6
C _d	C(CH ₄)	8.107270131198E6	2.615	1.04255373628718E6
H	C(CH ₄)	*	*	*

Table B.19: Derived force-field parameters of CH₄ inside Co₂(dobdc). Three parameters (A_{ij} , B_{ij} , C_{ij}) with the units (K, \AA^{-1} , $\text{K}\text{\AA}^6$) are shown where the Buckingham potential is adopted. Otherwise, the 12-6 Lennard-Jones potential is used. *Obtained directly from the Lorentz-Berthelot mixing rule with parameters given in Table B.4.

Atom 1	Atom 2	A_{ij} (K)	B_{ij} (\AA^{-1})	C_{ij} ($\text{K}\text{\AA}^6$)
Ni	C(CH ₄)	6.26384595148783E8	5.570	1.49531649092313E5
O _a	C(CH ₄)	7.05641182505456E7	3.485	5.1792527648207E5
O _b	C(CH ₄)	2.35754129502551E7	3.340	5.1792527648207E5
O _c	C(CH ₄)	1.11652872331501E7	2.895	5.1792527648207E5
C _a	C(CH ₄)	2.03351862897907E7	3.295	8.93617488246153E5
C _b	C(CH ₄)	2.03756494281288E7	3.095	8.93617488246153E5
C _c	C(CH ₄)	1.05755990417555E8	3.960	8.93617488246153E5
C _d	C(CH ₄)	2.8361875631197E6	2.330	8.93617488246153E5
H	C(CH ₄)	*	*	*

Table B.20: Derived force-field parameters of CH₄ inside Ni₂(dobdc). Three parameters (A_{ij} , B_{ij} , C_{ij}) with the units (K, \AA^{-1} , $\text{K}\text{\AA}^6$) are shown where the Buckingham potential is adopted. Otherwise, the 12-6 Lennard-Jones potential is used. *Obtained directly from the Lorentz-Berthelot mixing rule with parameters given in Table B.4.

Atom 1	Atom 2	A_{ij} (K)	B_{ij} (\AA^{-1})	C_{ij} ($\text{K}\text{\AA}^6$)
Zn	C(CH ₄)	7.10575752704405E7	4.140	3.37868002319772E5
O _a	C(CH ₄)	3.14694857681871E7	3.260	4.31604397068391E5
O _b	C(CH ₄)	2.47000874761906E7	3.385	4.31604397068391E5
O _c	C(CH ₄)	8.2587100593377E6	2.755	4.31604397068391E5
C _a	C(CH ₄)	5.44747086236311E7	3.765	7.44681240205128E5
C _b	C(CH ₄)	2.94697180743885E7	3.280	7.44681240205128E5
C _c	C(CH ₄)	1.52664987032116E8	4.050	7.44681240205128E5
C _d	C(CH ₄)	2.6974417891162E6	2.390	7.44681240205128E5
H	C(CH ₄)	*	*	*

Table B.21: Derived force-field parameters of CH₄ inside Zn₂(dobdc). Three parameters (A_{ij} , B_{ij} , C_{ij}) with the units (K, \AA^{-1} , $\text{K}\text{\AA}^6$) are shown where the Buckingham potential is adopted. Otherwise, the 12-6 Lennard-Jones potential is used. *Obtained directly from the Lorentz-Berthelot mixing rule with parameters given in Table B.4.

Parameter	Mn ₂ (dobdc)	Cu ₂ (dobdc)	Fe ₂ (dobdc)	Zn ₂ (dobdc)
$n_{sat,1}$ (mmol g ⁻¹)	7.5	6.3	7.0	7.6
S_1 (-R)	9.1	8.4	9.1	8.8
E_1 (kJ mol ⁻¹)	17.1	14.6	18.3	16.5
$n_{sat,2}$ (mmol g ⁻¹)	3.4	3.0	3.9	5.0
S_2 (-R)	9.5	9.0	8.8	10.9
E_2 (kJ mol ⁻¹)	12.0	10.4	13.3	12.2

Table B.22: Dual-site Langmuir parameters for experimental isotherm fits.

	CO ₂ (25, 40, 50 °C)	CH ₄ (25, 40, 50 °C)
$q_{sat,A}$		6.24
b_A		11.11
E_A		33.59
v_A		0.77
$q_{sat,B}$		39.79
b_B		11.57
E_b		18.99
v_B		1.23

Table B.23: Dual-site Langmuir-Freundlich parameters for Mg₂(dobpdc) experimental isotherm fits.

Framework	Pore Volume (cm ³ g ⁻¹)
Mn ₂ (dobdc)	0.63
Cu ₂ (dobdc)	0.54
Fe ₂ (dobdc)	0.53
Zn ₂ (dobdc)	0.45
Mg ₂ (dobpdc)	1.39

Table B.24: Pore volumes used in total adsorption calculations.

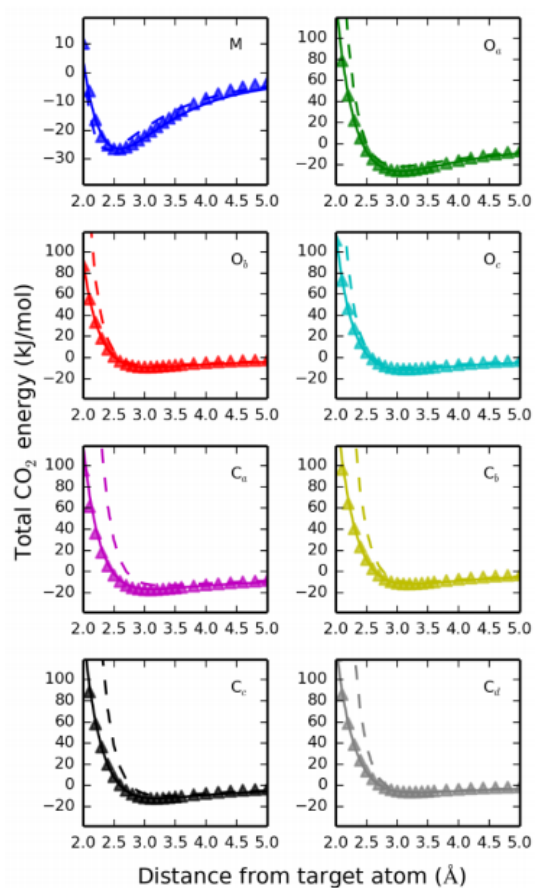


Figure B.1: Comparison of CO₂-framework interaction energies in Fe₂(dobdc) obtained from the DFT calculations (triangular markers), the DFT-derived force field (solid line), and the UFF force field (dashed line) along the various approaching paths.

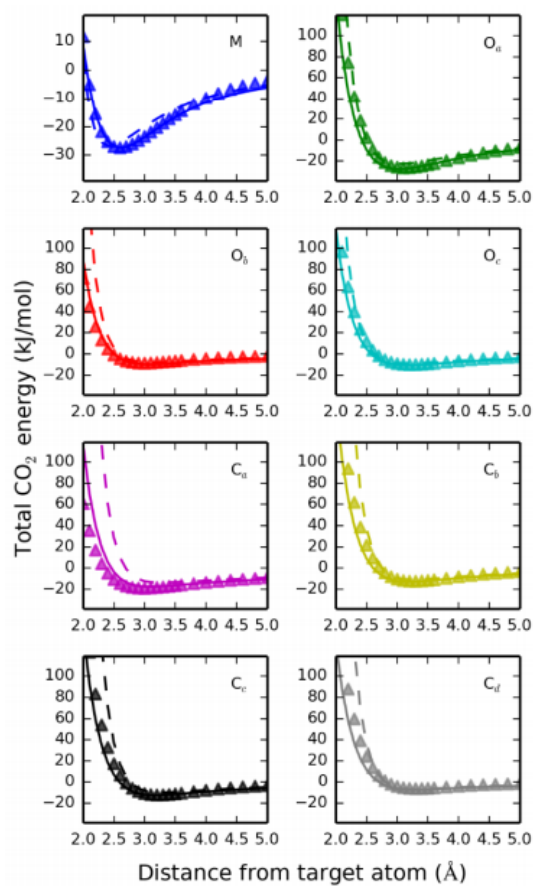


Figure B.2: Comparison of CO₂-framework interaction energies in Ni₂(dobdc) obtained from the DFT calculations (triangular markers), the DFT-derived force field (solid line), and the UFF force field (dashed line) along the various approaching paths.

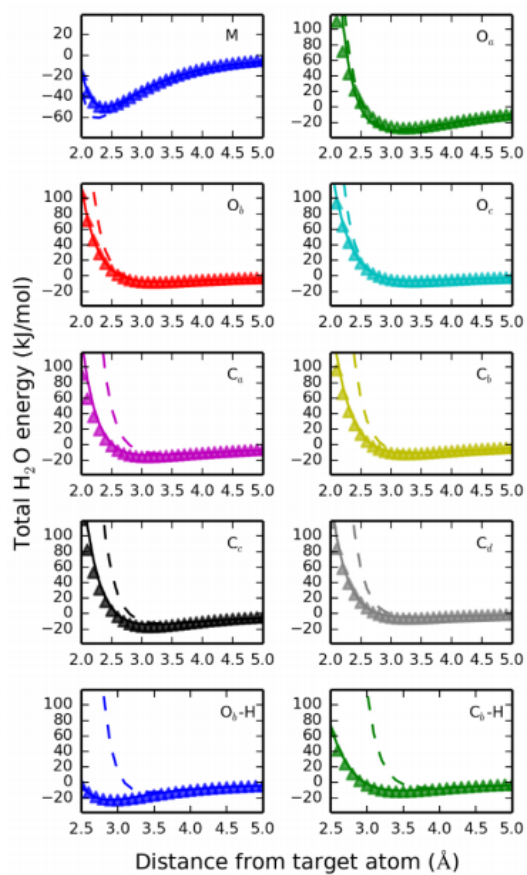


Figure B.3: Comparison of H₂O-framework interaction energies in Mn₂(dobdc) obtained from the DFT calculations (triangular markers), the DFT-derived force field (solid line), and the UFF force field (dashed line) along the various approaching paths.

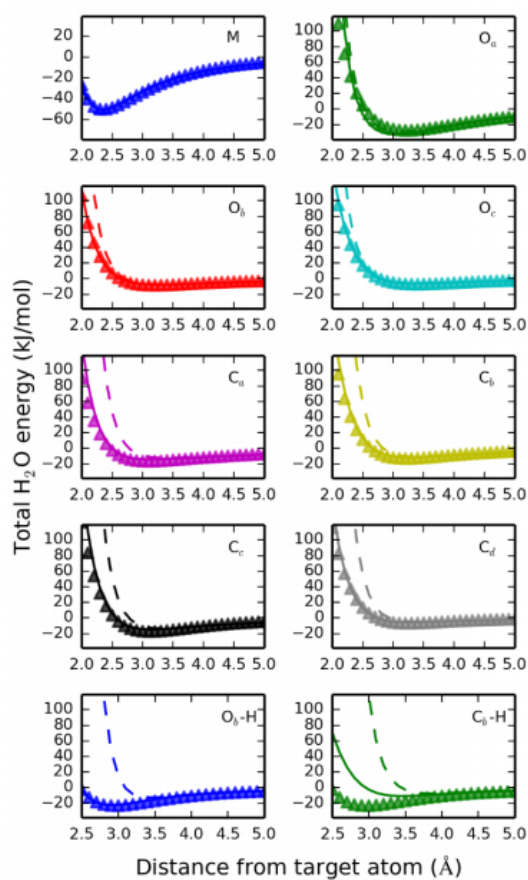


Figure B.4: Comparison of H₂O-framework interaction energies in Fe₂(dobdc) obtained from the DFT calculations (triangular markers), the DFT-derived force field (solid line), and the UFF force field (dashed line) along the various approaching paths.

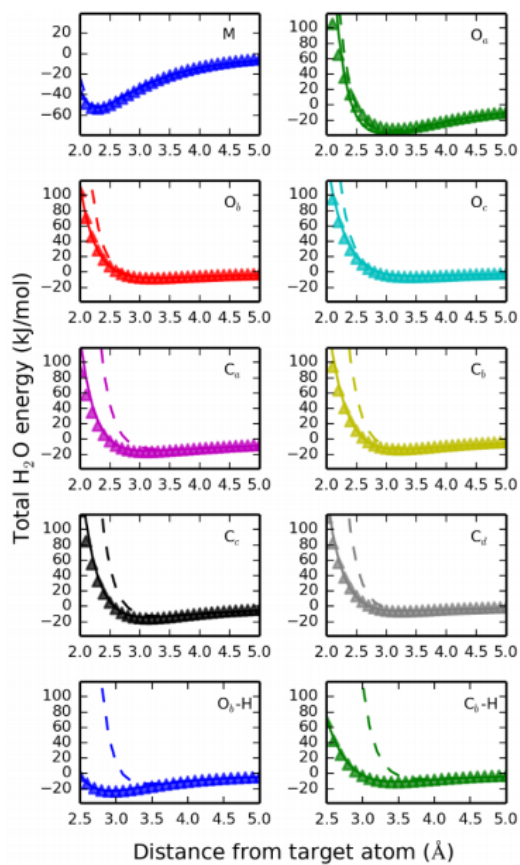


Figure B.5: Comparison of H₂O-framework interaction energies in Ni₂(dobdc) obtained from the DFT calculations (triangular markers), the DFT-derived force field (solid line), and the UFF force field (dashed line) along the various approaching paths.

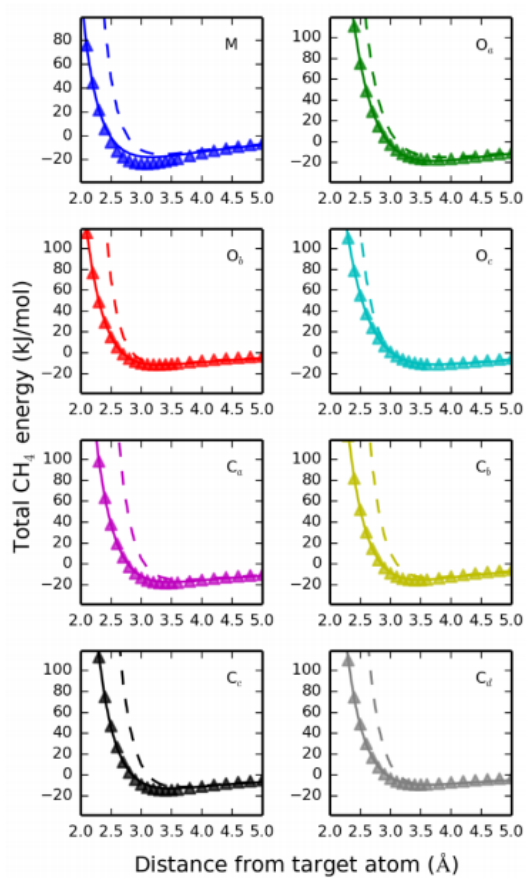


Figure B.6: Comparison of CH₄-framework interaction energies in Mg₂(dobdc) obtained from the DFT calculations (triangular markers), the DFT-derived force field (solid line), and the UFF force field (dashed line) along the various approaching paths.

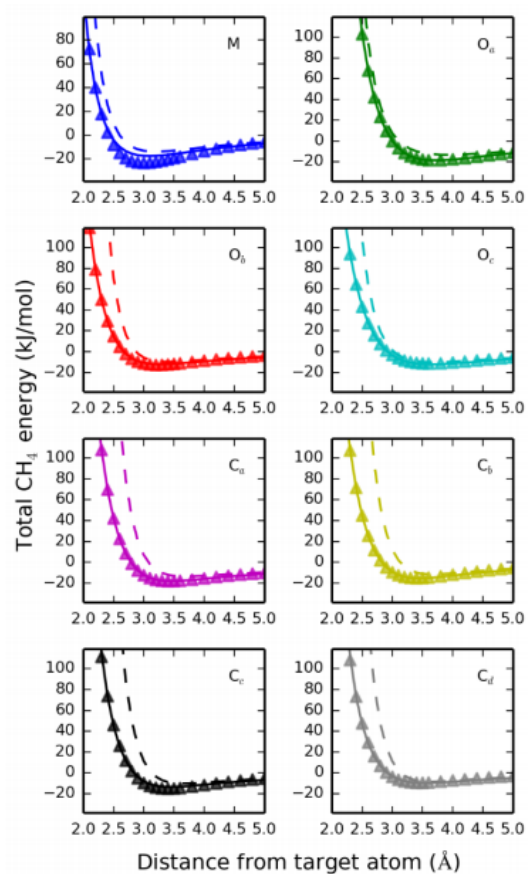


Figure B.7: Comparison of CH₄-framework interaction energies in Mn₂(dobdc) obtained from the DFT calculations (triangular markers), the DFT-derived force field (solid line), and the UFF force field (dashed line) along the various approaching paths.

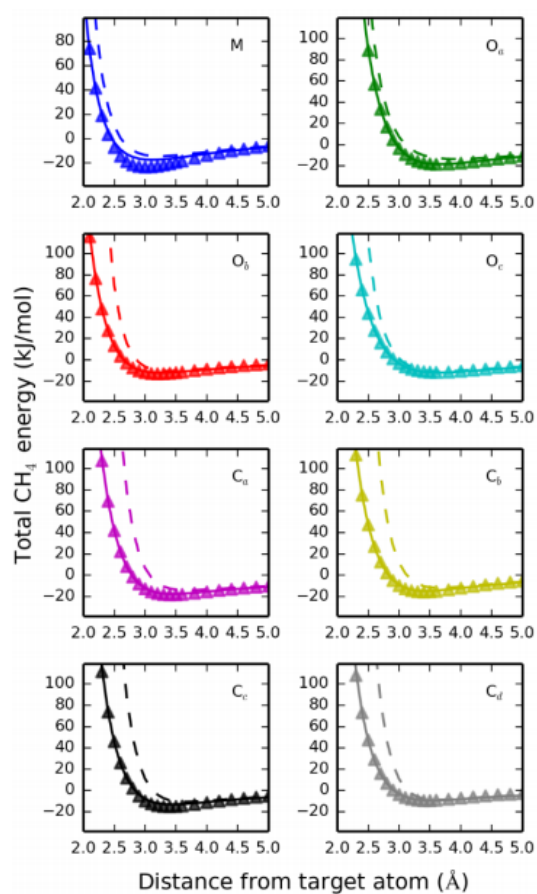


Figure B.8: Comparison of CH_4 -framework interaction energies in $\text{Fe}_2(\text{dobdc})$ obtained from the DFT calculations (triangular markers), the DFT-derived force field (solid line), and the UFF force field (dashed line) along the various approaching paths.

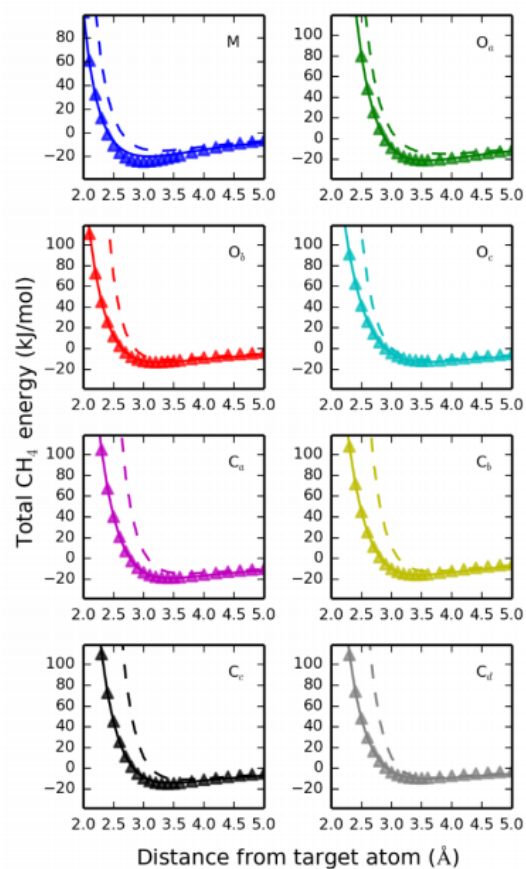


Figure B.9: Comparison of CH₄-framework interaction energies in Ni₂(dobdc) obtained from the DFT calculations (triangular markers), the DFT-derived force field (solid line), and the UFF force field (dashed line) along the various approaching paths.

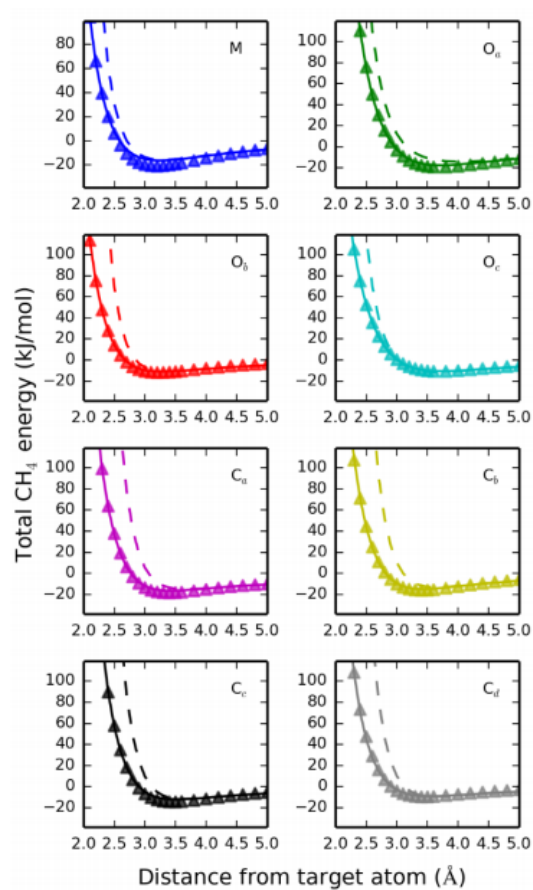


Figure B.10: Comparison of CH₄-framework interaction energies in Zn₂(dobdc) obtained from the DFT calculations (triangular markers), the DFT-derived force field (solid line), and the UFF force field (dashed line) along the various approaching paths.

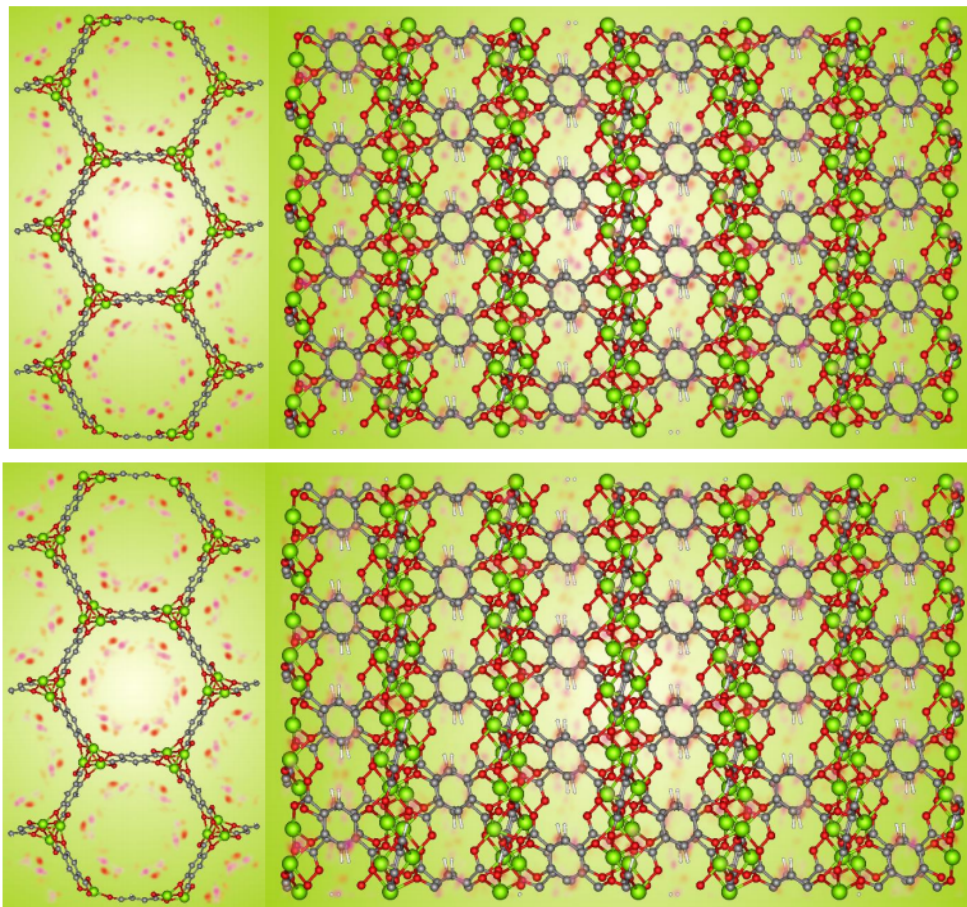


Figure B.11: (top) Probability density plots from two different views computed using the DFT-derived force field for 216 CO_2 molecules in a $\text{Mg}_2(\text{dobdc})$ cell at 100 K. Orange clouds represent the density corresponding to the oxygen atoms in CO_2 , whereas magenta clouds correspond to the density from the carbon atoms. (bottom) Probability density plots from two different views computed using the UFF force field for 216 CO_2 molecules in a $\text{Mg}_2(\text{dobdc})$ cell at 100 K. Orange clouds represent the density corresponding to the oxygen atoms in CO_2 , whereas magenta clouds correspond to the density from the carbon atoms. Framework color key – C = gray, O = red, H = white, Mg = lime green.

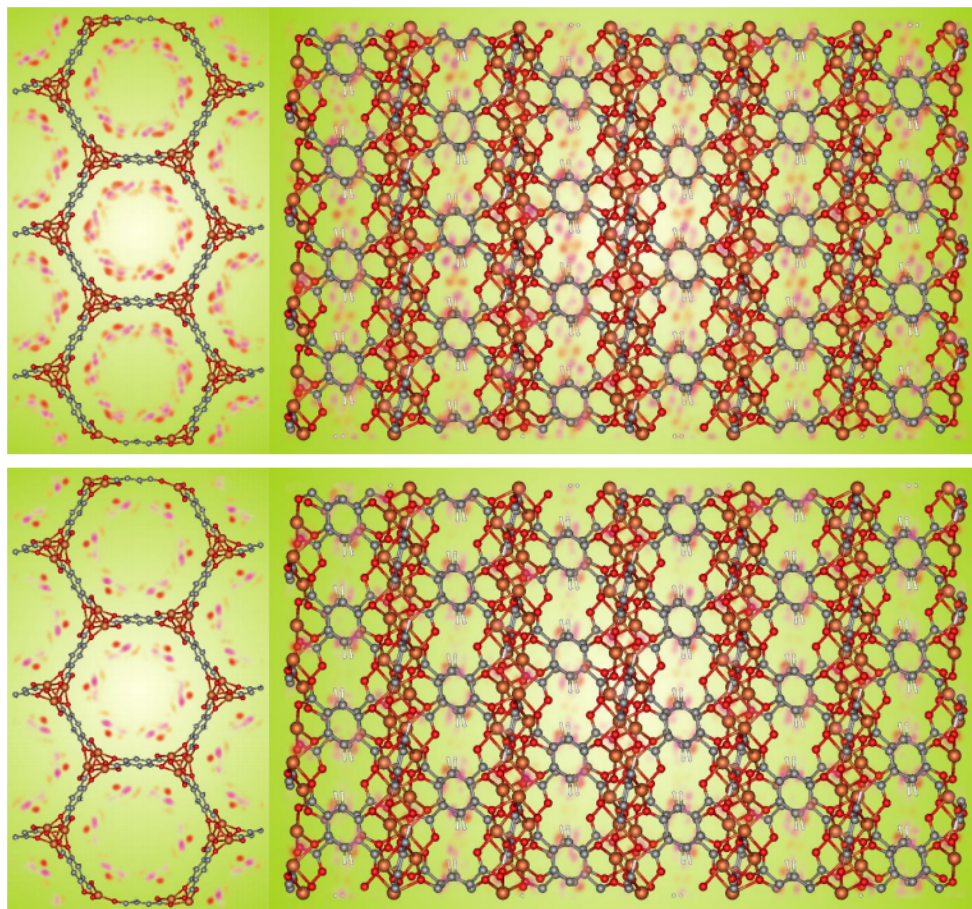


Figure B.12: (top) Probability density plots from two different views computed using the DFT-derived force field for 216 CO_2 molecules in a $\text{Fe}_2(\text{dobdc})$ cell at 100 K. Orange clouds represent the density corresponding to the oxygen atoms in CO_2 , whereas magenta clouds correspond to the density from the carbon atoms. (bottom) Probability density plots from two different views computed using the UFF force field for 216 CO_2 molecules in a $\text{Fe}_2(\text{dobdc})$ cell at 100 K. Orange clouds represent the density corresponding to the oxygen atoms in CO_2 , whereas magenta clouds correspond to the density from the carbon atoms. Framework color key – C = gray, O = red, H = white, Fe = orange.

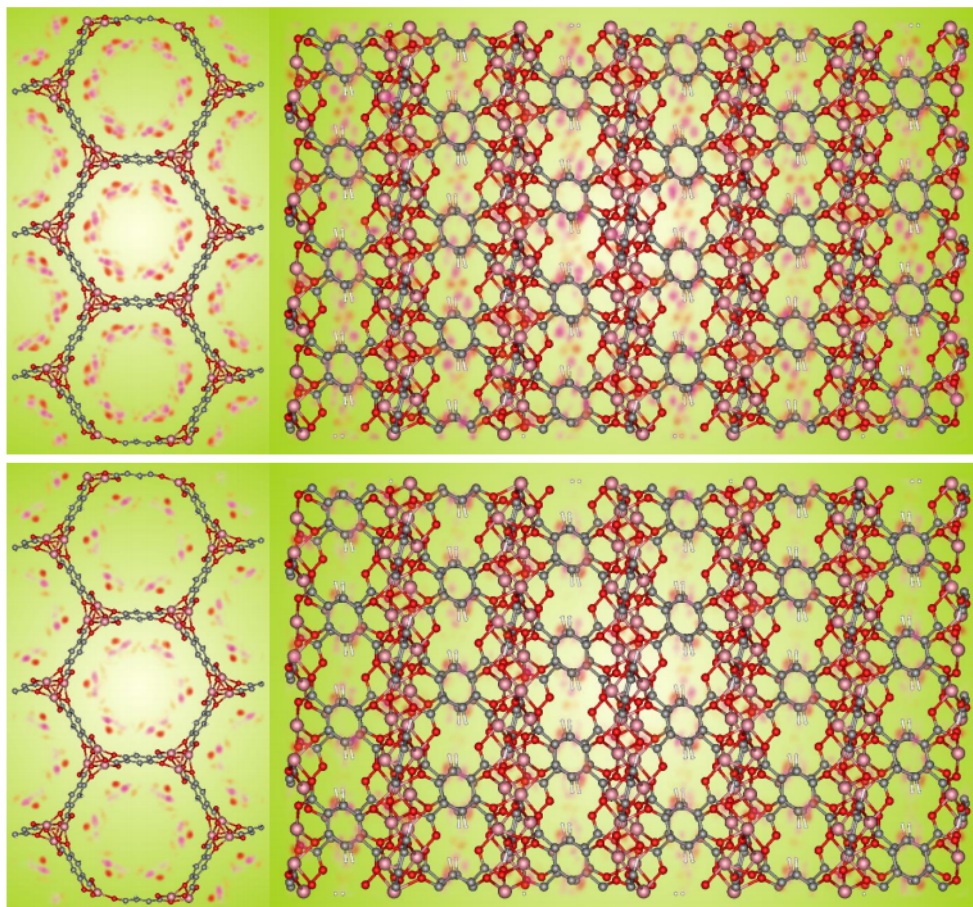


Figure B.13: (top) Probability density plots from two different views computed using the DFT-derived force field for 216 CO_2 molecules in a $\text{Co}_2(\text{dobdc})$ cell at 100 K. Orange clouds represent the density corresponding to the oxygen atoms in CO_2 , whereas magenta clouds correspond to the density from the carbon atoms. (bottom) Probability density plots from two different views computed using the UFF force field for 216 CO_2 molecules in a $\text{Co}_2(\text{dobdc})$ cell at 100 K. Orange clouds represent the density corresponding to the oxygen atoms in CO_2 , whereas magenta clouds correspond to the density from the carbon atoms. Framework color key – C = gray, O = red, H = white, Co = pink.

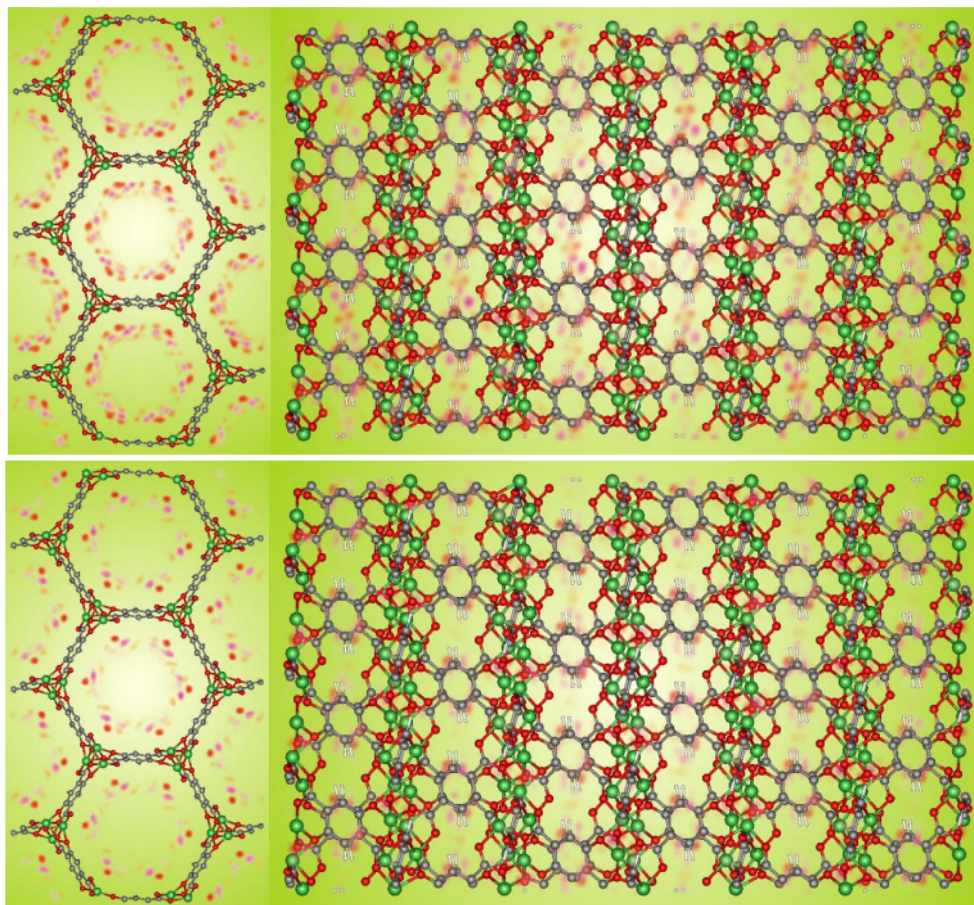


Figure B.14: (top) Probability density plots from two different views computed using the DFT-derived force field for 216 CO_2 molecules in a $\text{Ni}_2(\text{dobdc})$ cell at 100 K. Orange clouds represent the density corresponding to the oxygen atoms in CO_2 , whereas magenta clouds correspond to the density from the carbon atoms. (bottom) Probability density plots from two different views computed using the UFF force field for 216 CO_2 molecules in a $\text{Ni}_2(\text{dobdc})$ cell at 100 K. Orange clouds represent the density corresponding to the oxygen atoms in CO_2 , whereas magenta clouds correspond to the density from the carbon atoms. Framework color key – C = gray, O = red, H = white, Ni = green.

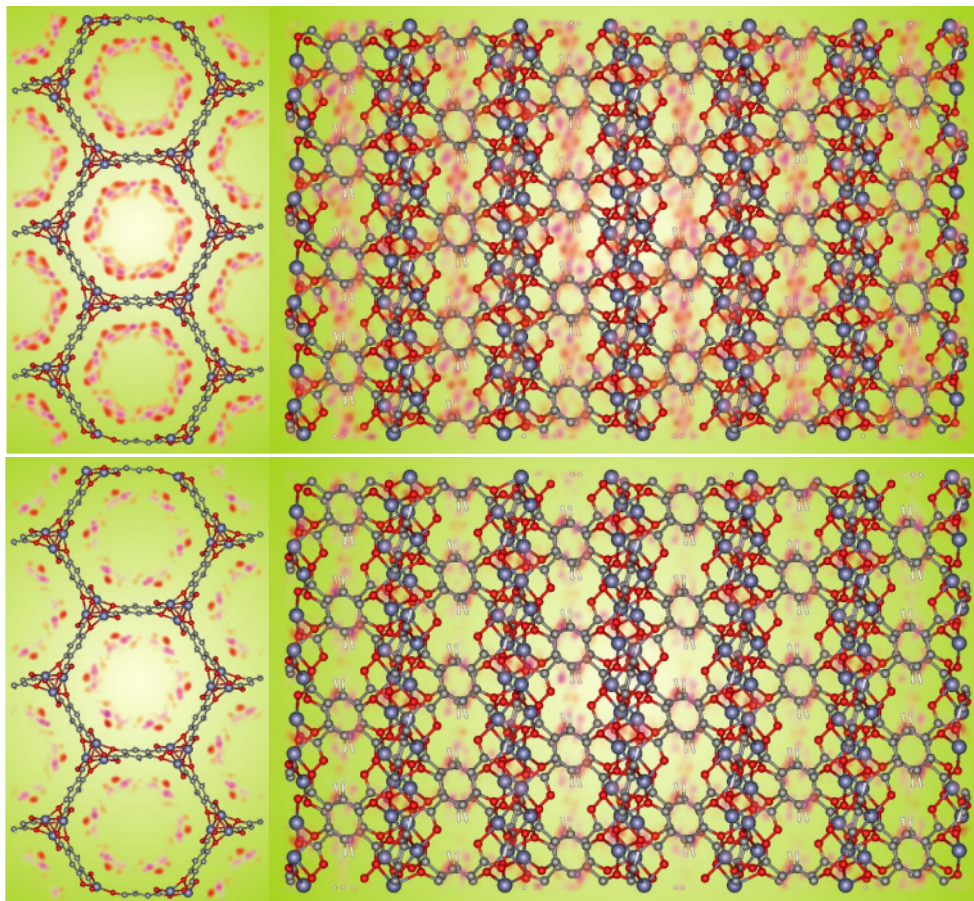


Figure B.15: (top) Probability density plots from two different views computed using the DFT-derived force field for 216 CO_2 molecules in a $\text{Zn}_2(\text{dobdc})$ cell at 100 K. Orange clouds represent the density corresponding to the oxygen atoms in CO_2 , whereas magenta clouds correspond to the density from the carbon atoms. (bottom) Probability density plots from two different views computed using the UFF force field for 216 CO_2 molecules in a $\text{Zn}_2(\text{dobdc})$ cell at 100 K. Orange clouds represent the density corresponding to the oxygen atoms in CO_2 , whereas magenta clouds correspond to the density from the carbon atoms. Framework color key – C = gray, O = red, H = white, Zn = slate.

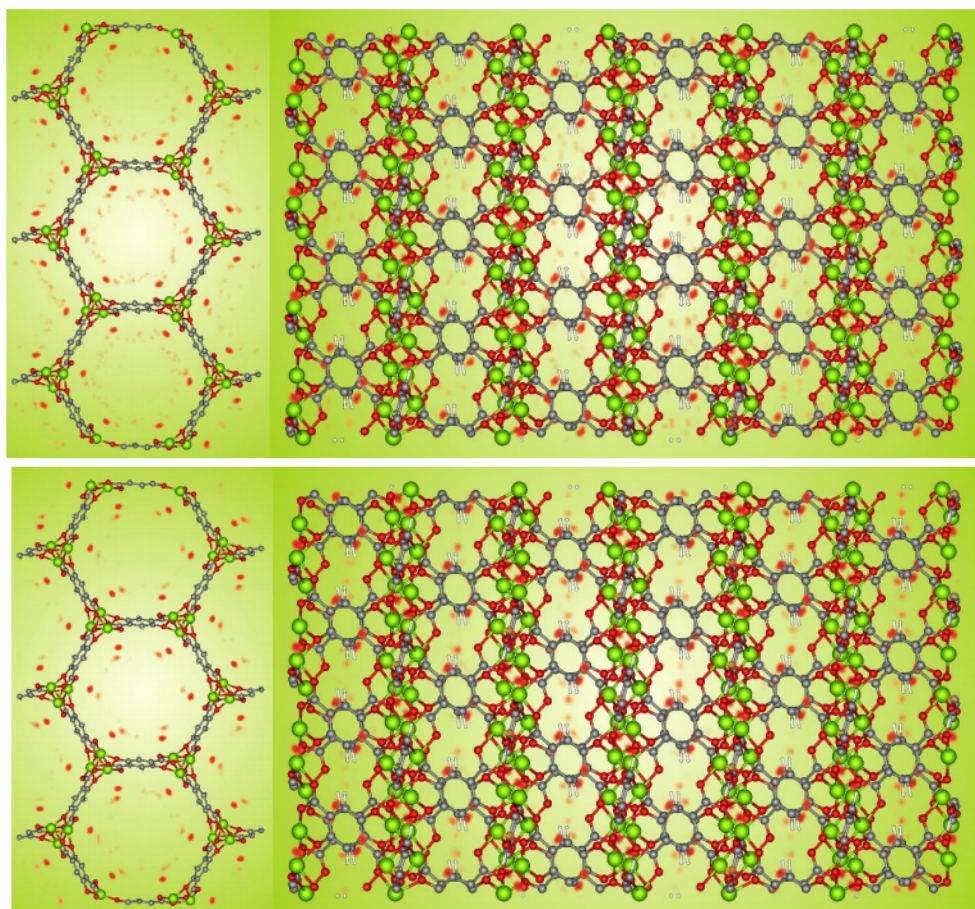


Figure B.16: (top) Probability density plots from two different views computed using the DFT-derived force field for 216 H₂O molecules in a Mg₂(dobdc) cell at 100 K. Orange clouds represent the density corresponding to the oxygen atoms in H₂O. (bottom) Probability density plots from two different views computed using the UFF force field for 216 H₂O molecules in a Mg₂(dobdc) cell at 100 K. Orange clouds represent the density corresponding to the oxygen atoms in H₂O. Framework color key – C = gray, O = red, H = white, Mg = lime green.

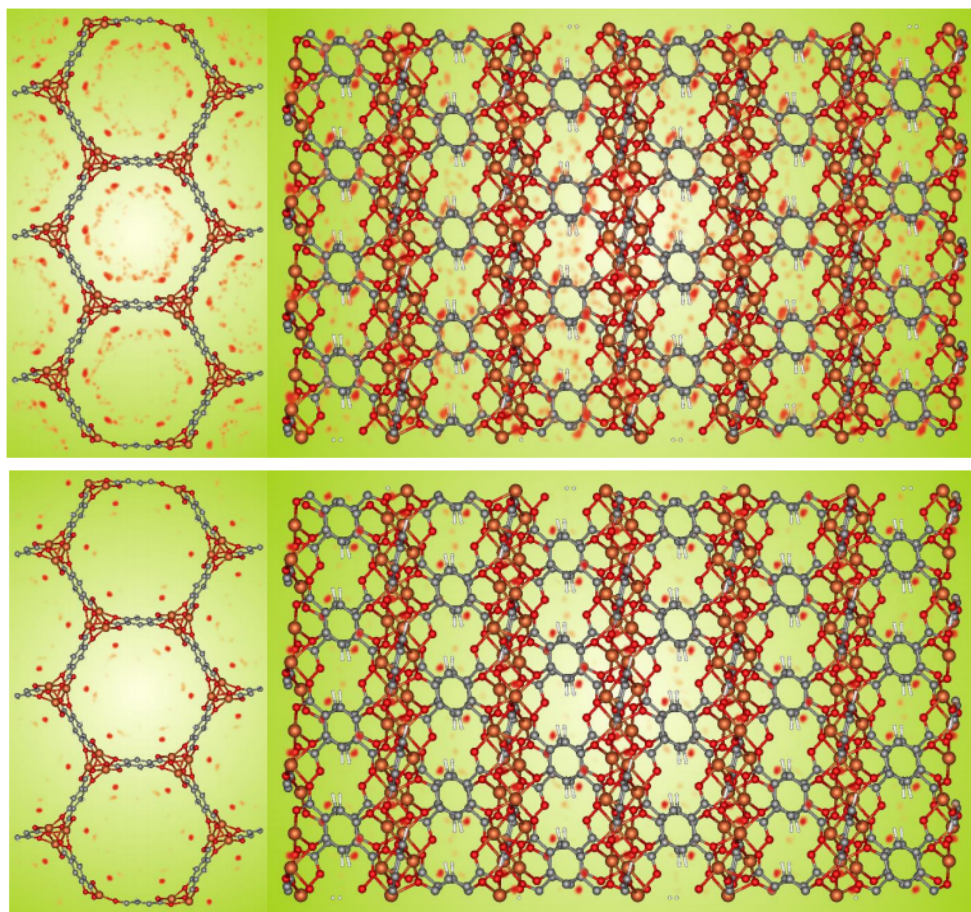


Figure B.17: (top) Probability density plots from two different views computed using the DFT-derived force field for 216 H_2O molecules in a $\text{Fe}_2(\text{dobdc})$ cell at 100 K. Orange clouds represent the density corresponding to the oxygen atoms in H_2O . (bottom) Probability density plots from two different views computed using the UFF force field for 216 H_2O molecules in a $\text{Fe}_2(\text{dobdc})$ cell at 100 K. Orange clouds represent the density corresponding to the oxygen atoms in H_2O . Framework color key – C = gray, O = red, H = white, Fe = orange.

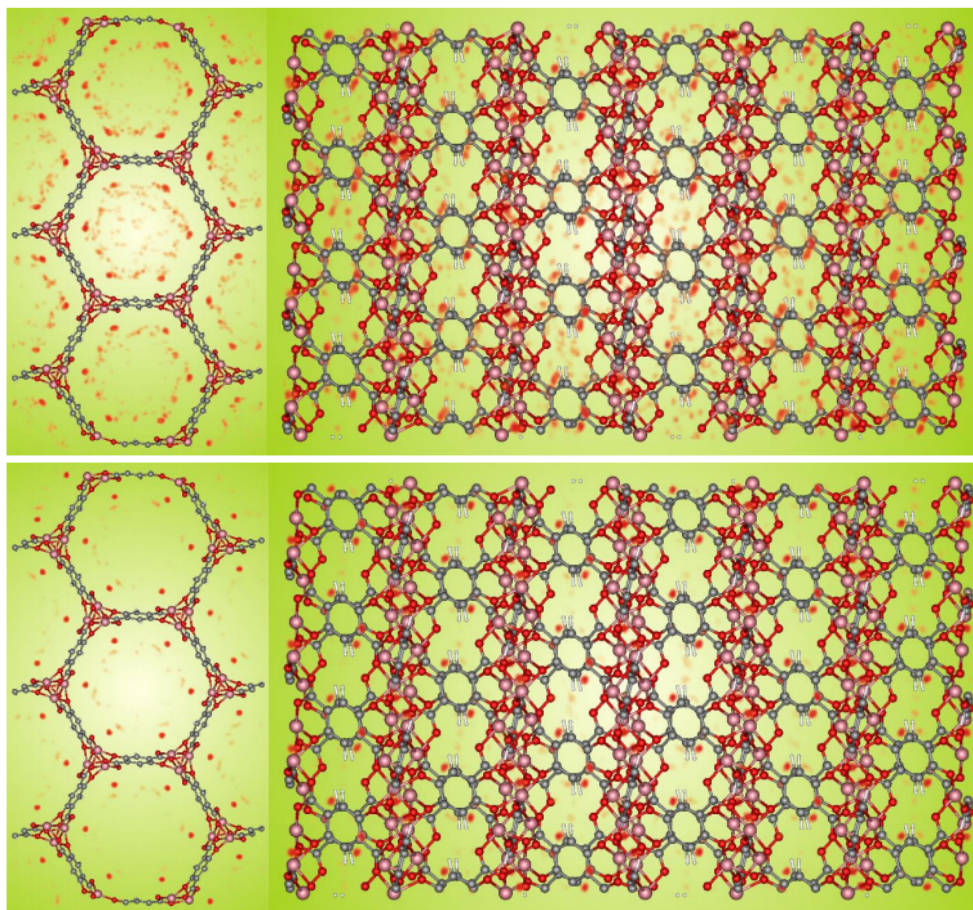


Figure B.18: (top) Probability density plots from two different views computed using the DFT-derived force field for 216 H₂O molecules in a Co₂(dobdc) cell at 100 K. Orange clouds represent the density corresponding to the oxygen atoms in H₂O. (bottom) Probability density plots from two different views computed using the UFF force field for 216 H₂O molecules in a Co₂(dobdc) cell at 100 K. Orange clouds represent the density corresponding to the oxygen atoms in H₂O. Framework color key – C = gray, O = red, H = white, Co = pink.

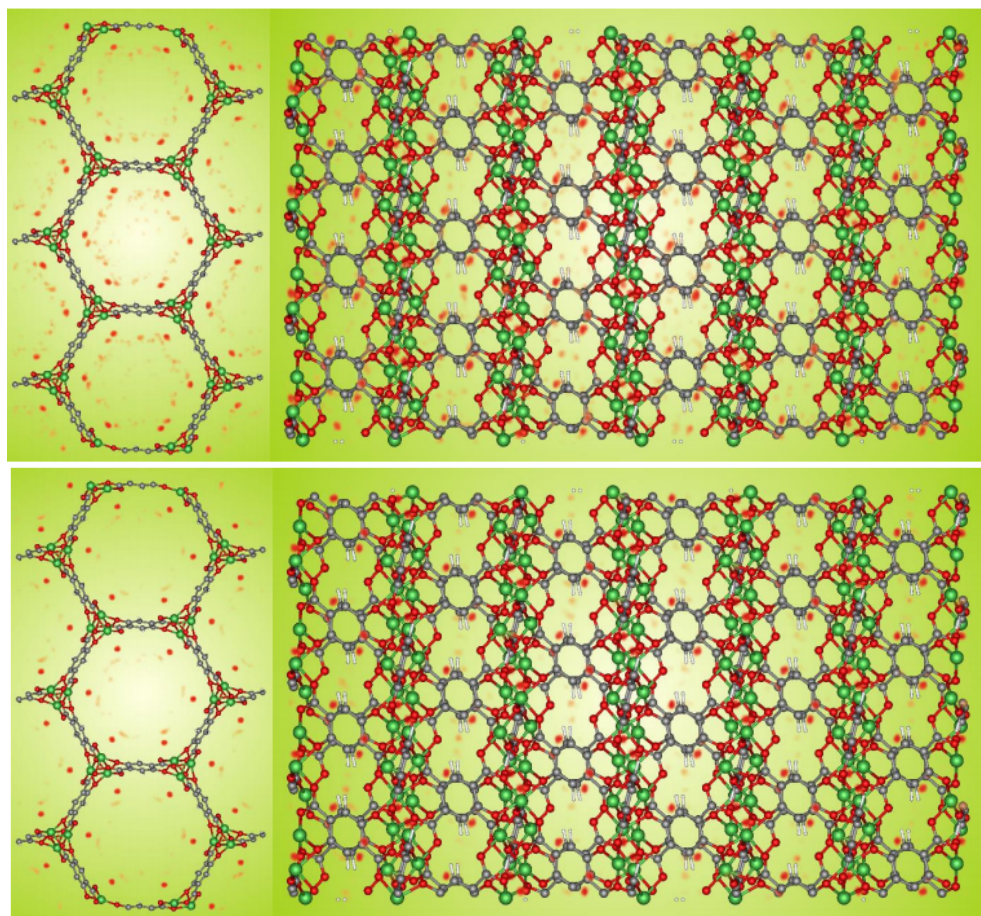


Figure B.19: (top) Probability density plots from two different views computed using the DFT-derived force field for 216 H_2O molecules in a $\text{Ni}_2(\text{dobdc})$ cell at 100 K. Orange clouds represent the density corresponding to the oxygen atoms in H_2O . (bottom) Probability density plots from two different views computed using the UFF force field for 216 H_2O molecules in a $\text{Ni}_2(\text{dobdc})$ cell at 100 K. Orange clouds represent the density corresponding to the oxygen atoms in H_2O . Framework color key – C = gray, O = red, H = white, Ni = green.

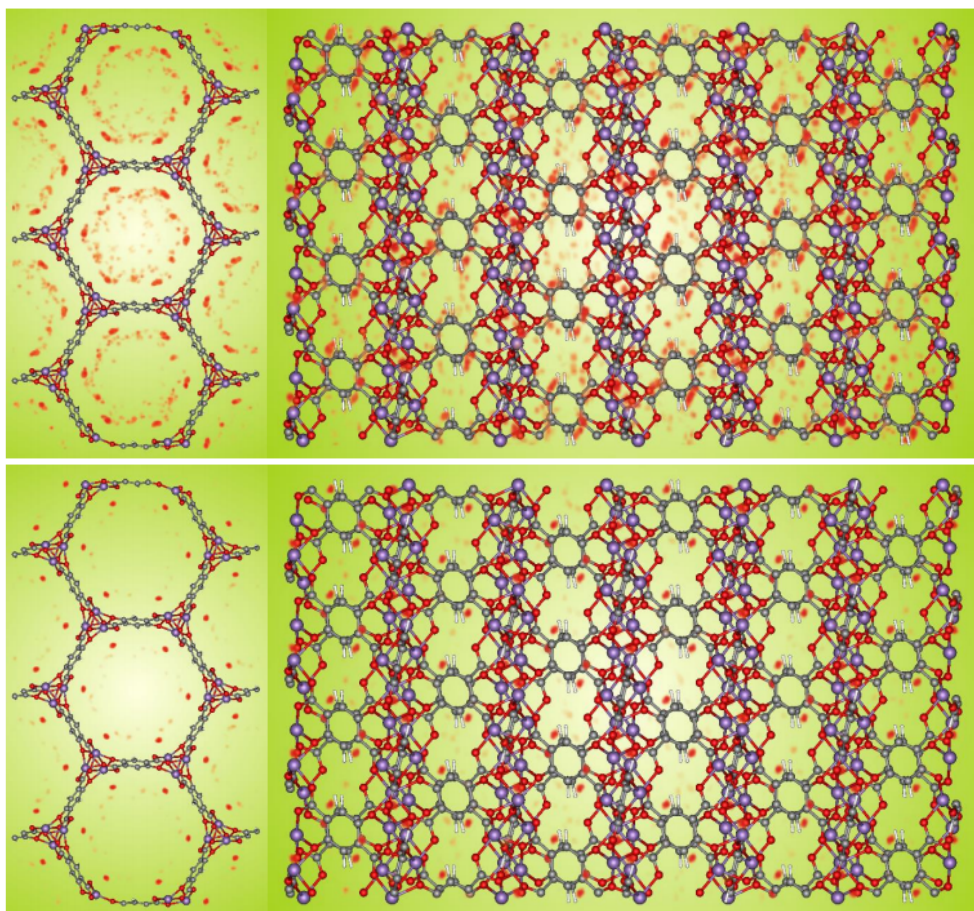


Figure B.20: (top) Probability density plots from two different views computed using the DFT-derived force field for 216 H_2O molecules in a $\text{Mn}_2(\text{dobdc})$ cell at 100 K. Orange clouds represent the density corresponding to the oxygen atoms in H_2O . (bottom) Probability density plots from two different views computed using the UFF force field for 216 H_2O molecules in a $\text{Mn}_2(\text{dobdc})$ cell at 100 K. Orange clouds represent the density corresponding to the oxygen atoms in H_2O . Framework color key – C = gray, O = red, H = white, Mn = purple.

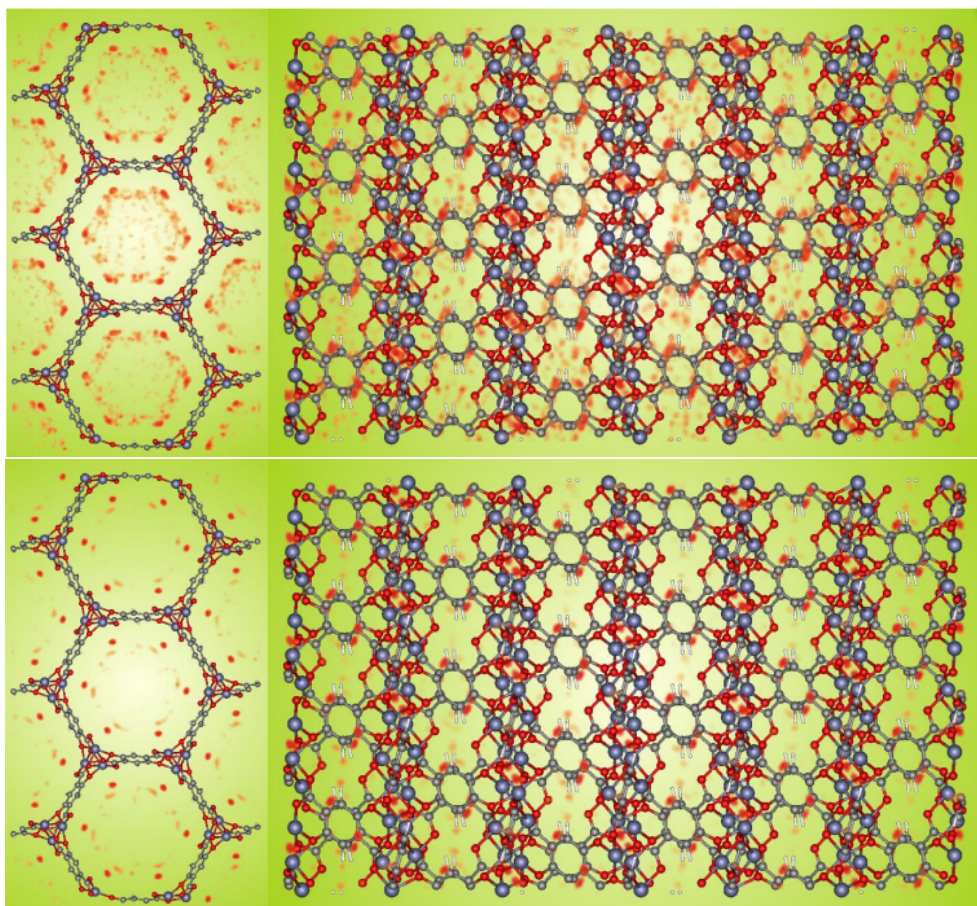


Figure B.21: (top) Probability density plots from two different views computed using the DFT-derived force field for 216 H_2O molecules in a $\text{Zn}_2(\text{dobdc})$ cell at 100 K. Orange clouds represent the density corresponding to the oxygen atoms in H_2O . (bottom) Probability density plots from two different views computed using the UFF force field for 216 H_2O molecules in a $\text{Zn}_2(\text{dobdc})$ cell at 100 K. Orange clouds represent the density corresponding to the oxygen atoms in H_2O . Framework color key – C = gray, O = red, H = white, Zn = slate.

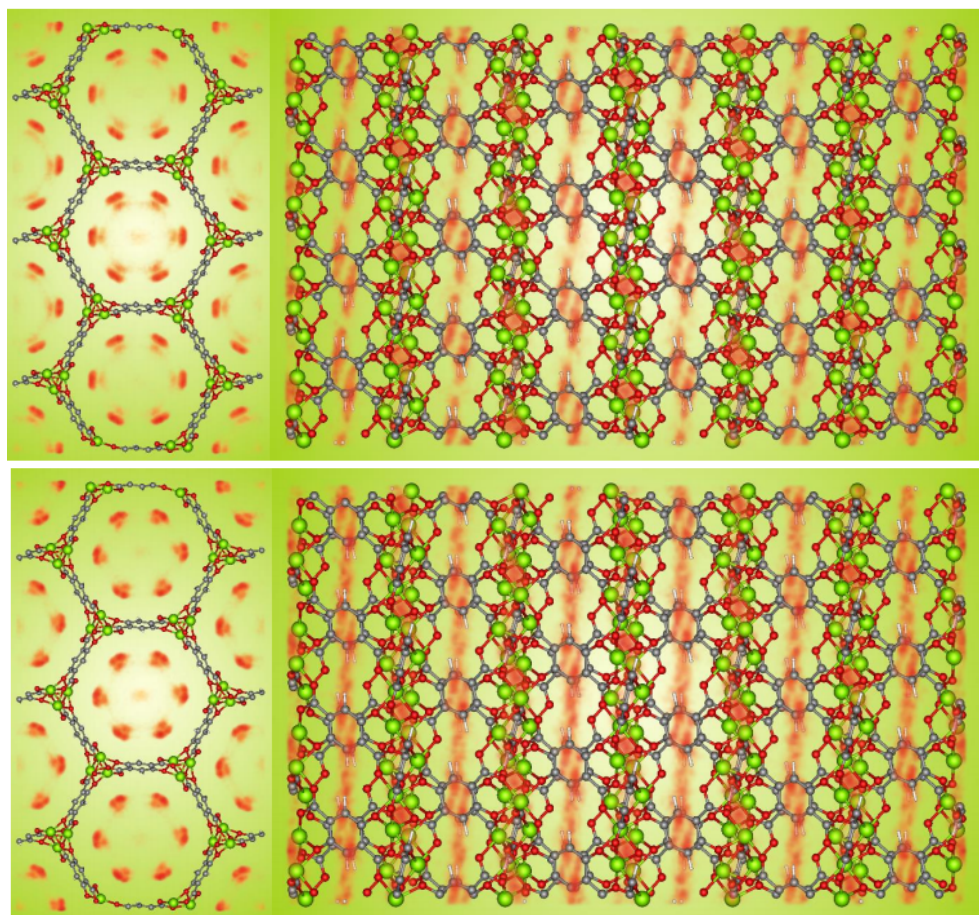


Figure B.22: (top) Probability density plots from two different views computed using the DFT-derived force field for 216 CH_4 molecules in a $\text{Mg}_2(\text{dobdc})$ cell at 100 K. Orange clouds represent the density corresponding to the carbon atoms in CH_4 . (bottom) Probability density plots from two different views computed using the UFF force field for 216 CH_4 molecules in a $\text{Mg}_2(\text{dobdc})$ cell at 100 K. Orange clouds represent the density corresponding to the carbon atoms in CH_4 . Framework color key – C = gray, O = red, H = white, Mg = lime green.

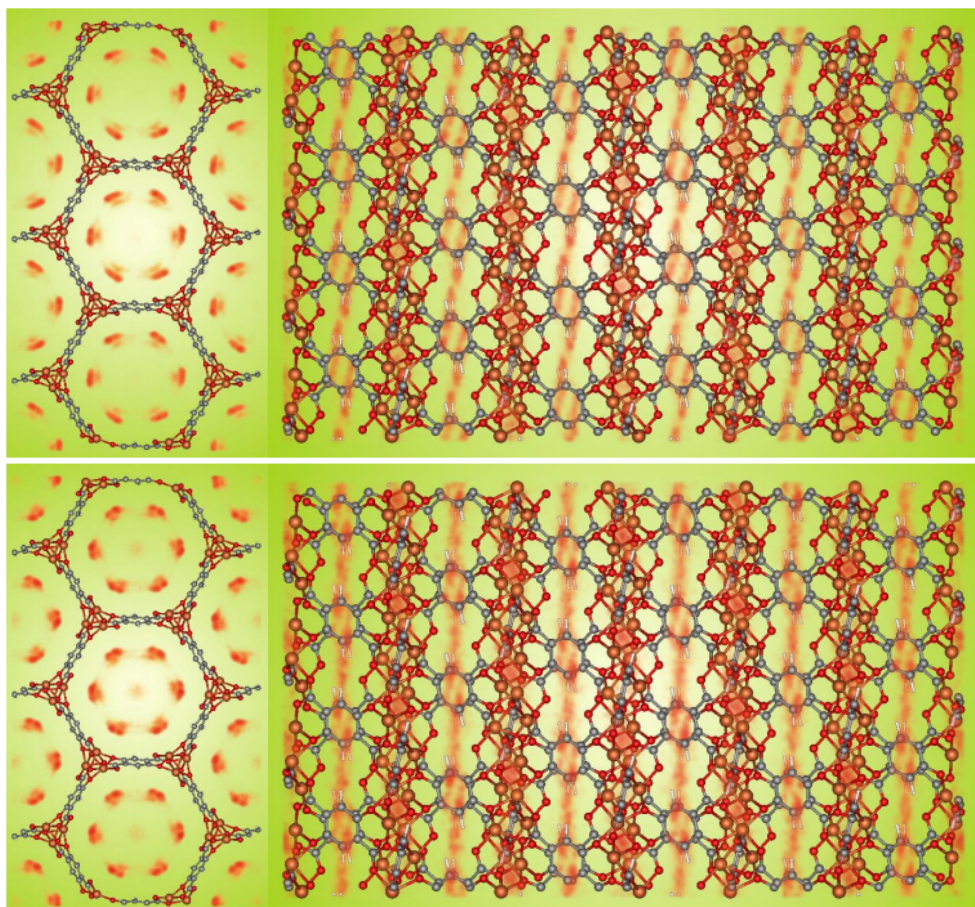


Figure B.23: (top) Probability density plots from two different views computed using the DFT-derived force field for 216 CH_4 molecules in a $\text{Fe}_2(\text{dobdc})$ cell at 100 K. Orange clouds represent the density corresponding to the carbon atoms in CH_4 . (bottom) Probability density plots from two different views computed using the UFF force field for 216 CH_4 molecules in a $\text{Fe}_2(\text{dobdc})$ cell at 100 K. Orange clouds represent the density corresponding to the carbon atoms in CH_4 . Framework color key – C = gray, O = red, H = white, Fe = orange.

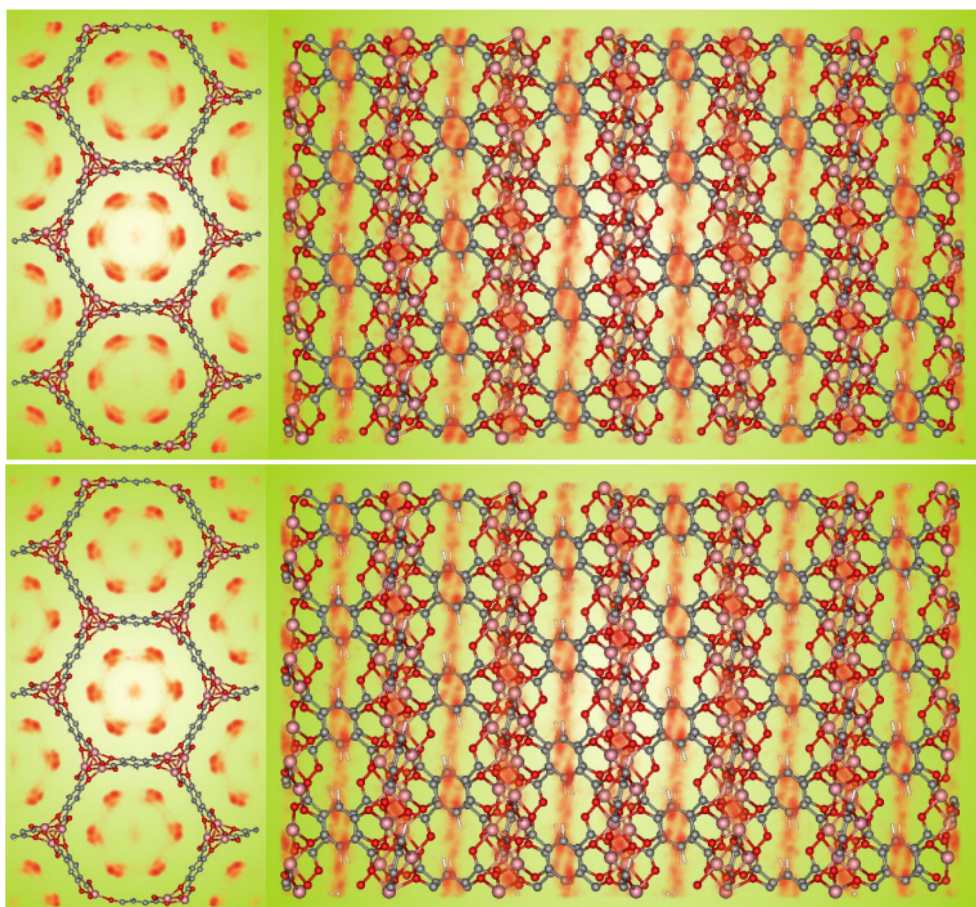


Figure B.24: (top) Probability density plots from two different views computed using the DFT-derived force field for 216 CH_4 molecules in a $\text{Co}_2(\text{dobdc})$ cell at 100 K. Orange clouds represent the density corresponding to the carbon atoms in CH_4 . (bottom) Probability density plots from two different views computed using the UFF force field for 216 CH_4 molecules in a $\text{Co}_2(\text{dobdc})$ cell at 100 K. Orange clouds represent the density corresponding to the carbon atoms in CH_4 . Framework color key – C = gray, O = red, H = white, Co = pink.

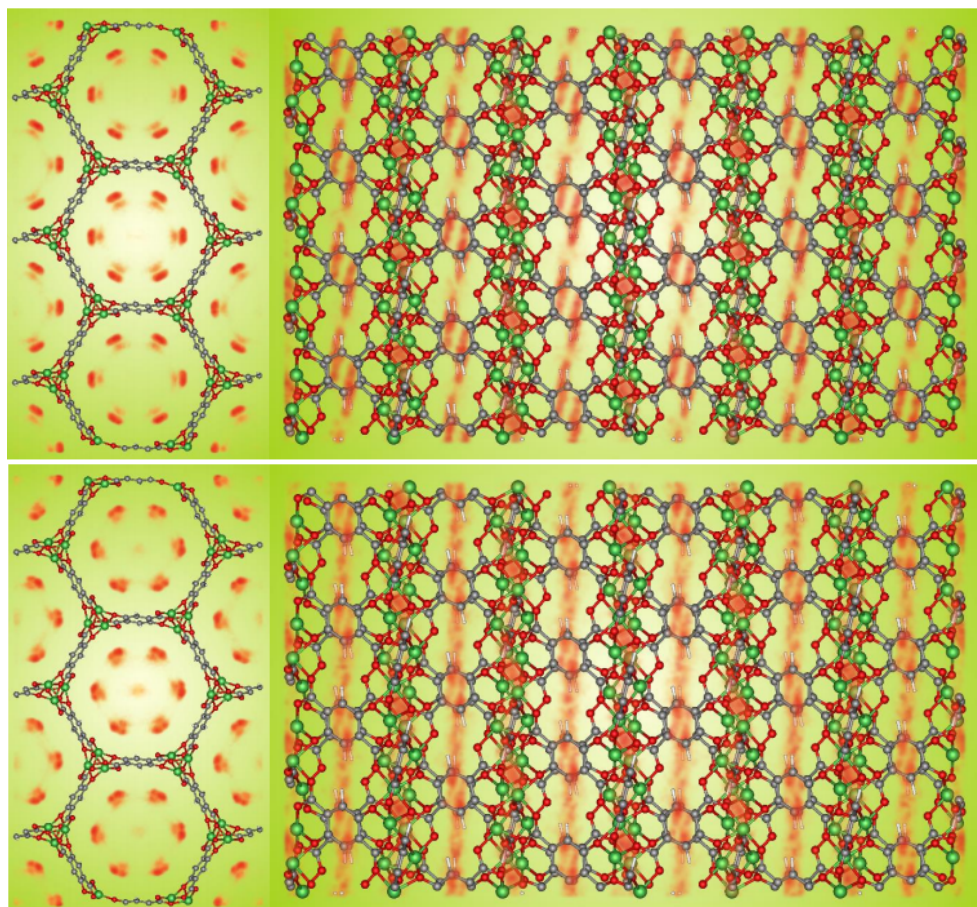


Figure B.25: (top) Probability density plots from two different views computed using the DFT-derived force field for 216 CH_4 molecules in a $\text{Ni}_2(\text{dobdc})$ cell at 100 K. Orange clouds represent the density corresponding to the carbon atoms in CH_4 . (bottom) Probability density plots from two different views computed using the UFF force field for 216 CH_4 molecules in a $\text{Ni}_2(\text{dobdc})$ cell at 100 K. Orange clouds represent the density corresponding to the carbon atoms in CH_4 . Framework color key – C = gray, O = red, H = white, Ni = green.

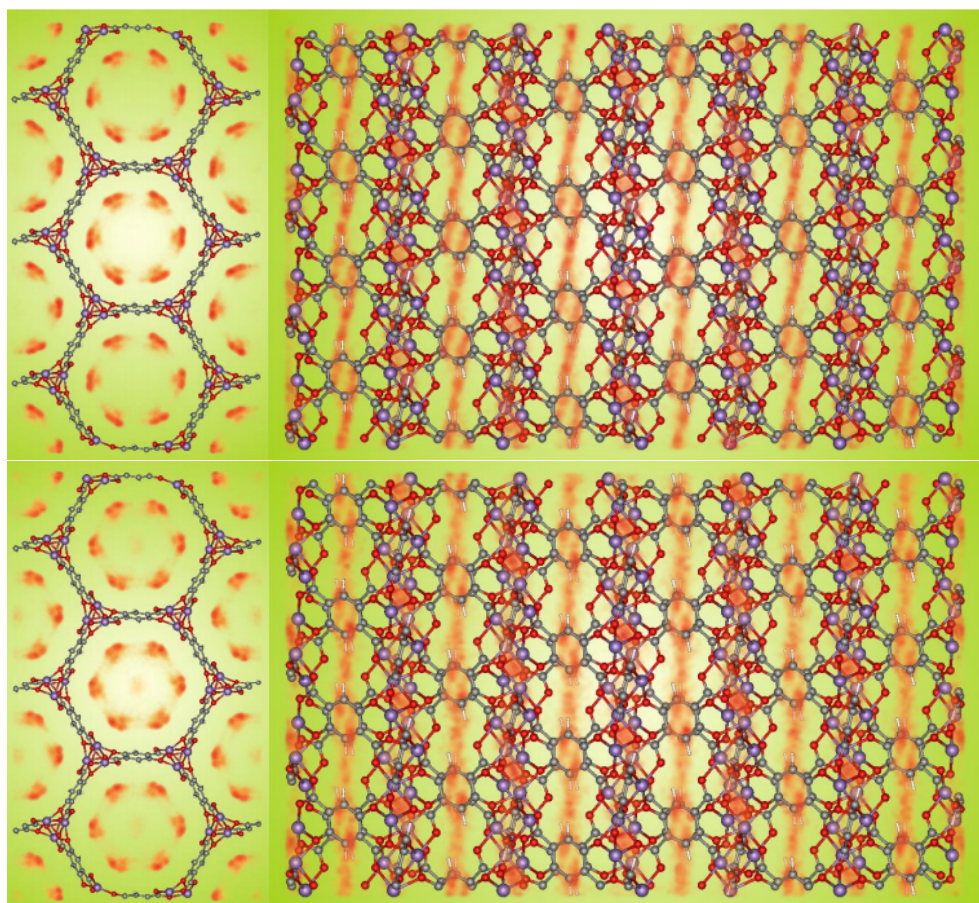


Figure B.26: (top) Probability density plots from two different views computed using the DFT-derived force field for 216 CH_4 molecules in a $\text{Mn}_2(\text{dobdc})$ cell at 100 K. Orange clouds represent the density corresponding to the carbon atoms in CH_4 . (bottom) Probability density plots from two different views computed using the UFF force field for 216 CH_4 molecules in a $\text{Mn}_2(\text{dobdc})$ cell at 100 K. Orange clouds represent the density corresponding to the carbon atoms in CH_4 . Framework color key – C = gray, O = red, H = white, Mn = purple.

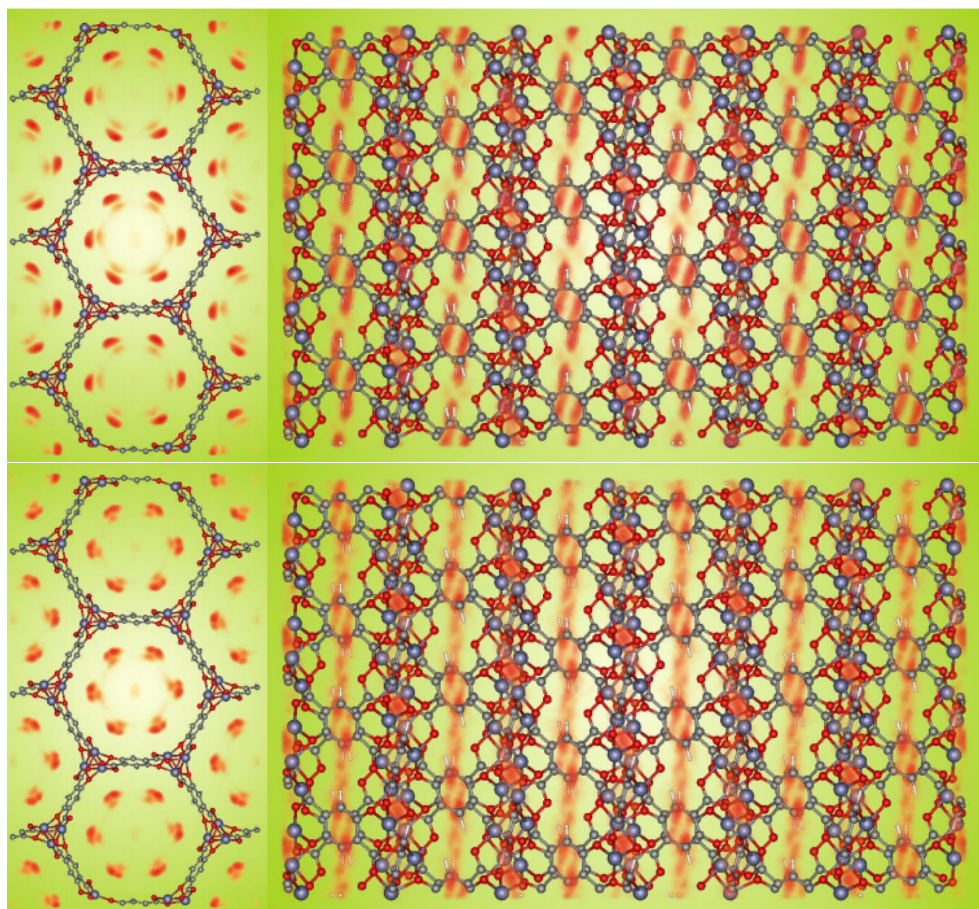


Figure B.27: (top) Probability density plots from two different views computed using the DFT-derived force field for 216 CH_4 molecules in a $\text{Zn}_2(\text{dobdc})$ cell at 100 K. Orange clouds represent the density corresponding to the carbon atoms in CH_4 . (bottom) Probability density plots from two different views computed using the UFF force field for 216 CH_4 molecules in a $\text{Zn}_2(\text{dobdc})$ cell at 100 K. Orange clouds represent the density corresponding to the carbon atoms in CH_4 . Framework color key – C = gray, O = red, H = white, Zn = slate.

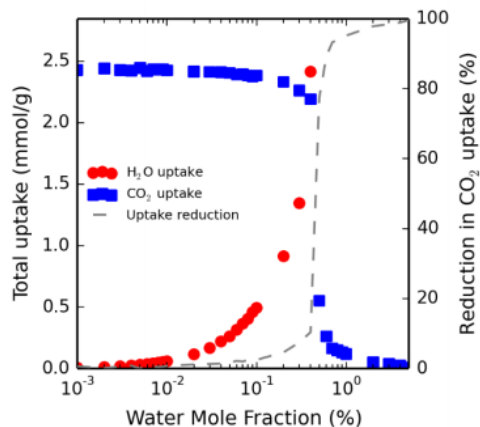


Figure B.28: Computed $\text{CO}_2/\text{H}_2\text{O}$ mixture isotherms in $\text{Ni}_2(\text{dobdc})$ at 313 K and 0.15 bar using the DFT-derived force fields for the framework and EPM2/Tip4p-Ew for the guests. The red circular markers symbolize H_2O adsorption, whereas the blue square markers symbolize CO_2 adsorption.

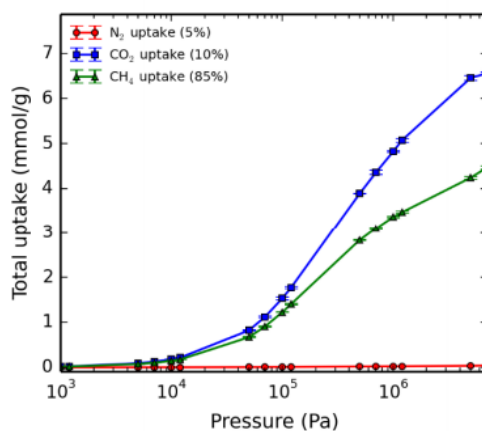


Figure B.29: Computed $\text{N}_2/\text{CO}_2/\text{CH}_4$ mixture isotherms in $\text{Ni}_2(\text{dobdc})$ at 313 K using the DFT-derived force fields where applicable. The red circular markers symbolize N_2 adsorption, the green triangular markers symbolize CH_4 adsorption, and the blue square markers symbolize CO_2 adsorption. The mole fraction of gases in the reservoir is fixed at all pressures to 0.05 N_2 , 0.1 CO_2 , and 0.85 CH_4 .

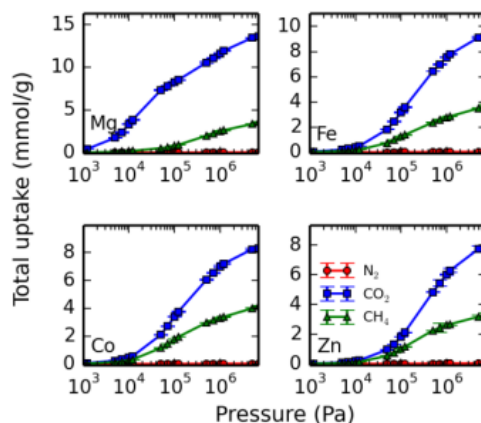


Figure B.30: Computed $\text{N}_2/\text{CO}_2/\text{CH}_4$ mixture isotherms in $\text{Mg}_2(\text{dobdc})$ (top left), $\text{Fe}_2(\text{dobdc})$ (top right), $\text{Co}_2(\text{dobdc})$ (bottom left), and $\text{Zn}_2(\text{dobdc})$ (bottom right) at 287 K using the DFT-derived force fields where applicable. The red circular markers symbolize N_2 adsorption, the green triangular markers symbolize CH_4 adsorption, and the blue square markers symbolize CO_2 adsorption. The mole fraction of gases in the reservoir is fixed at all pressures to 0.05 N_2 , 0.1 CO_2 , and 0.85 CH_4 .

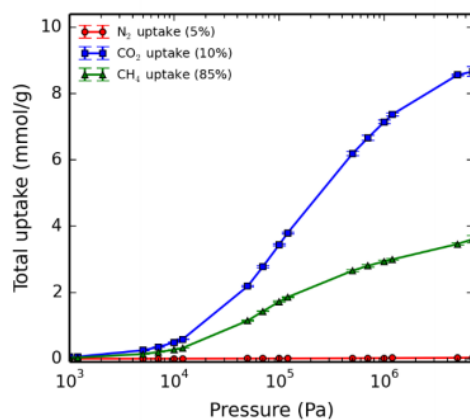


Figure B.31: Computed $\text{N}_2/\text{CO}_2/\text{CH}_4$ mixture isotherms in $\text{Ni}_2(\text{dobdc})$ at 287 K using the DFT-derived force fields where applicable. The red circular markers symbolize N_2 adsorption, the green triangular markers symbolize CH_4 adsorption, and the blue square markers symbolize CO_2 adsorption. The mole fraction of gases in the reservoir is fixed at all pressures to 0.05 N_2 , 0.1 CO_2 , and 0.85 CH_4 .

Appendix C

Additional Information for The Effect of the Coord. Unsaturated Metal Sites on CH₄ Diffusion in M₂(dobdc)

C.1 Simulation Structures

M₂(dobdc) structures were obtained from <https://github.com/rociomer/DFT-derived-force-field/>, which contains optimized structures and force field files from [163]. Geometry optimizations were performed for each framework using density functional theory (DFT) with periodic boundary conditions as implemented in the Vienna Ab initio Simulation Package (VASP). [111] All structural optimizations were performed with PBE [182] functionals, a plane wave basis set, projector augmented wave (PAW) pseudopotentials, and periodic boundary conditions. [182, 112, 14] For additional computational details, please see [163]. Framework densities of the structures used in the MD simulations are listed in Table C.1.

The topology input files for MD simulations in LAMMPS were generated using TopoTools. [106]

Framework	Density (kg/m ³)
Mg ₂ (dobdc)	887.62344
Ni ₂ (dobdc)	1162.4801
Zn ₂ (dobdc)	1195.8873

Table C.1: Framework densities for simulation structures.

P (bar)	Uptake (molec/uc)	\pm Err	Uptake (mol/kg)	\pm Err	Uptake (molec/M ⁺²)
0.1	0.590	0.027	0.135	0.006	0.016
0.25	1.411	0.079	0.323	0.018	0.039
0.5	2.825	0.098	0.646	0.022	0.078
1	5.342	0.284	1.223	0.065	0.148
1.5	7.815	0.150	1.789	0.034	0.217
2	10.074	0.272	2.307	0.062	0.279
2.5	12.320	0.095	2.821	0.021	0.342
3	14.127	0.409	3.235	0.093	0.392
3.5	16.118	0.579	3.690	0.132	0.447
4	17.894	0.365	4.097	0.083	0.497
4.5	19.436	0.341	4.450	0.078	0.539
5	20.963	0.210	4.800	0.048	0.582
10	30.590	0.587	7.005	0.134	0.849
15	35.756	0.714	8.188	0.163	0.993
20	39.210	0.459	8.978	0.105	1.089
25	41.621	0.269	9.531	0.061	1.156
30	43.694	0.446	10.005	0.102	1.213
35	45.266	0.157	10.365	0.036	1.257
40	46.377	0.494	10.620	0.113	1.288
45	47.527	0.264	10.883	0.060	1.320
50	48.436	0.484	11.091	0.110	1.345
100	53.986	0.324	12.362	0.074	1.499

Table C.2: Computed isotherms for CH₄ in Mg₂(dobdc) at 313 K. Reported uptake is absolute uptake.

C.2 GCMC Results

Uptakes at Pressures of Interest Tables C.2 – C.4 contain simulation results for CH₄ isotherms computed in the three different M₂(dobdc) frameworks. These simulations were computed at 313 K using the DFT-derived force field reported in [163]. Results of these simulations were used to determine how many CH₄ molecules should be in each unit cell at a given pressure, so that the MD simulations (*NVT*) could correspond to the experimental measurements.

P (bar)	Uptake (molec/uc)	\pm Err	Uptake (mol/kg)	\pm Err	Uptake (molec/M ⁺²)
0.1	0.984	0.085	0.175	0.015	0.027
0.25	2.402	0.071	0.428	0.012	0.066
0.5	4.586	0.212	0.818	0.037	0.127
1	8.811	0.348	1.572	0.062	0.244
1.5	12.643	0.291	2.255	0.052	0.351
2	15.950	0.768	2.845	0.137	0.443
2.5	18.632	0.192	3.324	0.034	0.517
3	21.210	0.557	3.784	0.099	0.589
3.5	23.030	0.551	4.109	0.098	0.639
4	25.218	0.709	4.499	0.126	0.700
4.5	26.972	0.479	4.812	0.085	0.749
5	28.180	0.250	5.027	0.044	0.782
10	36.705	0.331	6.548	0.059	1.019
15	40.950	0.255	7.306	0.045	1.137
20	43.806	0.513	7.815	0.091	1.216
25	45.797	0.521	8.170	0.092	1.272
30	47.544	0.427	8.482	0.076	1.320
35	48.709	0.199	8.690	0.035	1.353
40	50.063	0.302	8.932	0.054	1.390
45	50.971	0.154	9.094	0.027	1.415
50	51.841	0.221	9.249	0.039	1.440
100	56.526	0.376	10.085	0.067	1.570

Table C.3: Computed isotherms for CH₄ in Ni₂(dobdc) at 313 K. Reported uptake is absolute uptake.

P (bar)	Uptake (molec/uc)	\pm Err	Uptake (mol/kg)	\pm Err	Uptake (molec/M ⁺²)
0.1	0.898	0.044	0.076	0.003	0.012
0.25	2.236	0.123	0.191	0.010	0.031
0.5	4.468	0.270	0.382	0.023	0.062
1	8.484	0.391	0.725	0.033	0.117
1.5	12.859	0.226	1.099	0.019	0.178
2	16.589	0.135	1.418	0.011	0.230
2.5	20.192	0.672	1.727	0.057	0.280
3	23.618	0.485	2.020	0.041	0.328
3.5	27.000	0.650	2.309	0.055	0.375
4	30.167	0.573	2.580	0.049	0.418
4.5	32.874	0.460	2.811	0.039	0.456
5	36.057	0.541	3.084	0.046	0.500
10	54.474	0.548	4.659	0.046	0.756
15	65.172	0.529	5.574	0.045	0.905
20	72.337	0.564	6.187	0.048	1.004
25	77.518	0.491	6.630	0.042	1.076
30	81.774	0.437	6.994	0.037	1.135
35	84.656	0.498	7.241	0.042	1.175
40	87.616	0.757	7.494	0.064	1.216
45	90.024	0.418	7.700	0.035	1.250
50	91.894	0.410	7.860	0.035	1.276
100	103.855	0.277	8.883	0.023	1.442

Table C.4: Computed isotherms for CH₄ in Zn₂(dobdc) at 313 K. Reported uptake is absolute uptake.

Pressure (bar)	Mg		Ni		Zn	
	HoA (kJ/mol)	\pm Error	HoA (kJ/mol)	\pm Error	HoA (kJ/mol)	\pm Error
0.1	17.46576	0.140238	19.41317	0.272917	16.63618	0.354938
0.25	17.36592	0.293759	19.47048	0.169914	16.68471	0.329310
0.5	17.43851	0.659792	19.77341	0.741455	17.04255	0.198329
1	17.68060	0.605232	20.20187	0.574700	17.00342	0.401564
1.5	17.80357	0.433070	19.92559	0.478541	17.07887	0.595414
2	17.82673	0.323447	20.51955	0.471442	17.30797	0.567072
2.5	17.80028	0.527727	20.33382	1.017480	17.52647	0.502438
3	18.23100	0.355127	20.51982	0.410047	17.57432	0.354756
3.5	18.39537	0.681541	20.39657	0.464302	17.64671	0.822201
4	18.28353	0.433902	20.78463	0.924833	17.62578	0.275455
4.5	18.18461	0.407001	20.50934	0.612617	17.57693	0.842719
5	18.42685	0.484191	20.75975	1.065210	17.76930	0.951618
10	18.35127	0.528932	20.09200	0.412622	18.17098	0.755624
15	18.53032	1.142198	19.98061	2.690755	17.90694	0.466694
20	18.80894	1.331081	19.02915	0.523020	17.75958	1.210206
25	18.45913	0.867517	18.79395	1.072827	17.59838	1.113844
30	18.17353	0.842588	19.09307	1.257149	17.73942	0.689361
35	17.83445	0.792461	18.61296	0.730453	17.52590	1.116280
40	17.52362	0.816489	19.15964	2.191538	17.45033	0.660649
45	18.70382	0.981731	18.97014	1.019315	17.83637	0.864441
50	18.45238	1.160942	18.67939	1.737658	17.47948	1.053793
100	18.32517	1.382739	17.95629	0.520190	17.30850	2.010175

Table C.5: Computed heats of adsorption versus pressure for CH_4 in $\text{Mg}_2(\text{dobdc})$, $\text{Ni}_2(\text{dobdc})$, and $\text{Zn}_2(\text{dobdc})$ at 313 K.

Heats of Adsorption at Pressures of Interest Table C.5 lists the CH_4 heats of adsorption (HoA) computed in the three $\text{M}_2(\text{dobdc})$ frameworks studied here at all pressures. These HoAs were computed from GCMC simulations at 313 K using the DFT-derived force field reported in [163].

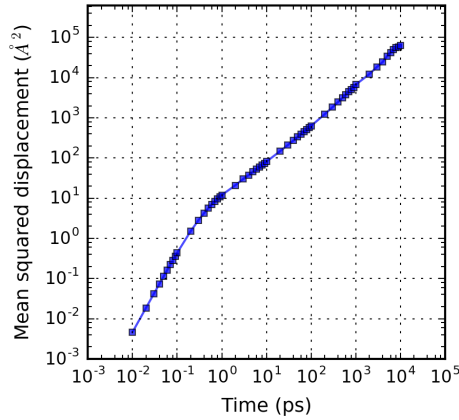


Figure C.1: Log-log plot of the MSD for CH₄ in Mg₂(dobdc) computed using the DFT-derived force field at 313 K and a loading corresponding to 1.0 bar.

Mean-squared Displacements The D_s coefficients for CH₄ in each M₂(dobdc) framework were calculated by taking the slope of the mean-squared displacement (MSD) at long times from equilibrium MD simulations (Equation C.1),

$$D = \frac{1}{2dN} \lim_{t \rightarrow \infty} \frac{d}{dt} \left\langle \sum_i^N (r_i(t) - r_i(0))^2 \right\rangle, \quad (\text{C.1})$$

where d is the dimensionality of the system (3, for proper comparison with experiment), N is the number of CH₄ molecules in the system, and r_i is the center of mass of CH₄ molecule i .

As an illustration of these results, Figures C.1 – C.3 plot the results for the MSD's from NVT simulations in all three metal frameworks corresponding to uptakes at 1.0 bar, while Figures C.4 – C.6 plot the fits to the MSD's from NVT simulations in all three metal frameworks corresponding to uptakes at 1.0 bar.

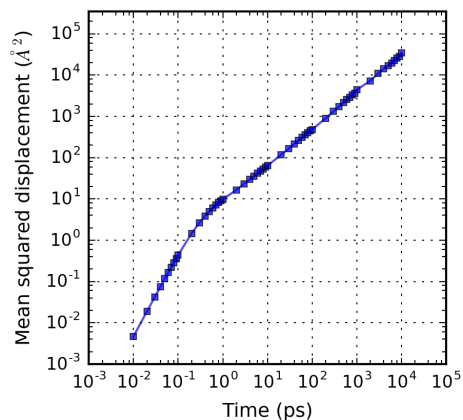


Figure C.2: Log-log plot of the MSD for CH_4 in $\text{Ni}_2(\text{dobdc})$ computed using the DFT-derived force field at 313 K and a loading corresponding to 1.0 bar.

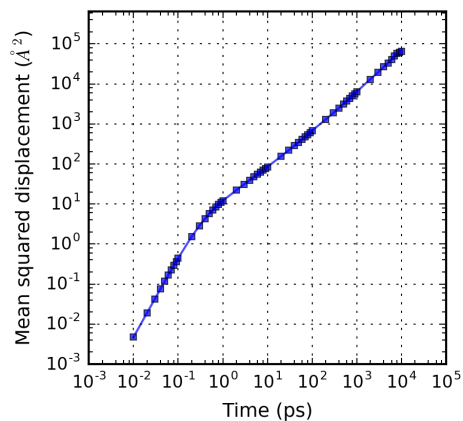


Figure C.3: Log-log plot of the MSD for CH_4 in $\text{Zn}_2(\text{dobdc})$ computed using the DFT-derived force field at 313 K and a loading corresponding to 1.0 bar.

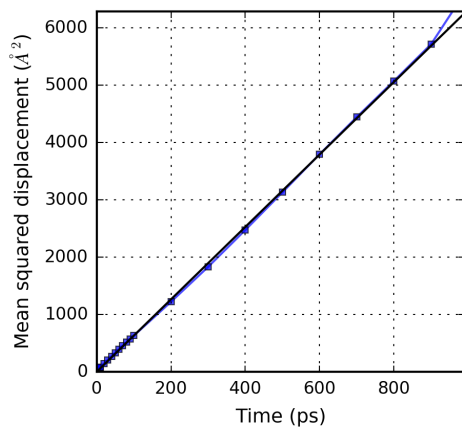


Figure C.4: Linear fit to the MSD for CH₄ in Mg₂(dobdc) at long timescales computed using the DFT-derived force field at 313 K and a loading corresponding to 1.0 bar.

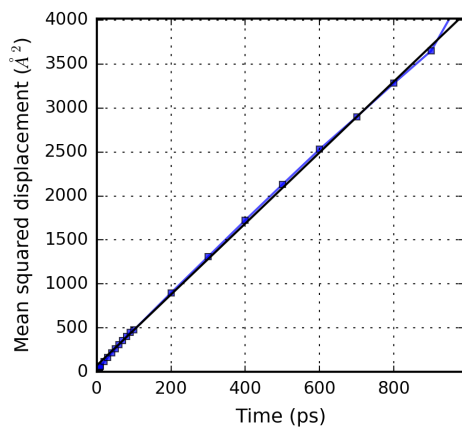


Figure C.5: Linear fit to the MSD for CH₄ in Ni₂(dobdc) at long timescales computed using the DFT-derived force field at 313 K and a loading corresponding to 1.0 bar.

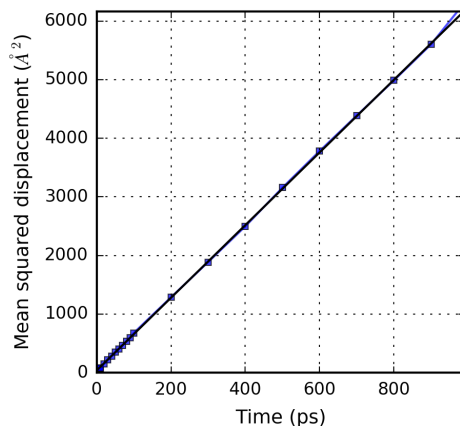


Figure C.6: Linear fit to the MSD for CH₄ in Zn₂(dobdc) at long timescales computed using the DFT-derived force field at 313 K and a loading corresponding to 1.0 bar.

C.3 Self-diffusion Coefficients

The self-diffusion (D_s) coefficients of CH₄ in the three M₂(dobdc) frameworks computed using the DFT-derived force field at 313 K are plotted versus pressure in Figure C.7. Numeric values are listed in Table C.6.

To compare the DFT-derived force field with generic force fields, the D_s coefficients for CH₄ in the three M₂(dobdc) frameworks were also computed at 313 K using the UFF force field (Figure C.8; Table C.7) [189].

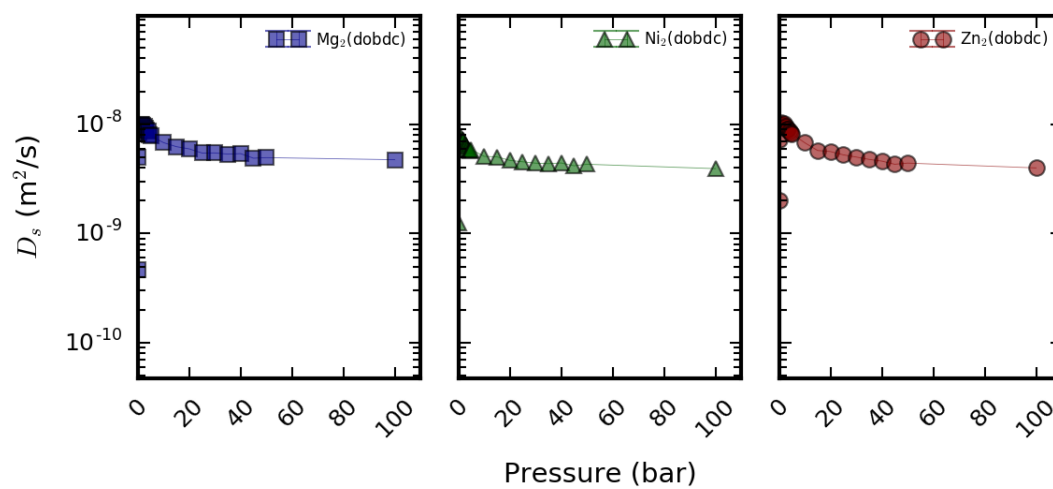


Figure C.7: D_s coefficients for CH_4 plotted versus pressure at 313 K for the three different metal frameworks computed using the DFT-derived force field.

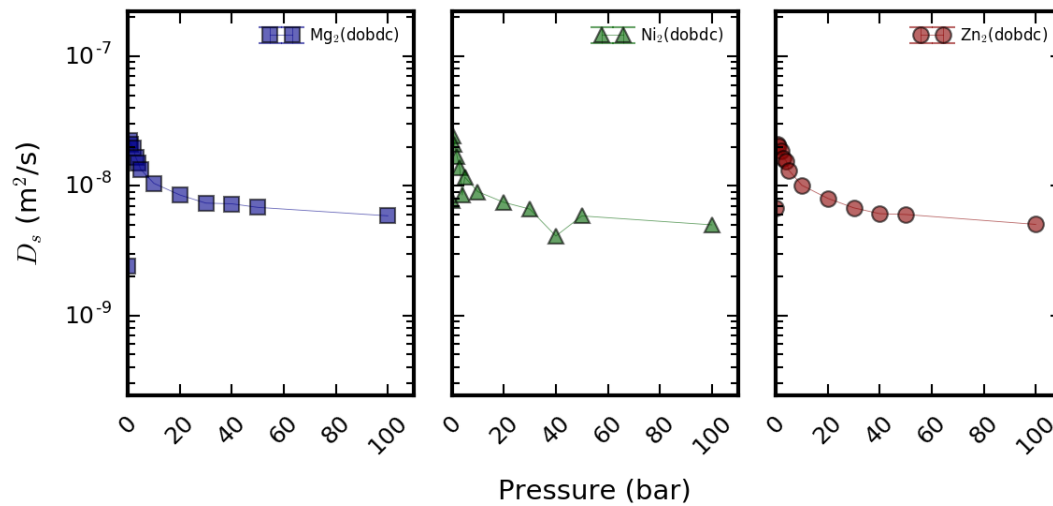


Figure C.8: D_s coefficients for CH_4 plotted versus pressure at 313 K for the three different metal frameworks computed using the UFF force field.

Pressure (bar)	Mg		Ni		Zn	
	D ($\text{\AA}^2/\text{ps}$)	\pm Error	D ($\text{\AA}^2/\text{ps}$)	\pm Error	D ($\text{\AA}^2/\text{ps}$)	\pm Error
0.1	0.04702	0.00884	0.12608	0.03149	0.20262	0.03501
0.25	0.49964	0.03134	0.68843	0.03106	0.72369	0.05860
0.5	0.83875	0.08548	0.71862	0.08444	0.99577	0.05751
1.0	0.98760	0.06730	0.76847	0.07151	1.02861	0.00484
1.5	0.98566	0.03580	0.72789	0.05295	0.97169	0.04683
2.0	0.96969	0.01847	0.70429	0.01896	1.01703	0.10085
2.5	0.96291	0.06031	0.65599	0.01693	0.95693	0.07436
3.0	0.92575	0.04508	0.63409	0.01355	0.89867	0.04150
3.5	0.87894	0.01619	0.59333	0.01472	0.89201	0.02520
4.0	0.86910	0.05631	0.58348	0.00351	0.87201	0.02084
4.5	0.80746	0.02905	0.56944	0.01699	0.82686	0.04076
5.0	0.78191	0.01426	0.58713	0.01902	0.81701	0.01229
10.0	0.67840	0.02065	0.50787	0.01301	0.67653	0.02082
15.0	0.62327	0.00869	0.50242	0.00884	0.57510	0.01184
20.0	0.59509	0.03736	0.46668	0.00337	0.56233	0.00948
25.0	0.54523	0.01931	0.45354	0.01174	0.52453	0.01042
30.0	0.54609	0.01994	0.44036	0.01114	0.50091	0.00494
35.0	0.53283	0.01120	0.43616	0.01285	0.47661	0.00860
40.0	0.53832	0.00829	0.44202	0.00558	0.45979	0.02206
45.0	0.48863	0.02686	0.41675	0.03324	0.43024	0.02287
50.0	0.49474	0.00754	0.43020	0.00586	0.44091	0.03239
100.0	0.47319	0.02278	0.39244	0.01459	0.39829	0.00513

Table C.6: D_s coefficients for CH_4 calculated using the DFT-derived force field at 313 K versus pressure for all three $\text{M}_2(\text{dobdc})$ structures studied in this work.

Pressure (bar)	Mg		Ni		Zn	
	D ($\text{\AA}^2/\text{ps}$)	\pm Error	D ($\text{\AA}^2/\text{ps}$)	\pm Error	D ($\text{\AA}^2/\text{ps}$)	\pm Error
0.1	0.23939	0.04664	0.77268	0.11181	0.67142	0.10505
0.5	2.22147	0.15433	2.40804	0.12110	2.09279	0.07407
1.0	2.10549	0.16306	2.09355	0.03392	2.01523	0.03391
2.0	1.96805	.077347	1.69341	0.04832	1.84494	0.01074
3.0	1.66014	0.13670	1.38125	0.13504	1.63564	0.10718
4.0	1.49549	0.06420	0.84941	0.60098	1.55409	0.05869
5.0	1.33257	0.03043	1.16556	0.04646	1.31975	0.04984
10.0	1.04384	0.02414	0.89997	0.01919	1.00944	0.04993
20.0	0.84852	0.04649	0.74421	0.02699	0.79892	0.03130
30.0	0.73432	0.02179	0.66020	0.01057	0.67506	0.01125
40.0	0.72534	0.01490	0.40903	0.28930	0.60853	0.00179
50.0	0.68065	0.01437	0.58461	0.01788	0.59974	0.02119
100.0	0.58590	0.02539	0.49885	0.00756	0.50306	0.00361

Table C.7: D_s coefficients for CH_4 calculated using UFF at 313 K versus pressure for all three $\text{M}_2(\text{dobdc})$ structures studied in this work.

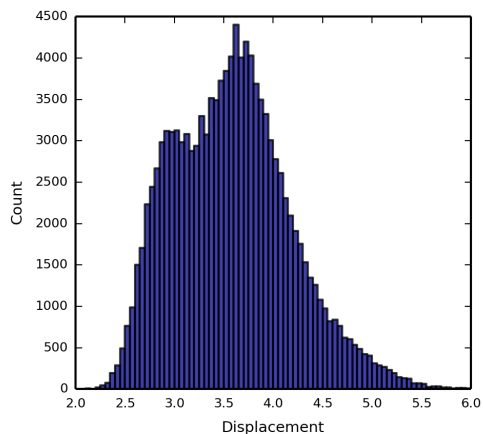


Figure C.9: Histogram of the shortest metal-CH₄ distance for all CH₄ molecules from three combined trajectories in Mg₂(dobdc) at 313 K and 0.1 bar. The displacement is in units of angstroms (Å).

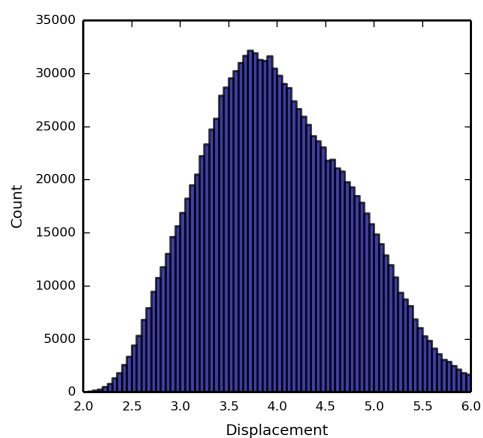


Figure C.10: Histogram of the shortest metal-CH₄ distance for all CH₄ molecules from three combined trajectories in Mg₂(dobdc) at 313 K and 1.0 bar. The displacement is in units of angstroms (Å).

C.4 CH₄ Binding Site Analysis

Considering that most of the CH₄ binds above the metal site in all three frameworks under all conditions considered in this work, histograms of the metal-CH₄ distances during three combined trajectories were created for each framework (Figures C.9 – C.14).

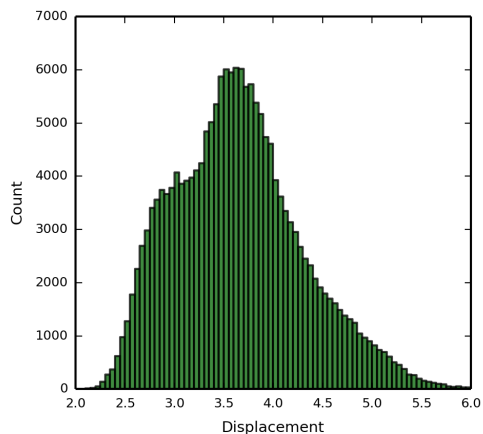


Figure C.11: Histogram of the shortest metal-CH₄ distance for all CH₄ molecules from three combined trajectories in Ni₂(dobdc) at 313 K and 0.1 bar. The displacement is in units of angstroms (Å).

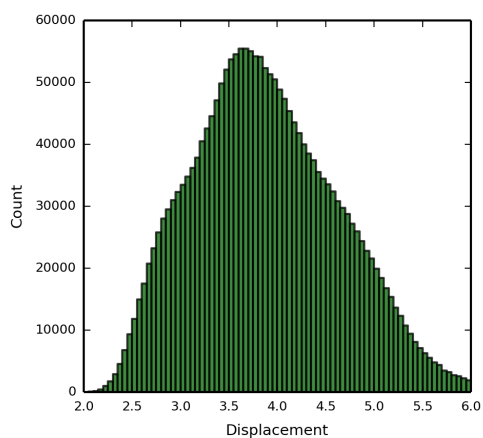


Figure C.12: Histogram of the shortest metal-CH₄ distance for all CH₄ molecules from three combined trajectories in Ni₂(dobdc) at 313 K and 1.0 bar. The displacement is in units of angstroms (Å).

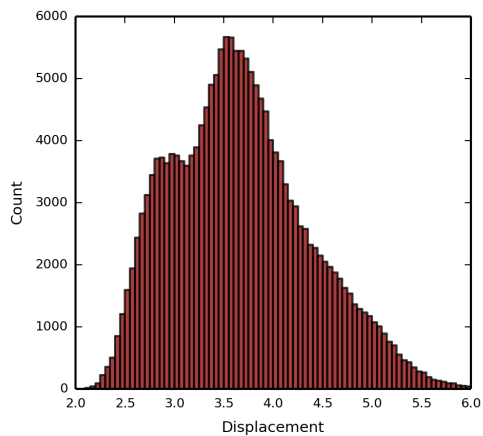


Figure C.13: Histogram of the shortest metal-CH₄ distance for all CH₄ molecules from three combined trajectories in Zn₂(dobdc) at 313 K and 0.1 bar. The displacement is in units of angstroms (Å).

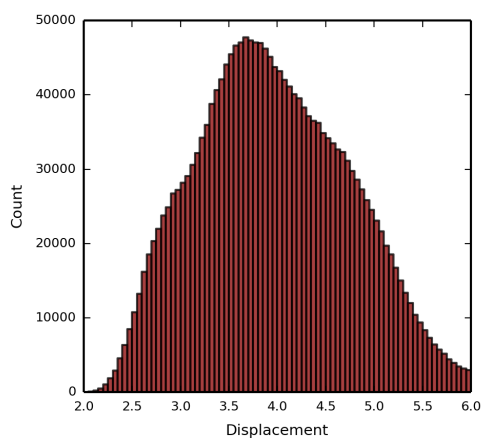


Figure C.14: Histogram of the shortest metal-CH₄ distance for all CH₄ molecules from three combined trajectories in Zn₂(dobdc) at 313 K and 1.0 bar. The displacement is in units of angstroms (Å).

Appendix D

Hypothetical COP-5 Structures

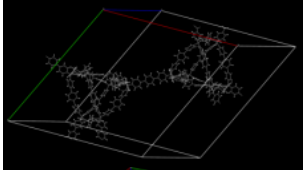
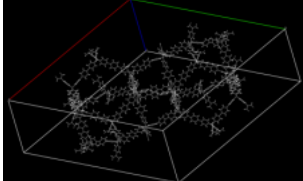
Net	PV ^a	BET SSA ^b	FV % ^c	Structure
acs-a	8.32599	4424	94.0	
afi	5.95609	5870	91.3	

Table D.1: Summary of porosities of hypothetical COP-5 structures with different topologies. ^aPore volumes were determined using a probe atom of radius 1.5 Å and the Voronoi decomposition technique implemented in the Zeo++ open-source software package. Units are in cm³ g⁻¹. ^bBET SSAs were calculated from predicted N₂ isotherms using GCMC simulations; units are in m² g⁻¹. [230, 142] ^cThe free volume percentage of each hypothetical COP-5 structure with a different topology was calculated using the *Atoms Volume and Surface* calculation with a 0.75 Å grid interval implemented in Materials Studio.

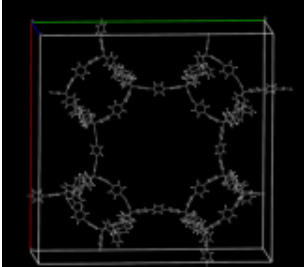
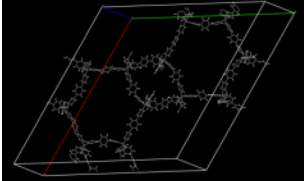

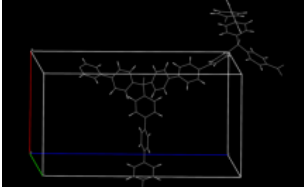
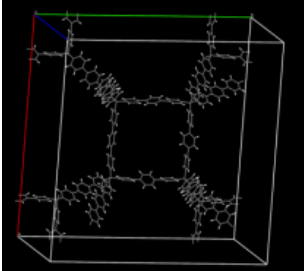
Net	PV ^a	BET SSA ^b	FV % ^c	Structure
atn	5.25608	5341	91.3	
can	5.60174	4397	92.1	
cdl	1.25919	4145	78.4	
cds	1.32973	3454	79.0	
crb	4.90567	5007	90.9	

Table D.2: Summary of porosities of hypothetical COP-5 structures with different topologies. ^aPore volumes were determined using a probe atom of radius 1.5 Å and the Voronoi decomposition technique implemented in the Zeo++ open-source software package. Units are in cm³ g⁻¹. ^bBET SSAs were calculated from predicted N₂ isotherms using GCMC simulations; units are in m² g⁻¹. [230, 142] ^cThe free volume percentage of each hypothetical COP-5 structure with a different topology was calculated using the *Atoms Volume and Surface* calculation with a 0.75 Å grid interval implemented in Materials Studio.

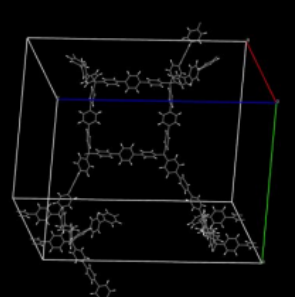
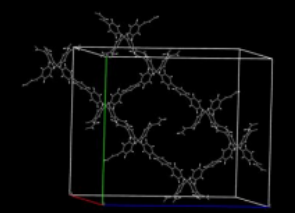
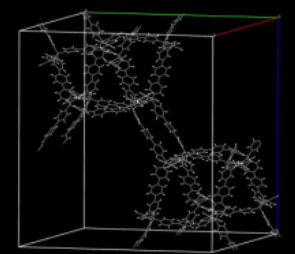
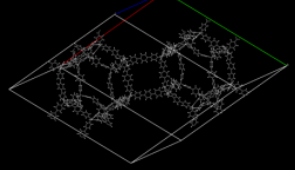
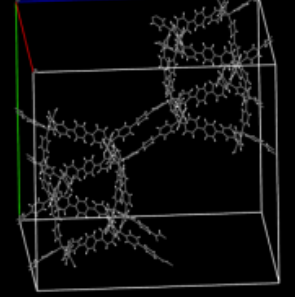
Net	PV ^a	BET SSA ^b	FV % ^c	Structure
dft	5.65201	5176	91.8	
dia	4.3985	5302	90.1	
gis	6.11607	5213	92.3	
gme	6.74483	5407	92.9	
gsi	3.72872	6042	88.8	

Table D.3: Summary of porosities of hypothetical COP-5 structures with different topologies. ^aPore volumes were determined using a probe atom of radius 1.5 Å and the Voronoi decomposition technique implemented in the Zeo++ open-source software package. Units are in cm³ g⁻¹. ^bBET SSAs were calculated from predicted N₂ isotherms using GCMC simulations; units are in m² g⁻¹.^[230, 142] ^cThe free volume percentage of each hypothetical COP-5 structure with a different topology was calculated using the *Atoms Volume and Surface* calculation with a 0.75 Å grid interval implemented in Materials Studio.

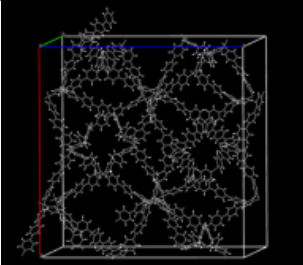
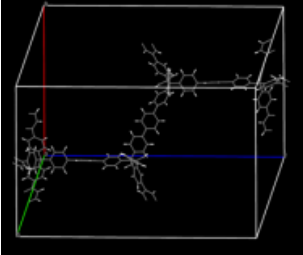
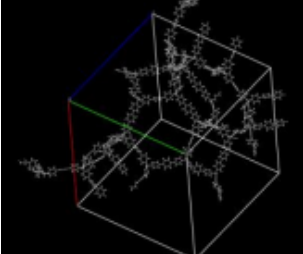
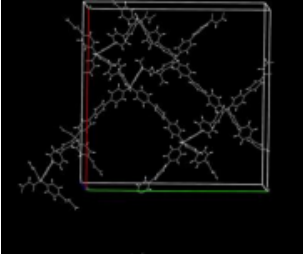
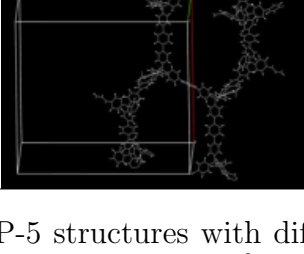
Net	PV ^a	BET SSA ^b	FV % ^c	Structure
lcs	4.15473	5835	89.6	
lon	4.56469	5312	90.3	
lta	7.15643	6638	93.2	
mdf	1.06604	4416	77.1	
mmt	3.75653	6965	88.8	

Table D.4: Summary of porosities of hypothetical COP-5 structures with different topologies. ^aPore volumes were determined using a probe atom of radius 1.5 Å and the Voronoi decomposition technique implemented in the Zeo++ open-source software package. Units are in cm³ g⁻¹. ^bBET SSAs were calculated from predicted N₂ isotherms using GCMC simulations; units are in m² g⁻¹. [230, 142] ^cThe free volume percentage of each hypothetical COP-5 structure with a different topology was calculated using the *Atoms Volume and Surface* calculation with a 0.75 Å grid interval implemented in Materials Studio.

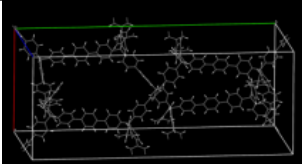
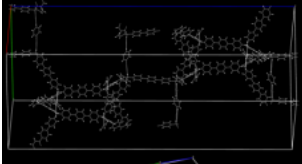
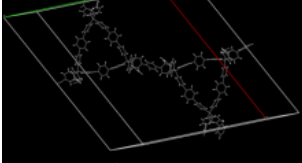
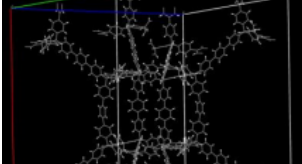

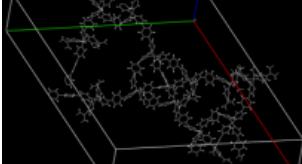
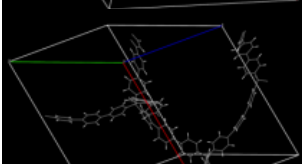
Net	PV ^a	BET SSA ^b	FV % ^c	Structure
mok	1.98096	4268	83.1	
mon	5.70284	5388	91.9	
npo	6.59508	4609	92.8	
pcb	5.88562	5215	92.1	
qdl	0.90678	2961	75.0	
qtz-a	10.48	6314	95.1	
qtz	3.37346	3785	88.0	

Table D.5: Summary of porosities of hypothetical COP-5 structures with different topologies. ^aPore volumes were determined using a probe atom of radius 1.5 Å and the Voronoi decomposition technique implemented in the Zeo++ open-source software package. Units are in cm³ g⁻¹. ^bBET SSAs were calculated from predicted N₂ isotherms using GCMC simulations; units are in m² g⁻¹.^[230, 142] ^cThe free volume percentage of each hypothetical COP-5 structure with a different topology was calculated using the *Atoms Volume and Surface* calculation with a 0.75 Å grid interval implemented in Materials Studio.

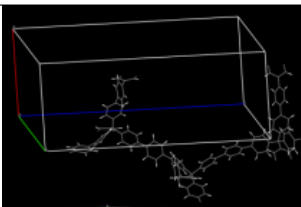
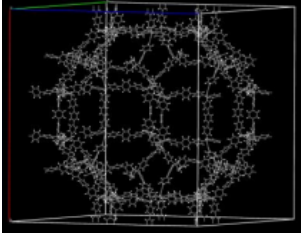
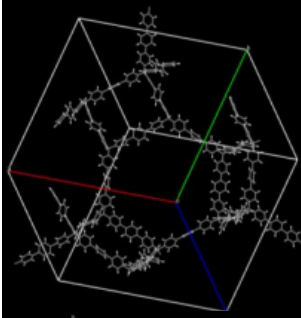
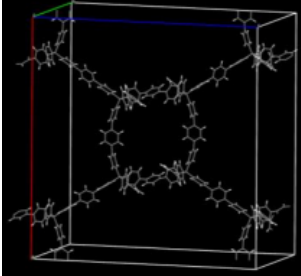
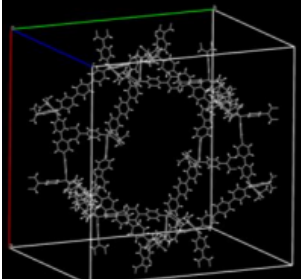
Net	PV ^a	BET SSA ^b	FV % ^c	Structure
qzd	0.88413	3298	74.9	
rho	7.25385	5057	93.3	
sod	5.8475	4584	92.0	
sra	5.12534	5277	91.2	
tzs	5.21705	5637	91.3	

Table D.6: Summary of porosities of hypothetical COP-5 structures with different topologies. ^aPore volumes were determined using a probe atom of radius 1.5 Å and the Voronoi decomposition technique implemented in the Zeo++ open-source software package. Units are in cm³ g⁻¹. ^bBET SSAs were calculated from predicted N₂ isotherms using GCMC simulations; units are in m² g⁻¹. [230, 142] ^cThe free volume percentage of each hypothetical COP-5 structure with a different topology was calculated using the *Atoms Volume and Surface* calculation with a 0.75 Å grid interval implemented in Materials Studio.

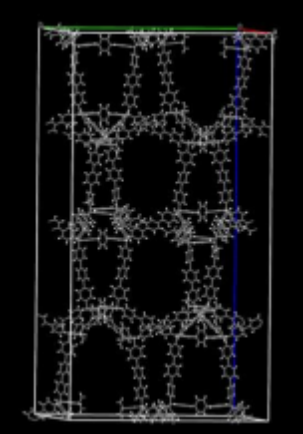
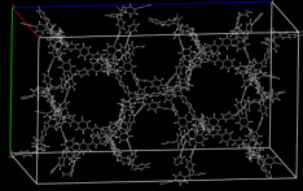
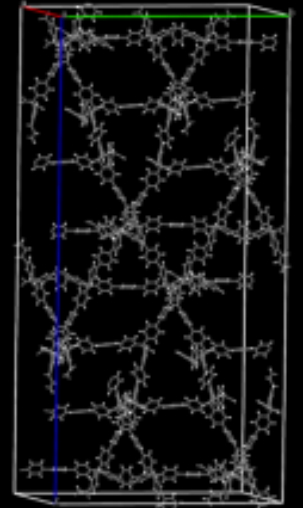
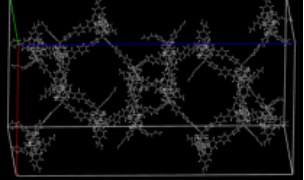
Net	PV ^a	BET SSA ^b	FV % ^c	Structure
ukc	4.64296	5158	90.5	
ukd	3.74124	6937	88.7	
ukm	2.98754	5490	87.0	
umi	5.2882	5335	91.4	

Table D.7: Summary of porosities of hypothetical COP-5 structures with different topologies. ^aPore volumes were determined using a probe atom of radius 1.5 Å and the Voronoi decomposition technique implemented in the Zeo++ open-source software package. Units are in cm³ g⁻¹. ^bBET SSAs were calculated from predicted N₂ isotherms using GCMC simulations; units are in m² g⁻¹. [230, 142] ^cThe free volume percentage of each hypothetical COP-5 structure with a different topology was calculated using the *Atoms Volume and Surface* calculation with a 0.75 Å grid interval implemented in Materials Studio.

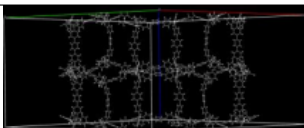
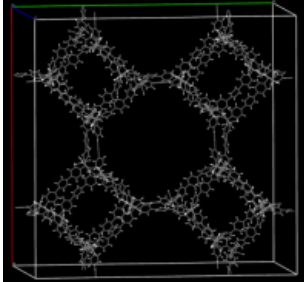
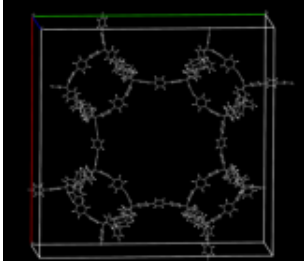
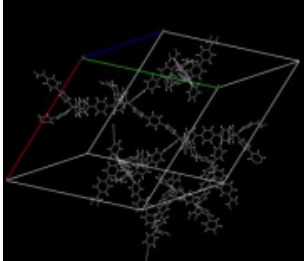
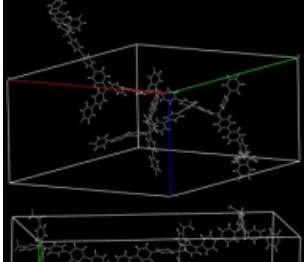
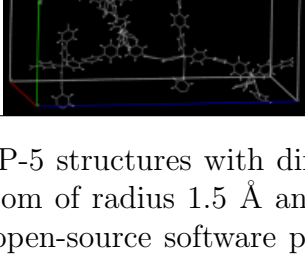
Net	PV ^a	BET SSA ^b	FV % ^c	Structure
umk	6.07776	5490	92.2	
umq	5.44662	5099	91.6	
umr	5.3071	5121	91.3	
unf	3.12429	6713	87.3	
uni	4.29182	6718	90.0	
uoc	4.35235	4997	90.0	

Table D.8: Summary of porosities of hypothetical COP-5 structures with different topologies. ^aPore volumes were determined using a probe atom of radius 1.5 Å and the Voronoi decomposition technique implemented in the Zeo++ open-source software package. Units are in cm³ g⁻¹. ^bBET SSAs were calculated from predicted N₂ isotherms using GCMC simulations; units are in m² g⁻¹.^[230, 142] ^cThe free volume percentage of each hypothetical COP-5 structure with a different topology was calculated using the *Atoms Volume and Surface* calculation with a 0.75 Å grid interval implemented in Materials Studio.

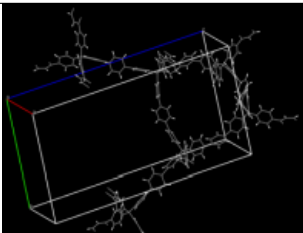
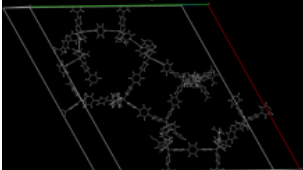
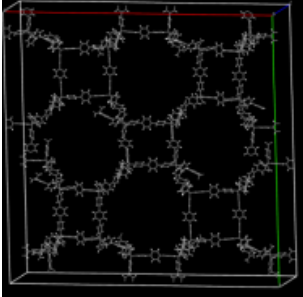
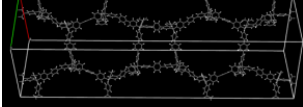
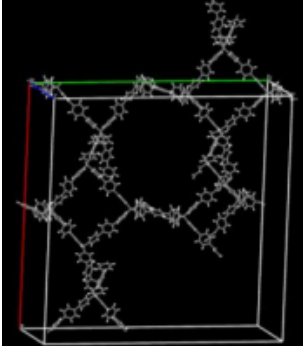
Net	PV ^a	BET SSA ^b	FV % ^c	Structure
uoo	2.48331	6839	85.2	
uoq	5.0021	6861	90.9	
uos	4.35987	4.35987	90.0	
uoy	4.26775	5106	89.8	
uoz	4.04385	6884	89.3	

Table D.9: Summary of porosities of hypothetical COP-5 structures with different topologies. ^aPore volumes were determined using a probe atom of radius 1.5 Å and the Voronoi decomposition technique implemented in the Zeo++ open-source software package. Units are in cm³ g⁻¹. ^bBET SSAs were calculated from predicted N₂ isotherms using GCMC simulations; units are in m² g⁻¹. [230, 142] ^cThe free volume percentage of each hypothetical COP-5 structure with a different topology was calculated using the *Atoms Volume and Surface* calculation with a 0.75 Å grid interval implemented in Materials Studio.

Appendix E

Additional Information for Design of 2D and 3D COFs for ANG Storage Applications

E.1 *In Silico* Bond Formation using Zeo++

Starting from the dibromo compound, the linker structure files are modified before beginning the *in silico* assembly procedure so as to remove any atoms that would disappear upon the formation of the bond. These are then replaced with dummy atoms at the connection points. Using the Zeo++ *Framework Builder* tool [142, 230, 141], the modified linkers are then aligned according to a given topological net such that the dummy atoms are placed overlapping to one another, or as close to overlapping as possible. The Zeo++ *Framework Builder* works by minimizing the root mean square displacement between linkage sites on each molecule, such that for a given input combination of net and linkers, the output is the framework that minimizes the total root mean square displacement. However, if the displacement exceeds a specified threshold, or if the trial structure contains overlapping atoms, then the framework is discarded.

Based purely on combinatorics, the number of structures expected to be formed from 90 linear, 6 trigonal, and 15 tetragonal linkers, in combination with 839 nets given the constraints of two linkers per structure and linker symmetry matching net vertex symmetry, is 1,705,914. The calculation is outlined below:

of C_4 linkers per set: 6

of C_3 linkers per set: 15

of C_2 linkers per set: 90

of nets with 1 vertex, coordination number 4: 3 2D nets + 231 3D nets = 234

of nets with 1 vertex, coordination number 3: 4 2D nets + 79 3D nets = 83

of nets with 2 vertices, coordination numbers 4 and 4: 17 2D nets + 293 3D nets = 310

of nets with 2 vertices, coordination numbers 4 and 3: 29 2D nets + 94 3D nets = 123

of nets with 2 vertices, coordination numbers 3 and 3: 9 2D nets + 100 3D nets = 109

C₄ + C₄ linkers: 6 x 234 + 6 x 5 x 310 = 10,704

C₄ + C₃ linkers: 6 x 15 x 123 = 11,070

C₄ + C₂ linkers: 6 x 90 x 234 = 126,360

C₃ + C₃ linkers: 15 x 83 + 15 x 14 x 109 = 24,135

C₃ + C₂ linkers: 15 x 90 x 83 = 112,050

Subtotal: 10,704 + 11,070 + 126,360 + 24,135 + 112,050 = 284,319

Total: 284,319 * 6 sets of linkers = **1,705,914 structures theoretically possible**

This number is solely provided as an upper bound and does not take into account external factors such as parsing errors encountered with some of the nets on the RCSR and certain linkers only being able to combine with certain linkers, which effectively decrease this number.

E.2 Structural Optimization in LAMMPS

All structures are minimized as follows: first, an energy minimization of the system is performed by iteratively adjusting atomic positions via steepest descent until one of the stopping criteria (1e-08 stopping tolerance for both the energy and the forces, 10000 max iterations of the minimizer, or 100000 max number of force/energy evaluations) is satisfied; then, the lattice dimensions are optimized by isotropically scaling lattice vectors and atomic positions via steepest descent until one of the stopping criteria is satisfied; finally, atomic positions of the system are iteratively adjusted using the FIRE [10] optimizer until one of the stopping criteria is satisfied. Details on the potentials and cut-offs used are given in the main text.

For the energy stopping criterion, the specified energy tolerance of 1e-08 is unitless; it is met when the energy change between successive iterations divided by the energy magnitude is less than or equal to it. For the force stopping criterion, the specified force tolerance of 1e-08 is in units of kcal mol⁻¹ Å⁻¹ (using the *real* style units); it is the length of the global force vector for all atoms. Since many of the components will be near zero after minimization, it acts as an upper bound on the final force on any component of any atom.

The last two steps (unit cell optimization via steepest descent, atomic coordinates optimization via FIRE) are repeated two more times with the same stopping criteria before saving the final structure/lattice parameters. On average, each structural optimization takes about a minute to run using a serial compiled LAMMPS binary.

Given the large number of structures, minimization jobs are set to timeout after five minutes when preparing LAMMPS input using *lammps_interface* and to timeout after twenty

minutes during the LAMMPS minimization step. Without these timeouts set, the jobs will take longer to complete than anticipated on a given set of processors, because one or two poorly-assembled structures will use the bulk of the computational time. The way these timeouts were determined is as follows: for a set of about one hundred test structures, 80% of the input files had been generated by *lammps_interface* after five minutes, and those jobs that were not yet complete usually contained extraneous or missing bonds in the structure; this is because when there are missing bonds in a structure, it is sometimes the case that there are disconnected fragments, so *lammps_interface* identifies more than one “molecule” and therefore takes a lot longer to find all the bonds and write the LAMMPS topology file. On the other hand, approximately 90% of the structural minimization jobs in LAMMPS had converged after twenty minutes. As such, we felt confident in throwing out structures if they were taking longer than five minutes to generate a LAMMPS topology file using *lammps_interface* and longer than twenty minutes to optimize in LAMMPS; even if they converged, most remaining structures would not be carried over to the next step due to bad features present.

E.3 Removing Poorly Converged Structures

It is important to be able to identify poorly assembled structures in a high-throughput manner so that structures which are not chemically reasonable do not end up in the database.

The first step in identifying bad structures is to remove structures which contain *unbound* atoms. These can easily be identified using Zeo++ by running the command *network -strinfo [structure name].cssr*, which returns an output file that looks like:

```
[structure name].strinfo  [chemical formula]  [num] segments: [num] \
framework(s) (1D/2D/3D [num*] [num] [num] ) and [num*] molecule(s). \
Identified dimensionality of framework(s): [num] [num] [num].
```

If either of the numbers followed by an asterisk above ([num*]) are non-zero in the output file, then the framework (a) is not a 2D-layered or 3D-extended structure (though periodic; e.g. composed of periodic 1D chains), and/or (b) contains unbound atoms. Such frameworks were removed from the database.

However, the above two criteria are not enough to identify all poorly-assembled structures. There is a third type of unacceptable structure that can occur when the Zeo++ *Framework Builder* successfully writes a structure which is chemically unreasonable and contains extraneous bonds. These extraneous bonds arise because *lammps_interface* determines the number of bonds in each framework via the distance between neighboring atoms; an extraneous bond may form if during framework assembly two atoms from neighboring linkers end up closer to each other than the length of the bond which is formed, but not close enough to be flagged as overlapping. For example, a proton around a formed amine

bond might end up too close to the nitrogen such that *lammps_interface* will identify this as a -H-N- bond, even though it will also have identified the -H-C- bond. As neither Zeo++ nor *lammps_interface* “know” that a proton cannot have two such bonds, the structure will not be flagged and we must intervene.

To flag this class of bad structures and remove them from the database, we compare the *expected* number of bonds to be formed per unit cell in a given framework with the number of bonds *actually* formed by the Zeo++ *Framework Builder*. We wrote a Python script which uses manually encoded dictionaries containing the number of bonds in each linker as well as the number of linkage sites for each linker (the bonds were extracted from each linker’s MOL2 file). During the structure assembly process, a file is generated for each framework by Zeo++ containing the number of each linker per unit cell (the *ratio* file). This file is read to determine the number of linkers in each framework’s unit cell. Combined with the above information, the expected number of bonds in one unit cell of the framework is calculated. Assuming M molecules of *linkerA* and N molecules of *linkerB* are incorporated per unit cell of framework, the number of *internal* bonds is simply $M * (\# \text{ bonds in } linkerA) + N * (\# \text{ bonds in } linkerB)$. The number of *external* bonds, or those coming from bonds formed, is given by $0.5 * (M * (\text{connectivity of } linkerA) + N * (\text{connectivity of } linkerB))$. Averaging over the two linkers is important because they are not necessarily present in equal amounts.

The expected number of bonds in one unit cell of each framework is then compared to that found in the LAMMPS topology files generated by *lammps_interface*, which computes bonds by measuring the distances between atoms and comparing to threshold values. If there is a mismatch between the expected and actual number of bonds in a structure, the framework is flagged and removed from the database.

E.4 Lists of Linkers in Library

Tables E.1 – E.9 list the IUPAC names of the 111 different types of linkers which we used in the assembly of the carbon-carbon-bonded frameworks, along with the identifier we use in the database. Starting from the dibromo compound, we modify the linkers before beginning the *in silico* assembly process so as to remove any atoms which disappear upon the formation of the bond. The light green balls in all the figures represent the dummy atoms which were used as connection points in the *in silico* assembly process, where linkers were aligned so that the light green dummy atoms were placed overlapping to one another. These were placed approximately 0.75 Å along the original C–Br bond (approximately half the length of the average C–C single bond [33]), and the Br atoms then deleted from the linker structure files. In these figures, carbon atoms are illustrated as gray balls, oxygen atoms as red balls, nitrogen atoms as light blue balls, sulfur atoms as yellow balls, fluorine atoms as yellow-green balls, and hydrogen atoms as white balls.

Furthermore, note that for each of the linkers listed below, there exist a set of linkers where the bromines are substituted by derivatives of either the bond-forming aldehyde or amine groups, as would correspond to the formation of imine-bonded frameworks (Figure

E.3) and a loss of water. Similarly, two more sets of linker terminations exist with various carbon, oxygen, nitrogen, and hydrogen atoms around the connection sites, as would correspond to the formation of amide bonds (Figure E.1) and amine bonds (Figure E.2) between linkers. These dummy atoms were placed roughly 0.55 Å out along the direction of the bond to be formed, so that in the crude *in silico* assembled structures containing amide and amine bonds, the newly formed bonds would be 1.1 Å in length. On the other hand, for the imine bond forming linkers, these dummy atoms were placed roughly 0.65 Å out along the direction of the bond to be formed, so that in the crude *in silico* assembled structures containing imine bonds, the newly formed bonds would be 1.3 Å in length. These crude structures of course have to then be optimized, as there is not a single “correct” bond length for a given bond type, but a range of bond lengths which depends on the chemical environment. Note that for the five sets of precursors to the imine, amide, and amine bonded structures, we do not filter by commercial availability, although we did confirm that many of them were indeed commercially available.

Tables E.1 – E.7 list the linear (C_1 or C_2 symmetry) linkers. Table E.8 lists the trigonal (C_3 or D_3 symmetry) linkers. Table E.9 lists the tetragonal (C_4 , D_4 , or T_d symmetry) linkers. The “Linker #” is the identifier that is used in the database to refer to that linker in filenames. The images in Tables E.1 – E.9 are for the 111 carbon-carbon bond forming precursors only; so as to not list another 555 very similar images, Figures E.1 – E.3 describe the linker terminations of the five other sets of linker terminations used in the formation of the amide, amine, and imine bonded structures, from which the reader can see that replacing the green dummy atoms in Tables E.1 – E.9 with the linker terminations shown will result in the other 555 linkers.

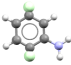
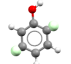
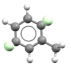
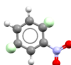
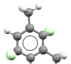
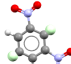
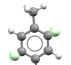
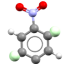
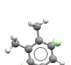
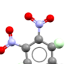
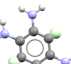
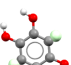
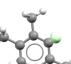
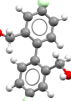
Linker #	IUPAC Name	Structure
1	2,5-dibromoaniline	
2	2,5-dibromophenol	
3	2,5-dibromotoluene	
4	1,4-dibromo-2-nitrobenzene	
5	2,5-dibromo-1,3-dimethylbenzene	
6	2,5-dibromo-1,3-dinitrobenzene	
7	1,4-dibromo-2,5-dimethylbenzene	
8	1,4-dibromo-2,5-dinitrobenzene	
9	1,4-dibromo-2,3-dimethylbenzene	
10	1,4-dibromo-2,3-dinitrobenzene	
11	3,6-dibromobenzene-1,2,4,5-tetraamine	
12	3,6-dibromobenzene-1,2,4,5-tetraol	
13	1,4-dibromo-2,3,5,6-tetramethylbenzene	
14	(4,4'-dibromo-[1,1'-biphenyl]-2,2'-diyl)dimethanol	

Table E.1: List of linear linkers used in the assembly of the C–C frameworks.

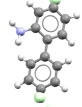
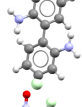

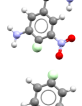
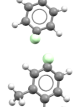
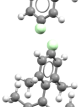
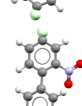
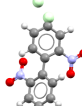
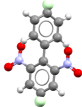
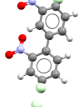
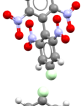

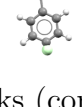

Linker #	IUPAC Name	Structure
15	4,4'-dibromo-[1,1'-biphenyl]-2-amine	
16	4,4'-dibromo-[1,1'-biphenyl]-2,2'-diamine	
17	4,4'-dibromo-5,6'-dinitro-[1,1'-biphenyl]-2,3'-diamine	
18	4,4'-dibromo-5,5'-dinitro-[1,1'-biphenyl]-2,3'-diamine	
19	4,4'-dibromo-1,1'-biphenyl	
20	4,4'-dibromo-2,2'-dimethyl-1,1'-biphenyl	
21	4,4'-dibromo-2,2',6,6'-tetramethyl-1,1'-biphenyl	
22	4,4'-dibromo-2-nitro-1,1'-biphenyl	
23	4,4'-dibromo-2,2'-dinitro-1,1'-biphenyl	
24	4,4'-dibromo-2,6-dinitro-1,1'-biphenyl	
25	4,4'-dibromo-2,3'-dinitro-1,1'-biphenyl	
26	4,4'-dibromo-2,2',6,6'-tetranitro-1,1'-biphenyl	
27	2,7-dibromo-4-nitro-9,10-dihydrophenanthrene	
28	4,4'-dibromo-3-nitro-1,1'-biphenyl	

Table E.2: List of linear linkers used in the assembly of the C-C frameworks (cont).


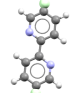
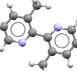
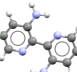
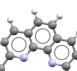
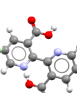
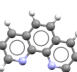
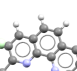
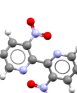
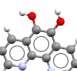
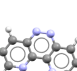
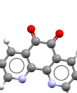
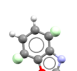
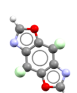
Linker #	IUPAC Name	Structure
29	4,4'-dibromo-5,5'-dinitro-[1,1'-biphenyl]-2,2'-diamine	
30	5,5'-dibromo-2,2'-bipyridine	
31	5,5'-dibromo-3,3'-dimethyl-2,2'-bipyridine	
32	5,5'-dibromo-2,2'-bipyridine-3,3'-diamine	
33	3,8-dibromo-2,9-dimethyl-1,10-phenanthroline	
34	5,5'-dibromo-[2,2'-bipyridine]-3,3'-dicarboxylic acid	
35	3,8-dibromo-1,10-phenanthroline	
36	3,8-dibromo-2-methyl-1,10-phenanthroline	
37	5,5'-dibromo-3,3'-dinitro-2,2'-bipyridine	
38	3,8-dibromo-1,10-phenanthroline-5,6-diol	
39	3,8-dibromodipyrido[3,2-c:2',3'-e]pyridazine	
40	3,8-dibromo-1,10-phenanthroline-5,6-dione	
41	4,7-dibromobenzoxazole	
42	4,8-dibromo[1,2-d:4,5-d']bisoxazole	

Table E.3: List of linear linkers used in the assembly of the C-C frameworks (cont).

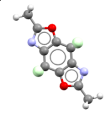
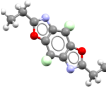
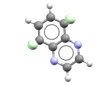
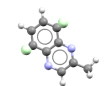
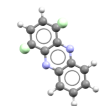
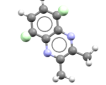
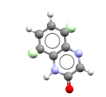
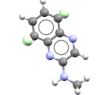
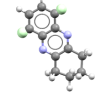
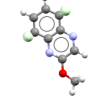
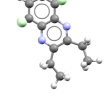
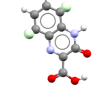
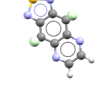
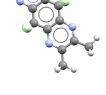
Linker #	IUPAC Name	Structure
43	4,8-dibromo-2,6-dimethylbenzo[1,2-d:4,5-d']bis(oxazole)	
44	4,8-dibromo-2,6-diethylbenzo[1,2-d:4,5-d']bis(oxazole)	
45	5,8-dibromoquinoxaline	
46	5,8-dibromo-2-methylquinoxaline	
47	1,4-dibromophenazine	
48	5,8-dibromo-2,3-dimethylquinoxaline	
49	5,8-dibromoquinoxalin-2(1H)-one	
50	5,8-dibromo-N-methyl-2-quinoxalinamine	
51	6,9-dibromo-1,2,3,4-tetrahydrophenazine	
52	5,8-dibromo-2-methoxyquinoxaline	
53	5,8-dibromo-2,3-diethylquinoxaline	
54	5,8-dibromo-3-oxo-3,4-dihydroquinoxaline-2-carboxylic acid	
55	4,9-dibromo-[1,2,5]thiadiazolo[3,4-g]quinoxaline	
56	4,9-dibromo-6,7-dimethyl-[1,2,5]thiadiazolo[3,4-g]quinoxaline	

Table E.4: List of linear linkers used in the assembly of the C–C frameworks (cont).

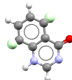
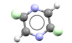
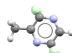
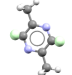
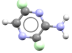
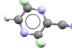
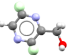
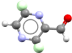
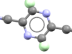
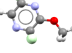
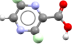
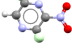
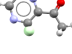
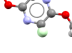
Linker #	IUPAC Name	Structure
57	5,8-dibromoquinazolin-4(1H)-one	
58	2,5-dibromopyrazine	
59	2,5-dibromo-3-methylpyrazine	
60	2,5-dibromo-3,6-dimethylpyrazine	
61	3,6-dibromo-2-pyrazinamine	
62	3,6-dibromopyrazine-2-carbonitrile	
63	(3,6-dibromopyrazin-2-yl)methanol	
64	3,6-dibromopyrazine-2-carbaldehyde	
65	3,6-dibromopyrazine-2,5-carbonitrile	
66	2,5-dibromo-3-methoxypyrazine	
67	3,6-dibromopyrazine-2-carboxylic acid	
68	2,5-dibromo-3-nitropyrazine	
69	1-(3,6-dibromopyrazin-2-yl)ethan-1-one	
70	2,5-dibromo-3,6-methoxypyrazine	

Table E.5: List of linear linkers used in the assembly of the C–C frameworks (cont).

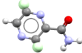
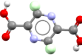
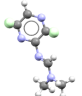
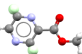
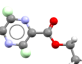
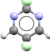
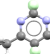
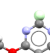
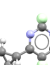
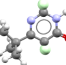
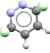
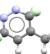
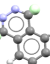
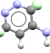
Linker #	IUPAC Name	Structure
71	3,6-dibromopyrazine-2-carboxamide	
72	3,6-dibromopyrazine-2,5-dicarboxylic acid	
73	(E)-N'-(3,6-dibromopyrazin-2-yl)-N,N-dimethylformimidamide	
74	methyl 3,6-dibromopyrazine-2-carboxylate	
75	ethyl 3,6-dibromopyrazine-2-carboxylate	
76	2,5-dibromopyrimidine	
77	2,5-dibromo-4-methylpyrimidine	
78	2,5-dibromo-4-methoxypyrimidine	
79	2,5-dibromo-4-cyclopropylpyrimidine	
80	2,5-dibromo-6-(1,1-dimethylethyl)-4(3H)-pyrimidinone	
81	3,6-dibromopyridazine	
82	3,6-dibromo-4-methylpyridazine	
83	1,4-dibromophthalazine	
84	3,6-dibromo-4-pyridazinamine	

Table E.6: List of linear linkers used in the assembly of the C–C frameworks (cont).

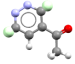
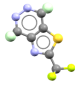
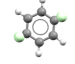
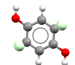
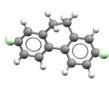

Linker #	IUPAC Name	Structure
85	1-(3,6-dibromo-4-pyridazinyl)-ethanone	
86	4,7-dibromo-2-(trifluoromethyl)-thiazolo[4,5-d]pyridazine	
87	1,4-dibromobenzene	
88	2,5-dibromohydroquinone	
89	2,7-dibromo-9,10-dihydrophenanthrene	
90	6,13-dibromopentacene	

Table E.7: List of linear linkers used in the assembly of the C–C frameworks (cont).


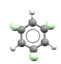

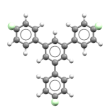
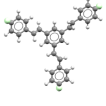
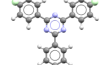
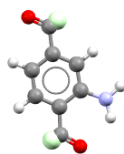
Linker #	IUPAC Name	Structure
91	2,4,6-tribromo-1,3,5-triazine	
92	1,3,5-tribromobenzene	
93	tris(4-bromophenyl)amine	
94	1,3,5- tris(4-bromophenyl)benzene	
95	1,3,5-tris((4-bromophenyl)-ethynyl)benzene	
96	2,4,6-tris(4-bromophenyl)-1,3,5-triazine	

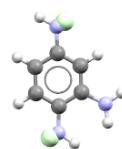
Table E.8: List of trigonal linkers used in the assembly of the C–C frameworks.

Linker #	IUPAC Name	Structure
97	5,10,15,20-tetrakis-(4'-bromo-biphenyl-4-yl)-porphyrin	
98	5,10,15,20-tetrakis-(4-bromophenyl)-porphyrin	
99	3,3',5,5'-tetrabromo-1,1'-biphenyl	
100	3,3',5,5'-tetrabromo-2,2'-biphenyldiol	
101	3,3',5,5'-tetrabromo-2,2'-biphenyldiamine	
102	2,2',7,7'-tetrabromo-9,9'-spirobianthracene	
103	2,2',7,7'-tetrabromo-9,9'-spirobifluorene	
104	3,3',5,5'-tetrabromo-2,2',4,4'-biphenyltetraol	
105	3,3',5,5'-tetrabromo-4,4'-biphenyldiol	
106	3,3',5,5'-tetrabromo-2,2',4,4'-biphenyltetraamine	
107	3,3',5,5'-tetrabromo-4,4'-biphenyldiamine	
108	1,3,6,8-tetrabromopyrene	
109	tetrabromomethane	
110	1,3,5,7-tetrabromoadamantane	
111	tetrabromosilane	

Table E.9: List of tetragonal linkers used in the assembly of the C–C frameworks.

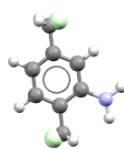
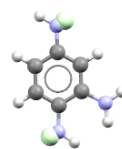


(a) C=O terminations



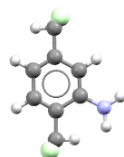
(b) N-H terminations

Figure E.1: Example of the linker terminations for *linker1* (aniline) used in the *in silico* formation of the *amide* bonds. The light green spheres represent dummy atoms.

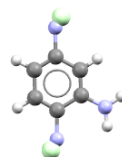
(a) CH₂ terminations

(b) N-H terminations

Figure E.2: Example of the linker terminations for *linker1* (aniline) used in the *in silico* formation of the *amine* bonds. The light green spheres represent dummy atoms.



(a) C-H terminations



(b) N terminations

Figure E.3: Example of the linker terminations for *linker1* (aniline) used in the *in silico* formation of the *imine* bonds. The light green spheres represent dummy atoms.

Bond type	Framework ID	Density (kg/m ³)	DC (v STP/v)
imine	linker109_N_linker87_CH_dia	94.0	94.3
imine	linker109_N_linker87_CH_dia_interp_2	188.0	114.5
imine	linker109_N_linker87_CH_dia_interp_3	282.0	135.9
imine	linker109_N_linker87_CH_dia_interp_5	470.1	149.5
imine	linker109_N_linker87_CH_dia_interp_4	376.1	153.3
imine*	linker109_CH_linker87_N_dia	92.6	93.7
imine*	linker109_CH_linker87_N_dia_interp_2	185.2	120.8
imine*	linker109_CH_linker87_N_dia_interp_3	277.9	147.3
imine*	linker109_CH_linker87_N_dia_interp_4	370.5	165.9

Table E.10: Properties of COF-300 analogues in the database, grouped by bond type and ordered by increasing DC. The bond type *imine** refers to analogues with inverted imine bonds.

E.5 Additional Investigation of Experimentally Synthesized Examples

Here we provide further comparison of our structures to experimental structures of COF-300 and TAPB-PDA COF. [219, 204, 151, 223]

The densities and 65-bar DCs computed for the COF-300 frameworks in the database are listed in Table E.10. Notably, the methane DC is not actually largest in the most interpenetrated form of COF-300, but rather in the four-fold interpenetrated structure. To our knowledge, methane adsorption isotherms have not yet been measured in COF-300 so we are unable to compare to experimental results. Nonetheless, the reported density of the as-synthesized COF-300 structure is 660.0 kg/m³ [219], whereas the density that the authors calculate for their interpenetrated structure model is 540.0 g/cm³, higher than the 470.0 kg/m³ density we predict for the analogous structure in the database.

We briefly investigate how the ANG storage performance may change for these structures if the imine bond were inverted in Table E.10. Interestingly, the analogous structure for each framework with the imine bond flipped has a lower density than the “original” and – with the exception of the non-interpenetrated structure – a higher 65-bar DC, suggesting that synthesizing COF-300 with inverted bonds would enhance its methane storage capacity.

TAPB-PDA COF is known to crystallize in the **hcb** topology, but for comparison, we have listed two additional frameworks in Table E.11 – structures in the **hca** and **hnb** nets. As for COF-300 above, we investigate what would happen upon the inversion of the imine bond in this framework; however, unlike COF-300, inversion of the bond does not appear to influence neither the densities nor the DCs of the corresponding frameworks. To our knowledge, methane adsorption isotherms have not yet been measured in TAPB-PDA COF, so we cannot compare to experimental measurements.

Bond type	Framework ID	Density (kg/m ³)	DC (v STP/v)
imine	linker96_N_linker87_CH_hcb	142.2	115.2
imine	linker96_N_linker87_CH_hca	97.8	97.7
imine	linker96_N_linker87_CH_hnb	119.3	106.2
imine*	linker96_CH_linker87_N_hcb	145.1	116.3
imine*	linker96_CH_linker87_N_hca	96.4	96.4
imine*	linker96_CH_linker87_N_hnb	118.0	105.9

Table E.11: Properties of TAPB-PDA COF analogues in the database, grouped by bond type. The bond type *imine** refers to analogues with inverted imine bonds.

E.6 Additional GCMC Results

Calculating Heats of Desorption

The isosteric heats of desorption, HoD, were calculated during the simulation using the usual expression:

$$\text{HoD} = -Q_{st} = \frac{\langle EN \rangle - \langle E \rangle \langle N \rangle}{\langle N^2 \rangle - \langle N \rangle^2} - RT,$$

where $\langle \rangle$ is the average over the simulation run, N is the number of adsorbate molecules at each sample, and E is the energy of the adsorbate molecules at each sample.

Thermodynamic properties calculated from GCMC simulations for the 2D layered structures (Figures E.4 – E.5) and 3D structures (Figures E.6 – E.7) are shown below. Figures E.4 and E.6 show the distributions in the heats of desorption (HoDs) for the different sets of structures at both the storage and depletion pressures, whereas Figures E.5 and E.7 show the distribution in the HoDs and uptakes versus the framework densities.

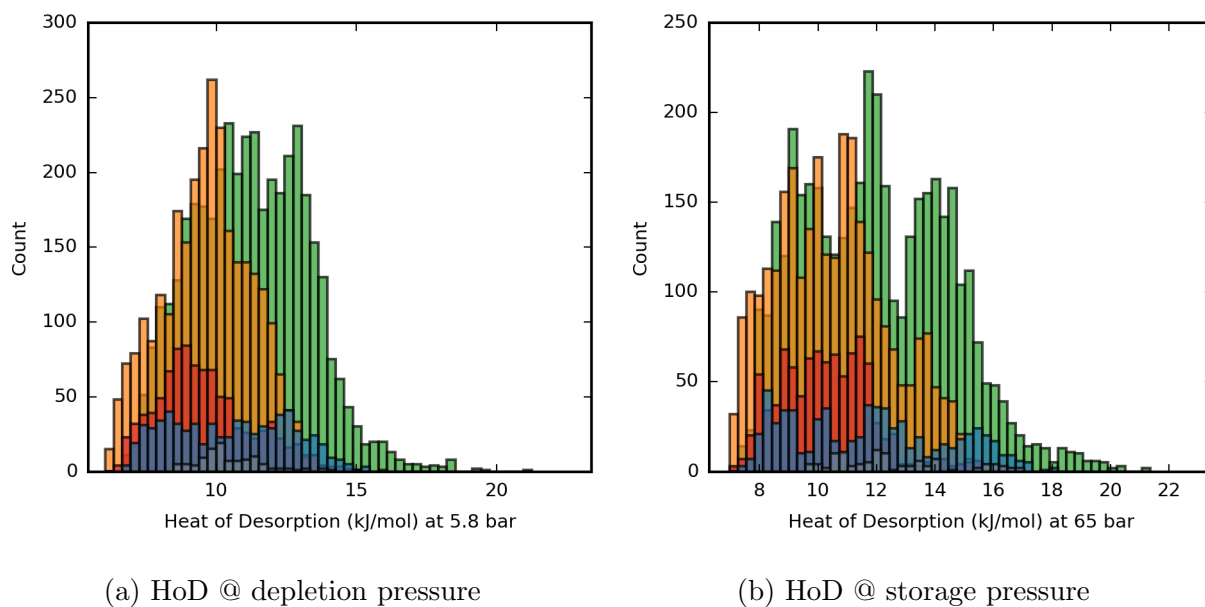


Figure E.4: Histograms of HoDs at the methane depletion and storage pressures for the 2D structures. All results calculated at 298 K. Color key: blue=amide, red=amine, orange=imine, green=C-C, grey=mixed.

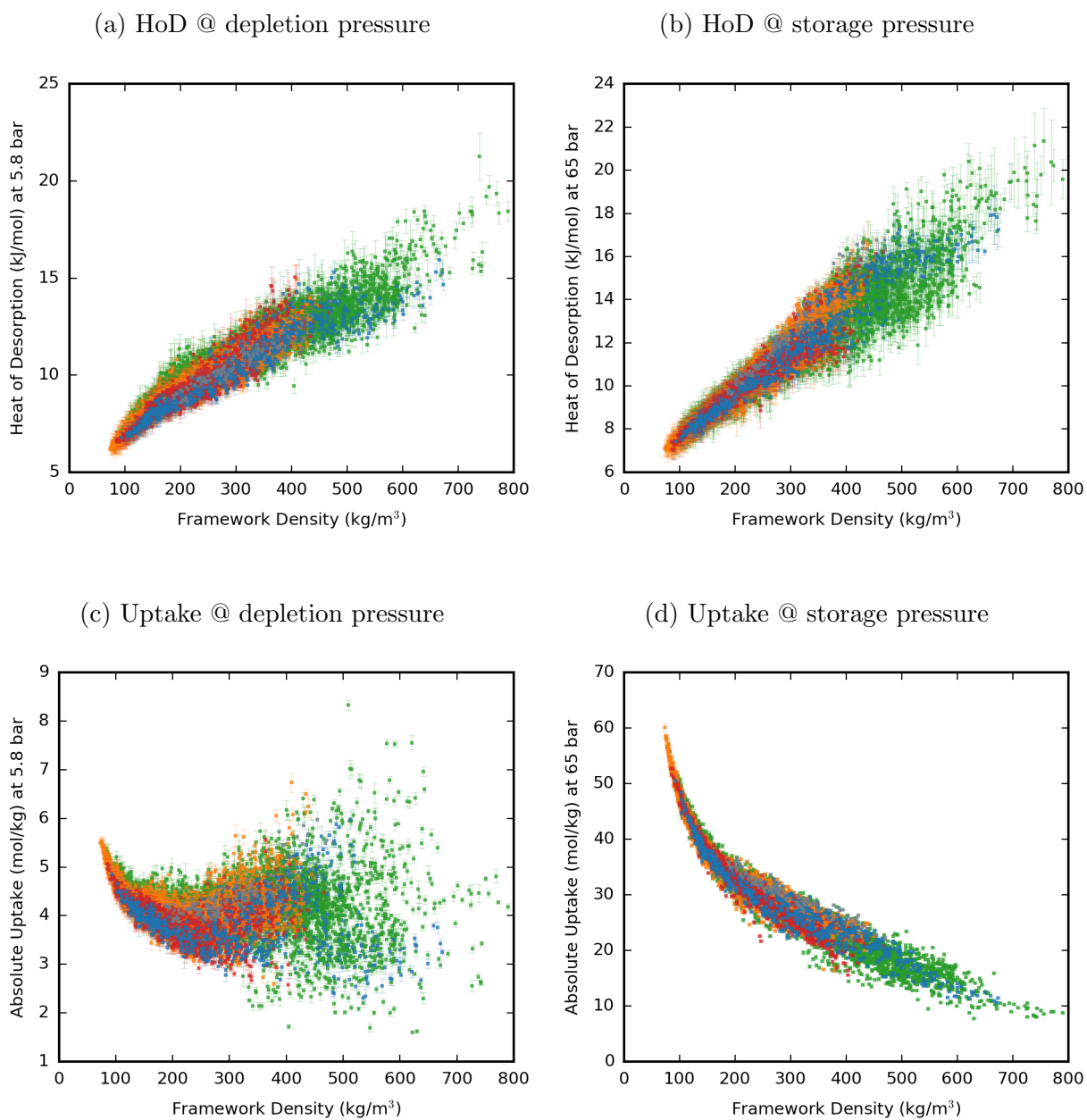


Figure E.5: Plots of the HoDs (a and b) and uptakes (c and d) for methane at the depletion and storage pressures versus the framework densities for the 2D structures. All results calculated at 298 K. Color key: blue=amide, red=amine, orange=imine, green=C-C, grey=mixed.

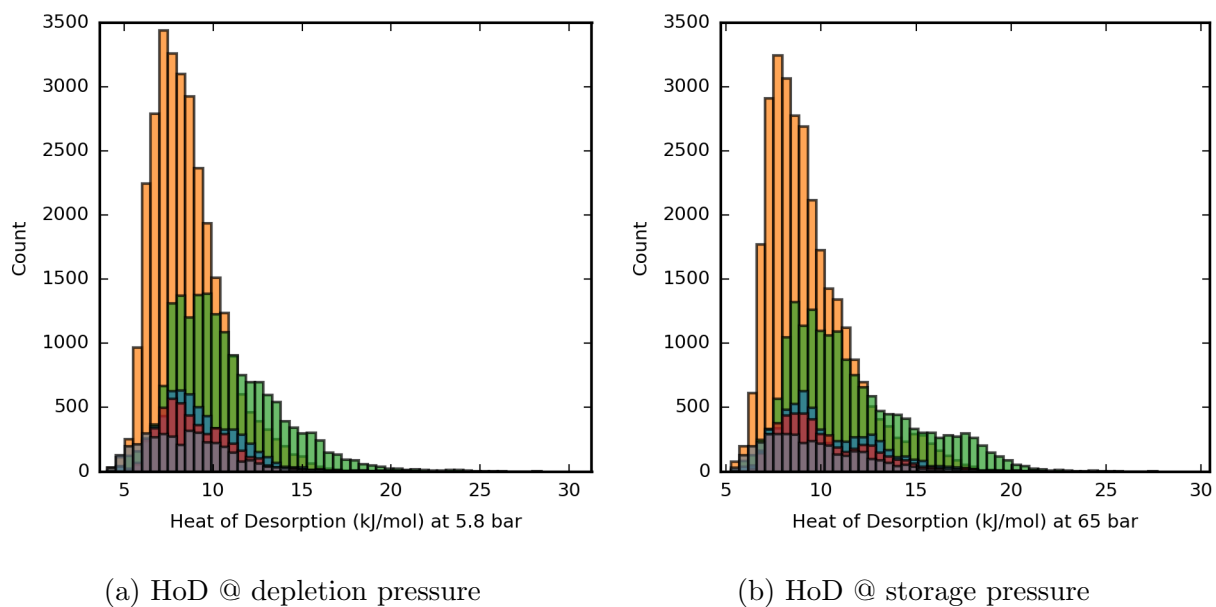


Figure E.6: Histograms of HoDs at the methane depletion and storage pressures for the 3D structures. All results calculated at 298 K. Color key: blue=amide, red=amine, orange=imine, green=C-C, grey=mixed.

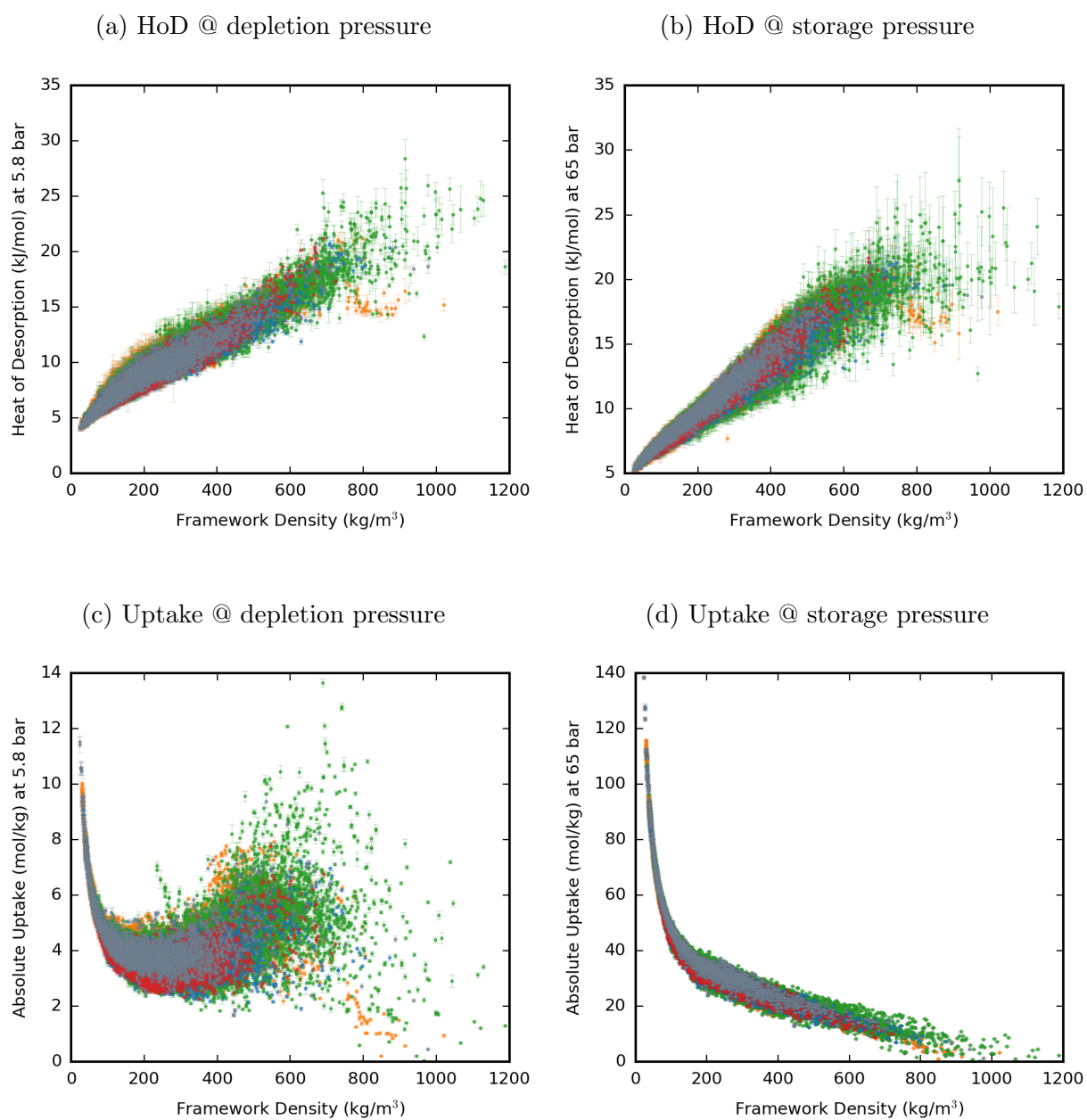


Figure E.7: Plots of the HoDs (a and b) and uptakes (c and d) for methane at the depletion and storage pressures versus the framework densities for the 3D structures. All results calculated at 298 K. Color key: blue=amide, red=amine, orange=imine, green=C-C, grey=mixed.

Helium Void Fractions

The helium void fractions were calculated using Widom insertions for all frameworks in the database for comparison to other databases and for verifying the convergence of the blocked pockets below. In the GCMC simulations, the void fractions were also used to convert from absolute adsorption to excess adsorption. Both the helium void fractions and excess adsorption calculations are available on the Materials Cloud. Note that we do not discuss the DC trends in this work as a function of void fraction because these are simply the inverse of those for the framework density.

Blocked Pockets Convergence

In order to confirm that 100 MC cycles per cubic angstrom is enough to generate satisfactory blocked pockets files for the GCMC simulations, we took a set of 98 structures, selected using a diversity selection algorithm which includes all 111 unique linker scaffolds, and calculated their accessible pore volume. Of these 98 structures, 7 had inaccessible pores. For these 7 frameworks, we generated blocked pockets files using 10, 50, 100, 150, 200, 250, and 1000 MC insertions per cubic angstrom with Zeo++, and computed the helium void fraction using Widom insertions with the various blocking spheres generated. The results are illustrated in Figure E.8.

Although there is a significant jump in the void fraction going from using no blocked pockets to using blocked pockets generated with 10 MC cycles per cubic angstrom, the void fraction does not noticeably decrease after that, showing that the void fraction is indeed sufficiently converged even after 10 cycles per cubic angstrom. Structures for which the void fraction is relatively flat across all values are those in which the inaccessible volume is insignificant compared to the accessible volume in a structure.

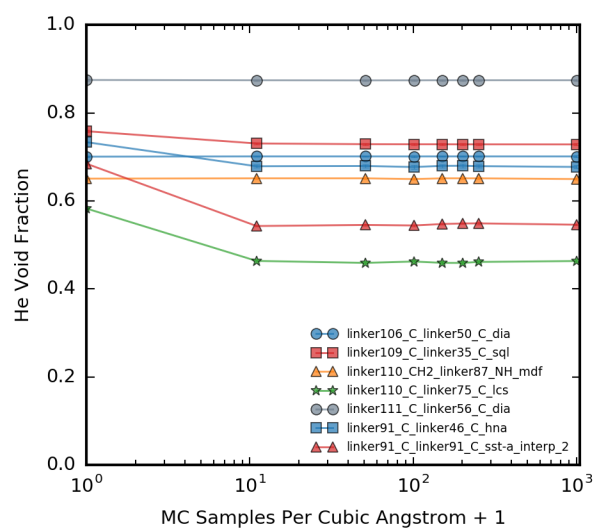


Figure E.8: Convergence of the helium void fraction from Widom insertions as a function of the number of MC samples used to generate the blocked pockets file for simulation.

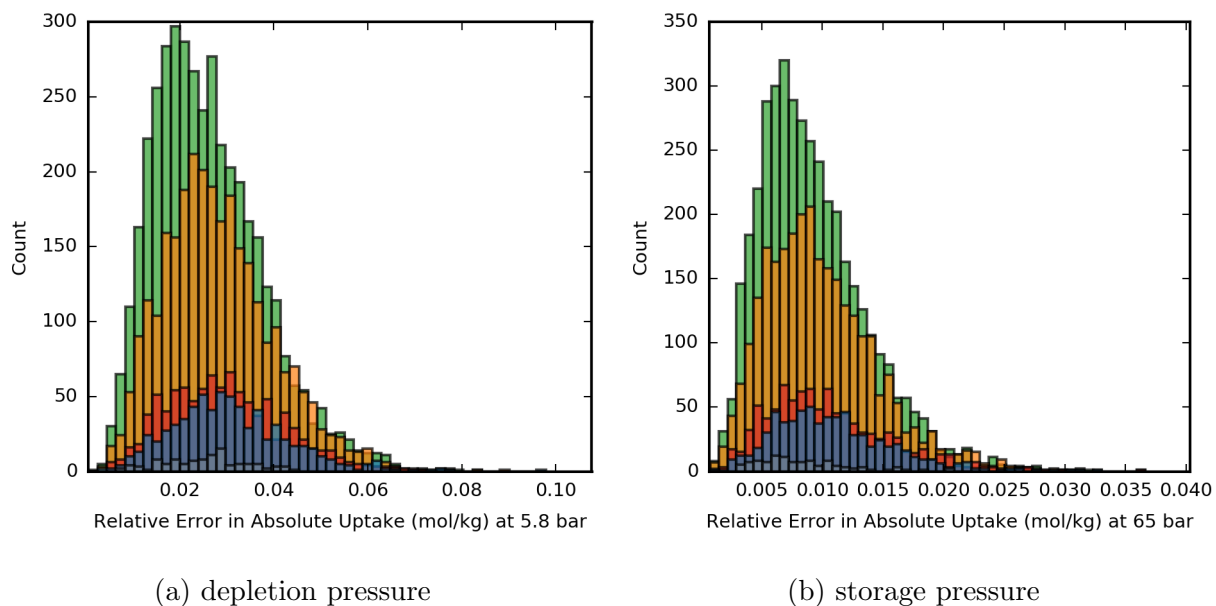


Figure E.9: Histograms of the relative error in the average total methane uptake calculated for each 2D structure from GCMC simulations at the depletion and storage pressure, respectively.

E.7 GCMC Simulation Error

In order to verify that GCMC simulations were run for a sufficiently long time and that thermodynamic averages were converged, we computed the relative error for the average total methane uptake for each structure and plotted the results as histograms (Figures E.9 and E.10). We define the relative error as the standard error divided by the thermodynamic average corresponding to that error. The error is slightly larger for the 3D structures than for the 2D structures using the same number of simulation cycles (5,000 initialization cycles, followed by 5,000 production cycles). The number of cycles was chosen so as to minimize the amount of computational time used while also maintaining an acceptably low error.

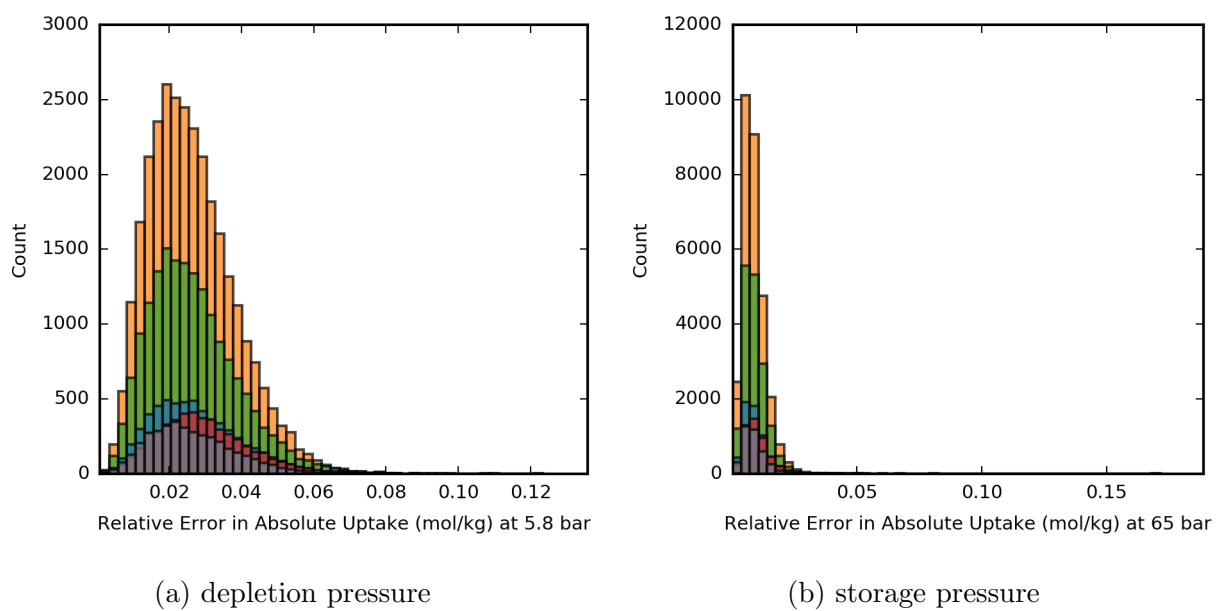


Figure E.10: Histograms of the relative error in the average total methane uptake calculated for each 3D structure from GCMC simulations at the depletion and storage pressure, respectively.

E.8 List of Topological Nets Used

All topological nets satisfying the symmetry constraints of the linkers were downloaded from the RCSR and used to make COFs, although not all nets successfully resulted in an assembled framework. Nets in **bold** indicate that the net contains one unique edge, and thus was used in the formation of the amide, amine, and imine bonded structures from two *non-linear* linkers (but note that amide, amine, and imine bonded structures can still be formed from nets with more than one type of edge so long as *one* linker is linear). For the carbon-carbon bonded structures, there is no restriction on the number of vertices or edges that can be used to assemble a structure so long as the symmetry of the vertices matches that of the linkers.

Total 2D: 48

nets: bew, bex, bey, car, cem, cem-d, cpj, cqj, cqk, cqd, cqe, dha, dhb, dhc, dhd, fes, fsz, fxt, hca, hca-a, **hcb**, hna, hnb, htb, htb-a, kgd-a, **kgm**, krj, krq, krr, krs, krt, kru, krw, krw, krw, kry, mcm, pna, pnb, pnc, pnd, pne, pnf, png, **sql**, tts, usm

Total 3D: 791

nets: acs-a, acs-f, acs-g, afi, afw, afw-a, afw-c, afx, afy, aht, alb-a, **ana**, ana-a, ana-f, apc, apd, asf, ast, asv, atn, ato, att, atv, aww, baa, bab, bac, bad, bae, baf, bag, bah, bai, baj, bak, bal, bam, ban, bao, bap, baq, bar, bas, bat, bau, bav, baw, bax, bay, baz, bba, bbb, bbc, bbd, bbe, bbf, bbg, bbh, bbi, bbj, bbk, bbl, bbn, bbo, bbp, bbq, bbr, bbs, bbu, bbv, bbw, bbx, bby, bbz, bca, bcb, bcd, bce, bcf, bcj, bck, bcm, bcn, bco, bcp, bcq, bcr, bcu-f, bcu-g, bcu-h, bcu-t, bcv, bcw, bcx, bcy, bcz, bda, bel, bik, bmn, bne, bnl, bod, boe, **bor**, bor-a, **bor-c**, bor-c*, bow, bpa, bpb, bpc, bpd, bpe, bpf, bpg, bph, bpi, bpj, bpl, bpm, bpn, bpo, bpp, bpr, bps, bpt, bpu, bpv, brl, bsv, bto, bto-e, bto-z, bva, bwt, byl, cag, cag-b, can, cbo, cbt, cda, cdl, cdm, cdn, cdp, cds, cds-a, cds-b, cds-c, cdt, cdz, cfc, cha, clh, coe, crb, crb-a, crb-b, crr, crt, csq-a, **css**, **ctn**, ctn-a, **ctn-c**, ctn-d, cua, cus, cys-a, ddc, deh, dei, dei-z, dft, dgn, **dia**, dia-a, dia-a-a, dia-a-c, **dia-b**, **dia-c**, **dia-c3**, dia-c3*, **dia-c4**, **dia-c6**, dia-f, dia-g, dma, dmb, dmc, dmd, dme, dmf, dmp, dmp-c, dum, eab, edi, edi-c, edp, elv, eri, eta, eta-c, eta-c3, eta-c4, etb, etb-e, etc, etc-c3, etd, ete, etf, etg, eth, eti, etj, etk, etl, etm, etn, eto, etp, etq, ets, fau, fel, fgl, flu-a, fof, fog, frl, fry, ftc, ftd, fte, ftf, ftg, fth, fti, ftj, ftk, ftl, ftm, ftu, fto, ftp, ftq, ftr, fts, ftt, ftu, ftv, ftx, fty, ftz, fua, fub, fud, fue, fuf, fug, fuh, fui, fuj, ful, fum, fun, fuo, fup, fur, fus, fut, fuu, fuv, fuw, fuy, fuz, fva, fvb, fvc, fvd, fve, fvf, fvg, fvh, fvi, fvj, fvk, fvl, fvm, fvn, fvo, fvp, fvq, fvr, fvs, fvt, fvu, fvv, fvw, fvx, fwz, gah, ggl, gie, gis, gme, gsi, gsi-c, gwg, hal, hbo, hcb-c, hcb-c3, hec, hed, hee, hef, hjm, hof, hst, icc-a, **icd**, icd-a, icf, icm, ict, ins, ins-c, iph, irl, isq, isx, itv, jbw, jea, jeb, jph, jst, kea, kfi, law, lbt, **lcs**, lcs-a, **lcs-b**, lcs-f, **lcv**, lcv-a, lcv-a-c, **lcv-c**, lcv-f, lcy-a, lev, lfm, lfm-c, lig, lig-c, lil, lim, llw-z, lni, lon, lon-a, lon-b, los, lqm, lrj, lta, ltj, ltl, **lvt**, lvt-a, **lvt-b**, **lvt-c**, maw, maz, mdf, mer, mft, mgc-a, mgg, **mhq-z**, mjb, mmt, moa, moc, mog, mog-c, mok, mon, mot, mot-e, mou, msp, mvy, nab, nat, nba, **nbo**, nbo-a, nbo-a-e, **nbo-b**, **nbo-c**, **nbo-c3**, nbo-z, neb, nfa, nfb, nfc, nip, niq, nir, nnd, nob, noc, nod, nof, nof-c, noh, noi, noj, nol, nom, noq, nor, nox, npo, npo-a, nta, ntb, nts-a, nva, nvb, off, ofo, oft, omy, oso, pbg, pbg-e, pbk, pbp, pbp-e, pbz, pbz-b, pbz-e, pcb, pcb-b, pcl, pcu-g, pcu-g-e, pcu-h, pcu-h-e, pcu-h-e-c, pem, phi, phw, phx, ptd, **pth**, pth-a, **pto**, pto-a, ptr, **pts**, pts-a, **pts-c**, pts-f, pts-g, pyd, qdl, **qld-z**, **qtz**, qtz-a, **qtz-b**, **qtz-c**, qtz-c*, **qtz-c3**, **qtz-c4**, **qtz-c6**, qtz-f, qtz-g, qtz-h, qza, qzd, qzd-a, raa, rab, rac, rae, raf, rag, rho, **rhr**, rhr-a, **rhr-b**, sas, sat, sca, scu-a, scu-h, sdt, sgn, sgn-z, sgn-z-c, she-a, shp-a, sie, sin, six, siy, siz, **sod**, sod-a, **sod-b**, sod-f, sod-g, sod-h, sow, sqc-a, **sql-c***, sql-c*, **sql-c3***, sql-c3*, sql-c3**, **sql-c6**, sra, sra-b, sra-c, srb, srd, srd-l, **srs**, srs-a, srs-a-c, srs-a-e, **srs-b**, srs-b*, **srs-c**, srs-c*, srs-c3, **srs-c4**, srs-c4*, **srs-c8**, **ssa**, ssa-a, **ssb**, ssb-a, **ssc**, ssc-a, ssd, ssd-e, sse, ssf, sst, sst-a, sst-e, stj, sto, stp-a, stu, stw, stx, sty, sur, sxc-d, sxt, tbd, **tbo**, tbo-a, tcb, ten, tfa, tfa-c, tfb, tfc, tfc-c, tfg, tfh, tfi, tfk, tfl, tfn, tfo, tfq, tfv, tfz, the-a, thh, thj, ths, ths-b, ths-c, ths-e, ths-z, tna, tof, tpd, tpt-a, tsc, ttc, ttd, ttf, ttg, ttt-a, twf-a, twt, twt-b, twt-c, twt-c3, twt-e, tzs, ucn, ucp, uka, ukb, ukc, ukd, uke, ukf, ukh, uki, ukj, ukk, ukl, ukm,

ukn, uko, ukp, ukr, uks, ukt, uku, ukv, ukw, ukx, uky, ula, uld, uld-c, uld-z, uld-z-c, ulf, ulf-c, ulg, ulh, uli, ulj, ulk-z, ull, ulm, uma, umb, umb-z, umc, umd, ume, umf, umg, umh, umi, umj, umk, uml, umm, umn, umo, umq, umr, ums, umu, umv, umw, umx, umy, umz, una, unb, unc, unc-c, und, une, unf, ung, unh, uni, uni-d, unj, unj-c, unl, unm, unn, unn-z, uno, unp, unr, uns, unt, unu, unv, unw, unx, uny, uoa, uoa-z, uob, uoc, uod, uoe, uof, uog, uoh, uoi, uoj, uol, uom, uon, uoo, uop, uoq, uos, uot, uou, uov, uow, uox, uoy, uoz, upa, upb, upc, upd, ure, usf, uta, uta-e, utb, utb-z, utc, utg, utj, utk, utm, utn, uto, utp, utq, vab, vba, vbb, vfi, wbl, wei, wfa, wiw, wix, wiy, wiz, wje, wjf, wjg, wjh, wji, wse, wut, xaa, xad, xai, xbe, xbl, xca, xcb, xci, xda, xik, xux, ycq, ycr, ycr-z, yug, yyz, zec, zme, zni, zst

For excellent visualizations of the 2D-layered and 3D nets, please see <http://rcsr.anu.edu.au/layers> and <http://rcsr.anu.edu.au/nets>, respectively.

E.9 Ranking of ANG Storage Materials

Tables E.12 – E.21 list the top ten predicted materials for ANG storage for each group of structures in the database. Tables E.12 – E.16 list the top ten 2D frameworks for each bond type, and Tables E.17 – E.21 list the top ten 3D frameworks for each bond type.

Framework ID	Density (kg/m ³)	DC (v STP/v)
linker99_CO_linker2_NH_sql	365.5	184.9
linker99_CO_linker58_NH_sql	348.0	185.0
linker99_CO_linker68_NH_sql	413.7	185.1
linker99_CO_linker57_NH_sql	434.4	185.3
linker108_CO_linker81_NH_sql	370.1	186.0
linker99_CO_linker64_NH_sql	388.8	186.0
linker108_CO_linker1_NH_sql	384.1	187.8
linker99_CO_linker42_NH_sql	451.3	188.5
linker99_CO_linker87_NH_sql	335.0	189.4
linker99_CO_linker81_NH_sql	348.4	189.6

Table E.12: Best 2D amide bonded frameworks in order of increasing DC.

Framework ID	Density (kg/m ³)	DC (v STP/v)
linker99_CH2_linker49_NH_sql	405.1	175.5
linker99_CH2_linker81_NH_sql	310.2	175.5
linker99_CH2_linker62_NH_sql	347.2	175.6
linker99_CH2_linker84_NH_sql	332.6	175.7
linker99_CH2_linker57_NH_sql	404.5	176.6
linker99_CH2_linker64_NH_sql	352.2	177.4
linker99_CH2_linker65_NH_sql	391.7	177.8
linker99_CH2_linker45_NH_sql	379.8	178.2
linker99_CH2_linker83_NH_sql	382.6	179.8
linker99_CH2_linker42_NH_sql	422.3	184.3

Table E.13: Best 2D amine bonded frameworks in order of increasing DC.

Framework ID	Density (kg/m ³)	DC (v STP/v)
linker107_N_linker46_CH.sql	385.2	184.9
linker108_N_linker42_CH.sql	412.9	185.1
linker99_N_linker45_CH.sql	343.6	185.3
linker107_N_linker42_CH.sql	404.1	185.7
linker99_N_linker49_CH.sql	364.2	186.3
linker99_N_linker41_CH.sql	331.0	186.5
linker102_N_linker42_CH.sql	415.4	186.8
linker107_N_linker41_CH.sql	349.9	187.0
linker99_N_linker42_CH.sql	384.4	187.2
linker99_N_linker83_CH.sql	347.3	187.8

Table E.14: Best 2D imine bonded frameworks in order of increasing DC.

Framework ID	Density (kg/m ³)	DC (v STP/v)
linker103_C_linker19_C.sql	346.3	186.5
linker91_C_linker84_C_hcb	412.0	186.7
linker91_C_linker76_C_hcb	368.0	186.9
linker103_C_linker39_C.sql	396.3	186.9
linker91_C_linker85_C_hcb	484.7	188.7
linker103_C_linker38_C.sql	431.0	189.1
linker91_C_linker41_C_hcb	468.4	189.2
linker91_C_linker81_C_hcb	367.8	190.0
linker103_C_linker40_C.sql	414.1	190.9
linker103_C_linker35_C.sql	382.7	194.3

Table E.15: Best 2D carbon-carbon bonded frameworks in order of increasing DC.

Framework ID	Density (kg/m ³)	DC (v STP/v)
linker107_CH.linker92_N_bex	408.2	186.7
linker108_CH.linker92_N_bex	419.1	190.4
linker99_CH.linker92_N_pnd	387.1	190.6
linker107_CH.linker91_N_bex	419.3	192.0
linker99_CH.linker91_N_pnd	393.9	192.5
linker105_CH.linker92_N_bex	403.5	192.8
linker105_CH.linker91_N_bex	417.7	196.9
linker99_CH.linker92_N_bex	377.4	197.3
linker99_CH.linker91_N_bex	388.9	199.8
linker108_CH.linker91_N_bex	421.3	202.2

Table E.16: Best 2D mixed bond frameworks in order of increasing DC.

Framework ID	Density (kg/m ³)	DC (v STP/v)
linker105_CO.linker42_NH.qzd	374.8	193.9
linker99_NH.linker103_CO.pth	434.6	194.1
linker105_CO.linker86_NH.qzd	433.0	194.3
linker99_CO.linker47_NH.qzd	372.5	194.5
linker105_NH.linker103_CO.pth	458.8	195.1
linker108_CO.linker67_NH.lvt.interp_2	390.5	195.2
linker101_CO.linker99_NH.pth	415.8	196.1
linker99_NH.linker101_CO.pth	415.8	196.3
linker108_NH.linker101_CO.pth	451.6	196.3
linker108_NH.linker100_CO.pth	469.3	198.1

Table E.17: Best 3D amide bonded frameworks in order of increasing DC.

Framework ID	Density (kg/m ³)	DC (v STP/v)
linker108_CH2_linker47_NH_qzd	356.1	188.3
linker99_NH_linker106_CH2_pth	395.8	188.6
linker101_CH2_linker108_NH_pts	398.8	189.0
linker108_NH_linker101_CH2_pts	398.8	189.3
linker108_NH_linker104_CH2_pts	437.3	189.9
linker102_CH2_linker103_NH_pth	379.7	190.0
linker103_NH_linker102_CH2_pth	379.7	190.1
linker104_CH2_linker108_NH_pts	437.3	190.4
linker99_NH_linker101_CH2_pth	360.3	192.8
linker108_CH2_linker92_NH_pto	395.4	197.5

Table E.18: Best 3D amine bonded frameworks in order of increasing DC.

Framework ID	Density (kg/m ³)	DC (v STP/v)
linker101_N_linker107_CH_pts	365.5	195.9
linker102_CH_linker103_N_pth	374.2	195.9
linker102_N_linker103_CH_pth	373.2	196.0
linker108_N_linker104_CH_pth	386.9	196.2
linker103_CH_linker102_N_pth	373.2	196.6
linker105_N_linker92_CH_pto	383.2	196.8
linker108_N_linker101_CH_pth	356.9	199.0
linker103_CH_linker100_N_pts	400.1	199.3
linker101_CH_linker108_N_pth	356.9	199.4
linker100_N_linker103_CH_pts	400.1	199.8

Table E.19: Best 3D imine bonded frameworks in order of increasing DC.

Framework ID	Density (kg/m ³)	DC (v STP/v)
linker99_C_linker91_C_stw	438.7	205.1
linker108_C_linker87_C_uon	381.2	205.4
linker91_C_linker91_C_dia-g	454.1	205.9
linker108_C_linker58_C_uon	396.0	206.5
linker91_C_linker91_C_nbo-a	391.8	206.7
linker108_C_linker81_C_uon	395.2	207.3
linker91_C_linker91_C_lcs-f	416.0	208.4
linker91_C_linker91_C_qtz-h	484.4	209.3
linker91_C_linker91_C_bod	507.1	209.8
linker91_C_linker91_C_tbd	503.1	216.8

Table E.20: Best 3D carbon-carbon bonded frameworks in order of increasing DC.

Framework ID	Density (kg/m ³)	DC (v STP/v)
linker108_CH_linker92_N_lil	329.5	199.0
linker108_CH_linker91_N_lil	344.8	200.4
linker91_CH_linker91_N_clh	353.6	204.9
linker91_N_linker91_CH_clh	353.6	205.1
linker91_N_linker92_CH_clh	325.6	206.2
linker92_CH_linker91_N_clh	325.6	206.5
linker92_N_linker91_CH_clh	333.5	206.6
linker99_CH_linker91_N_phx	334.9	206.8
linker105_CH_linker91_N_phx	355.8	206.8
linker91_CH_linker92_N_clh	333.5	208.1

Table E.21: Best 3D mixed bond frameworks in order of increasing DC.

Structures with Large DCs (> 190 v STP/v)

Complete lists of all 2D and 3D structures with DCs greater than 190 v STP/v.

2D Frameworks

In order of increasing DC:

Framework ID, Density (kg/m³), DC (v STP/v)

linker91_C.linker81_C.hcb, 367.881320667, 190.079670689
linker108.CH.linker92_N.bex, 419.110063669, 190.441112991
linker99.CH.linker92_N.pnd, 387.173679089, 190.675493533
linker103_C.linker40_C.sql, 414.157589563, 190.957591623
linker107.CH.linker91_N.bex, 419.393938738, 192.026373675
linker99.CH.linker91_N.pnd, 393.960781166, 192.532706025
linker105.CH.linker92_N.bex, 403.589345522, 192.805567278
linker103_C.linker35_C.sql, 382.763351215, 194.344326516
linker105.CH.linker91_N.bex, 417.794068375, 196.9895885
linker99.CH.linker92_N.bex, 377.466154624, 197.357708539
linker99.CH.linker91_N.bex, 388.930306044, 199.843564363
linker108.CH.linker91_N.bex, 421.345724469, 202.219217927

3D Frameworks

In order of increasing DC:

Framework ID, Density (kg/m³), DC (v STP/v)

linker105_C.linker35_C.dia.interp_2, 409.827436139, 190.005803698
linker105.CO.linker41_NH.qzd, 329.829205316, 190.019398716
linker99.NH.linker89_CO.qtz.interp_2, 348.07938934, 190.028118112
linker99_N.linker103.CH.pts, 338.754367919, 190.030093817
linker108_C.linker88_C.lon, 423.072020707, 190.045078962
linker100_C.linker42_C.qtz, 413.29968127, 190.050262438
linker102.CH2.linker103_NH.pth, 379.702585757, 190.051865713
linker108.CO.linker42_NH.qdl, 360.579964785, 190.058581052
linker107_N.linker92.CH.tfk, 298.265974408, 190.093925777
linker110_C.linker94_C.ctn, 297.066163812, 190.102542686
linker100_C.linker41_C.qtz, 347.426263162, 190.11357405
linker103_NH.linker102.CH2.pth, 379.702585757, 190.122209802
linker108_C.linker35_C.lvt.interp_2, 344.257066459, 190.171936218
linker111.CO.linker92_NH.jph, 388.375099804, 190.179357801
linker108.CO.linker71_NH.lvt.interp_2, 389.168006366, 190.218507341
linker99.CO.linker43_NH.qzd, 378.079188538, 190.292675014
linker101_NH.linker99.CO.pts, 413.756757611, 190.293495144
linker102_C.linker96_C.xux.interp_2, 334.036335056, 190.303233987
linker108.CO.linker46_NH.qzd, 348.286757627, 190.338521108

linker107.CH.linker100.N.bto-e, 325.550290091, 190.338807683
linker108.C.linker42.C.lon, 519.468770344, 190.349309979
linker100.N.linker107.CH.bto-e, 325.550290091, 190.354009938
linker104.CH2.linker108.NH.pts, 437.353294814, 190.40496791
linker99.C.linker62.C.lon, 345.27672562, 190.427016793
linker99.C.linker49.C.lon, 412.062272153, 190.438843048
linker111.C.linker91.C.moa, 333.967476401, 190.461820465
linker98.C.linker92.C.jph, 366.965603465, 190.528234667
linker99.C.linker59.C.lon, 323.565694054, 190.529945682
linker100.CH.linker58.N.lvt.interp_3, 365.178259004, 190.545910353
linker106.CO.linker99.NH.pth, 451.564451635, 190.551698916
linker101.C.linker39.C.uoo.interp_2, 394.774274216, 190.57549464
linker108.NH.linker101.CO.pts, 448.810519213, 190.58267548
linker105.CO.linker47.NH.qzd, 399.16348844, 190.594920563
linker99.NH.linker106.CO.pth, 451.564451635, 190.596920265
linker99.C.linker99.C.rhr, 358.177273134, 190.62920648
linker104.N.linker99.CH.bto-e, 309.693003432, 190.633800259
linker108.CO.linker62.NH.qtz, 404.91189368, 190.660502314
linker108.CO.linker83.NH.qzd, 336.534289591, 190.672096563
linker108.NH.linker105.CO.ssb, 424.146240674, 190.67304015
linker99.CH.linker104.N.bto-e, 309.693003432, 190.683440377
linker108.C.linker38.C.lvt.interp_2, 384.467565501, 190.697262962
linker108.CH.linker92.N.hof, 313.668941446, 190.713626352
linker102.N.linker106.CH.pth, 382.450576869, 190.73601037
linker100.CO.linker102.NH.pts, 415.531596661, 190.738960359
linker108.N.linker91.CH.pto, 399.907423491, 190.739388297
linker100.C.linker87.C.dia, 337.195808296, 190.756521216
linker110.C.linker39.C.cds, 450.863326959, 190.800492717
linker92.C.linker92.C.sod-f, 358.609210807, 190.806274437
linker111.C.linker108.C.brl, 359.683806905, 190.888982565
linker108.C.linker91.C.stw, 508.244985237, 190.905674371
linker102.CH.linker91.N.ins, 398.925598384, 190.908738525
linker108.NH.linker4.CO.dmp, 361.900133342, 190.911465856
linker103.CH.linker105.N.pth, 370.747468738, 190.928450628
linker99.N.linker41.CH.vba.interp_2, 356.217287282, 190.961058002
linker99.C.linker88.C.lon, 345.968715524, 191.02071475
linker102.NH.linker100.CO.pts, 415.531596661, 191.031898389
linker100.C.linker58.C.dia, 348.318867684, 191.040205657
linker106.CH.linker99.N.pth, 345.194719948, 191.070070788
linker100.CO.linker86.NH.qzd, 436.932825553, 191.077676114
linker91.C.linker91.C.nof, 564.492689922, 191.102564445
linker99.CH.linker84.N.tcb, 386.692804781, 191.108264299

linker105_CO.linker54_NH_qdl, 407.589395711, 191.119557209
linker99_C.linker42_C_qtz, 396.268116033, 191.120614308
linker103_C.linker87_C_cds, 384.540945498, 191.17479063
linker92_C.linker91_C_hee, 440.912934929, 191.216189228
linker99_C.linker41_C_qtz, 327.941522195, 191.223975208
linker99_N.linker104_CH_pth, 354.486013814, 191.394777245
linker92_C.linker92_C_tbd, 431.066736632, 191.399645386
linker99_CH.linker91_N_phw, 312.044431892, 191.457350747
linker108_NH.linker51_CO_qzd, 387.895115247, 191.461130744
linker108_CH.linker91_N_tfk, 312.289424124, 191.462943805
linker111_C.linker91_C_pts-f, 345.412988939, 191.488123234
linker103_C.linker81_C_cds, 388.950885115, 191.501640273
linker107_CO.linker86_NH_qzd, 437.04937356, 191.507774129
linker91_C.linker92_C_etc, 454.178261206, 191.541924509
linker100_C.linker39_C_uoo_interp_2, 395.658622374, 191.555188411
linker110_C.linker96_C_jea, 365.710939281, 191.563310167
linker108_C.linker2_C_qtz, 344.166361168, 191.567778293
linker110_C.linker81_C_lon, 426.629860904, 191.682759807
linker99_C.linker92_C_tbo, 429.870602307, 191.700524655
linker102_CH2.linker92_NH_xux, 386.597999077, 191.708194425
linker105_CO.linker47_NH_qdl, 398.429219864, 191.779475121
linker99_C.linker39_C_dia_interp_2, 353.214619524, 191.812821798
linker105_C.linker92_C_tbo, 485.317349363, 191.852225648
linker103_C.linker96_C_phw_interp_2, 369.98320413, 191.876575792
linker107_N.linker47_CH_qzd, 320.497472461, 191.892406229
linker98_C.linker91_C_phx, 324.458783632, 191.89431866
linker105_C.linker76_C_qtz, 427.026621529, 191.970294386
linker110_C.linker76_C_dia, 426.693806115, 191.975237389
linker99_C.linker41_C_dia, 355.00092678, 192.015638731
linker109_N.linker47_CH_cds, 313.369538149, 192.020910571
linker108_C.linker76_C_gis, 409.619703272, 192.101185748
linker99_C.linker81_C_lon, 295.889734001, 192.101808259
linker99_NH.linker47_CO_qdl, 363.24032679, 192.110768857
linker108_CO.linker47_NH_qdl, 385.299775746, 192.127533886
linker91_C.linker91_C_ssb-a, 357.506977408, 192.155721647
linker108_C.linker58_C_gis, 406.189446802, 192.176728703
linker105_C.linker91_C_tbo, 508.891928629, 192.178789156
linker99_N.linker103_CH_pth, 343.127651109, 192.228179848
linker92_C.linker91_C_etc, 454.178261206, 192.274825215
linker99_CO.linker42_NH_qdl, 345.687553758, 192.335231489
linker110_C.linker81_C_dia, 430.616457899, 192.340730027
linker103_C.linker76_C_cdl, 392.682850816, 192.375782195

linker108_CO.linker68_NH.qtz, 433.233342282, 192.393334386
linker107_N.linker90_CH.cdl, 380.483728427, 192.415361809
linker91_C.linker92_C.hee, 440.912934929, 192.422391866
linker108_NH.linker72_CO.lvt.interp_2, 450.401255232, 192.433038324
linker99_C.linker2_C.lon, 316.005686567, 192.472416624
linker108_C.linker41_C.qtz, 387.054005016, 192.502149782
linker103_CH.linker99_N.pth, 343.127651109, 192.518567614
linker99_CO.linker86_NH.qzd, 404.573170107, 192.539600494
linker103_CH.linker108_N.pth, 373.323354267, 192.540560568
linker109_C.linker99_C.pts, 364.231323027, 192.58379409
linker100_C.linker76_C.dia, 346.539359375, 192.622525564
linker99_C.linker45_C.lon, 383.743416062, 192.662440856
linker91_C.linker91_C.hef, 516.484446155, 192.672521193
linker98_C.linker92_C.phx, 315.799879794, 192.682490309
linker108_NH.linker57_CO.dmp, 389.490801241, 192.697076125
linker110_C.linker87_C.dia, 396.306250697, 192.721952423
linker111_C.linker92_C.bor, 389.268398619, 192.863029816
linker99_C.linker40_C.dia.interp_2, 382.995258123, 192.882732714
linker99_NH.linker101_CH2.pth, 360.318586561, 192.896010429
linker111_C.linker99_C.pts, 366.26946567, 192.928400281
linker99_CO.linker42_NH.qzd, 347.954701194, 192.9359556
linker108_C.linker3_C.uon, 411.845983976, 192.954152818
linker105_C.linker84_C.qtz, 455.894855512, 193.002639377
linker107_NH.linker40_CO.qtz.interp_2, 388.933093356, 193.003059026
linker101_CH.linker104_N.pts, 405.858623374, 193.024624651
linker108_C.linker92_C.stj, 477.788367534, 193.030421212
linker108_CO.linker67_NH.qtz, 434.625382891, 193.051677754
linker110_C.linker76_C.lon, 422.316188579, 193.056975253
linker104_N.linker101_CH.pts, 405.858623374, 193.075341061
linker100_CH.linker104_N.pts, 388.209150584, 193.102685485
linker108_C.linker76_C.qtz, 324.704740538, 193.107179194
linker103_C.linker58_C.cds, 393.458477355, 193.142093227
linker108_C.linker41_C.dia, 436.574799434, 193.183594152
linker110_C.linker39_C.cdl, 450.44122566, 193.244990632
linker99_NH.linker47_CO.qzd, 364.206618483, 193.250833987
linker99_C.linker35_C.dia.interp_2, 348.689938921, 193.25487299
linker111_C.linker92_C.dmd, 370.221329134, 193.288740608
linker103_CO.linker99_NH.pth, 434.647575237, 193.311584831
linker108_NH.linker104_CO.pth, 503.039187666, 193.330338992
linker103_C.linker58_C.cdl, 392.539063888, 193.357168321
linker110_N.linker107_CH.bto-e, 392.73802323, 193.360391942
linker108_C.linker81_C.gis, 408.706671424, 193.379615881

linker108_NH.linker42_CO.qzd, 359.652639006, 193.408466045
linker99_CO.linker47_NH.qdl, 371.839427077, 193.41397958
linker103_C.linker76_C.cds, 394.214932892, 193.459708345
linker91_C.linker91_C.etc, 523.027687364, 193.51655534
linker111_C.linker108_C.pts, 407.554713296, 193.528032337
linker106_CH.linker108_N.pth, 376.588585299, 193.552030527
linker108_NH.linker54_CO.qzd, 391.405975416, 193.562944445
linker109_C.linker108_C.pts, 406.846224642, 193.569603625
linker104_N.linker100_CH.pts, 388.209150584, 193.610222851
linker99_NH.linker42_CO.qzd, 340.305404699, 193.620114578
linker105_C.linker81_C.qtz, 427.626382129, 193.675158092
linker108_N.linker103_CH.pth, 373.323354267, 193.678515655
linker108_CO.linker54_NH.qzd, 395.255564807, 193.72992463
linker99_C.linker76_C.lon, 296.577927263, 193.776388701
linker99_CH.linker81_N.tcb, 361.421137508, 193.945776111
linker105_CO.linker42_NH.qzd, 374.819492861, 193.949996568
linker99_C.linker41_C.ukk, 412.042901945, 193.977756115
linker108_C.linker59_C.uon, 423.913352261, 194.048264224
linker98_C.linker91_C.jph, 389.974472878, 194.053101714
linker99_C.linker58_C.lon, 298.086154013, 194.08058006
linker108_C.linker39_C.dia.interp_2, 404.113366772, 194.090852802
linker105_N.linker90_CH.cds, 374.885158774, 194.102108672
linker99_NH.linker103_CO.pth, 434.647575237, 194.157140046
linker108_CH.linker99_N.pts, 406.609610236, 194.173559657
linker111_C.linker92_C.ctn, 427.1360757, 194.201468977
linker108_N.linker106_CH.pth, 376.588585299, 194.234159646
linker108_C.linker81_C.qtz, 326.598348855, 194.257741564
linker105_N.linker90_CH.cdl, 376.686957897, 194.264226622
linker108_C.linker58_C.qtz, 324.976209337, 194.276653153
linker103_C.linker81_C.cdl, 394.685948076, 194.303705044
linker101_N.linker100_CH.pts, 369.321786189, 194.352667969
linker105_CO.linker86_NH.qzd, 433.062861407, 194.370588737
linker104_C.linker38_C.dia.interp_2, 426.71512517, 194.38766055
linker99_N.linker108_CH.pts, 406.609610236, 194.457810997
linker99_C.linker41_C.lon, 362.400438316, 194.461959434
linker99_C.linker87_C.lon, 287.662853687, 194.471904046
linker108_C.linker41_C.uon, 466.463910633, 194.484747982
linker99_CO.linker47_NH.qzd, 372.530948209, 194.503247339
linker99_CH.linker58_N.tcb, 361.332568402, 194.530496788
linker108_C.linker40_C.lvt.interp_2, 378.749946018, 194.587870074
linker100_CH.linker101_N.pts, 369.321786189, 194.609105533
linker91_C.linker91_C.she-a, 393.526940817, 194.708308113

linker108_C_linker87_C_qtz, 315.606936499, 194.766126231
linker110_C_linker58_C_dia, 424.612626152, 194.80467023
linker109_C_linker109_C_uni, 330.020046501, 194.81154287
linker99_C_linker64_C_lon, 350.505129317, 194.938530808
linker105_NH_linker103_CO_pth, 458.809168258, 195.142218812
linker104_CH_linker108_N_pth, 386.963898478, 195.158640944
linker100_C_linker81_C_dia, 343.469739119, 195.279999382
linker108_CO_linker67_NH_lvt_interp_2, 390.570041508, 195.289662613
linker91_C_linker93_C_clh, 329.366027057, 195.404718048
linker91_C_linker92_C_tbd, 452.079145665, 195.43880373
linker102_CH_linker92_N_xux, 374.660084929, 195.443155744
linker103_CH_linker92_N_hst, 358.205545382, 195.448316445
linker91_C_linker91_C_cds-a, 519.978517578, 195.582682408
linker92_CH_linker91_N_bpa, 354.212384429, 195.657779278
linker103_N_linker102_CH_pth, 374.295006064, 195.774427995
linker107_CH_linker101_N_pts, 365.56796268, 195.812801966
linker93_C_linker91_C_clh, 329.366027057, 195.897746939
linker103_CH_linker91_N_hst, 371.700959413, 195.915962745
linker93_C_linker92_C_clh, 310.517822054, 195.928348822
linker110_N_linker105_CH_bto-e, 398.192425225, 195.948256074
linker108_C_linker64_C_uon, 454.741896204, 195.973650655
linker101_N_linker107_CH_pts, 365.56796268, 195.978854341
linker102_CH_linker103_N_pth, 374.295006064, 195.993648362
linker102_N_linker103_CH_pth, 373.299179995, 196.034618666
linker108_C_linker93_C_pto, 350.50888283, 196.104126559
linker108_C_linker62_C_uon, 447.944360909, 196.175658139
linker101_CO_linker99_NH_pth, 415.870541736, 196.177147881
linker108_N_linker104_CH_pth, 386.963898478, 196.213573499
linker99_NH_linker101_CO_pth, 415.870541736, 196.327147635
linker108_NH_linker101_CO_pth, 451.640599718, 196.377248389
linker91_N_linker92_CH_bpa, 354.212384429, 196.491162041
linker108_C_linker91_C_nox, 443.735298017, 196.579974938
linker91_C_linker91_C_hec, 479.969486099, 196.580763849
linker103_CH_linker102_N_pth, 373.299179995, 196.625762218
linker109_C_linker92_C_xux, 347.226622685, 196.653171762
linker91_C_linker91_C_sod-f, 418.60549782, 196.720247142
linker92_C_linker91_C_tbd, 452.079145665, 196.721230593
linker111_C_linker111_C_uni, 331.826475737, 196.752963258
linker111_C_linker92_C_xux, 353.042675197, 196.796070915
linker105_N_linker92_CH_pto, 383.206545243, 196.889232209
linker108_C_linker91_C_stj, 512.010542018, 197.037969659
linker102_CH_linker91_N_xux, 401.092931289, 197.073049414

linker109_NH.linker92_CO_jph, 382.255708205, 197.346356256
linker108_C.linker76_C_dia, 366.292071696, 197.429581732
linker108_CH2.linker92_NH_pto, 395.474516348, 197.513082545
linker99_C.linker92_C_stw, 408.148452999, 197.517412165
linker99_C.linker91_C_tbo, 452.056633609, 197.716305842
linker92_C.linker92_C_dia-g, 406.818394827, 197.860417481
linker109_C.linker91_C_xux, 374.583466835, 197.873989783
linker99_C.linker87_C_ukk, 326.73314133, 197.918308448
linker108_C.linker76_C_uon, 402.990427204, 197.943378822
linker91_C.linker91_C_rab, 543.710040748, 198.020772317
linker99_C.linker76_C_ukk, 336.744720727, 198.034754095
linker108_NH.linker100_CO_pth, 469.385766932, 198.138166855
linker108_C.linker58_C_dia, 366.782478173, 198.214776935
linker108_C.linker61_C_uon, 430.006335588, 198.568968117
linker111_C.linker91_C_ctn, 437.112724692, 198.751812898
linker111_C.linker91_C_moc, 359.301215124, 198.792072623
linker108_C.linker1_C_uon, 411.462337233, 198.965742263
linker108_CH.linker92_N_lil, 329.560395746, 199.025632598
linker108_C.linker87_C_dia, 357.409926749, 199.064697842
linker108_N.linker101_CH_pth, 356.956257863, 199.074690233
linker108_C.linker87_C_ukk, 381.104936703, 199.320637918
linker103_CH.linker100_N_pts, 400.148738915, 199.326685461
linker99_C.linker81_C_ukk, 335.627943147, 199.333447425
linker101_CH.linker108_N_pth, 356.956257863, 199.410130367
linker108_C.linker41_C_lon, 439.333048883, 199.698499548
linker111_C.linker91_C_xux, 373.854502975, 199.720301201
linker91_C.linker91_C_srd-l, 526.20080751, 199.750647111
linker92_C.linker92_C_ttd, 399.894471038, 199.763805673
linker100_N.linker103_CH_pts, 400.148738915, 199.803594654
linker91_C.linker91_C_hee, 467.188865524, 199.904632208
linker108_C.linker81_C_dia, 365.249127403, 200.402135501
linker108_CH.linker91_N_lil, 344.861532939, 200.420314123
linker108_C.linker76_C_lon, 369.831838267, 200.440802721
linker108_C.linker81_C_ukk, 390.987790648, 201.059385872
linker91_C.linker91_C_pbp, 565.431913255, 201.148834085
linker108_C.linker2_C_uon, 414.92407274, 201.179832276
linker108_C.linker76_C_ukk, 389.976189302, 201.40394484
linker108_C.linker58_C_lon, 369.702644098, 201.66490141
linker99_C.linker58_C_ukk, 333.839032867, 201.718919663
linker99_C.linker99_C_ana, 391.106313093, 202.004818298
linker92_C.linker92_C_lcs-f, 378.768842184, 202.088837541
linker108_C.linker81_C_lon, 370.420192988, 202.774937788

linker108_C_linker87_C_lon, 359.566063564, 202.848493155
linker108_C_linker58_C_ukk, 391.65161619, 203.356708631
linker91_C_linker91_C_rag, 540.503549623, 204.811726149
linker91_CH_linker91_N_clh, 353.680095746, 204.958050668
linker99_C_linker91_C_stw, 438.713925634, 205.171240133
linker91_N_linker91_CH_clh, 353.680095746, 205.189199744
linker108_C_linker87_C_uon, 381.212185495, 205.492194009
linker91_C_linker91_C_dia-g, 454.107961755, 205.963467853
linker91_N_linker92_CH_clh, 325.640927659, 206.22060552
linker108_C_linker58_C_uon, 396.042865963, 206.543428214
linker92_CH_linker91_N_clh, 325.640927659, 206.550881194
linker92_N_linker91_CH_clh, 333.526140816, 206.695494435
linker91_C_linker91_C_nbo-a, 391.82275561, 206.744768886
linker99_CH_linker91_N_phx, 334.947491509, 206.808591001
linker105_CH_linker91_N_phx, 355.813926073, 206.864600037
linker108_C_linker81_C_uon, 395.208217331, 207.39578187
linker91_CH_linker92_N_clh, 333.526140816, 208.120454446
linker91_C_linker91_C_lcs-f, 416.024843181, 208.430226657
linker91_C_linker91_C_qtz-h, 484.481026118, 209.366971474
linker91_C_linker91_C_bod, 507.181650423, 209.884881056
linker91_C_linker91_C_tbd, 503.174099394, 216.894110699

Worst Performing Structures

Properties of the worst ten 2D ANG storage materials from the database are summarized in Table E.22, and properties of the worst ten 3D materials are summarized in Table E.23.

From the 2D-layered structures, the framework predicted to be the absolute worst for ANG storage is the carbon-carbon bonded structure *linker109_C_linker92_C_mcm*, which has a density of 738.5 kg/m³ and a predicted DC of only 62.1 v STP/v. Similarly, from the 3D set of structures, the framework predicted to be the worst for ANG storage is the carbon-carbon bonded structure *linker105_C_linker44_C_qtz*, which has a density of 965.2 kg/m³ and a DC of 4.4 v STP/v.

Type	Framework ID	Density (kg/m ³)	DC (v STP/v)
C-C	linker109_C.linker92_C_mcm	738.5	62.1
C-C	linker109_C.linker51_C_sql	755.4	68.5
C-C	linker111_C.linker47_C_sql	768.6	71.0
C-C	linker109_C.linker47_C_sql	750.3	73.8
C-C	linker111_C.linker54_C_sql	789.7	80.4
C-C	linker109_C.linker80_C_sql	696.8	80.4
C-C	linker109_C.linker54_C_sql	772.8	81.4
C-C	linker109_C.linker52_C_sql	709.4	84.3
C-C	linker111_C.linker50_C_sql	724.4	85.2
C-C	linker106_C.linker53_C_kgm	629.7	86.6

Table E.22: Worst ten 2D-layered methane storage materials in the database.

Type	Framework ID	Density (kg/m ³)	DC (v STP/v)
C-C	linker105_C.linker44_C_qtz	965.2	4.4
C-C	linker110_C.linker2_C_mdf	1065.8	5.5
C-C	linker110_C.linker41_C_cdl	1119.9	8.4
C-C	linker107_C.linker44_C_qtz	944.8	11.5
C-C	linker110_C.linker61_C_mdf	1102.9	12.7
imine	linker108_N.linker7_CH_tcb_interp_2	848.4	15.3
C-C	linker107_C.linker4_C_lvt_interp_3	868.0	15.6
C-C	linker105_C.linker4_C_lvt_interp_3	869.2	16.1
C-C	linker106_C.linker44_C_qtz	787.9	16.8
mixed	linker110_CO.linker104_NH_cda	976.5	17.5

Table E.23: Worst ten 3D methane storage materials in the database.

Sample Adsorption Isotherms

As an example, methane adsorption isotherms were computed for the best five and worst five ANG storage frameworks in the database; these results are illustrated in Figure E.11. Each point on these plots is the result of a GCMC simulation at 298 K and the corresponding pressure.

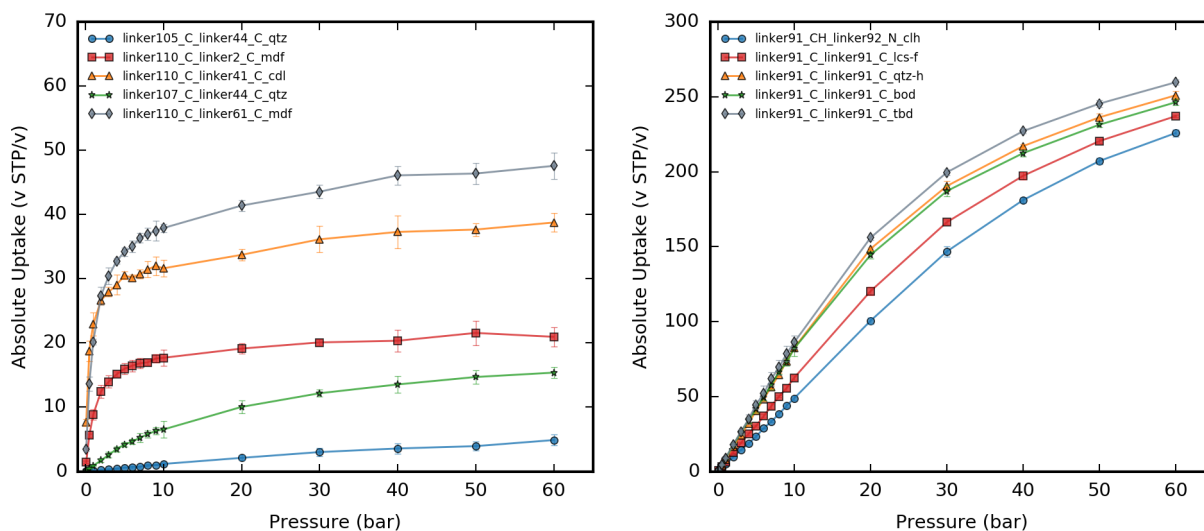


Figure E.11: Sample methane adsorption isotherms for the worst five (left) and best five (right) ANG storage structures in the database.

E.10 Estimate of Computational Time Used

To guide researchers who would like to take a similar structure generation approach in their projects, Table E.24 lists estimates of the computational time used at each step of the structure generation process presented in this work. The most computationally intensive parts of this process are the structure optimization, the interpenetrated structure generation, and the GCMC simulation steps.

Step	Time Estimate	Multiplier	Total (CPU days)
Linker assembly	5 min/linker	666	2
Structure generation	5 seconds/struct	1,705,914	98
Geometric property calculation ^a	2 min/struct	470,072	652
Bad structure removal ^b	< 1 sec/struct	470,074	$O(\text{minutes})$
Structure optimization ^c	15 min/struct	69,840	727
Interp. structure generation	10 min/struct	69,840	485
Blocked pockets calculation ^d	5 min/struct	69,840 x 10%	24
GCMC simulations ^e	10 min/struct	69,840	485

Table E.24: Estimate of computational time used at each step of the structure generation process. The multiplier is in each case the number of structures processed at each step, except in the case of the linker assembly, where the multiplier is the number of linkers. ^aThe geometric property calculation step includes the calculation of accessible and inaccessible surface areas, pore volumes, and structure info using Zeo++. ^bNote that while the removal of bad structures does not take very long in and of itself, it depends on the output from the geometric property calculation step above. ^cTime estimate includes time for generating the LAMMPS input files using *lammmps_interface* (5 min/struct) and running the optimization job in LAMMPS (10 min/struct). ^dThe multiplier for the blocked pockets calculation is only 10% of the structures in the database because this step was only carried out for structures in the database which were found to contain inaccessible pore volume. ^eTime estimate includes high pressure, low pressure, and Widom insertion calculations.

E.11 ARPA-E MOVE Program ANG Storage Target

In 2012, the ARPA-E Methane Opportunities for Vehicular Energy (MOVE) Program [2] set a target for the amount of energy that a vehicular fuel tank powered on ANG should deliver to a vehicle so as to be competitive with compressed natural gas. As such, the program establishes an overall system energy density requirement that should meet or exceed CNG at 250 bar (9.2 MJ/L); this requirement is thus set to 12.5 MJ/L, such that after accounting for 25% packing loss, the system is still able to provide 9.2 MJ/L to the vehicle. Although specific natural gas storage and depletion pressures are not prescribed, it is specified that the engine inlet pressure must be greater than 70 psig, or 4.83 bar, and that the system should not exceed 3600 psi, or 250 bar. After converting to volumetric adsorption units (outlined below), we see that this translates to a DC target of roughly 314 v STP/v. This has been shown in recent work [181, 201] to be an unattainable target for microporous materials, with an upper bound closer to 200 v STP/v approached by many of the top-performing ANG storage materials to date. [146, 149]

$$\begin{aligned}
 \text{Volumetric energy density} &= \frac{12.5 \text{ MJ}}{1 \text{ L}_{\text{adsorb.}}} \times \frac{1 \text{ m}^3 \text{ CH}_4}{0.717 \text{ kg CH}_4} \times \frac{1000 \text{ L CH}_4}{1 \text{ m}^3 \text{ CH}_4} \times \frac{16.043 \text{ g CH}_4}{1 \text{ mol CH}_4} \\
 &\quad \times \frac{1 \text{ kg CH}_4}{1000 \text{ g CH}_4} \times \frac{1 \text{ mol CH}_4}{890.8 \text{ kJ CH}_4} \times \frac{1000 \text{ kJ CH}_4}{1 \text{ MJ CH}_4} \\
 &= 313.98 \text{ L}_{\text{CH}_4@ \text{STP}}/\text{L}_{\text{adsorbate}} = \text{v STP}/\text{v}
 \end{aligned}$$

Bibliography

- [1] R. A. Alvarez et al. In: *Proc. Natl. Acad. Sci.* 109.17 (2012), pp. 6435–6440.
- [2] ARPA-E. *Methane Opportunities for Vehicular Energy*. Accessed: 2018-05-21. 2012. URL: <http://arpa-e.energy.gov/?q=arpa-e-programs/move>.
- [3] J. E. Bachman et al. In: *J. Am. Chem. Soc.* 139.43 (2017), pp. 15363–15370.
- [4] N. Badi and J.-F. Lutz. In: *Chem. Soc. Rev.* 38.12 (2009), pp. 3383–3390.
- [5] Y.-S. Bae and R. Q. Snurr. In: *Angew. Chem., Int. Ed.* 50.49 (2011), pp. 11586–11596.
- [6] D. Banerjee et al. In: *Nat. Commun.* 7 (2016), ncomms11831.
- [7] M. Bastos-Neto et al. In: *Adsorption* 11.2 (2005), pp. 147–157.
- [8] F. S. Bates et al. In: *Science* 336.6080 (2012), pp. 434–440.
- [9] T. Ben et al. In: *Angewandte Chemie* 121.50 (2009), pp. 9621–9624.
- [10] E. Bitzek et al. In: *Phys. Rev. Lett.* 97.17 (2006), p. 170201.
- [11] M. Bixon and S. Lifson. In: *Tetrahedron* 23.2 (1967), pp. 769–784.
- [12] R. Blinc et al. In: *Phys. Rev. Lett.* 33 (1974), p. 1192.
- [13] E. D. Bloch et al. In: *J. Am. Chem. Soc.* 133 (2011), p. 14814.
- [14] P. E. Blochl. In: *Phys. Rev. B: Condens. Matter Mater. Phys.* 50 (1994), p. 17953.
- [15] C. Bonneau et al. In: *Acta Crystallogr., Sect. A: Found. Crystallogr.* 60.6 (2004), pp. 517–520.
- [16] J. Borycz et al. In: *J. Phys. Chem. C* 118 (2014), p. 12230.
- [17] P. G. Boyd et al. In: *J. Phys. Chem. Letters* 8.2 (2017), pp. 357–363.
- [18] J. K. Bristow, D. Tiana, and A. Walsh. In: *J. Chem. Theory Comput.* 10.10 (2014), pp. 4644–4652.
- [19] D. Britt et al. In: *Proc. Natl. Acad. Sci. U.S.A.* 106 (2009), p. 20637.
- [20] P. T. Callaghan. In: *Magn. Reson. Imaging* 14.7 (1996), pp. 701–709.
- [21] P. T. Callaghan, M. A. Le Gros, and D. N. Pinder. In: *J. Chem. Phys.* 79 (1983), p. 6372.

- [22] C. Campaña, B. Mussard, and T. K. Woo. In: *J. Chem. Theory Comput.* 5 (2009), p. 2866.
- [23] P. Canepa et al. In: *Phys. Rev. Lett.* 110 (2013), p. 026102.
- [24] F. Casanova, J. Perlo, and B. Blümich. In: Springer, 2011, pp. 1–10.
- [25] S. R. Caskey, A. G. Wong-Foy, and A. J. Matzger. In: *J. Am. Chem. Soc.* 130 (2008), p. 10870.
- [26] J. M. Castillo et al. In: *Mol. Simul.* 35 (2009), p. 1067.
- [27] D. L. Chen et al. In: *Chem. Eng. Sci.* 124 (2015), pp. 109–117. ISSN: 00092509.
- [28] L. Chen, C. A. Morrison, and T. Duren. In: *J. Phys. Chem. C* 116 (2012), p. 18899.
- [29] H. Childs et al. In: *High Performance Visualization-Enabling Extreme-Scale Scientific Insight 20124456* (2012), p. 357.
- [30] C. Chmelik. In: *Microporous Mesoporous Mater.* (2015). ISSN: 13871811.
- [31] S. Clarke and J. DeBruyn. *Vehicle conversion to natural gas or biogas*. Accessed: 2018-05-03. 2012. URL: <http://www.omafra.gov.on.ca/english/engineer/facts/12-043.htm>.
- [32] A. P. Côté et al. In: *Science* 310.5751 (2005), pp. 1166–1170.
- [33] T.L. Cottrell. *The Strengths of Chemical Bonds*. 2nd ed. Butterworths, London, 1958.
- [34] R. M. Cotts et al. In: *J. Magn. Reson.* 266 (1989), pp. 252–266.
- [35] D. M. D’Alessandro, B. Smit, and J. R. Long. In: *Angew. Chem., Int. Ed.* 49 (2010), p. 6058.
- [36] P. Dauber-Osguthorpe et al. In: *Proteins: Struct., Funct., Genet.* 4 (1988), p. 31.
- [37] R. Dawson, A. I. Cooper, and D. J. Adams. In: *Prog. Polym. Sci.* 37.4 (2012), pp. 530–563.
- [38] R. Dawson, A. I. Cooper, and D. J. Adams. In: *Polym. Int.* 62.3 (2013), pp. 345–352.
- [39] H. Demir et al. In: *J. Mater. Chem. A* 3 (2015), p. 23539.
- [40] H. Deng et al. In: *Science* 327.5967 (2010), pp. 846–850.
- [41] H. Deng et al. In: *Science* 336.6084 (2012), pp. 1018–1023.
- [42] M. Diaz-Garcia and M. Sanchez-Sanchez. In: *Microporous Mesoporous Mater.* 190 (2014), p. 248.
- [43] C. S. Diercks and O. M. Yaghi. In: *Science* 355.6328 (2017), eaal1585.
- [44] P. D. C. Dietzel, R. Blom, and H. Fjellvag. In: *Eur. J. Inorg. Chem.* 2008 (2008), p. 3624.
- [45] P. D. C. Dietzel et al. In: *Angew. Chem., Int. Ed.* 44 (2005), p. 6354.
- [46] P. D. C. Dietzel et al. In: *Chem. Commun.* (2006), p. 959.

- [47] F. Duarte et al. In: *J. Phys. Chem. B* 118 (2014), p. 4351.
- [48] D. Dubbeldam et al. In: *Fluid Phase Equilib.* 261 (2007), p. 152.
- [49] D. Dubbeldam et al. In: *Mol. Simul.* 35.12-13 (2009), pp. 1084–1097.
- [50] S. V. Dvinskikh and I. Furo. In: *J. Magn. Reson.* 148 (2001), p. 73.
- [51] A. L. Dzubak et al. In: *Nat. Chem.* 4 (2012), p. 810.
- [52] M. Eddaoudi et al. In: *Science* 295.5554 (2002), pp. 469–472.
- [53] *Engineering ToolBox, Liquefied Natural Gas*. webpage accessed April 2, 2018. 2008. URL: https://www.engineeringtoolbox.com/liquefied-natural-gas-ling-d_1092.html (visited on 04/02/2018).
- [54] H. Fang et al. In: *J. Phys. Chem. C* 116 (2012), p. 10692.
- [55] P. E. Fanta. In: *Synthesis* 1974.01 (1974), pp. 9–21.
- [56] O. K. Farha et al. In: *J. Am. Chem. Soc.* 134.36 (2012), pp. 15016–15021.
- [57] X. Feng, X. Ding, and D. Jiang. In: *Chem. Soc. Rev.* 41.18 (2012), pp. 6010–6022.
- [58] M. Fernandez et al. In: *Microporous Mesoporous Mater.* 105 (2007), p. 124.
- [59] J. D. Figueroa et al. In: *Int. J. Greenhouse Gas Control* 2.1 (2008), pp. 9–20.
- [60] E. M. Forman et al. In: *Microporous Mesoporous Mater.* 248 (2017), p. 158.
- [61] A. C. Forse et al. In: *Nat. Energy* 2 (2017), p. 16216.
- [62] A. C. Forse et al. In: *J. Am. Chem. Soc.* 140.5 (2018), pp. 1663–1673.
- [63] D. Frenkel et al. In: *Comput. Phys.* 11.4 (1997), pp. 351–354.
- [64] I. Furó and S. V. Dvinskikh. In: *Magn. Reson. Chem.* 40 (2002), S3.
- [65] H. Furukawa and O. M. Yaghi. In: *J. Am. Chem. Soc.* 131.25 (2009), pp. 8875–8883.
- [66] H. Furukawa et al. In: *Science* 341 (2013), p. 1230444.
- [67] S. J. Geier et al. In: *Chem. Sci.* 4 (2013), p. 2054.
- [68] R. B. Getman et al. In: *Chem. Rev.* 112.2 (2012), pp. 703–723.
- [69] T. G. Glover et al. In: *Chem. Eng. Sci.* 66 (2011), p. 163.
- [70] G. Gody et al. In: *Nat. Commun.* 4 (2013), p. 2505.
- [71] C. A. Grande and R. Blom. In: *Energy Procedia* 26 (2012), p. 2.
- [72] S. Grimme. In: *J. Comput. Chem.* 27 (2006), p. 1787.
- [73] Amit Gupta et al. In: *Mol. Simul.* 29.1 (2003), pp. 29–46.
- [74] D. Gygi et al. In: *Chem. Mater.* 28 (2016), p. 1128.
- [75] E. Haldoupis et al. In: *J. Phys. Chem. C* 119 (2015), p. 16058.
- [76] S. S. Han and W. A. Goddard III. In: *J. Phys. Chem. C* 112.35 (2008), pp. 13431–13436.

- [77] S. S. Han, J. L. Mendoza-Cortés, and W. A. Goddard III. In: *Chem. Soc. Rev.* 38.5 (2009), pp. 1460–1476.
- [78] S. S. Han et al. In: *J. Am. Chem. Soc.* 130.35 (2008), pp. 11580–11581.
- [79] M. D. Hanwell et al. In: *J. Cheminf.* 4.1 (2012), p. 17.
- [80] M. D. Hanwell et al. *Avogadro: an open-source molecular builder and visualization tool. Version 1.1.1.* 2012.
- [81] M. Haranczyk. *Zeo++*. Version 0.3. using June 20, 2017 release throughout this work. URL: <http://www.zeoplusplus.org/> (visited on 06/20/2017).
- [82] M. Haranczyk et al. In: *Phys. Chem. Chem. Phys.* 15.48 (2013), pp. 20937–20942.
- [83] J. G. Harris and K. H. Yung. In: *J. Phys. Chem.* 99 (1995), p. 12021.
- [84] Y.-S. Ho and H.-Z. Fu. In: *Inorg. Chem. Commun.* 73 (2016), pp. 174–182.
- [85] J. P. Holdren et al. In: *National Science and Technology Council OSTP. Washington, USA* (2011).
- [86] W. G. Hoover. In: *Phys. Rev. A: At., Mol., Opt. Phys.* 31 (1985), p. 1695.
- [87] H. W. Horn, W. C. Swope, and J. W. Pitera. In: *J. Chem. Phys.* 123 (2005), p. 194504.
- [88] H. W. Horn et al. In: *J. Chem. Phys.* 120 (2004), p. 9665.
- [89] Robert W Howarth, Renee Santoro, and Anthony Ingraffea. In: *Clim. Change* 106.4 (2011), pp. 679–690.
- [90] J. M. Huck et al. In: *Energy Environ. Sci.* 7.12 (2014), pp. 4132–4146.
- [91] J. E. Huheey and T. L. Cottrell. 1958.
- [92] K. Jackowski and M. Jaszunski. Ed. by Karol Jackowski and Michal Jaszunski. Cambridge, UK: Royal Society of Chemistry, 2016. ISBN: 9781849735568.
- [93] C. J. Jameson. “Chapter 1 Fundamental Intramolecular and Intermolecular Information from NMR in the Gas Phase”. In: (2016), pp. 1–51.
- [94] J.-X. Jiang et al. In: *J. Am. Chem. Soc.* 130.24 (2008), pp. 7710–7720.
- [95] H. Jo et al. In: *ChemSusChem* 10 (2017), p. 541.
- [96] H. Jobic et al. In: *J. Phys. Chem. B* 110 (2006), p. 2195.
- [97] W. L. Jorgensen et al. In: *J. Chem. Phys.* 79 (1983), p. 926.
- [98] H. M. El-Kaderi et al. In: *Science* 316.5822 (2007), pp. 268–272.
- [99] M. Kadi et al. In: *Langmuir* 18 (2002), p. 5015.
- [100] J. Kaerger et al. In: *Chem. Eng. and Technol.* 32.10 (2009), pp. 1494–1511.
- [101] H. Kamberaj, R. J. Low, and M. P. Neal. In: *J. Chem. Phys.* 122 (2005), p. 224114.
- [102] J. Karger and H. Spindler. In: *J. Am. Chem. Soc.* 113 (1991), p. 7571.

- [103] P. Katekomol et al. In: *Chem. Mater.* 25.9 (2013), pp. 1542–1548.
- [104] S. Keskin, T. M. van Heest, and D. S. Sholl. In: *ChemSusChem* 3 (2010), p. 879.
- [105] J. Kim et al. In: *J. Am. Chem. Soc.* 135 (2013), p. 7545.
- [106] Axel Kohlmeyer. *TopoTools*. 2017.
- [107] X. Kong et al. In: *J. Am. Chem. Soc.* 134 (2012), p. 14341.
- [108] X. Kong et al. In: *J. Am. Chem. Soc.* 134.35 (Sept. 2012), pp. 14341–4. ISSN: 1520-5126.
- [109] M. Korth et al. In: *J. Chem. Theory Comput.* 6.1 (2009), pp. 344–352.
- [110] J. Kowalewski. Vol. 22. C. 1990, pp. 307–414. ISBN: 0125053223.
- [111] G. Kresse and J. Furthmüller. In: *Phys. Rev. B* 54 (16 Oct. 1996), pp. 11169–11186.
- [112] G. Kresse and D. Joubert. In: *Phys. Rev. B* 59 (3 Jan. 1999), pp. 1758–1775.
- [113] R. Krishna and J. M. van Baten. In: *J. Membr. Sci.* 360 (2010), p. 323.
- [114] R. Krishna and J. M. van Baten. In: *Phys. Chem. Chem. Phys.* 13 (2011), p. 10593.
- [115] R. Krishna and Jasper M van Baten. In: *Phys. Chem. Chem. Phys.* 15.21 (June 2013), pp. 7994–8016. ISSN: 1463-9084.
- [116] K. V. Kumar et al. In: *Chem. Rev.* 117.3 (2017), pp. 1796–1825.
- [117] R. J. Kuppler et al. In: *Coord. Chem. Rev.* 253.23-24 (Dec. 2009), pp. 3042–3066. ISSN: 00108545.
- [118] K. Lee et al. In: *Phys. Rev. B: Condens. Matter Mater. Phys.* 82 (2010), p. 081101.
- [119] K. Lee et al. In: *Chem. Mater.* 27 (2015), p. 668.
- [120] K. Lee et al. In: *Chem. Mater.* 27.3 (2015), pp. 668–678.
- [121] W. R. Lee et al. In: *Chem. Sci.* 6 (2015), p. 3697.
- [122] E. W. Lemmon, M. L. Huber, and M. O. McLinden. In: *Ref. Fluid Thermodyn. Transp. Prop.* (2012).
- [123] B. Li et al. In: *J. Am. Chem. Soc.* 136.17 (2014), pp. 6207–6210.
- [124] H. Li et al. In: *J. Am. Chem. Soc.* 120.33 (1998), pp. 8571–8572.
- [125] J. Li et al. In: *Nat. Mater.* 10 (2011), p. 507.
- [126] L.-C. Lin et al. In: *Nat. Mater.* 11 (2012), p. 633.
- [127] L.-C. Lin et al. In: *Angew. Chem., Int. Ed.* 52 (2013), p. 4410.
- [128] L.-C. Lin et al. In: *Angew. Chem.* 125 (2013), p. 4506.
- [129] L.-C. Lin et al. In: *J. Chem. Theory Comput.* 10 (2014), p. 1477.
- [130] Lujia Liu et al. In: *J. Am. Chem. Soc.* 135.47 (2013), pp. 17731–17734.
- [131] W. Lu et al. In: *Chem. Mater.* 22.21 (2010), pp. 5964–5972.

- [132] J.-F. Lutz et al. In: *Science* 341.6146 (2013), p. 1238149.
- [133] C. F. Macrae et al. In: *J. Appl. Crystallogr.* 39.3 (2006), pp. 453–457.
- [134] M. J. D. Mahboub, A. Ahmadpour, and H. Rashidi. In: *J. Fuel Chem. Technol.* 40.4 (2012), pp. 385–389.
- [135] M. W. Mahoney and W. L. Jorgensen. In: *J. Chem. Phys.* 112 (2000), p. 8910.
- [136] J. A. Maier et al. In: *J. Chem. Theory Comput.* 11.8 (2015), pp. 3696–3713.
- [137] Y. Mao and Y. Zhang. In: *J. Nanotechnol. Eng. Med.* 3 (2012), p. 031009.
- [138] P. Mark and L. Nilsson. In: *J. Phys. Chem. A* 105 (2001), p. 9954.
- [139] R. M. Marti et al. In: *J. Phys. Chem. C* 121 (2017), p. 25778.
- [140] M. G. Martin and J. I. Siepmann. In: *J. Phys. Chem. B* 102 (1998), p. 2569.
- [141] R. L. Martin and M. Haranczyk. In: *Cryst. Growth Des.* 14.5 (2014), pp. 2431–2440.
- [142] R. L. Martin, B. Smit, and M. Haranczyk. In: *J. Chem. Inf. Model.* 52.2 (2011), pp. 308–318.
- [143] R. L. Martin et al. In: *J. Phys. Chem. C* 117.39 (2013), pp. 20037–20042.
- [144] R. L. Martin et al. In: *J. Phys. Chem. C* 118.41 (2014), pp. 23790–23802.
- [145] R. L. Martin et al. In: *J. Am. Chem. Soc.* 136.13 (2014), pp. 5006–5022.
- [146] J. A. Mason, Mike Veenstra, and J. R. Long. In: *Chem. Sci.* 5.1 (2014), pp. 32–51.
- [147] J. A. Mason et al. In: *Energy Environ. Sci.* 4 (2011), p. 3030.
- [148] J. A. Mason et al. In: *J. Am. Chem. Soc.* 137 (2015), p. 4787.
- [149] J. A. Mason et al. In: *Nature* 527.7578 (2015), pp. 357–361.
- [150] *Materials Cloud*. URL: <https://www.materialscloud.org> (visited on 03/14/2018).
- [151] M. Matsumoto et al. In: *J. Am. Chem. Soc.* 139.14 (2017), pp. 4999–5002.
- [152] S. L. Mayo, B. D. Olafson, and W. A. Goddard III. In: *J. Phys. Chem.* 94 (1990), p. 8897.
- [153] S. L. Mayo, B. D. Olafson, and W. A. Goddard III. In: *J. Phys. Chem.* 94.26 (1990), pp. 8897–8909.
- [154] R. E. D. McClung. In: *eMagRes* (2007).
- [155] T. M. McDonald et al. In: *J. Am. Chem. Soc.* 134 (2012), p. 7056.
- [156] T. M. McDonald et al. In: *Nature* 519 (2015), p. 303.
- [157] N. B. McKeown, P. M. Budd, and D. Book. In: *Macromol. Rapid Commun.* 28.9 (2007), pp. 995–1002.
- [158] G. P McTaggart-Cowan, C. C. O. Reynolds, and W. K. Bushe. In: *Int. J. Environ. Stud.* 63.4 (2006), pp. 421–440.

- [159] J. L. Mendoza-Cortés, T. A. Pascal, and W. A. Goddard III. In: *J. Phys. Chem. A* 115.47 (2011), pp. 13852–13857.
- [160] J. L. Mendoza-Cortés et al. In: *J. Phys. Chem. A* 114.40 (2010), pp. 10824–10833.
- [161] J. L. Mendoza-Cortés et al. In: *J. Phys. Chem. Lett.* 3.18 (2012), pp. 2671–2675.
- [162] V. C. Menon and S. Komarneni. In: *J. Porous Mater.* 5.1 (1998), pp. 43–58.
- [163] R. Mercado et al. In: *J. Phys. Chem. C* 120.23 (2016), pp. 12590–12604.
- [164] A. R. Millward and O. M. Yaghi. In: *J. Am. Chem. Soc.* 127 (2005), p. 17998.
- [165] P. J. Milner et al. In: *J. Am. Chem. Soc.* 139 (2017), p. 13541.
- [166] J. P. Barbosa Mota et al. In: *Carbon* 35.9 (1997), pp. 1259–1270.
- [167] A. L. Myers and J. M. Prausnitz. In: *AIChE J.* 11.1 (1965), pp. 121–127.
- [168] H. Nada and J. P. J. M. van der Eerden. In: *J. Chem. Phys.* 118 (2003), p. 7401.
- [169] S. A. Nosé. In: *Mol. Phys.* 52 (1984), p. 255.
- [170] N. M. O’Boyle et al. In: *J. Cheminf.* 3 (2011), p. 33.
- [171] Takahiro Ohkubo et al. In: *J. Phys. Chem. B* 106.25 (2002), pp. 6523–6528.
- [172] M. O’Keeffe et al. In: *Acc. Chem. Res.* 41.12 (2008), pp. 1782–1789.
- [173] D. Ongari et al. In: *Langmuir* 33.51 (2017), pp. 14529–14538.
- [174] S. Pakhira, K. P. Lucht, and J. L. Mendoza-Cortés. In: *J. Phys. Chem. C* 121.39 (2017), pp. 21160–21170.
- [175] Has Mukh A Patel et al. In: *Nat. Commun.* 4 (2013), p. 1357.
- [176] C. Pei, T. Ben, and S. Qiu. In: *Mater. Horiz.* 2.1 (2014), pp. 11–21.
- [177] C. Pei et al. In: *Chem. Commun.* 50.46 (2014), pp. 6134–6136.
- [178] M. Peksa, J. Lang, and F. Stallmach. In: *Microporous Mesoporous Mater.* 205 (2015), p. 11.
- [179] M. Peksa et al. In: *Microporous Mesoporous Mater.* 216 (2015), p. 75.
- [180] X. Peng et al. In: *AIChE J.* 61 (2015), p. 677.
- [181] Yang Peng et al. In: *J. Am. Chem. Soc.* 135.32 (2013), pp. 11887–11894.
- [182] J. P. Perdew, K. Burke, and M. Ernzerhof. In: *Phys. Rev. Lett.* 77 (18 Oct. 1996), pp. 3865–3868.
- [183] S. Plimpton. In: *J. Comput. Phys.* 117 (1995), pp. 1–19.
- [184] R. Poloni et al. In: *J. Phys. Chem. Lett.* 5 (2014), p. 861.
- [185] Jeffrey J Potoff and J Ilja Siepmann. In: *AIChE J.* 47.7 (2001), pp. 1676–1682.
- [186] A.-K. Pusch et al. In: *Adsorption* 18.5-6 (Sept. 2012), pp. 359–366. ISSN: 0929-5607.
- [187] W. L. Queen et al. In: *Chem. Sci.* 5.12 (2014), pp. 4569–4581.

- [188] A. K. Rappe and W. A. Goddard. In: *J. Phys. Chem.* 95 (1991), p. 3358.
- [189] A. K. Rappé et al. In: *J. Am. Chem. Soc.* 114.25 (1992), pp. 10024–10035.
- [190] J. Řezáč et al. In: *J. Chem. Theory Comput.* 5.7 (2009), pp. 1749–1760.
- [191] S. W. Rick. In: *J. Chem. Phys.* 120 (2004), p. 6085.
- [192] N. L. Rosi et al. In: *J. Am. Chem. Soc.* 127 (2005), p. 1504.
- [193] A. N. Rudenko, S. Bendt, and F. J. Keil. In: *J. Phys. Chem. C* 118 (2014), p. 16218.
- [194] F. Salles et al. In: *ACS Nano* 4 (2010), p. 143.
- [195] Sandia National Labs. *LAMMPS*. using July 30, 2016 release throughout this work. URL: <http://lammps.sandia.gov> (visited on 07/30/2016).
- [196] R. Sanz et al. In: *Dalt. Trans.* 42 (2013), p. 2392.
- [197] A. Schoedel, Z. Ji, and O. M. Yaghi. In: *Nat. Energy* 1.4 (Apr. 2016), p. 16034. ISSN: 2058-7546.
- [198] P. M. Schoenecker et al. In: *Ind. Eng. Chem. Res.* 51 (2012), p. 6513.
- [199] R. L. Siegelman et al. In: *J. Am. Chem. Soc.* 139.30 (2017), pp. 10526–10538.
- [200] J. M. Simmons et al. In: *Energy Environ. Sci.* 4 (2011), p. 2177.
- [201] C. M. Simon et al. In: *Energy Environ. Sci.* 8.4 (2015), pp. 1190–1199.
- [202] A. G. Slater and A. I. Cooper. In: *Science* 348.6238 (2015), aaa8075.
- [203] B. Smit et al. World Scientific, 2014.
- [204] B. J. Smith et al. In: *Chem. Commun.* 52.18 (2016), pp. 3690–3693.
- [205] F. Stallmach et al. In: *Angew. Chem. Int. Ed. Engl.* 45.13 (Mar. 2006), pp. 2123–6. ISSN: 1433-7851.
- [206] F. Stallmach et al. In: *Microporous Mesoporous Mater.* 205 (Aug. 2015), pp. 36–39. ISSN: 13871811.
- [207] S. Stapf, R. Kimmich, and R.-O. Seitter. In: *Phys. Rev. Lett.* 75.15 (1995), p. 2855.
- [208] J. J. P. Stewart. In: *J. Mol. Model.* 13.12 (2007), pp. 1173–1213.
- [209] E. Stöckel et al. In: *Chem. Commun.* 2 (2009), pp. 212–214.
- [210] K. Sumida et al. In: *Chem. Rev.* 112.2 (2011), pp. 724–781.
- [211] S. Surble et al. In: *J. Am. Chem. Soc.* 128 (2006), p. 14889.
- [212] A. Sutrisno and Y. Huang. In: *Solid State Nucl. Magn. Reson.* 49-50 (Feb. 2013), pp. 1–11. ISSN: 1527-3326.
- [213] O. Talu and A. L. Myers. In: *AIChE J.* 47.5 (2001), pp. 1160–1168.
- [214] J. M. H. Thomas and A. Trewin. In: *J. Phys. Chem. C* 118.34 (2014), pp. 19712–19722.

- [215] M. Tong et al. In: *Chem. Eng. Sci.* 168 (2017), pp. 456–464.
- [216] D. Topgaard. In: *J. Magn. Reson.* 275 (2017), p. 98.
- [217] T. M. Tovar et al. In: *J. Am. Chem. Soc.* 138 (2016), p. 11449.
- [218] A. Trewin and A. I. Cooper. In: *Angew. Chem., Int. Ed.* 49.9 (2010), pp. 1533–1535.
- [219] F. J. Uribe-Romo et al. In: *J. Am. Chem. Soc.* 131.13 (2009), pp. 4570–4571.
- [220] R. Valiullin et al. In: *Nature* 443 (2006), p. 965.
- [221] K. Vanommeslaeghe et al. In: *J. Comput. Chem.* 31.4 (2010), pp. 671–690.
- [222] C. Vega, E. Sanz, and J. L. F. Abascal. In: *J. Chem. Phys.* 122 (2005), p. 114507.
- [223] E. Vitaku and W. R. Dichtel. In: *J. Am. Chem. Soc.* 139.37 (2017), pp. 12911–12914.
- [224] P. J. Waller, F. Gándara, and O. M. Yaghi. In: *Acc. Chem. Res.* 48.12 (2015), pp. 3053–3063.
- [225] P. J. Waller et al. In: *J. Am. Chem. Soc.* 138.48 (2016), pp. 15519–15522.
- [226] Krista S Walton and R. Q. Snurr. In: *J. Am. Chem. Soc.* 129.27 (2007), pp. 8552–8556.
- [227] L. Wang, T. Maxisch, and G. Ceder. In: *Phys. Rev. B: Condens. Matter Mater. Phys.* 73 (2006), p. 195107.
- [228] Michael Q Wang and Hann S Huang. Tech. rep. Argonne National Lab., IL (US), 2000.
- [229] C. D. Wick, M. G. Martin, and J. I. Siepmann. In: *J. Phys. Chem. B* 104 (2000), p. 8008.
- [230] T. F. Willems et al. In: *Microporous Mesoporous Mater.* 149.1 (2012), pp. 134–141.
- [231] E. B. Winn. In: *Phys. Rev.* 80 (1950), p. 1024.
- [232] H. Wu, W. Zhou, and T. Yildirim. In: *J. Am. Chem. Soc.* 131.13 (2009), pp. 4995–5000. ISSN: 00027863.
- [233] S. Xiang et al. In: *Nat. Commun.* 3 (2012), p. 954.
- [234] Z. Xiang and D. Cao. In: *J. Mater. Chem. A* 1.8 (2013), pp. 2691–2718.
- [235] Z. Xiang, S. Leng, and D. Cao. In: *J. Phys. Chem. C* 116.19 (2012), pp. 10573–10579.
- [236] Z. Xiang et al. In: *J. Phys. Chem. C* 113.34 (2009), pp. 15106–15109.
- [237] Z. Xiang et al. In: *J. Phys. Chem. C* 116.9 (2012), pp. 5974–5980.
- [238] Z. Xiang et al. In: *Adv. Mater.* 26.20 (2014), pp. 3315–3320.
- [239] Z. Xiang et al. In: *Angew. Chem., Int. Ed.* 53.9 (2014), pp. 2433–2437.
- [240] Z. Xiang et al. In: *J. Am. Chem. Soc.* 137.41 (2015), pp. 13301–13307.
- [241] Y. Xu et al. In: *Chem. Soc. Rev.* 42.20 (2013), pp. 8012–8031.

- [242] D.-A. Yang et al. In: *Energy Environ. Sci.* 5 (2012), p. 6465.
- [243] S. Yeh. In: *Energy Policy* 35.11 (2007), pp. 5865–5875.
- [244] D. Yuan et al. In: *Adv. Mater.* 23.32 (2011), pp. 3723–3725.
- [245] Y.-B. Zhang et al. In: *J. Am. Chem. Soc.* 135.44 (2013), pp. 16336–16339.
- [246] W. Zhou, H. Wu, and T. Yildirim. In: *J. Am. Chem. Soc.* 130 (2008), p. 15268.
- [247] S. Ziaii, G. T. Rochelle, and T. F. Edgar. In: *Ind. Eng. Chem. Res.* 48.13 (2009), pp. 6105–6111.